NONLINEAR FINITE ELEMENT ANALYSIS OF REINFORCED CONCRETE EXTERIOR BEAM-COLUMN JOINTS WITH NONSEISMIC DETAILING

A Thesis
Presented to
The Academic Faculty

by

James B. Deaton

In Partial Fulfillment
of the Requirements for the Degree
Doctor of Philosophy

School of Civil and Environmental Engineering
Georgia Institute of Technology
May 2013

NONLINEAR FINITE ELEMENT ANALYSIS OF REINFORCED CONCRETE EXTERIOR BEAM-COLUMN JOINTS WITH NONSEISMIC DETAILING

Approved by:

Dr. Kenneth M. Will, Advisor
School of Civil and Env. Engineering
Georgia Institute of Technology

Dr. Bruce R. Ellingwood
School of Civil and Env. Engineering
Georgia Institute of Technology

Dr. Lawrence F. Kahn
School of Civil and Env. Engineering
Georgia Institute of Technology

Dr. T. Russell Gentry
School of Architecture
Georgia Institute of Technology

Dr. Leroy Z. Emkin
School of Civil and Env. Engineering
Georgia Institute of Technology

Date Approved: 17 December 2012

For he was looking forward to the city that has foundations, whose designer and builder is God.

Hebrews 11:10, The Holy Bible (ESV)

ACKNOWLEDGEMENTS

I must begin by expressing my tremendous appreciation and respect for my advisor, Dr. Kenneth M. Will. Thank you for your support, guidance, and patience during my tenure in graduate school. I am grateful to have had the opportunity to learn from your example and discerning eye. Thank you also for the freedom to develop this project into its current form and pursue something that genuinely interested me.

I am also deeply appreciative to Dr. Lawrence F. Kahn for always being willing to discuss research questions and for the chance to work together on some interesting structural failures over the years. If Dr. Will taught me what I know of finite element analysis, you have taught me what I know of concrete.

I would like to thank Dr. Bruce R. Ellingwood, Dr. Roberto T. Leon, Dr. Leroy Z. Emkin, and Dr. T. Russell Gentry for the time and effort spent serving on my committee and for pushing me toward deeper understanding of my topic—this research benefited greatly from your expertise and input.

Financial support from the Georgia Tech Computer-Aided Structural Engineering (CASE) Center is gratefully acknowledged.

I owe much credit for the premise of this work to my friend and colleague, Dr. Murat Engindeniz, whose experimental work highlighted the fascinating failure processes in beam-column joints over the course of many departmental seminars and left me wondering: *Could I model that?* I am similarly indebted to Dr. Laura Lowes for organizing a blind prediction competition on beam-column joint response—it was while attending an ACI convention session summarizing the results of this competition that the present project began to coalesce in my mind.

I owe much credit for the success of this work to TNO DIANA for their technical

support to this project during its various phases. Special thanks are due to Dr. Pranesh Chatterjee and Dr. Maziar Partovi for their expert counsel and unending patience responding to my emails.

Thank you to Dr. Murat Engindeniz and Dr. Umut Akgüzel for reviewing portions of this thesis.

I would like to thank the researchers and staff in the CASE Center for their technical and practical help throughout my time at Georgia Tech. Thanks also to my officemates for years of generative conversations: Dr. Efe Guney, Dr. Jong-Han Lee, Dr. Gwangseok Na, and soon-to-be Drs. Mustafa Can Kara, Julian Diaz-Ospina, Borja Zarco, and Parsa Banihashemi. I owe a great debt of gratitude to my friends David Ashley, Dr. Kennan Crane, Dr. John Richardson, Dr. Shane Johnson, and Dr. Brett Holland for helping me navigate research roadblocks and the graduate school experience. Thank you also to Jason and Shane Ardell, whose assistance with regular expressions and data processing saved me countless hours.

To the brothers and sisters in our church who have walked through this season with me: You have gone far beyond the call of duty to love and support me and my family. Every prayer and act of service was felt and deeply appreciated. To my second family, the Mooneys: Thank you also for your frequent encouragement. To my parents, Jimmy and Wanda Deaton: Thank you for a lifetime of love, support, and belief in me.

Words cannot do justice to the unending supply of patience, love, and grace bestowed upon me by my wife Gina during these past years. I will probably never fully know the depth of the sacrifices you have made to allow me to pursue this dream.

And finally, to my beautiful and brilliant daughter Norah whose entire life until now has been parented by a father in graduate school: I am all yours.

TABLE OF CONTENTS

LIST OF TABLES

LIST OF FIGURES

SUMMARY

This research investigated the behavior of nonseismically detailed reinforced concrete exterior beam-column joints subjected to bidirectional lateral cyclic loading using nonlinear finite element analysis (NLFEA).

Beam-column joints constitute a critical component in the load path of reinforced concrete buildings due to their fundamental role in integrating the overall structural system. Earthquake reconnaissance reports reveal that failure of joints has contributed to partial or complete collapse of reinforced concrete buildings designed without consideration for large lateral loads, resulting in significant economic impact and loss of life. Such infrastructure exists throughout seismically active regions worldwide, and the large-scale risk associated with such deficiencies is not fully known. Computational strategies provide a useful complement to the existing experimental literature on joint behavior and are needed to more fully characterize the failure processes in seismically deficient beam-column joints subjected to realistic failure conditions. Prior to this study, vulnerable reinforced concrete corner beam-column joints including the slab had not been analyzed using nonlinear finite element analysis and compared with experimental results.

The first part of this research focused on identification and validation of a constitutive modeling strategy capable of simulating the behaviors known to dominate failure of beam-column joints under cyclic lateral load using NLFEA. This prototype model was formulated by combining a rotating smeared crack concrete constitutive model with a reinforcing bar plasticity model and nonlinear bond-slip formulation. This model was systematically validated against experimental data, and parametric studies were conducted to determine the sensitivity of the response to various material properties. The

prototype model was then used to simulate the cyclic response of four seismically deficient beam-column joints which had been previously evaluated experimentally. The simulated joints included: a one-way exterior joint, a two-way beam-column exterior corner joint, and a series of two-way beam-column-slab exterior corner joints with varying degrees of seismic vulnerability. The two-way corner joint specimens were evaluated under simultaneous cyclic bidirectional lateral and cyclic column axial loading. For each specimen, the ability of the prototype model to capture the strength, stiffness degradation, energy dissipation, joint shear strength, and progressive failure mechanisms (e.g. cracking) was demonstrated.

CHAPTER I

INTRODUCTION

1.1 Scope

This document outlines a research program to numerically investigate the behavior of reinforced concrete exterior beam-column joints with seismically deficient detailing when subjected to multiaxial reversed cyclic loading.

1.2 Behavior of Seismically Deficient Beam-Column Joints

Reinforced concrete buildings constructed prior to the adoption of seismic design provisions embody design deficiencies which have resulted in significant economic and life losses during earthquakes. Such infrastructure exists ubiquitously throughout seismically active regions worldwide, and the large-scale risk of such seismic deficiencies is not fully known. Beam-column joints constitute a critical component in the seismic resilience of such structures, due to the fundamental role played in integrating the overall structural system in buildings.

Over the past decades, the seismic vulnerability of exterior beam-column joints has been documented repeatedly in earthquake reconnaissance reports, in which joint failure has been identified as a contributing factor in the total loss of vertical load carrying capacity and collapse of gravity-load-designed buildings in many cases [202]. A representative corner joint failure from the 1999 Kocaeli (Izmit), Turkey, earthquake is shown in Figure 1.1.

Exterior corner joints in gravity-load-designed buildings typically sustain significantly greater damage during seismic events in comparison to interior joints for several well-known reasons, documented by Engindeniz [60]: (1) they are the least confined of

Source: Sezen [202]

Figure 1.1: Characteristic Failure of an Exterior Corner Joint

all building joints, due to the presence of beams on only two adjacent faces of the joint, (2) axial forces in exterior columns are typically less than that of interior columns under gravity loads and can be significantly reduced further due to overturning effects during lateral loads, (3) beam eccentricities and the unsymmetric presence of the slab lead to increased torsion transferred into the joint from the beams, (4) biaxial bending of the column due to the combined actions of two orthogonal frames results in increased axial stresses at the interior and exterior corners of the column in the joint region, and (5) they experience the greatest effect from overall torsion of the building during earthquakes due to being typically located the furthest distance from the building's center of rigidity.

Prior to the adoption of seismic design provisions and/or in areas of low seismicity, such joints were typically designed only to resist gravity loads, with little or no consideration given to the possibility of load reversal and the subsequent redistribution of force throughout the structure when subjected to lateral forces arising from seismic

events. After conducting an extensive review of detailing manuals (ACI 315) and design codes (ACI 318) from over five decades, and through consultation with practicing structural engineers, Beres et al. [26] identified seven key design details characteristic of seismically deficient beam-column joints. Representative interior and exterior joints with nonseismic detailing are illustrated in Figure 1.2 and possess the following characteristics: (1) longitudinal reinforcement ratio in the columns less than 2%, (2) column reinforcement lap splices located at the maximum moment region just above floor levels, (3) widely spaced column ties providing little confinement to concrete, (4) little or no transverse shear reinforcement within the beam-column joint, (5) discontinuous beam bottom reinforcement with insufficient embedment length into the joint region, susceptible to complete loss of anchorage under load reversal, (6) construction joints directly above or below the beam-column joint, and (7) columns with bending moment capacity less than that of beams (strong beam-weak column), susceptible to soft-story mechanisms. The literature synonymously refers to joints possessing such deficiencies as: "pre-1970", "lightly reinforced", "gravity-load-designed (GLD)", and "nonseismically detailed" joints. Joints belonging to this category may have been built prior to the development of seismic design specifications, or constructed improperly due to lack of enforcement of existing building codes.

As the seismic inadequacy of much existing infrastructure was established, extensive research programs were initiated to quantify the influence of each of these deficiencies (and other parameters) on the performance of beam-column connections, as well as to categorize the strength hierarchy under cyclic lateral loading. Detailed reviews of prior experimental work on inadequate joints have been recently presented elsewhere by Celik [31], Engindeniz [61], and Park [178]. These reviews found that the majority of prior experimental work focused on one-way systems which possessed neither transverse beams nor slab, were often only loaded unidirectionally, and in many cases were

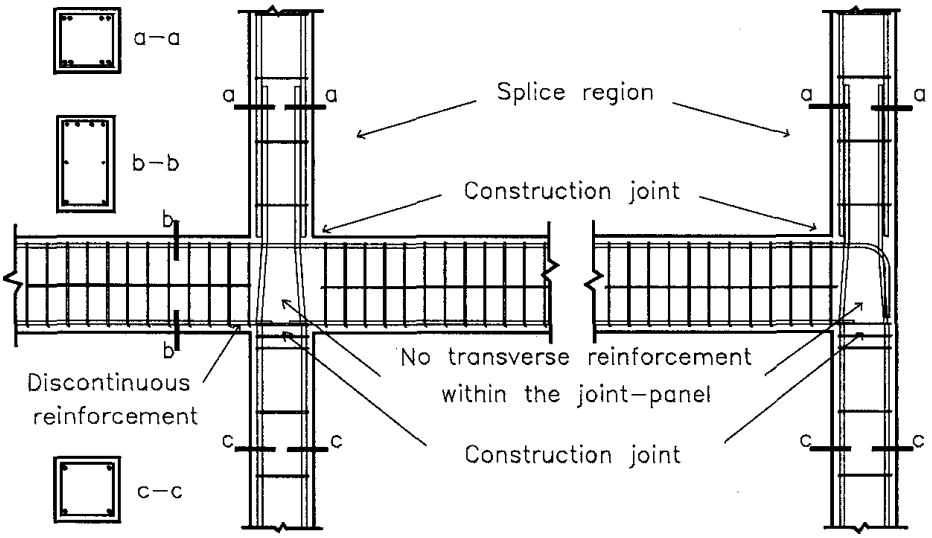

Source: Beres et al. [26]

Figure 1.2: Seismic Deficiencies in Interior and Exterior Beam-Column Joints

constructed at reduced scale—all simplifications which may have resulted in an experimental response exhibiting significant deviation from the actual behavior of full-scale connections in a laterally loaded, three-dimensional, gravity-load-designed building.

To address these limitations and evaluate the performance of beam-column joints under more realistic conditions, several recent studies have been published in which the response of bidirectional cyclic loading on corner joint performance was either directly or indirectly evaluated. Hertanto [80], Chen [35], and Akgüzel [9, 10, 11] experimentally evaluated pre-1970s corner joints in as-built and rehabilitated configurations without slab under cyclic bidirectional lateral loading and simultaneous cyclic column axial force which simulated overturning effects. Engindeniz et al. [60, 62] tested a series of full-scale corner beam-column joints with integral slab possessing multiple seismic deficiencies under bidirectional cyclic loading, and evaluated the efficacy of various FRP retrofit schemes. Park and Mosalam [179, 180] investigated the experimental response of a series of full-scale corner beam-column-slab joints which lacked transverse reinforcements in the joint core, under bidirectional cyclic lateral loading and cyclic column

(a) (b) (c)

Figure 1.3: Experimental Exterior Corner Joint Specimens: (a) Akgüzel et al. [9], (b) Engindeniz et al. [60], (c) Park and Mosalam [179]

compression. Balsamo et al. [21] and Di Ludovico et al. [44] tested a full-scale torsionally unbalanced three-story structure with inadequate seismic detailing subjected to a ground motion oriented so as to maximize the effect of overall torsion on the response of the building, primarily evaluating the global response of the system in both its pre- and post-rehabilitated configurations along with the performance of key joints, including rehabilitated corner joints. Several of these experimental programs are depicted in Figure 1.3.

Together, these studies confirmed that bidirectional lateral loading generates significantly higher demands on the joint than those predicted during more simplified, one-way exterior joint experiments commonly reported in the literature. The key findings were as follows: Corner joints with nonseismic detailing were shown to be susceptible to rapid degradation of strength and stiffness under bidirectional loading at relatively low interstory drift levels ($< 2\%$) [60]. The resultant joint shear force developed under bidirectional loading was shown to be significantly larger than the shear force developed in a primary direction by unidirectional loading, which—together with reduced

column axial force due to overturning effects—resulted in a remarkable reduction in joint shear capacity [9]. The column capacity was reduced due to loss of anchorage and section losses at the opposite interior and exterior corners due to biaxial bending, as previous studies have observed [116]. Slab-induced torsion resulted in significantly increased and nonuniform strains in beam longitudinal reinforcement in comparison to those predicted based on strong-axis beam moments, accelerating both pull-out of beam bottom bars and failure of the joint [60].

1.3 Need for Numerical Simulation of Beam-Column Joints

Despite the progress shown in the studies cited above, the behavior of corner joints with seismically deficient detailing under bidirectional loading is still not fully understood, and many factors need to be investigated to better characterize the strength and ductility of such joints. Recent recommendations from Joint ACI-ASCE Committee 352 (*Joints and Connections in Monolithic Concrete Structures*) specifically state the need for further research concerning the behavior of existing joints with nonseismic detailing: "Joints in structures built before the development of current design guidelines do not conform to the current requirements. These joints need to be studied in detail to establish their adequacy and to develop evaluation guidelines for building rehabilitation" [6].

While many experimental studies have been employed to this end, even the most extensive experimental studies cannot fully capture the interaction of the large number of variables contributing to the performance of the joint. Additionally, full-scale experimental studies incur significant cost, both in terms of money and time, which limits the number of parameters which may be investigated in the laboratory. Numerical simulation provides a useful complement to precise experimental research by addressing some of these challenges.

The finite element method is a powerful tool by which the behavior of beam-column

joints can be efficiently explored under a variety of conditions. Three-dimensional nonlinear finite element analysis provides a continuum-level representation of the internal joint stress and strain distribution, progression of damage, and force transfer mechanisms.

To date, the analysis of nonseismically detailed joints under more realistic conditions (such as exterior corner joints with transverse beams and slab subjected to bidirectional loading) has been limited due to the scarcity of suitable experimental data necessary for model validation. Because of this, most numerical simulations of beam-column joints have focused on one-way joints for which extensive experimental data existed. However, as the complexity of joint experimentation has progressed and more realistic joints have been evaluated (as previously described in this chapter and shown in Figure 1.3), numerical models incorporating floor members and bidirectional cyclic loading may now be developed and validated.

Based on this opportunity, a methodology for nonlinear finite element analysis of three-dimensional joint specimens must be systematically identified. Such a model must necessarily account for many types of complex nonlinear material behavior, including the failure of concrete under a triaxial stress state (compression crushing, shear failure as identified through principal tensile stress, localized tension softening or tension stiffening, and crack propagation), damage evolution and elastic degradation under cyclic loading, plasticity in reinforcing steel, the influence of concrete confinement on concrete strength, and degradation of bond, ranging from simple bond-slip to complete loss of anchorage.

Once a nonlinear finite element-based joint simulation methodology has been verified against experimental results, such analyses offer many practical applications. Parametric studies can be performed to explore the influence of various factors on the behavior of the joint under many combinations. Such factors requiring further inquiry include: (1) the effect of concrete compressive strength, (2) the effect of column axial

load ratio on joint shear failure, (3) the effect of various joint transverse reinforcement configurations on joint confinement, (4) the influence of the slab on load transfer from the floor system into the joint, (5) the influence of increased beam moment capacity due to the presence of the slab and the resulting decrease in the column-to-beam moment ratio, (6) the influence of torsion due to beam eccentricities, and (7) the influence of the slab on the yielding and potential loss of anchorage of beam longitudinal reinforcement. While many of these factors have been methodically studied for one-way joints, the significance of each parameter needs to be quantified for two-way joints and critically compared with the current knowledge of joint behavior.

Further applications of a finite element modeling approach for joints are numerous. Experimental studies can be more effectively planned, and novel retrofit schemes may be evaluated prior to laboratory testing to eliminate all but the most promising [39]. Such a modeling approach would also provide further groundwork for seismic fragility assessment, analysis of system behavior of RC frames, and the rapid calibration of simplified joint models. Advancing the knowledge of finite element analysis of three-dimensional beam-column joints will simultaneously advance the efficacy of such analytical techniques as a predictive, and not merely descriptive, tool. Thus, forensic engineers in the future may be able to rapidly design rehabilitation measures for existing damaged structures based on numerical analysis.

1.4 Organization of Thesis

The current chapter described the seismic vulnerability of older reinforced concrete beam-column joints and established the need to develop a numerical strategy to further investigate the behavior of joints possessing such deficiencies.

Chapter 2 presents a comprehensive literature review of prior work simulating the response of reinforced concrete beam-column joints using nonlinear continuum finite element analysis. Best practices for joint simulation were summarized, and current gaps

in the literature were identified.

Chapter 3 describes the selection of a constitutive model to simulate the response of plain concrete. The details of this prototype model were described and systematically validated against experimental data. Parameter studies were conducted to determine the sensitivity of the prototype model to various material properties.

Chapter 4 details the extension of the prototype constitutive model for the analysis of reinforced concrete, including the effects of reinforcing bar plasticity and nonlinear bond-slip. The ability of the prototype model to simulate pull-out failure of reinforcements, the behavior of anchored bars, and cyclic shear failure were verified with experimental data.

Chapter 5 describes the application of the prototype model to simulate the response of four seismically deficient beam-column joints under reversed cyclic loading, including a one-way joint, a two-way exterior corner joint, and a series of two-way exterior corner beam-column-slab joints. A critical appraisal of the prototype model for analysis of such joints is provided.

Chapter 6 summarizes the principal findings of this research project and suggests topics for future inquiry.

Appendix A is a visual supplement to the literature review in Chapter 2, showing the mesh and a sample plot from each study comparing experimental to numerical response.

Appendix B documents the hardware and software specifications used, the finite element model material definition input for each beam-column joint simulation, and the Python code used throughout this study to generate simulation input files and post-process results. This transparency is intended to provide sufficient detail to ensure reproducibility of all results.

CHAPTER II

STATE-OF-THE-ART REPORT ON JOINT FEA

Extensive research has been conducted on finite element analysis of reinforced concrete beam-column joints. The objective of this chapter is to present the results of a comprehensive literature search of prior efforts in this domain and to elaborate on key issues and best practices demonstrated by prior researchers.

2.1 Objective

Beam-column joints constitute a critical component in the load path of reinforced concrete buildings due to their fundamental role in integrating the overall structural system. Earthquake reconnaissance reports reveal that failure of joints has led to partial or complete collapse of reinforced concrete buildings designed without consideration for large lateral loads, resulting in significant economic impact and loss of life. Such infrastructure exists ubiquitously throughout seismically active regions worldwide, and the large-scale risk associated with such deficiencies is not fully known.

With the recent shift towards performance-based design, methods for beam-column joint simulation have received renewed interest due to their perceived robustness in addressing research questions of practical importance. The most recent guidelines published by Joint ACI-ASCE Committee 352 (*Joints and Connections in Monolithic Concrete Structures*) identify several areas needing research, which include: (a) the effect of eccentric beams on joint failure due to torsion, (b) evaluation of current codified limits on joint shear, (c) the influence of joint failure and force redistribution in indeterminate frames, (d) evaluation of innovative joint designs, (e) evaluation of joint response under biaxial loading, (f) the performance of gravity-load-designed joints subjected to

seismic loading, and finally (g) evaluation of innovative rehabilitation means such as the performance of FRP-repaired joints [6].

While application of the finite element method may be used to investigate each of these scenarios (and many others), the degree to which it can accurately capture the complex failure processes for each of the above scenarios is not fully known. The use of the finite element method in performance-based design of beam-column joints may thus require further evaluation and validation against relevant experimental data prior to widespread adoption in engineering practice.

While many experimental studies have been employed to better understand beam-column joint behavior, even the most extensive experimental studies cannot fully capture the interaction of the large number of variables contributing to the performance of the joint. Additionally, full-scale experimental studies incur significant cost, both in terms of finances and time, which limits the number of parameters which may be investigated. As such, numerical simulation provides a useful complement to experimental research by addressing some of these challenges.

This review thus seeks to determine the boundaries of the state of the art in beam-column joint analysis. Such a review will assist interested researchers by identifying relevant modeling strategies and constitutive frameworks to simulate various types of joint geometries, reinforcing details, failure modes, and loading protocols.

2.2 Background on Beam-Column Joint Modeling

Over the past decades, investigation of reinforced concrete beam-column joints via analytical methods has been the focus of numerous research efforts. Attempts to analyze joint response include average plane stress models, strut and tie models, single strut mechanisms, empirical methods, and finite element simulations [178].

The behavior of reinforced concrete beam-column joints is complex, and the required behaviors an analytical model must capture are numerous. Depending on the

design philosophy employed, a joint may fail due to a combination of mechanisms such as diagonal joint shear cracking, flexural cracking and hinging of beams, yielding of reinforcement, and excessive bond slip resulting in complete loss of anchorage of beam longitudinal bars. Of these failure modes, prior studies have demonstrated that accurate beam-column joint simulation depends most significantly on the model's ability to capture joint shear deformation and bond slip [31].

Efforts to model these mechanisms using the finite element method can be grouped into two approaches: (a) simplified joint macromodels and (b) continuum finite element models.

2.2.1 Simplified Joint Macromodels

Simplified joint models have traditionally been utilized to study nonlinear system behavior of reinforced concrete planar frames. Such models represent the joint core with a collection of rigid links connected by translational or rotational springs which account for shear deformation, beam hinging, and loss of anchorage.

Typically calibrated against experimental tests on joint subassemblages, simplified joint models have been implemented in frame analysis software with the goal of predicting global system behavior and evaluating specific performance criteria at low computational cost. Such models have been used for performance based seismic design, the probabilistic assessment of gravity-load-designed frames, and progressive collapse analysis.

Primary contributions in this domain have been provided by the following researchers: Alath and Kunnath [14], Biddah and Ghobarah [27], Youssef and Ghobarah [233], Lowes and Altoontash [127], Mitra and Lowes [145], Altoontash [16], Shin and LaFave [204], and Celik and Ellingwood [32]. In-depth reviews of these studies have been provided elsewhere by Thiess [216] and Celik [31]. A graphic illustrating the construction of representative simplified models is shown in Figure 2.1.

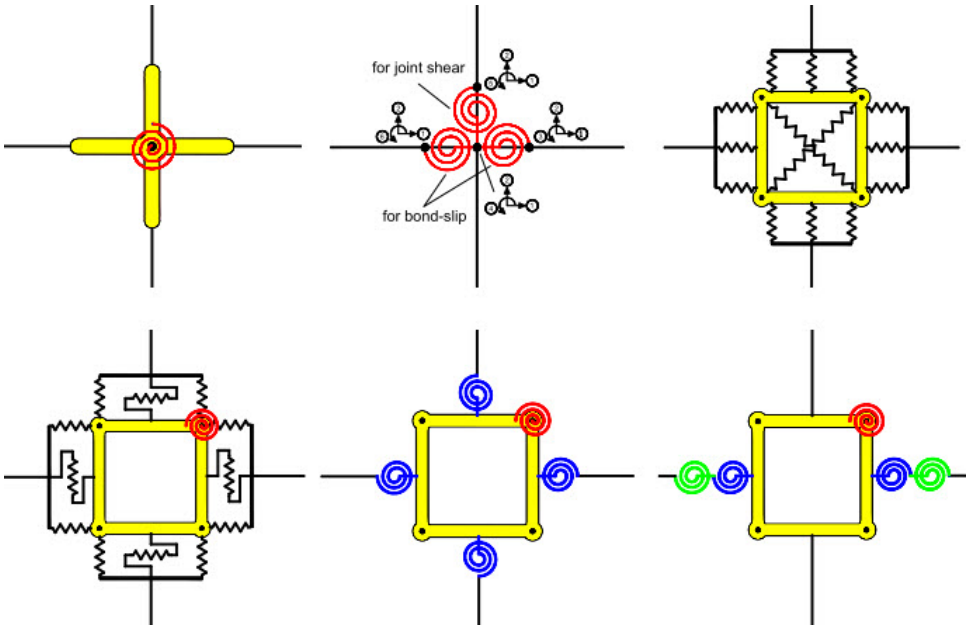

Source: Celik and Ellingwood [31]

Figure 2.1: Simplified Joint Macromodels

Despite the obvious utility of simplified models for evaluation of system response, simplified joint models provide scarce information regarding the internal state of stress and damage throughout the joint region. Such models have typically been applied in the context of two-dimensional analysis.

2.2.2 Continuum Modeling

Three-dimensional nonlinear finite element analysis, in contrast, provides a continuum-level representation of the major factors influencing joint response. In this approach, most or all components are discretely modeled and there is no theoretical limitation to the degree of geometric complexity which can be represented analytically.

While continuum-type models are unsuitable for simulation of overall system behavior on a frame- or structure-level due to high computational cost, such models provide the opportunity to examine the detailed internal behavior of joint regions, including the distribution of stress and strain, the progression of damage throughout the joint, and force transfer mechanisms. As such, this approach has been an ideal candidate for

previous studies in which joints were parametrically investigated under a variety of geometric, reinforcing, and loading conditions.

Such models typically account for complex nonlinear material behavior using a more general constitutive framework, representing the failure of concrete under a triaxial stress state (compression crushing, shear failure as identified through principal tensile stress, localized tension softening or tension stiffening), damage evolution and elastic degradation under cyclic loading, plasticity in reinforcing steel, the effect of concrete confinement, and discrete modeling of bond slip.

2.2.3 Scope of Literature Review

Given the need to systematically study the response of beam-column joints in a variety of more realistic three-dimensional configurations, continuum finite element analysis is identified as the focus of this study due to its ability to describe the detailed internal state of simulated joints.

2.3 Review of Continuum Finite Element Analyses of Joints

The following section provides a systematic review of prior efforts to simulate the response of beam-column joints using continuum finite element analysis. The body of the review focuses on constitutive modeling and insights into joint behavior. At the end of the review, Table 2.1 catalogues relevant model details, including the software used, geometry of the joint simulated, reinforcement design, loading protocol, finite element types used, failure modes observed, and constitutive laws employed. A critical synthesis of the state of the art follows.

While this review focuses on analysis of reinforced concrete building joints, additional studies believed to be relevant to the discussion are incorporated, including analyses of several prestressed/post-tensioned, rehabilitated (FRP), and bridge joints.

Since these structures experience similar failure mechanisms under cyclic load, simulation strategies may be applicable to building joints as well. In addition, larger frames simulated by continuum FEA were included in cases where the beam-column joint response played a significant role in system response.

In Appendix A, a visual complement to this review is provided. For each paper, a representative finite element mesh and a graph comparing numerical results to experimental data are presented.

2.3.1 1970–1989

In 1972, Will et al. [231] published one of the first research studies employing the finite element method in the analysis of reinforced concrete beam-column joints. A plane-stress analysis was conducted of an exterior corner joint in which the column was under constant axial load and the beam was incrementally loaded, tested by Uzumeri et al. [221]. In this study, both concrete and steel reinforcement were modeled using four-node plane stress elements. Concrete was modeled as isotropic and linear elastic prior to cracking, at which point cracks were manually introduced normal to the maximum principal stress direction by reducing the modulus of elasticity normal to the crack direction equal to zero, implying brittle fracture. A linear bond stress-slip relationship was incorporated between the concrete and steel elements via linkage elements. Transverse reinforcements were neglected. The moment-rotation response of the beam as well as the stress distribution in one of the exterior column rebars were shown to correlate with experimental results.

In 1981, Noguchi [157] published an analysis of the nonlinear behavior of planar reinforced concrete interior beam-column connections under monotonic loading. Numerical results were compared with experiments conducted by Kamimura and Hamada [96]. Linear strain (6-node) elements were used to model the concrete. Longitudinal

reinforcement was also modeled using linear strain triangles to account for dowel action, while transverse reinforcement was modeled using truss elements; the constitutive model of each utilized a bilinear curve with strain hardening. The concrete constitutive model was an orthotropic hypoelastic model based on the equivalent unaxial strain concept by Darwin and Pecknold [40]. Cracks were discretely modeled using crack-link springs placed along cracking directions predetermined based on the experimental results. The cracking model assumed brittle failure; the crack-link stiffness was set to zero upon initiation of cracking at a point. Shear transfer through aggregate interlock was neglected. Bond slip was modeled using the bond-link element proposed by Ngo and Scordelis [155]. This study showed increased story deflections as the bond properties degraded, which resulted in compression failure at the joint face. The model overestimated the beam bar yield strengths, which the authors attributed to lack of a post-peak compressive stress-softening relationship.

Three years later, Noguchi and Naganuma [165] extended the previous models of Noguchi [157] in several notable ways. While analyzing the same experimental specimens within a largely similar constitutive framework, the modeling approach was extended to capture the cyclic response of the beam-column joint. The linear strain triangle elements for longitudinal reinforcement were replaced with bar elements, utilizing the cyclic bond slip relations proposed by Morita and Kaku [151]. Additionally, the post-crushing behavior of the concrete was simulated using a nonlinear strain-softening curve, as previously recommended. A brittle cracking model was again used, and the crack-link element stiffness was gradually regained upon crack closure. The proposed model accurately captured the hysteretic force-drift, joint distortions, and beam bar bond slip responses. The numerical analyses demonstrated that the combination of bond deterioration of beam longitudinal bars and joint shear cracking was a key factor in degradation of the restoring force capability of the joint subassemblages.

Van Mier [222] conducted numerical analysis of a portal frame under monotonic

loading using the software DIANA. The numerical response was validated against experimental results from Stroband and Kolpa [211]. The concrete constitutive model accounted for the tensile response using a smeared crack model with constant stress cutoff, linear tension softening, and constant shear retention. To simulate concrete crushing, a plasticity model based on the Mohr-Coulomb criterion [36] was employed. Steel reinforcements were assumed elastic perfectly plastic and embedded in concrete host elements using perfect bond. Quadratic plane stress elements were used to model the concrete while truss elements simulated reinforcements. The Mohr-Coulomb failure criterion was shown to significantly underestimate the strength of the concrete in a three-dimensional state of stress, yet the model was able to accurately describe the crack patterns experimentally observed throughout the portal frame. The experimental results indicated a splitting failure in the plane of the portal frame, which the two-dimensional analysis was unable to capture. The authors suggest a more refined, three-dimensional model to ameliorate this limitation.

2.3.2 1990–1999

Kwak and Filippou [113] studied the response of an interior reinforced concrete beam-column joint with special emphasis given to the modeling of bond. A finite element model was developed and validated against experimental beam-column joint tests conducted by Viwathanatepa et al. [229]. Concrete tensile failure was based on crack band theory and incorporated using a rotating smeared crack model. The equivalent uniaxial response in compression was governed by a modified version of the Hognestad parabola [82], expressed in the principal stress space. If the state of stress exceeded the Kupfer biaxial failure envelope [111], the strain softening response was simulated according to the orthotropic model proposed by Darwin and Pecknold [40]. For reinforcements, a bi-linear relationship with strain hardening was adopted for steel behavior and a trilinear relationship was used for simulating bond slip. Concrete was modeled using quadratic

isoparametric elements, steel with truss elements, and bond slip with bond-link elements. Excellent agreement was demonstrated between numerical and experimental results. The numerical investigation demonstrated that bond slip affects the subassemblage response more significantly than tension stiffening. In fact, bond slip was shown to account for approximately one-third of the total deformation of the subassemblage near the ultimate load. While tension stiffening was shown to play a minor role in predicting the response of the joint, its use was recommended as a means of reducing numerical instability in the model.

Conley [39] published one of the initial studies on finite element analysis of lightly reinforced interior beam-column joints using the software ABAQUS. The nonlinear response of concrete was modeled using a plasticity-based smeared crack formulation. This modeling framework allows the specification of not only uniaxial compression and tension curves, but also the effects of tension stiffening and shear retention as tensile failure progresses. The concrete was modeled using plane stress elements and the reinforcement was discretely modeled and embedded in host concrete elements. The smeared crack formulation in this study is developed for monotonic loading, so the response was correlated to the envelope of the cyclic response of experimental specimens tested by Pessiki [183]. The analytical results were shown to be accurate for relatively low levels of load, but diverged significantly from experimental results at or near the failure point, embodying a nearly elastic perfectly plastic response. When typical descending post-peak tensile stress-strain curves exhibiting tension stiffening were used, the solution encountered numerical difficulties. To reduce these convergence problems, the input parameters were modified to allow very large plastic strains in both tension and compression for stresses slightly larger than the strength, allowing the solution to progress beyond the failure point.

Mosalam, Gergely, and White [152] conducted one of the first simulations of reinforced concrete beam-column joints which incorporated the effects of the slab and

transverse beam stubs, as well as 3D solid modeling. A gravity-load-designed (GLD) joint cyclically tested by Durrani and Wight [47] was chosen as an experimental benchmark due to its exhibiting all characteristics identified as seismically deficient by Beres et al. [26]. The specimen was modeled using the software DIANA. The concrete compressive response was described by a Von Mises yield criterion with associated plastic flow, while tensile response was simulated in a smeared cracking framework which allowed for multiple non-orthogonal cracks at each point [41]. Steel reinforcement material response was based on the Von Mises yield criterion; perfect bond was assumed. The numerical procedure was able to closely reproduce the experimentally determined force-drift envelope, and once validated, the modeling approach was used to simulate joints both with and without the presence of the floor slab and transverse beam stubs (bare joints). The joint strength, story drift, and energy dissipation were shown to depend significantly on the presence of the slab and its influence on shear deformations in the joint panel. For instance, the presence of the slab reduced the percentage of drift due to joint shear distortion from 50% to 25%, and increased the strength of the joint panel by approximately 40%. The authors cited the need to directly incorporate the effects of bond slip in order to accurately capture the influence of insufficient beam bottom bar anchorage.

Pantazopoulou and Bonacci [173] conducted two-dimensional finite element analyses of interior and exterior beam-column joint subassemblages under monotonic load. The modeling framework was validated against specimens tested by Kitayama et al. [108]. The simulations were used to perform parametric investigations of the effect of joint reinforcement, bond condition along beam longitudinal reinforcements, and column axial load. Concrete was modeled using quadrilateral plane stress elements within a constitutive framework based on the Modified Compression Field Theory (MCFT) [226]. Reinforcement was modeled by nonlinear truss elements using a trilinear model with strain hardening. A contact element was utilized to simulate both satisfactory and

unsatisfactory bond conditions between concrete and steel [18]. The study concluded that while joint transverse reinforcement confines the joint core and contributes to the overall shear resistance of the joint, the contribution of the joint core to shear resistance of the joint decreases as the transverse reinforcement volume increases. Additionally, the analysis demonstrated that yielding of joint transverse reinforcement leads to rapid deterioration of the joint performance. Transverse beams were shown effective in precluding joint shear failure due to increased confinement of the joint core.

Barzegar and Maddipudi [22, 23] published a study in which an exterior planar joint was analyzed which contained both transverse beam stubs and a slab. A finite element code was developed in this research which represented concrete failure by the five-parameter Willam-Warnke criterion [232] in conjunction with the hypoelastic constitutive model developed by Stankowski and Gerstle [210]. The fracture energy based smeared crack formulation proposed by de Borst and Nauta [41] was used, allowing for multiple nonorthogonal fixed cracks to occur at each integration point. Mesh objectivity was achieved based on the crack band width model of Bažant and Oh [24]. The simulation strategy relied upon quadratic solid elements for concrete, while reinforcement was modeled using truss elements and connected to host elements via the bond slip relation of Elwi and Hrudey [58]. An exterior joint tested by Durrani and Zerbe [48] was chosen for validation purposes. The joint contained seismic detailing and was simulated under monotonic loading, although the experimental specimen was cyclically loaded. Under upward loading of the beam, the ultimate capacity was overpredicted by 9%, while under downward loading, the ultimate capacity was overpredicted by 5%; both cases exhibited higher post-cracking stiffness than was experimentally observed. The authors attributed these discrepancies to the inability of the monotonically loaded model to capture concrete and bond degradation which occurred under cyclic processes in the experiments. The models failed to converge after the onset of significant cracking

and yielding of reinforcements in the beam and joint core, despite reasonable computation of the ultimate capacities. Extensive cracking in the slab and transverse beam was demonstrated under downward loading, indicating significant participation in the force transfer mechanism in the joint.

In 1997, Noguchi and Kashiwazaki [159, 100] advanced their earlier studies of beam-column joints by publishing one of the first analyses of an interior beam-column joint under two-directional loading. In this study, both one- and two-way interior joints constructed with high-strength concrete were simulated and validated against experiments conducted by Kashiwazaki et al. [99] and Lee et al. [115]. The finite element code ABAQUS was used in this study; the concrete material model was defined by user subroutine. Concrete was represented using solid elements with an assumed orthotropic hypoelastic model based on an equivalent uniaxial strain concept. Failure in compression was governed by the 3-parameter Willam-Warnke yield criterion [232]. The ascending portion of the compressive uniaxial curve was defined by the Fafitis-Shah model [63], while the descending portion was defined by the Kent-Park model [105] to account for the confining effect of transverse beams and lateral reinforcement. A smeared crack model was used in which the stiffness normal to the crack direction was set to zero upon exceeding a tension cut-off. Reinforcements were modeled by truss elements and assumed perfect bond. For both one– and two–way interior joints with transverse beams, the predicted initial stiffness was higher than that observed in experiments, although the numerical model closely matched the experimentally observed maximum story shear force and joint shear failure mechanism. The authors attributed the stiffness overestimation both to an inability of the smeared crack model to capture a local flexural crack in the beam as well as the assumption of perfect bond of steel reinforcement.

Elmorsi et al. [55, 57] developed a modeling approach to simulate the one-way, cyclic response of interior beam-column joints using higher-order inelastic plane stress elements. The joint core was modeled using a single twelve-node element embodying

a cubic displacement field to better capture shear deformations, and the core was surrounded by ten-node transition elements which connected to frame elements simulating beams and columns. Flexural reinforcements were modeled using inelastic truss and bond link elements, while transverse reinforcements were represented using smeared reinforcements. The concrete constitutive model was based on a smeared fixed crack model with enhancements for representing shear deformations [56]. Steel reinforcement was modeled using the Menegotto-Pinto model [142], which accounts for yielding, strain hardening, and the Bauschinger effect. A modified version of the Eligehausen model [54] represented bond slip. The numerical models, implemented in the software PC-ANSR, were validated against experiments conducted by Viwathanatepa et al. [228] and Kaku and Asakusa [95]. The model accurately accounted for bond slip response as well as joint shear deformation under cyclic loading.

Vollum [230] conducted finite element analysis beam-column connections subjected to monotonic loading for the purpose of validating strut and tie models. Simulations of one-way exterior joints both with and without transverse reinforcement were conducted using ANSYS. Solid brick elements were used to represent concrete, while smeared reinforcements assuming perfect bond were used to simulate steel bars. Failure of concrete was governed by the Willam-Warnke criterion [232] along with bi-linear tension softening. The numerical response was compared with experiments conducted by Ortiz [190]. While the models were able to more accurately predict the response of specimens containing joint transverse reinforcements, the computational strategy was unable to capture the extensive cracking which occurred within the joint core, and accurate failure loads were not obtained. Additionally, the initial stiffness of the connection was overestimated because of the assumption of perfect bond. Difficulties in obtaining a converged numerical solution led the author to abandon a continuum joint modeling approach in favor of strut and tie models.

Fleury et al. [64] proposed a continuum modeling approach for interior beam-column

joints with particular emphasis given to bond slip simulation under cyclic loading. The bond law proposed by Eligehausen et al. [54] was modified and implemented in the context of continuous bond reinforcement, instead of discrete springs. Concrete was modeled using plane stress membrane elements with an orthotropic smeared fixed crack representation of tensile failure, while a plasticity theory incorporating isotropic hardening and associated flow was otherwise invoked. The nonlinear bond slip law was invoked only within the joint and extended a short distance within the beams. The numerical model was implemented in the finite element package CODE ASTER, and the joint model was validated against specimens tested by Del Toro Rivera [42]. In early cycles, the analytical results accurately predicted the peak resistance and residual displacements, but subsequent cycles revealed less agreement with experimental observations, particularly a lack of pinching and overestimation of energy dissipation. The authors attributed this deviation to an overestimation of bond resistance in the joint as well as inadequacy of the smeared crack model to capture joint shear distortion, evidenced by a total lack of observed pinching in cases where only perfect bond was assumed. They further suggested a steel reinforcement material law incorporating the Bauschinger effect. This model was later developed into a simplified joint component model suitable for use in frame analysis [65].

Lowes [123, 125] studied the behavior of reinforced concrete bridge beam-column joints using the finite element code FEAP. While this study focused on bridge applications, the analytical framework employed is relevant to the analysis of building beam-column joints. Lowes employed a plasticity-based constitutive framework extending the models developed by Govindjee and Hall [71, 70]. This model allowed for the development of multiple, discrete cracks under tensile loading, a reduction in stiffness and strength due to moderate compressive loading, and supports the transition from tension to compression due to load reversal. A model for anchorage bond-zone response

was developed and validated against a wide range of experimental configurations, characterizing bond stress versus slip behavior for both monotonic and cyclic loading [126]. A steel constitutive relation based on the Menegotto-Pinto hysteresis model [142] was used. Models of beam-column connections were able to accurately predict severe damage of anchorage zones, shear failure within the connection, and the development of flexural mechanisms. Lowes additionally recommended three-dimensional finite element analysis to best capture the primary response modes exhibited by reinforced concrete joints.

Lundgren [129] conducted experimental and analytical research regarding the performance of one-way frame corner joints with various splicing configurations. A series of two- and three-dimensional finite element models were developed using the software DIANA. The two-dimensional model was used for parametric evaluation of loading conditions. For all models, the tensile response of concrete was captured using a rotating smeared crack model based on the Modified Compression Field Theory [226], with softening described by the Hordijk stress-strain curve [84]. In the three-dimensional analyses, both concrete and primary reinforcements were modeled with brick elements, with the bond response simulated using a model developed by the author [130]. The compressive hardening response followed the Thorenfeldt stress-strain curve [217], modified for increased ductility due to confinement by the relation proposed by Selby and Vecchio [199]. In the two-dimensional analyses, concrete was modeled with plane stress elements, reinforcements with truss elements, and bond-slip with interface elements. In the 2D case, the compression response was assumed elastic perfectly plastic, and the bond-slip relation was specified according to the CEB-FIP Model Code 1990 [30] guidelines for the quality characterization "unconfined/other". All analyses captured the failure mechanisms observed experimentally, namely, bending failure with yielding of reinforcement, spalling in the compression zone, fracture of the splice, and inclined cracking in the joint. A subsequent reanalysis using a fixed smeared crack model

demonstrated the superiority of a rotating crack model in capturing joint failure; the fixed crack model was unable to accurately capture the progression of joint cracking.

2.3.3 2000–2004

Sritharan, Priestley, and Seibel [209] conducted nonlinear simulations of various bridge joint configurations subjected to cyclic actions. Numerical models were developed using a commercial user subroutine developed for ABAQUS called ANAMAT, the results of which were validated with experiments conducted by the authors. In the ANAMAT framework, the non-rotating orthogonal smeared crack model proposed by Rashid [187] was used while the confined compressive response followed the uniaxial relationship proposed by Mander et al. [139]. The steel constitutive relationship incorporated strain hardening, hysteresis, low cycle fatigue characteristics, and bond slip, and was incorporated in the global model by superimposing its stiffness onto the plane stress host concrete elements. In order to better account for the strain penetration effect at the joint interface, a system of nonlinear springs was specified at the face of the column. While the monotonically loaded finite element model was capable of representing the backbone of the experimental cyclic force-displacement response, several deficiencies were identified in the modeling approach for some specimens in identifying the precise progression of cracking and tension forces in reinforcement. The authors attributed these discrepancies to potential overestimation of the tension stiffening effect and shear transfer capability after crack formation. The fixed orthogonal crack approach was shown unsatisfactory in representing the experimentally observed progression of cracking, and a rotating crack model was recommended. A three-dimensional discretization of the specimen was also recommended to better represent the influence of spatially distributed reinforcement. Nonetheless, the proposed simulation strategy accurately described the force transfer mechanism within the joint region and global force-displacement characteristics of the joint subassemblages.

Hamil [75] conducted an extensive research program consisting of both experimental and numerical investigations into the behavior of one-way exterior beam-column joint subassemblages. Parameters investigated included beam steel anchorage, concrete strength, joint ties and their position, joint aspect ratio, and type of reinforcement. Two different arrangements of beam reinforcement were considered: a bent-down beam top bar detail and a U-bar detail. Beam-column subassemblages were experimentally investigated under both monotonic and cyclic loading. Finite element analyses of monotonically loaded beam-column specimens were performed using the software SBETA. The model was able to accurately predict multiple failure mechanisms in the joint, including flexural failure of both the beam and column, joint failure due to shear effects, and joint failure due to loss of beam anchorage. The ultimate shear capacity of a joint was shown to equal the square root of its compressive cylinder strength. Joint ties were shown to be most effective when placed in the upper two-thirds of the joint (directly below beam top bars), while the use of U-bar beam reinforcement was shown to reduce the ultimate shear capacity of the joint by an average of 18%. Increasing the column axial stress to a value of 20 MPa was shown to enhance the shear capacity of the joint by 40%. Increasing the joint aspect ratio from 1.4 to 2.0 resulted in a reduction in shear capacity of approximately 25%. While the analytical approach showed good correlation with experimental results, the use of three-dimensional finite element modeling software was recommended, as this would provide a better framework for isolation of independent reinforcing bars within the concrete. This research program was conducted in concert with Baglin and Scott [19].

Baglin and Scott [19] performed finite element analyses of one-way external beam-column joints subjected to monotonic loading using the software SBETA. The presented analytical results were validated against 19 tests performed by the authors and Hamil [75]. The concrete was modeled using the BS8110pt2 compression relationship with a

linear compression strain-softening curve. Other key components of the concrete constitutive model included a brittle response in tension, variable shear retention, and the biaxial failure envelope proposed by Kupfer et al. [111]. Tension stiffening was neglected. A multilinear constitutive relation was employed for the steel reinforcement, and bond slip was treated locally within the concrete substrate. The presented finite element models accurately predicted the ultimate strength of the joint in most cases as well as the distribution of the tension bar anchorage stress. The validated model was then employed in a parametric study where the magnitude of the column load and joint tie arrangement were varied. The results of the parametric study demonstrated that increasing the column load toward a value of 20 MPa increases the ultimate capacity of the joint, while exceeding this value results in the opposite. The increase in column load was also shown to result in stiffening the joint as well as improving the anchorage of the top longitudinal beam bars within the joint. The addition of more closely-spaced ties within the joint increased the ultimate joint capacity by limiting the extension of joint shear cracks as well as confining the top bend in the beam longitudinal reinforcement.

Parvin and Granata [181] conducted nonlinear finite element analysis of reinforced concrete exterior beam-column joints strengthened using FRP composites. A combination of E-glass, kevlar, and carbon fiber fabrics were evaluated in various configurations under uni-directional monotonic loading. The simulations were conducted using the software ANSYS. Concrete material behavior was defined by a smeared crack model in tension and a plasticity model to capture compression crushing, while the steel material model was assumed bilinear. Reinforcements were simulated by truss elements embedded with perfect bond in solid finite elements representing concrete. FRPs were simulated using a multi-layer solid element which was attached to the concrete surface by a bond condition capable of representing both peeling and shearing effects. A comparison of numerical response to experimental data was not reported, nor was any information regarding the failure mechanism of the underlying reinforced concrete joint. The study

instead focused on the contributions of the FRP enhancements, demonstrating an increase in the flexural capacity of the beam-column joints by as much as 37%, a reduction in both the stresses in joint reinforcement and the concrete core up to 26%, and a joint rotation reduction of almost 50%.

Johansson [92] studied the response of reinforced concrete one-way frame corners under monotonic load. A series of planar knee joints with conventional and exploratory reinforcing configurations were experimentally evaluated and simulated using the software DIANA. The constitutive modeling approach for concrete was based on the Drucker-Prager failure criterion in compression [45] and a non-orthogonal multidirectional fixed smeared crack model in tension [41]. The compressive post-peak response followed the guidelines of the CEB-FIP Model Code 1990 [30] while the tension post-peak response followed the bilinear softening curve proposed by Gylltoft [72]. Reinforcement response was captured by a von Mises yield criterion with bilinear strain hardening, and interface behavior was modeled according to the CEB-FIP Model Code 1990 bond-slip law [30]. Varying bond conditions were evaluated: good/other and confined/unconfined, according to the CEB-FIP Model Code 1990 [30] guidelines. The joints were modeled in plane stress, with reinforcements represented by a combination of discrete truss bars and embedded reinforcements. A weak plane was introduced in the mesh to model the influence of a construction joint. The predicted numerical response showed good agreement with the experimental specimens both in terms of stiffness, strength degradation (within 10%), and observed crack patterns. The complete failure of the joint was not captured, however, due to numerical convergence difficulties. The authors recommended a modification of the compression failure algorithm to incorporate a characteristic length, which would reduce localization effects and improve mesh objectivity.

Emara and Hosny [59] presented one of the first simulations of an exterior two-way beam-slab-column joint. The focus of this study was to analytically assess the influence

of the slab on joint response. A slab which was experimentally evaluated by Kurose et al. [112] was modeled using a nonlinear finite element code developed by the authors, ASMBLY3D. The beams, column, and slab were modeled using solid brick elements, while truss elements were used for reinforcements. Bond slip elements were used within the joint core and extended a distance equal to the effective member depth into adjacent beams and columns. Anchorage of longitudinal beam reinforcement within the joint core was captured by fixing the terminating nodes of the bars to the exterior face of the joint. No details were provided regarding the constitutive frameworks employed in the simulation. A unidirectional, monotonic force was applied to the longitudinal beam until yielding was initiated in the slab reinforcements. By investigating the strain profiles in the slab, it was shown that slab participation in the force-transfer mechanism from the beam to the joint could be characterized over a contribution zone equal to approximately 25% of the length of the transverse beam on each side of the joint, thereby increasing the demand for torsional reinforcements in the transverse beams in these regions. As anchorage of beam top bars within the joint deteriorated, a significant increase in slab reinforcement strains was observed. Furthermore, the analytical and experimental observations showed that the presence of the slab resulted in an increase in beam ultimate capacity by as much as 25%, a factor capable of violating the strong column-weak beam design philosophy.

Hoehler and Ožbolt [81] conducted three-dimensional analyses of an exterior one-way reinforced concrete beam-column joint under cyclic loading using the finite element code MASA. The beam concrete constitutive relation is based on the microplane model with relaxed kinematic constraint [167]. The column concrete was linear elastic. A tri-linear cyclic model was used for steel reinforcement. Bond is represented using a microplane model via a layer of extremely fine three-dimensional elements surrounding each reinforcing bar. The results of the finite element analyses were validated against experimental data from Ma et al. [131]. The presented model accurately predicted the

hysteretic load-displacement curve for most cases, with exception to those exhibiting significant shear deformation. Prediction of the proper failure mode was shown to be highly dependent on a correct representation of the boundary conditions, both at supports and loading points. While shear sensitivity led to premature failure in some cases under repeated cycles, crack formation in the concrete and strain distribution in the reinforcement were realistically represented. The results suggest that incorporating the Bauschinger effect within the steel cyclic constitutive model would improve the shear sensitivity shown in the results, allowing cracks to close more easily during load reversals and thus improve the compression zone performance. A discrete bond model accounting for bond degradation during load reversal (asymmetric depending on load history) was recommended.

Ožbolt, Mayer, and Vocke [168] presented a study the same year in which a similar joint was modeled using the software MASA. In this study, finite element models were developed of exterior one-way beam-column joint specimens tested by Ehsani and Wight [49]. The tested joints embodied seismic detailing, designed to achieve ductile failure modes. The concrete constitutive framework was again based on the microplane approach [167], while steel was assumed elastic perfectly plastic. Concrete was modeled using solid brick elements which were connected to steel truss elements via perfect bond. Comparison of the numerical load-displacement response with experimental results showed good agreement until the peak load, at which point yielding of beam reinforcement initiated. While slightly overestimating the peak load, the numerical model showed greater strength degradation in subsequent cycles, as well as less pinching of the hysteresis loops, than the experimental response. However, the global failure mode and crack patterns were accurately characterized by the simulation.

By 2001, the models developed by Noguchi et al. [164] matured to a state which has since been applied in many subsequent analyses of beam-column joints. This model, henceforth termed the *Noguchi prototype*, consists of the material relationships described

as follows. The concrete constitutive framework was defined by an orthotropic hypoelastic model incorporating the equivalent unaxial strain concept by Darwin and Pecknold [40]. The ascending portion of the uniaxial compression curve was defined by the Saenz model [191], while the post-peak relation incorporated either the original or modified Kent-Park model [105, 177]. The failure surface under triaxial stress was governed by the five-parameter Willam-Warnke model [232]. Tension stiffening was defined according to the equation by Sato and Shirai [196]. The Morita-Kaku model was used to simulate the bond stress-slip relationship [151]. A compressive strength reduction factor developed by Noguchi et al. was considered for cracked concrete [89]. Cyclic concrete behavior was incorporated by the hysteretic relationship proposed by Naganuma and Ohkubo [154] while the steel cyclic response followed the Menegotto-Pinto model [142].

Kashiwazaki and Noguchi [102] applied the Noguchi prototype [40, 232, 191, 177, 196, 151] to simulate the response of interior one-way prestressed concrete beam-column joints using software developed by the authors [101]. Concrete was modeled using a combination of six- and eight-node plane stress elements, while longitudinal reinforcement and prestressing tendons were modeled using truss elements. Bond was represented using two orthogonal springs at each node. The monotonic numerical analyses were validated against cyclic tests performed by the authors. The results indicated that the shear capacity of a joint was largely unaffected by the prestressing forces, but the orientation of shear cracking was dependent upon the joint prestressing stresses. Additionally, the bond surrounding prestressing tendons deteriorated rapidly, demonstrating the insignificance of the effect of the bond condition on the shear capacity of the joint.

Zhang, Noguchi, and Kashiwazaki [235] conducted two-dimensional finite element analyses of interior one-way reinforced concrete beam-column joints featuring an exploratory retrofit consisting of externally attached steel plates using the finite element

code DIANA. The numerical models presented were validated against experimental tests of cyclically loaded interior joints which were conducted by Shiohara at Tokyo University [234]. Material constitutive models for concrete were specified by user subroutines and conformed to the Noguchi prototype [40, 232, 191, 177, 196, 151]. Four-node isoparametric plain stress elements were used to model concrete. Reinforcing bars were modeled using two-node truss elements and a bilinear stress-strain relation with Von Mises plasticity represented the constitutive response. Interface elements were used to simulate the bond slip between primary reinforcing bars and the concrete. In some models, diagonal discrete joint shear cracks were specified in advance to capture the effects of prior crack opening and closing which would occur during cyclic analysis using a monotonic load analysis. Various material configurations were investigated. The finite element models accounting for bond, smeared cracking, and discrete diagonal cracks were able to accurately represent the backbone curve of the hysteretic experimental response. Various response quantities were investigated including story shear-deflection response, the compressive principal stress distribution in the joint panel, the strain distribution in beam bars in the joint region, as well as the deformation and failure modes of the joint. The model was able to accurately represent the experimentally observed failure mode under simulated monotonic loading through discrete crack opening and closing.

Quek and Bian [186] performed nonlinear time history analysis of a reinforced concrete frame which was subjected to cyclic base excitation. A half-scale two-span two-story planar frame embodying low-ductility reinforcing details was experimentally evaluated by the authors and modeled using the finite element software DIANA. The frame was modeled using quadratic plane stress elements for concrete and truss elements for embedded reinforcements. The concrete compressive response was modeled using the

Drucker-Prager criterion [45], while a smeared crack formulation with tension softening and shear retention governed the tensile response. Reinforcement plasticity followed the Von Mises yield criterion, and perfect bond was assumed. The mode 1 and 2 frequencies computed by the finite element models were approximately 7% higher than those observed experimentally. The time history response of the frame due to cyclic base excitation revealed a slight overestimation of peak roof acceleration and an underestimation of roof displacements by approximately 10%. Comparison of the load-deformation response due to static lateral load revealed a significant overprediction of both the initial stiffness and strength of the frame. While the authors attributed this discrepancy to potential error in the computational approximation of the base shear and mean material properties used, prior studies incorporating perfect bond have exhibited similar overapproximation of stiffness.

Cervenka [34] presented the design analysis of a prestressed frame exterior one-way joint with integral slab [3] using the software ATENA. The primary objectives of this analysis were the prediction of the crack widths under service load as well as the ultimate load for the system. Both two- and three-dimensional finite element models were developed to investigate the joint behavior. For the plane stress analysis, a damage-based model by Cervenka was employed, while a fracture-plastic approach was used for the three-dimensional analysis [33]; both models are based on smeared cracks, crack band theory, and fracture energy. Failure in compression was based on the Kupfer orthotropic damage model in 2D [111], and the Menètrey-Willam surface in 3D [143]. The three-dimensional model predicted smaller crack widths than the two-dimensional model; this was attributed to its ability to capture crack propagation in the third direction resulting in smaller crack widths close to the concrete surface near reinforcements. When loaded to failure, the three-dimensional model was able to better predict the behavior after partial compressive failure at the joint face due to a more physically realistic representation of lateral confinement.

Li, Wu, and Pan [119] evaluated the performance of nonseismically detailed interior one-way narrow beam-wide column joints subjected to reverse cyclic loading using the finite element software WCOMD(2D). A fixed smeared cracking concrete constitutive model was employed which incorporated tension stiffening, compression stiffening, and variable shear transfer models. A bond slip relationship was specified to simulate the expected slippage of longitudinal reinforcement. A plane stress model was utilized. Analytical results were validated against experiments conducted by the authors [118], and a parametric investigation was conducted to determine the influence of joint transverse reinforcements, column axial load, and bond conditions on the behavior of the joint. Joint transverse reinforcement was shown to help maintain the strength of the joint despite a sustained loss of stiffness. No significant improvement on the bond conditions of longitudinal reinforcement in the beams and columns was observed due to increased joint transverse reinforcement. A parametric evaluation of column axial load indicated a limiting value for the magnitude of column axial load. When beams framed into the wide side of the column, the best performances were demonstrated for an axial load less than $0.4f'_cA_g$, while for wall-like joints (where the beams framed into the narrow side of the column), the best specimen performances were observed for axial load of zero and $0.2f'_cA_g$.

El Nabawy Atta et al. [50] conducted an extensive parametric investigation of factors influencing exterior, one-way beam-column joint behavior due to monotonic loading. A beam-column joint model was developed in ANSYS and validated against experiments conducted by Scott [197]. Concrete was modeled using solid elements, and the concrete constitutive response was characterized by the three-parameter Willam-Warnke failure criterion [232] in conjunction with a smeared crack formulation. Steel was modeled using truss elements with an isotropic elastoplastic relationship. The analytical model showed good agreement with experimental results. The parametric investigation evaluated the influence of seven parameters: concrete grade, column axial force, girder depth,

column dimensions, joint transverse reinforcement, reinforcement anchorage, and additional restraint due to haunches, transverse beams, and/or integral slab. When the concrete grade was increased, the ultimate capacity increased but a more brittle failure mode was observed due to lesser engagement of joint transverse reinforcements. Restraint due to slab, transverse beams, and an upper haunch all resulted in increased ultimate capacity of the joint. The authors concluded, however, that the distribution of hoop reinforcement in the joint core had the most significant influence in improving the system stiffness and ultimate capacity.

Hegger, Sherif, and Roeser [79] conducted two-dimensional plane stress analyses of exterior and interior reinforced concrete beam-column subassemblies under monotonic loading using the finite element software ATENA (formerly SBETA). The analytical results were validated against experiments performed by the authors. The concrete constitutive model employed accounted for the observed increase in ductility due to multi-axial compression (specified via the maximum post-peak displacement), and incorporated an effective compressive strength reduction to account for cracks parallel to compressive struts. A shear retention factor was specified to account for the reduction in the shear modulus as a function of the crack opening strain, with the failure criterion for the concrete based on a biaxial state of stress proposed by Kupfer et al. [111]. Steel reinforcement was modeled using an elastic perfectly plastic stress-strain relation. A perfect bond relationship was enforced between concrete and steel elements; bond slip effects were incorporated via local deformations in the concrete in the vicinity of reinforcements. A parametric investigation was performed and demonstrated that the shear behavior of exterior joints varies significantly from that of interior joints. The shear capacity of exterior beam-column joints was notably affected by the concrete compressive strength f'_c, the slenderness of the connection, the beam reinforcement (ratio, detailing, and anchorage), and the quantity of transverse reinforcement present in the joint. In contrast, the shear capacity of interior joints was shown to be essentially dependent only upon

the concrete compressive strength.

Goto and Joh [69] used finite element simulations to study the shear resistance of planar interior eccentric beam-column joints under cyclic loading. Four joints were tested by the authors, each with varying levels of beam eccentricity. All specimens were designed to fail by joint shear, which was achieved along with spalling of the joint cover and torsional cracking at the joint interface with the beams. The specimens were modeled under monotonic load using the software DIANA. A Drucker-Prager failure criterion [45] governed concrete crushing and followed the CEB Model Code 1990 [30] compressive stress-strain relationship. Tensile failure was simulated with a smeared crack model which followed the Hordijk tension softening relation [84]. Reinforcements were modeled using truss elements with a multilinear constitutive response, and were embedded within concrete brick elements via interface bond elements which followed the CEB Model Code 1990 bond slip relationship [30]. The analyses succeeded in identifying a joint shear failure in all cases, although the simulations predicted a slightly higher ultimate strength than was experimentally observed. The joint torsional moment and torsional deformation angle were accurately predicted, and parametric evaluation of beam eccentricities showed that the joint shear strength decreased with greater eccentric distance due to local failure not observed in concentric joints.

Kashiwazaki and Noguchi [103] later applied finite element analysis to study the seismic response of one-way interior eccentric beam-column joints. In this study, 8-node solid elements were used to model both concentric as well as an eccentric beam configurations. The Noguchi prototype [40, 232, 191, 177, 196, 151] was utilized with the assumption of perfect bond of reinforcements. Simulations were compared to experimental eccentric joint subassemblages tested by Hayashi et al. [78]. The numerical models accurately predicted flexural failure of the beam prior to joint shear failure. The

stiffness of the models significantly exceeded the experimental observations—a discrepancy which the authors attributed to the assumption of perfect bond—yet the maximum story shear force was computed within 5% of the experimental response. While the effects of eccentricity led to increased localized shear stress on the eccentric side of the joint, the story shear capacity did not deteriorate rapidly under torsion as expected since the system instead failed due to beam flexural yielding prior to joint shear failure. The authors cited the need for further inquiry into the failure of joints containing both excessive eccentricity as well as non-ductile reinforcement detailing.

Noguchi and Kashiwazaki [160] published another study around the same time which investigated the response of interior joints with transverse beams and integral slab subjected to unidirectional cyclic load. The modeling framework followed the Noguchi prototype [40, 232, 191, 177, 196, 151] and compared simulations with perfect and imperfect bond. Simulations were validated against experimental data from Suzuki et al. [212]. While load cycles were repeated multiple times at each drift level in the experiments, only one cycle per drift level was used in the finite element analysis to reduce computation time. Simulations incorporating perfect bond slightly overpredicted the initial stiffness and ductility in later cycles. Simulations representing imperfect bond captured both the stiffness and strength in early cycles accurately, but were unable to simulate the response under higher drift levels due to numerical convergence difficulties. Comparison of the accumulated strain energy consumption for each subassemblage component revealed that the more realistic assumption of imperfect bond significantly increased the energy demand on the joint core.

2.3.4 2005–2009

Mahini [136] conducted experimental and analytical research regarding the behavior of beam-column joints repaired using FRP composites. In this study, a series of tests were

conducted wherein various one-way exterior joint designs were tested under monotonic load, both before and after rehabilitation. Numerical models of the joints were developed using the finite element code ANSYS. The concrete constitutive model incorporated both a smeared crack model capable of representing shear retention as well as a failure surface under compressive loading which evolved according to a modified version of the Hognestad uniaxial compression model [113]. Concrete was modeled using solid elements while all reinforcements were modeled by truss elements. FRP composites were modeled using a solid element with an anisotropic material model incorporating a modified von Mises yield criterion. Perfect bond was assumed between concrete and both steel and FRP composite reinforcements. Comparison of the simulated load-deflection response with experimental data showed excellent agreement for the non-retrofitted control specimen. For the repaired specimens, reasonable agreement was demonstrated up to a ductility level of 2, after which the numerical response indicated higher strength than the experimental results. The authors attributed this overestimation to the assumption of perfect bond between the concrete and composite materials. Additionally, the simulations overpredicted the initial stiffness in most cases due to cracking that had developed during the experiments prior to repair but was neglected in the finite element analysis. Finally, numerical analysis was shown effective in determining the relocation of the beam plastic hinge due to FRP repair of the joint.

Shirai, Tajima, and Mishima [206, 214] conducted both two- and three-dimensional finite element analyses of interior one-way reinforced concrete beam-column connections subjected to both monotonic and cyclic loading using the computer code DIANA. The presented analytical results were validated against experimental data from Tajima et al. [213], in which the tested joints failed predominantly in shear. A decomposed-strain

smeared crack model was employed for the concrete constitutive relation, incorporating a Drucker-Prager type model with an associated flow rule for the nonlinear behavior of concrete in compression [45]. Tension stiffening and shear retention were explicitly incorporated in the analysis. Reinforcement was discretely modeled, and bond was simulated in longitudinal bars by means of interface/linkage elements between the steel and concrete elements, accounting for both bond slip and bond locking. The two-dimensional analyses, accounting for compression softening and bond slip behavior, accurately predicted the story shear / story drift angle under monotonic loading, but for this model the hysteretic behavior varied from what was observed experimentally. The three-dimensional analyses, accounting for compression softening and bond-locking action, accurately represented the observed post-peak cyclic deterioration and hysteretic loops, but overestimated the shear capacity of the joint. It was concluded that a three-dimensional analysis provides the best representation of the observed failure mode.

Noguchi [158] conducted three-dimensional finite element analyses of interior one- and two-way reinforced concrete beam-column joints subjected to monotonic uni- and bi-directional loads, employing software developed by the author. The analytical results were validated against cyclic tests of one- and two-way joints tested by Nakano et al. [156] and Shiohara et al. [219], respectively; the monotonic analytical results were compared with the hysteretic backbone curves for each tested specimen. The one-way joint had two lateral beams, while the spatial joint had four lateral beams as well as an integral slab. Material response conformed to the Noguchi prototype [40, 232, 191, 177, 196, 151], except that the Fafitis-Shah model [63] was used for the compressive pre-peak curve and both longitudinal and transverse reinforcements were discretely modeled with perfect bond. In both the analytical and experimental studies, beam flexural yielding occurred prior to joint shear failure. The results of this study demonstrated that assuming perfect bond leads to an overestimation of the initial stiffness with respect to the observed experimental behavior. Differences in principal compressive stress state

and accumulated absorbed strain energy were quantified for one- versus two-directional loading.

Mostofinejad and Talaeitaba [153] conducted three-dimensional finite element analyses of exterior one-way beam-column joints using the finite element code ANSYS. This study focused on capturing the damaged state of the joint due to monotonic loading prior to rehabilitation using FRP laminates. Seven rehabilitated configurations were critically evaluated. Solid elements with embedded transverse reinforcement were used for concrete, while link elements were used to model the longitudinal reinforcement. A smeared crack concrete model representing tensile cracking and compression crushing was used, and the failure criterion was based on the 5-parameter Willam-Warnke model [232]. FRPs were modeled using solid elements in conjunction with an anisotropic material model. Anchorage slip and anchorage extension of the longitudinal reinforcement was modeled based on the non-linear spring model proposed by Soroushian et al. [208]. Comparison of moment-curvature relationships with available experimental data suggested that the implemented model for anchorage slip using non-linear springs was appropriate. Ignoring the anchorage slip of longitudinal beam reinforcement led to an underestimation of the ductility and ultimate rotation of the joint up to 25%.

Mitra [146] conducted analytical research regarding reinforced concrete beam-column joints with the goal of developing a model applicable for performance based seismic design. As part of this study, a continuum finite element model of a beam-column joint was developed using the software package DIANA. The immediate joint region was modeled using continuum plane stress elements, while the beams and columns were modeled using frame elements. Reinforcements were modeled using truss elements and interface elements were used to simulate the bond condition. The Drucker-Prager model [45] was used for concrete compression failure in conjunction with the Popovics empirical uniaxial model [185]. The decomposed strain multi-directional fixed crack model was chosen for concrete in tension, with the post-peak response governed by the Hordijk

tension softening model [84]. The empirical bond slip model by Eligehausen [54] was chosen, and anchorage bond zone response was validated using experimental tests by Viwathanatepa et al. [228]. Both the crack patterns in the anchorage bond zone as well as the load-displacement response of the bond model showed good correlation with experimental observations. Simulations of beam-column joints tested by Oka and Shiohara [166] were attempted using the above approach, but a simplified modeling approach consisting of a series of nonlinear springs was eventually adopted instead due to convergence issues and the high computational cost of the continuum methodology for performance based design and frame analysis. Additionally, Mitra recommended the use of an explicit dynamics algorithm for simulation of non-ductile joint failure [147].

Eligehausen et al. [52, 53] investigated the response of gravity-load-designed (GLD) joints due to cyclic loading before and after retrofit. In this study, the finite element code MASA was utilized to simulate experimental tests conducted by Pampanin et al. [171, 172]. Concrete material response was modeled according to the microplane model proposed by Ožbolt et al. [167]. Reinforcement response was trilinear, with cyclic bond specified according to the model of Eligehausen et al. [54]. Solid finite elements were used for concrete, and reinforcements were connected to the concrete via discrete bond elements. Anchorage of hooked reinforcements in the joint core was captured by an additional spring element. The finite element simulations were successful in capturing the crack patterns and failure mechanism observed in various tests series characterized primarily by either beam flexural failure or joint shear failure. For the specimen characterized by beam flexural failure, a comparison of hysteretic response revealed that the ultimate capacity of the joint was overestimated by 10%, while at higher drift levels the finite element model predicted a more rapid degradation of strength than observed experimentally. For the specimen characterized by joint shear failure, the simulation of hysteretic response overestimated the ultimate capacity by 20%, but accurately captured the strength degradation and increased pinching observed at higher drift levels.

The authors suggest a more refined mesh in the joint core to avoid overestimation of initial stiffness and strength capacity.

Sharma, Eligehausen, et al. [203] shortly thereafter published the results of a similar study in which the response of both interior and exterior non-seismically detailed beam-column joints were investigated. The modeling approach was notably similar to that applied concurrently by Eligehausen et al. [52] using the finite element code MASA. A smeared crack approach based on a microplane model [167] was used in conjunction with a bond slip formulation proposed by Lettow [117]. The numerical analyses were validated against experimental tests of cyclically loaded interior and exterior joints tested by Jain and Murty [91]. The hysteretic response of the exterior joint showed close agreement with experimental results in terms of strength and stiffness degradation for the first five displacement cycles, but the solution failed to converge once significant joint shear cracking had occurred at approximately half the maximum displacement level applied experimentally. The hysteretic response of the interior joint showed better agreement with experimental results up to the ultimate strength for both positive and negative loading cycles, after which the strength of the specimens were overestimated by the analytical model in the positive cycles only. Convergence was not an issue for the interior joint, and simulation captured the highly pinched hysteretic response observed experimentally. A series of additional analyses were conducted using perfect bond and/or monotonic loading, but both cyclic load as well as bond slip were shown critical for an accurate prediction of crack orientation and failure mechanisms.

Manfredi, Verderame, and Lignola [140] simulated the response of one-way interior beam-column joints in order to investigate the strength hierarchy and evaluate the accepted use of joint shear as an index for joint performance. A control specimen tested by Zaid et al. [234] was used to validate finite element models developed using the software DIANA. While the experimental specimens were loaded cyclically, the numerical model was subjected to monotonic load only. A two-dimensional analysis was conducted in

which concrete was modeled using plane stress elements and reinforcements were modeled using three-node truss elements. The concrete constitutive model was represented by a plasticity model which followed the uniaxial compressive response proposed by Mander et al. [139] as well as a smeared crack model with an exponential tension softening branch. All reinforcements were assumed perfectly plastic. Perfect bond was specified for transverse reinforcements, while bond slip was simulated for longitudinal reinforcements via interface elements according to the nonlinear relationship specified in CEB-FIP Model Code 90 [30]. The numerical analysis showed good agreement with experimental results during the ascending portion of the load-deflection response, both in terms of shear force and stiffness. The post-peak softening response, however, was not captured satisfactorily by the numerical model, which the authors attributed to the neglect cyclic degradation due to monotonic loading only. Comparison with envelope curves further revealed that the model predicted the joint shear response more accurately than the column shear. The models accurately predicted the anchorage force and reinforcement stress in longitudinal bars as well as the final crack pattern observed in the subassemblage. The authors argued that joint shear stress was an unconservative index for evaluating vulnerability to joint shear failure, observing numerically that the joint shear stress increased even after apparent onset of joint shear failure and degradation of story shear.

Haach et al. [73] parametrically investigated the response of one-way exterior beam-column joints under monotonic load. Numerical simulations were developed using the software ABAQUS and validated against experiments conducted by the authors. A smeared crack model was used in conjunction with a linear tension stiffening relationship. The compressive yield surface was described by a plasticity model which followed the CEB-FIP Model Code 90 [30] compression hardening diagram. A metal plasticity model was used to simulate reinforcement response; perfect bond was assumed. Plane stress elements were used for concrete while reinforcements were modeled using truss elements.

The numerical results showed good agreement with experimentally determined reinforcement strains. The validated model was used to parametrically study the influence of the level of axial load, eccentricity of axial load, and joint transverse reinforcement ratio. Lower axial column load led to significant values of strain in joint transverse reinforcement earlier than specimens with higher axial column load, but the column axial load eccentricity showed little effect on the joint shear behavior. Increasing the joint transverse reinforcement ratio led to a more uniform joint stress distribution. Stirrups in the upper region of the joint core absorbed tensile forces arising from beam top reinforcement and improved the anchorage condition of these bars.

Kim and Vecchio [106] studied the response of a shear critical reinforced concrete plane frame subjected to cyclic loading. A one-span two-story frame was experimentally evaluated by Duong et al. [46] and simulated using the finite element software VECTOR2. While the beam-column joints embodied seismic details such as joint transverse reinforcement and beam longitudinal bar hooks, the connecting beams were shear critical and retrofitted with externally bonded FRPs. The constitutive framework was based on the Disturbed Stress Field Model (DSFM) [224], an extension of the Modified Compression Field Theory (MCFT) [226], and incorporated aspects of both fixed and rotating smeared crack philosophies. The uniaxial response in compression was modeled by the Popovics model [185] in the ascending regime and by the Montoya [150] as well as Palermo and Vecchio [170] curves in the post-peak regime. The steel reinforcement material model was elasto-plastic with strain hardening and incorporated the Bauschinger effect. Concrete was modeled by plane stress elements, longitudinal steel reinforcements and beam stirrups with truss elements, and other transverse steel reinforcements with smeared reinforcements. Anchorage of longitudinal reinforcing bars was simulated by fixing the end node of the bars to the concrete with perfect bond. FRP reinforcements were assumed linear elastic until fracture and modeled using truss

elements which were connected to concrete elements via bond link elements. Comparison of the mean ratio of computed to observed response revealed that the simulation accurately described the hysteresis of the frame with respect to peak load for each cycle (1.01) as well as displacements (0.99). The modeling technique also demonstrated accurate prediction of damage modes and final crack patterns.

Ibrahim and El-Badry [88] conducted an experimental and numerical investigation of the cyclic response of one-way exterior beam-column joints. The primary objective of this study was to evaluate the efficacy of various joint reinforcement details, including joints with and without standard joint transverse reinforcement as well as joints reinforced with double-headed studs. Numerical analysis was performed using the software ATENA. Concrete fracture was simulated using the Rankine failure criterion with exponential softening [36], while plasticity models such as the Menètrey-Willam [143] or Drucker-Prager [45] failure surfaces represented compressive failure. A constant axial load was applied to the column, while a single cycle was applied to the beam end for each displacement amplitude; load cycles were not repeated at each level as they were in the experiments. Concrete was modeled using 8-node solid brick elements, while all reinforcements were modeled with truss elements. The cyclic steel material response followed the Menegotto-Pinto model [142]. Perfect bond was assumed at all locations except for the interaction along the stems of the doubled-headed studs, along which the CEB-FIP Model Code 1990 bond-slip law was used [30]. An artificially high level of tension stiffening was incorporated in the model to improve the shear retention characteristics. Good agreement was observed between the experimental and numerical response. The ratio of simulated to observed peak loads had a mean value of 0.93. After yielding of reinforcements occurred, the numerical joint response was notably stiffer than the experimental response, which the authors attributed to the inaccurate representation of shear response as well as the lack of repeated load cycles at each drift level. The modeling approach was shown sufficient to predict the failure mode in either joint

shear and beam flexure, depending on the joint reinforcement configuration.

Kashiwazaki and Noguchi [104] evaluated the objectivity of the Noguchi prototype [40, 232, 191, 177, 196, 151] by conducting blind analysis of a series of joint subassemblages tested by Shiohara et al. [205]. The experimental specimens consisted of five one-way interior and exterior joints which were subjected to various configurations of reversed cyclic loading applied either to the column or beam ends, all designed to fail according to beam flexure prior to joint shear. Concrete was modeled using solid brick elements which were connected to steel truss elements via perfect bond. Comparison of story shear – story drift angle response for all specimens indicated that while the initial stiffness was overpredicted, the maximum story shear was represented accurately for all cases. The onset of beam flexural yielding was observed at the correct drift angle for all specimens except one. In the post-peak regime, however, the numerical response deviated significantly from the experimental results. The authors recommended an improved representation of shear deterioration and bond slip to increase the accuracy of the numerical models.

Kulkarni, Li, and Yip [109] conducted both experimental and analytical research into the behavior of precast hybrid-steel concrete connections subjected to cyclic loading. The beam-column joint subassemblages were one-way, planar systems. The analytical portion of this research included detailed finite element analyses of the joint specimens using the finite element code DIANA. The joint response was modeled using two-dimensional plane stress elements. Steel plates were modeled using plane stress continuum elements while reinforcing bars were modeled using truss elements. The material models used were as follows. The multi-directional fixed crack model was employed for concrete in tension with a linear tension softening curve. A constant stress cut-off criterion was used for concrete in tension, and the threshold angle for formation of new cracks was 15°. In compression, a Drucker-Prager yield surface with isotropic hardening and associated flow was used to simulate the crushing response [45]. During unloading

in tension, the secant stiffness was used, while for unloading in compression, the initial elastic stiffness was used. All steel reinforcements were modeled using the von Mises yield criterion with isotropic strain hardening and an associated flow rule. For reinforcing bars modeled using truss elements, bond slip was considered. The Newton-Raphson method was initially applied to solve the nonlinear equations, and was augmented by both the arc-length technique and line search method to improve the convergence of the system. Good correlation was achieved in representing the hysteretic story shear force - horizontal displacement relationship. Parameters evaluated included the influence of column axial load, connection plate thickness, and beam bottom reinforcement continuity.

Li, Tran, and Pan [121] presented a study in 2009 in which the cyclic response of lightly reinforced interior one-way beam-column joints was both experimentally and numerically investigated. One notable aspect of this study was that for several specimens, an effective slab was constructed as well as transverse beam stubs extending the same width as the effective slab. The beam stubs were incorporated to simulate the confining effect provided by transverse beams. Both strong beam-weak column and strong column-weak beam configurations were studied. Nonlinear three-dimensional finite element analyses were conducted using the software package DIANA. The compression response of concrete was governed by the Drucker-Prager yield surface [45] and isotropic hardening with an associated flow rule was utilized after yielding. The tensile response of concrete was modeled using a bi-linear relation to account for the softening effect after cracking. Unloading and reloading in compression was evaluated using the initial elastic stiffness, while in tension the secant modulus was used. Reinforcement was described using the von Mises yield criterion with isotropic strain hardening and associated flow. A bond slip law based on the CEB-FIP Model Code 1990 [30] was implemented. Twenty node quadratic brick elements were used for concrete, and each reinforcing bar

was modeled using truss elements. Good correlation was observed between experimental and numerical results, and all models exhibited significant pinching in the hysteresis loops as was exhibited in the experiments. The validated models were employed in parametric studies related to axial load and slab participation. For strong beam-weak column configurations, an axial load level of $0.25f'_cA_g$ led to an optimum enhancement of story shear by 7%, while for strong column-weak beam configurations, the optimum increase in story shear of 9% was demonstrated at an axial load of $0.35f'_cA_g$. The influence of slab participation was shown to be significant in a strong column-weak beam configuration, while in a strong beam-weak column configuration, the effect of the slab was marginal as the loss of torsional moment capacity of the transverse beams resulted in insignificant development and transfer of slab tensile forces into the joint core.

Kulkarni and Li [110, 120] conducted further experimental and analytical research into the behavior of exterior and interior one-way wide-beam-column joints. Finite element analyses were conducted using the software package DIANA. The modeling approach was notably similar to that employed by Li, Tran and Pan [121], described above. The concrete material model was based on nonlinear fracture theory to account for cracking [74], while the elasto-plastic behavior of concrete in compression and tension was incorporated using the model by Kulkarni et al. [109]. Numerical results showed good overall agreement with experimental results. The numerical models slightly overestimated the initial stiffness of the structure and were unable to predict the level of hysteretic pinching observed experimentally, while slightly underestimating the story shear capacity. The parametric study on the effect of transverse beams indicated that as the transverse beam reinforcement increased, the joint could resist a higher magnitude of joint shear forces and story shears and exhibit more effective transfer of beam bending moments to the column. For exterior joints, a column axial load level of $0.25f'_cA_g$ led to optimal joint shear performance, while for interior joints, a column axial load

level between 0.3–0.4$f'_c A_g$ led to optimal joint shear performance. The torsional performance of transverse beams dominated the joint response, and the numerical results suggested that the joint specimens reached their ultimate strength when the transverse beam lost its torsional capacity. Increasing the longitudinal reinforcement ratio by 50% was shown to enhance the maximum joint shear stress capacity by approximate 14%. Concrete grade did not exhibit much influence on the performance of the joint specimens.

Noguchi, Kashiwazaki, and Miura [163] conducted an investigation into the bond mechanism in interior joints subjected to bilateral load, addressing the prior approximation of perfect bond which often resulted in inaccurate representation of stiffness and strength. In this study, the Noguchi prototype [40, 232, 191, 177, 196, 151] was applied with bond-link elements to simulate both one- and two-way internal joint response when subjected to reverse cyclic loading. The finite element simulations were benchmarked against experiments conducted by Kishida et al. [107]. The two-way interior joint was loaded in such a way as to maximize the effect of biaxial bending of the column. The numerical models accurately described the maximum story shear force as well as the degradation of stiffness and resulting pinching of the hysteresis curve, while slightly overestimating the initial stiffness and underestimating the strength during post-peak cycles. Comparison of planar to two-way joint shear stress distribution revealed a much higher concentration of shear stress at the corners of the biaxially loaded joints, as expected. This study formed the basis for the next reviewed study in which a three-dimensional frame was simulated using the same approach.

The same year, Noguchi and Kashiwazaki [161, 162] conducted finite element analyses of a two-bay by two-bay, two-story reinforced concrete frame as well as an exterior joint subassembly with integral slab and two lateral beams, both subjected to bidirectional cyclic loading. The goal of this study was to investigate the influence of various interaction effects on joint shear strength, namely the presence of an integral slab

and eccentric lateral beams. The finite element formulation utilized the Noguchi prototype model [40, 232, 191, 177, 196, 151]. The analytical results slightly overestimated the maximum strengths exhibited by the experimental structures, although the initial stiffness and yielding mechanisms showed good correlation with experimental observations. The presence of the floor slab led to the yielding of beam bottom reinforcement near lateral beams before yielding of top reinforcement. Furthermore, this study presented the first successful simulation of the response of an exterior beam-column subassembly subjected to unsymmetric bidirectional loading.

2.3.5 2010+

Bindhu and Jaya [28] investigated the response of one-way exterior beam-column joints with diagonal cross bracing bars. The authors experimentally evaluated a series of joints with both conventional and diagonal joint detailing under cyclic lateral load and varying axial force. Numerical models were developed using the software ANSYS. Solid elements represented concrete, while reinforcements were modeled using truss elements. A smeared crack model was used in tension, while plasticity model was used in compression; the uniaxial compression response followed the curve proposed by Dasayi and Krishnan [43]. The steel material response was simulated using a bilinear kinematic model. While the experimental specimens were cyclically loaded, the numerical models were only loaded monotonically; the numerical response was compared to the envelope of the hysteretic experimental results. Examination of the load-displacement response revealed that the numerical models accurately captured the initial stiffness of the specimens, but the predicted strength after yielding was significantly higher than that experimentally observed. While all specimens failed from tensile cracking at the beam-joint interface, the joints with diagonal reinforcement showed minimal hairline cracking of the joint core. Furthermore, the specimens with diagonal confining bars showed improved ductility and energy absorption capacity over joints with standard detailing.

Pennucci et al. [182] studied the response of one-way exterior beam-column joints with various configurations of FRP upgrade. Numerical models were developed using the software ATENA and compared with a series of tests conducted by Antonopoulos and Triantafillou [17]. Concrete was simulated by high order shell elements in conjunction with a constitutive model capable of representing compression crushing and tensile cracking. Steel reinforcements were modeled using truss elements with the Menegotto-Pinto model [142]. The interface behavior of reinforcing bars followed the CEB-FIP Model Code 1990 [30] bond-slip law. A model proposed by Monti et al. [149] was used to represent the interface between the concrete surface and FRP wraps. FRP reinforcements were represented one-dimensionally and assumed to respond linearly until failure. The simulated specimens were loaded monotonically, although the experimental subassemblages were cyclically loaded. In order to stabilize the numerical post-peak response, the arc-length and line search algorithms were applied. Comparison of the numerical load-displacement response with the envelope of the cyclic experimental response showed close agreement in most cases; for several specimens the post-peak was either slightly over- or under-estimated. The validated model was used to parametrically investigate the influence of the FRP lay-up and concrete strength on the joint performance. The resistance of the joint was shown proportional to concrete strength, although the FRP contribution to the joint shear strength was unaffected by concrete strength. Additional gains were demonstrated when FRP fibers were oriented parallel to the beam axis.

Kang et al. [87, 97] performed finite element simulations of both reinforced and post-tensioned concrete exterior column-slab connections. The analyses were conducted using the software ABAQUS. The concrete damage plasticity framework was employed to simulate concrete failure. This constitutive model, developed by Lubliner et al. [128] and advanced by Lee and Fenves [114], utilizes a combination of non-associated multi-hardening tensile and compressive plasticity and scalar isotropic damaged elasticity to

describe the irreversible damage and stiffness degradation occurring during concrete fracture. The uniaxial compression response evolved according to the empirical model proposed by Carreira and Chu [29], while three different multi-linear relationships were evaluated to capture the tension stiffening effect. Concrete was modeled using solid brick elements, with reinforcements simulated by truss elements. Deformed reinforcing bars were embedded with perfect bond, while unbonded tendons were connected to concrete using either spring elements or a tube-to-tube contact element. Both implicit analysis and explicit dynamics analysis were considered for this study, but the explicit dynamics algorithm demonstrated greater numerical stability and was chosen for the prototype model. This modeling approach was validated against experiments of both reinforced concrete interior slab-column connections [218] as well as post-tensioned slab-edge column connections [66], all subjected to uni-directional, monotonic load. Excellent correlation was observed with experimental response for both the reinforced concrete and post-tensioned connections with respect to damage patterns and moment-drift response. The finite element analysis predicted the strain in bonded reinforcement with reasonable accuracy except when the experiment approached the final failure state, which the authors attributed to the assumption of perfect bond.

Sagbas, Vecchio, and Christopoulous [192, 193] conducted two-dimensional finite element analyses of reinforced concrete beam-column joint subassemblages subjected to reverse cyclic loads using the software VECTOR2, a finite element code incorporating a smeared, rotating crack model based on the Disturbed Stress Field Model (DSFM) [224]. The analyses were validated against a suite of experimental studies performed by numerous research groups, embodying both seismic and non-seismic detailing. Numerical models were developed to study various joint configurations, including both joints with deformed bar reinforcement and smooth reinforcement, interior and exterior one-way joints, joint panels with inadequate confinement, as well as a rehabilitation technique wherein the joint was augmented with diagonal haunch bars. Plane stress quadrilateral

elements were used for concrete, while truss elements were used to simulate reinforcements. Within the column anchorage zone, bond-link elements were used to connect reinforcing bars to concrete; otherwise, perfect bond was assumed. At the ends of reinforcements where sufficient anchorage was assumed, hooks were not modeled and the end nodes of reinforcement truss elements were perfectly bonded to the concrete. Key constitutive relationships employed included the modified Kent-Park model for compressive post-peak response [177], the concrete hysteretic model by Palermo and Vecchio [170], a steel model incorporating strain hardening and the Bauschinger effect proposed by Seckin [198], and the Eligehausen bond slip model [54]. The specimens were studied with primary focus on the shear deformations in the joint panel as well as bond slip effects on beam longitudinal bars. The presented results validated the efficacy of the DSFM in modeling cyclic effects in beam-column joints with regard to strength, hysteretic load-deformation response, predicted crack patterns, and failure modes. Additionally, the response of seismically-designed joints was more accurately predicted than that of joints with substandard seismic detailing, which exhibited less ductility. Even so, the strength and ductility for all specimens studied were computed within means of 5%, and energy dissipation within means of 10%.

Sasmal et al. [194, 195] investigated the behavior of one-way exterior joints upgraded via various rehabilitation schemes. The authors experimentally and numerically evaluated the response of a cyclically loaded, gravity-load-designed (GLD) exterior joint before and after retrofit using three configurations of CFRP wrap, GFRP wrap, and steel plates. The numerical analyses were conducted using the finite element code ATENA. The concrete constitutive model was based on the nonlinear fracture model for cracking by Menètrey-Willam [143] and the Rankine plasticity model [36]. Reinforcements were modeled using a bi-linear elastoplastic model with strain hardening, and the Bauschinger effect was incorporated using the Menegotto-Pinto model [142]. Steel-concrete interaction was simulated by the bond slip law from CEB-FIP Model Code

1990 [30]. The effect of anchorage due to curved bars was modeled by a truss strut in the joint core. FRPs were modeled using multi-layered isoparametric shell elements and bonded to the concrete surface via contact elements with a nonlinear bond slip law. The numerical model was shown capable of accurately capturing the load-displacement hysteresis prior to retrofit as well as the final damage mechanisms, characterized by failure of the beam bottom bar anchorage, joint shear cracking, and tensile cracking along the joint face.

Kai and Li [94] investigated the participation of both non-seismically and seismically detailed one-way interior joints in the progressive collapse response of a reinforced concrete frame. A series of joint subassemblages subjected to monotonic load were evaluated experimentally and simulated using the software ABAQUS. In the experimental specimens, the beam longitudinal reinforcement ratios and spacing of transverse reinforcement were varied. The constitutive model for concrete was based on the damaged plasticity model proposed by Lubliner et al. [128] with modifications by Lee and Fenves [114], and incorporated the post-peak models by Saenz [191] in compression and Gopalaratnam and Shah [68] in tension. Steel reinforcements were simulated using a bilinear stress-strain law with strain hardening. Concrete was modeled using brick elements; reinforcements were modeled using embedded truss elements. Elastic plates were placed at the ends of beams and columns to prevent stress concentrations arising from load application and boundary conditions. The simulated response closely followed the experimental results, but the models slightly over-predicted the initial stiffness while under-predicting the ultimate displacement—the authors attributed this difference to the inability of the simulated tension stiffening response to adequately capture averaged local bond-slip effects. A parametric investigation revealed that additional transverse reinforcement in the beam plastic hinge zone increased the strength by approximately 109%, and the authors recommended these additional reinforcements be placed within

a zone beginning at the joint face of length equal to 1.8 times the beam depth. Additional simulations were carried out to investigate the response of the interior beam-column joint when connected to an exterior joint with removed lower column (as in the progressive collapse case). In several of these simulations, a slab flange was considered. The presence of the slab was shown to increase the stiffness and strength of the frame, although the model was unable to capture the anticipated membrane effects due to the two-dimensional limitations of the finite element approach. Further simulations of indeterminate frames were recommended to further assess the catenary action arising under progressive collapse.

Mahini and Ronagh [137] later extended their earlier investigation [136] of FRP-rehabilitated, one-way exterior joints to evaluate the response of such systems under cyclic load. Numerical models of the joints were developed using the finite element code ANSYS and compared to experiments conducted by the authors. The concrete constitutive model incorporated both a smeared crack model capable of representing shear retention as well as a failure surface under compressive loading which evolved according to a modified version of the Hognestad uniaxial compression model [113]. Concrete was modeled using solid elements while all reinforcements were modeled by truss elements. FRP composites were modeled using a solid element with an anisotropic material model incorporating a modified von Mises yield criterion. Perfect bond was assumed between concrete and both steel and FRP composite reinforcements. The numerical model captured the hysteretic response of the plain joints more accurately than the FRP-upgraded joints, which the authors attributed to the assumption of perfect bond. As shown previously for the monotonic case, the use of FRP repair was shown effective in relocating plastic hinges away from the column faces in moment resisting frames under cyclic loading.

Akgüzel and Pampanin [10, 9, 11] experimentally and numerically studied the response of one- and two-way non-seismically detailed exterior joints subjected to both

bidirectional reversed cyclic lateral loading as well as cyclic column axial loading to simulate overturning effects. A series of two-thirds scale joint subassemblages were detailed to represent the performance of a first-floor exterior joint in a 6–9 story gravity-load-designed residential reinforced concrete building. The subassemblages were constructed with smooth reinforcing bars and possessed no transverse reinforcement in the joint core; various FRP retrofits were tested and simulated. Beam longitudinal bars were terminated in the joint core with 180° hooks. The finite element code MASA was used to simulate the joint response. Concrete material response was modeled according to the microplane model proposed by Ožbolt et al. [167]. Reinforcement response was trilinear, with cyclic bond specified according to the model of Eligehausen et al. [54] for smooth bars. Solid finite elements were used for concrete, while truss elements were used for reinforcements. Hooks were modeled using stiff bar elements. Longitudinal reinforcements were connected to the concrete via discrete bond elements, while transverse elements were modeled assuming perfect bond. A loading protocol was programmed for the finite element simulation to generate the bidirectional lateral cloverleaf pattern and cyclic axial column force history as used in the experimental program. Excellent agreement with test results was achieved for the one-way joints, both for force-drift response as well as prediction of crack patterns. For the one-way joint models, the force-drift response was predicted with a 10% margin of error over all drift levels. For the two-way joint model, the force-drift response matched very well up to 0.5% drift, after which the response was underestimated by a margin of approximately 25%. Due to numerical difficulties, the simulation could not progress to the full drifts evaluated experimentally. The two-way model accurately captured the progression of cracking exhibited in the tested specimens.

Al-Haddad et al. [12] investigated the response of non-seismically detailed one-way exterior joints before and after FRP and textile reinforced mortar (TRM) upgrades. The software package ANSYS was used to simulate the response of joint subassemblage

tests conducted by Al-Salloum et al. [13]. In these experiments, exterior joints with integral slab and insufficient seismic detailing were subjected to cyclic lateral load. The joint subassemblages were modeled using three-dimensional elements capable of simulating both cracking and crushing. The 3-parameter Willam-Warnke failure surface was used [232] in conjunction with a version of the Hognestad stress-strain curve [82], modified to incorporate a linear softening branch. A smeared crack model was used in tension. Reinforcements were assumed elastic perfectly-plastic, and perfect bond was used. FRP and TRM composites were modeled using a solid element with multiple orthotropic material layers. The simulations varied from the experimental program in that the slab was not modeled and only monotonic load was applied. Comparison of the simulated monotonic response with the envelope of the hysteretic load-displacement response revealed excellent agreement. For the case of the non-upgraded joint, the peak load was predicted within 1% with the displacement at peak load predicted within 11%. For all cases, the initial stiffness was slightly over predicted by FEA, and for the upgraded specimens, the strength was over predicted by FEA as well. The authors attribute the deviation between observed and simulated response to the assumption of perfect bond between both steel as well as FRP/TRM composites with the concrete.

Mazzarolo et al. [141] simulated the response of seismically deficient one-way interior joints subjected to reversed cyclic loading. The major feature of this research was the development of a new bond slip law for long anchored bars. The software MIDAS FEA was used to simulate the response of a number of bond-critical reinforced concrete systems, including a beam-column joint tested by Park [175]. Concrete was modeled in two dimensions using a total-strain-based, fixed smeared crack model. The softening behavior in tension was captured using Hordijk's model [84], while the compression response followed Thorenfeldt's model [217], modified to account for lateral confinement and cracking. Steel was modeled using truss elements with an elasto-plastic model with isotropic hardening. Various bond configurations were investigated, including perfect

bond as well as the CEB-FIP Model Code 1990 bond law [30] and a new bond-slip relationship, both specified via interface elements. Comparison of the hysteretic force-displacement response revealed that the model with perfect bond overestimated the strength, stiffness, and energy dissipation characteristics of the experimental response in each cycle. Introduction of the concrete-steel interface elements improved these metrics, with the models incorporating the proposed bond-slip producing the most accurate representation of the degradation seen in the experimental response. Additionally, the proposed long anchorage bond slip relationship was able to capture the formation of column plastic hinges as well as the progression of diagonal shear cracking within the joint core.

2.4 Critical Appraisal of Prior Efforts

In the previous section, approximately sixty peer-reviewed studies incorporating nonlinear finite element analysis of reinforced concrete beam-column joints were systematically reviewed. The studies most relevant and successful for simulation of deficient joints under cyclic loading are summarized as follows.

Noguchi et al. [165, 235, 160, 158, 104, 161] have made prolific contributions to the area of nonlinear FEA of beam-column joint response, ranging from the first cyclic simulation of a planar beam-column joint to recent simulations of two-way interior joints with slab subjected to reversed cyclic loading. Mosalam et al. [152] and Barzegar and Maddipudi [23] reported the first simulations of beam-column joint subassemblages containing both slab and transverse beam stubs—these studies successfully captured the joint strength, but only simulated monotonic loading. Li et al. [119, 121, 110, 120] have made significant contributions toward the simulation of beam-column joints under cyclic loading, including the cyclic analysis of lightly reinforced one-way joints with slab and transverse beam stubs as well as joints with wide beams or columns.

Sagbas and Vecchio [192, 193] simulated the response of a series of twelve nonseismically and seismically detailed one-way joints from the literature, perhaps the most extensive and accurate effort to date. Eligehausen et al. [52] simulated the cyclic response of a seismically deficient one-way exterior joint using microplane constitutive theories. Other notable contributions in the analysis of one-way joints under monotonic or cyclic loading were published by Baglin and Scott [19], Hoehler and Ožbolt [81], Heger et al. [79], Goto and Joh [69], Shirai et al. [206], Ibrahim and El-Badry [88], and Mazzarolo et al. [141].

Sasmal et al. [194, 195] and Mahini and Ronagh [137] both simulated the response of a nonseismically detailed reinforced concrete joints with FRP retrofit, successfully capturing the response pre- and post-rehabilitation. Akgüzel [10, 9, 11] also simulated the response of plain and repaired joints, including the first simulation of a seismically deficient exterior corner joint.

While these studies resulted in accurate prediction of the strength and failure modes, the majority of prior efforts have concentrated on the response of one-way joints. Two-way exterior corner joints subjected to bidirectional cyclic loading have not been previously simulated with nonlinear finite element analysis.

Specific attributes of the modeling approaches and constitutive theories from the literature are appraised in the following sections.

2.4.1 Matrix Synthesis

A tabular synthesis of key characteristics from the efforts described in the previous review is provided in Table 2.1; the parameters in this table are defined in Table 2.2. This synthesis presents the major details of each study in terms of software and types of finite elements used, joint geometry, joint reinforcement philosophy, loading protocol, observed failure modes, parameter studies conducted, and key characteristics of the constitutive models employed. A visual classification system for all continuum-type joint

Table 2.1: Database of Previous Research on Joint Finite Element Analysis (Parameters defined in Table 2.2)

First Author	Year	Ref	Software	Mesh Type	Element Types	Joint Geometry	Loading	Joint Design	Failure Mode	Parameter studies	Compression framework	Compression curve	Cracking framework	Tension curve	Steel model	Bond-slip curve
Will	1972	[231]	NA	II	2D/BL	1W/EXT	UNI/MON/AX	N	BS/BF	NA	Elastic	1L	SMR	Brittle	1L	1L
Noguchi	1981	[157]	NA	I	2D/TR/BL/DC	1W/INT	UNI/MON/AX	TR	JS/BS/BF	NA	Darwin	Saenz	DIS	Brittle	2L	Morita-Kaku
Noguchi	1984	[165]	NA	I	2D/TR/BL/DC	1W/INT	UNI/CYC/AX	N/TR	JS/BS/BF	TR/BOND	Darwin	NA	DIS	Brittle	2L	Morita-Kaku
Van Mier	1987	[222]	DIANA	III	2D/TR/PB	1W/EXT	UNI/MON	N	JS	NA	Mohr-Coul.	NA	SMR	1L/SFT	EPP	Perfect
Kwak	1990	[113]	author	I	2D/TR/BL	1W/INT	UNI/MON/CYC/AX	TR	BS	TS/BOND	Darwin	Hognestad	SMR/R	author	2L/SH	3L
Conley	1993	[39]	Abaqus	I	2D/TR/PB/PL	1W/INT	UNI/MON/AX	N	JS	NA	UDP	NA	SMR	TSTF	Plasticity/UD	Perfect
Mosalam	1994	[152]	DIANA	V	3D/TR/PB	1W/INT/S/TB	UNI/MON/CYC/AX	N	BS/BF	SLAB/TB	Von Mises	EPP	SMR/F/NO	1L/SFT	EPP	Perfect
Pantazopoulou	1994	[173]	NA	I/II	2D/TR/BL	1W/INT/EXT	UNI/MON/AX	N	JS/BS/BF	TR/BOND/AX/V	MCFT	MCFT	SMR/R	TSTF/MCFT	3L/SH	Multilinear
Barzegar	1997	[23]	author	VII	3D/TR/BL	1W/EXT/S/TBS	UNI/MON/AX	TR	BF/JS	NA	Stank./5-WW	NA	SMR/F/NO	2L/SFT	2L/SH	Elwi-Hrudey
Noguchi	1997	[159]	Abaqus/U	IV/VIII/IX	3D/TR/PB	1W/2W/INT/TB	UNI/2L/MON/AX	TR	JS/BF	NA	Murray/3-WW	Fafitis/KP	SMR	Brittle	2L	Perfect
Elmorsi	1998	[55]	PC-ANSR	I	2D/TR/BL	1W/INT	UNI/CYC	N/TR	JS/BS/BF	NA	NA	Saenz/KP	SMR	TSTF/Stevens	MEN-PIN	Eligehausen
Vollum	1998	[230]	ANSYS	II	2D/SR	1W/EXT	UNI/MON	N/TR	JS	TR/BOND	3-WW	NA	SMR	2L/SFT	NA	NA
Fleury	1999	[64]	Aster	I	2D/TR/BL/PB	1W/INT	UNI/CYC/AX/PL	TR	BF/BS	BOND	UDP	NA	SMR/F/O	NA	SH	Fleury
Lowes	1999	[123]	FEAP	II*	2D/TR/BL	1W/BR	UNI/MON/CYC	N/RH	JS/BS	NA	Govindjee-Hall*	NA	SMR/F/O	NA	MEN-PIN*	author
Lundgren	1999	[129]	DIANA	III	2D/3D/BL	1W/EXT	UNI/MON	TR/NS	SPL/BF/JS	BOND	MCFT	Thorenfeldt	SMR/R	Hordijk	SH	MC90/auth.
Sritharan	2000	[209]	ANAMAT	II*	2D/SR	UNI/BR	1W/MON	TR	BS/JS	NA	NA	Mander	SMR/F/O	NA	SH	Indirect
Hamil	2000	[75]	SBETA	II	2D/TR/PB	1W/EXT	UNI/MON/AX	N/TR	BF/JS/BS	FC/TR/AX/JG	NA	1L/SFT	NA	1L/SFT	2L/SH	NA
Baglin	2000	[19]	SBETA	II	2D/TR/PB	1W/EXT	UNI/MON/AX	N/TR	BF/JS/BS	AX/TR	NA	1L/SFT	NA	Brittle	2L/SH	NA
Parvin	2000	[181]	ANSYS	II	3D/TR/PB	1W/EXT	UNI/MON/AX	FRP	FRP	FRP	UDP	NA	SMR	NA	2L/SH	NA
Johansson	2000	[92]	DIANA	III	2D/TR/BL	1W/EXT	UNI/MON	NS/CJ	BF/BS/JS	BOND/GF	Drucker	MC90	SMR/F/NO	Gylltoft	2L/SH	MC90
Emara	2001	[59]	Asmbly3d	XI	3D/TR/BL/PB	2W/EXT/S/TB	UNI/MON	TR	NA	SLAB	NA	NA	NA	NA	NA	NA
Hoehler	2001	[81]	MASA	V	3D/TR/BL	1W/EXT	UNI/CYC	TR	BF/JS	NA	Microplane	Ozbolt	Microplane	NA	3L/SH	Microplane
Ožbolt	2001	[168]	MASA	V	3D/TR/BL	1W/EXT	UNI/CYC	TR	BF/BS	NA	Microplane	NA	Microplane	NA	EPP	NA
Kashiwazaki	2001	[102]	author	I	2D/TR/BL	1W/INT	UNI/MON/AX	PT	JS	NA	Darwin/Kupfer	Saenz/KP	SMR	Sata-Shirai	MEN-PIN	Morita-Kaku
Zhang	2002	[235]	DIANA/U	I	2D/TR/BL/DC	1W/INT	UNI/MON/AX	TR	JS/BF	BOND	Darwin/Kupfer	Saenz/KP	SMR	Sata-Shirai	2L	Morita-Kaku
Quek	2002	[186]	DIANA	I/II/III*	2D/TR/PB	1W/FRA	UNI/BE	N	BF/JS	NA	Drucker	NA	SMR/DIS	NA	Von Mises	NA
Cervenka	2002	[34]	ATENA	VII	3D/TR	1W/EXT	UNI/MON/AX	PT	NA	NA	Menètrey	NA	SMR/F/R	Hordijk	NA	MC90
Li	2003	[119]	WCOMD	I	2D/SR	1W/INT	UNI/CYC/AX	N	JS/BF	TR/AX	UDP/Aoyagi	NA	SMR/F	Hajime	Kato	Hajime
El Nabawy	2004	[50]	ANSYS	II	3D/TR/PB	1W/EXT	UNI/MON/AX	N	JS/BF	FC/AX/TR	3-WW	NA	SMR	NA	EPP	NA
Hegger	2004	[79]	ATENA	I/II	2D/TR/PB	1W/INT/EXT	UNI/MON	N/TR	JS/BS	FC/TR/RR/JG	Kupfer	1L/SFT	SMR	NA	EPP	NA
Goto	2004	[69]	DIANA	IV	3D/TR/BL	1W/INT/ECC	UNI/MON/AX	TR	JS	NA	Drucker	MC90/Naka.	SMR/F/NO	Hordijk	2L/3L/SH	MC90
Kashiwazaki	2004	[103]	author	IV	3D/TR/PB	1W/INT/ECC	UNI/MON/AX	TR	BF/JS	NA	Darwin/5-WW	Saenz/KP	SMR	Sata-Shirai	2L/3L/SH	NA
Noguchi	2004	[160]	author	VIII/X	3D/TR/BL/PB	2W/INT/TB/S	UNI/CYC/AX	TR	NA	BOND	Darwin/5-WW	Saenz/KP	SMR/F/R	Sata-Shirai	MEN-PIN	Morita-Kaku
Mahini	2005	[136]	ANSYS	V	3D/TR/PB	1W/EXT	UNI/MON/AX	TR/FRP	BF	NA	UDP	Hognestad*	SMR	NA	2L/SH	NA
Shirai	2006	[206]	DIANA	I/IV	2D/3D/TR/BL	1W/INT	UNI/MON/CYC/AX	TR	JS/BF	BOND	Drucker	Nakamura	SMR/F/NO	Oh-oka	2L/SH	MC90/Kaku
Noguchi	2006	[158]	author	VIII/X	3D/TR/PB	2W/INT/TB/S	UNI/2L/MON/CYC/AX	TR	BF/JS	SLAB/TB	Darwin/5-WW	Saenz/KP	SMR	NA	2L/SH	Perfect
Mostofinejad	2006	[153]	ANSYS	V	3D/TR/BL	1W/EXT	UNI/MON	N/FRP	BF/JS	FRP	5-WW	NA	SMR	NA	NA	Soroushian
Mitra	2007	[146]	DIANA	I*	2D/TR/BL	1W/INT	UNI/MON/AX	N	JS/BF/BS	NA	Drucker	Popovics	SMR/F/NO	Hordijk	EPP	Eligehausen
Eligehausen	2008	[52]	MASA	II	3D/TR/BL	1W/EXT	UNI/MON/CYC/AX	N/RH	JS/BF	AX/BOND	Microplane	NA	Microplane	NA	3L	Eligehausen
Sharma	2008	[203]	MASA	I/II	3D/TR/BL/PB	1W/INT/EXT	UNI/MON/CYC/AX	N	JS/BF	AX/BOND	Microplane	NA	Microplane	NA	3L	Lettow
Manfredi	2008	[140]	DIANA	I	2D/TR/BL	1W/INT	UNI/MON/AX	TR	JS/BF	NA	UDP	Mander	SMR	EXP/SFT	EPP	MC90
Haach	2008	[73]	Abaqus	II	2D/TR/PB	1W/EXT	UNI/MON/AX	N/TR	JS	AX/TR	Kupfer/UDP	MC90	SMR	1L/TSTF	UDP	Perfect
Kim	2008	[106]	VecTor2	I/II/III*	2D/TR/PB	1W/FRA	UNI/CYC/AX	SC/FRP	BF	NA	DSFM	Popov./Mont.	SMR/R	2L/SFT	Seckin	Perfect
Ibrahim	2008	[88]	ATENA	V	3D/TR/BL/BP	1W/EXT	UNI/CYC/AX	N/TR/NS	JS/BF	TR	Drucker	NA	Rankine	EXP/SFT	MEN-PIN	MC90
Kashiwazaki	2008	[104]	author	IV/V	3D/TR/PB	1W/INT/EXT	UNI/CYC/AX	TR	BF/JS	NA	Darwin/5-WW	Saenz/KP	SMR	Naganuma	MEN-PIN	Perfect
Kulkarni	2008	[109]	DIANA	I	2D/TR/BL	1W/INT	UNI/CYC/AX	HYB	JS	AX/BB	Drucker	MC90	SMR/F/NO	2L/SFT	EPP	NA
Li	2009	[121]	DIANA	IV/VI	3D/TR/BL	1W/INT/S/TBS	UNI/CYC	N	JS/BS/BF	AX/SLAB	Drucker	MC90	SMR/F/NO	2L/SFT	EPP	MC90
Kulkarni	2009	[110, 120]	DIANA	IV/V	3D/TR/BL	1W/INT/EXT/TBS	UNI/CYC	TR	BF/JS	AX/TB	Drucker	MC90	SMR/F/NO	2L/SFT	EPP	MC90
Noguchi	2009	[163]	author	IV/VIII	3D/TR/BL	1W/2W/INT/TB	UNI/2L/CYC	NS	JS/BF/BS	BOND/1v2W	Darwin/5-WW	Saenz/KP	SMR	Naganuma	MEN-PIN	Morita-Kaku
Noguchi	2009	[161]	author	XI	3D/TR/BL	2W/FRA/S/EB	2L/CYC	TR	NA	SLAB/TB	Darwin	Saenz/KP	SMR	Sata-Shirai	2L	Morita-Kaku
Bindhu	2010	[28]	ANSYS	V	3D/TR/PB	1W/EXT	UNI/MON/AX	NS	BF/JS	TR/AX	UDP	Desayi	SMR	NA	2L	Perfect
Pennucci	2010	[182]	ATENA	II	2D/TR/BL	1W/EXT	UNI/MON/AX	N/TR/FRP	JS/FRP	FRP/FC	NA	NA	NA	NA	MEN-PIN	MC90
Kang	2011	[97]	Abaqus	XII	3D/TR/BL/PB	2W/EXT/S	UNI/MON	PT	BF/SL	TS/BOND	CDP/Drucker	Carreira	CDP	TSTF/Var	2L	Perfect/UB
Sagbas	2011	[192]	VecTor2	I/II	2D/TR/BL	1W/INT/EXT	UNI/CYC/AX	N/TR/RH	BF/JSL/BS	NA	DSFM	Hognestad/KP	SMR/R	Bentz	Seckin	Eligehausen
Sasmal	2011	[195]	ATENA	II	3D/TR/BL	1W/EXT	UNI/CYC/AX	N/FRP	BS/JS	AX/TR	Menètrey	Van Mier	Rankine	EXP/SFT	MEN-PIN	MC90
Kai	2011	[94]	Abaqus	IV/V*	3D/TR/PB	1W/INT/EXT	UNI/MON/AX	N/TR	BF/JS	TR/SI/SLAB	CDP/Drucker	Saenz	CDP	Gopalaratnam	2L/SH	NA
Mahini	2011	[137]	ANSYS	V	3D/TR/PB	1W/EXT	UNI/CYC	TR/FRP	BF	NA	UDP	Hognestad*	SMR	1L/SFT	2L/SH	Perfect
Akguzel	2011	[9]	MASA	V/XII	3D/TR/BL	1W/2W/EXT/TB/S	UNI/BI/CYC/AX	N/FRP	JS/BF	NA	Microplane	NA	Microplane	NA	3L	Eligehausen
Al-Haddad	2012	[12]	ANSYS	V	3D/TR/PB	1W/EXT	UNI/MON/AX	N/FRP	JS	RH	3-WW	Hognestad*	SMR	NA	EPP	Perfect
Mazzarolo	2012	[141]	Midas FEA	IV	2D/TR/BL/PB	1W/INT	UNI/CYC	N	JS/BS/CH	BOND	MCFT	Thorenfeldt	SMR/F	Hordijk	SH	MC90/auth.

Table 2.2: Parameter Reference Key for Table 2.1

Category	Parameter Descriptions
All	NA: Information not available, 1L: linear, 2L: bilinear, 3L: trilinear
Software	Author: analysis conducted using code developed by authors, U: material model implemented via user subroutine in existing software
Mesh Types	See Figure 2.2. An asterisk (*) indicates the closest approximation.
Element Types	2D: plane stress (concrete), 3D: brick/solid elements (concrete), TR: 1D truss (rebar), BL: 1D bond-link spring, PB: perfect bond, DC: discrete crack link springs, SR: smeared reinforcement
Joint Features	1W: one-way, 2W: two-way, INT: interior, EXT: exterior, COR: corner, S: w/ slab, TB: w/ transverse beams, TBS: w/ transverse beam stubs, BR: bridge joint, FRA: frame, ECC: eccentric beams
Loading	UNI: uni-directional, BI: bi-directional, MON: monotonic, CYC: cyclic AX: column axial load, PL: beam pre-load, BE: base excitation
Joint Design	N: no joint transverse reinforcement, TR: joint transverse reinforcement provided, PT: prestressed/post-tensioned, FRP: externally bonded FRP, RH: other rehabilitation measures adopted, HYB: concrete-steel hybrid joint, SC: shear critical beams, NS/EXP: non-standard experimental design, CJ: construction joint
Failure Modes	JS: joint diagonal shear cracking, BF: beam failure, BS: bond slip/anchorage failure, SL: slab failure, TOR: joint torsion, FRP: delamination or debonding of FRPs, SPL: splitting failure in splice, CH: column hinging
Parameter Studies	TR: transverse reinforcement, BOND: bond condition, RH: rehabilitation, TB: transverse beam, BB: beam bottom bar continuity, TS: tension stiffening, GF: fracture energy, FC: concrete strength, V: shear input, RR: reinforcement ratio, JG: joint geometry/aspect ratio, 1v2W: 1-way vs. 2-way response, SI: statical indeterminacy
Compression Framework	*: modified version, UDP: undesignated plasticity model, Drucker: Drucker-Prager, Darwin: Darwin-Pecknold, 3WW: 3-parameter Willam-Warnke, 5WW: 5-parameter Willam-Warnke, Menètrey: Menètrey-Willam, DSFM: disturbed stress field model, MCFT: Modified compression field theory, CDP: Concrete damage plasticity, CDM: continuum damage mechanics model
Compression Curve	MC90: CEB-FIP Model Code 1990 model, KP: Kent-Park, SFT: softening
Cracking Framework	SMR: smeared cracking, DIS: discrete cracking, F: fixed smeared crack model, R: rotating smeared crack model, O: orthogonal smeared crack model, NO: non-orthogonal smeared crack model
Tension Curve	SFT: softening, TSTF: tension stiffening, EXP: exponential curve, VAR: various models evaluated
Steel Model	EPP: elastic perfectly plastic, SH: strain hardening, MEN-PIN: Menegotto-Pinto, UDP: undesignated plasticity model
Bond-slip Curve	MC90: CEB-FIP Model Code 1990 model, Indirect: concrete response modified to account for bond slip, UB: unbonded tendons

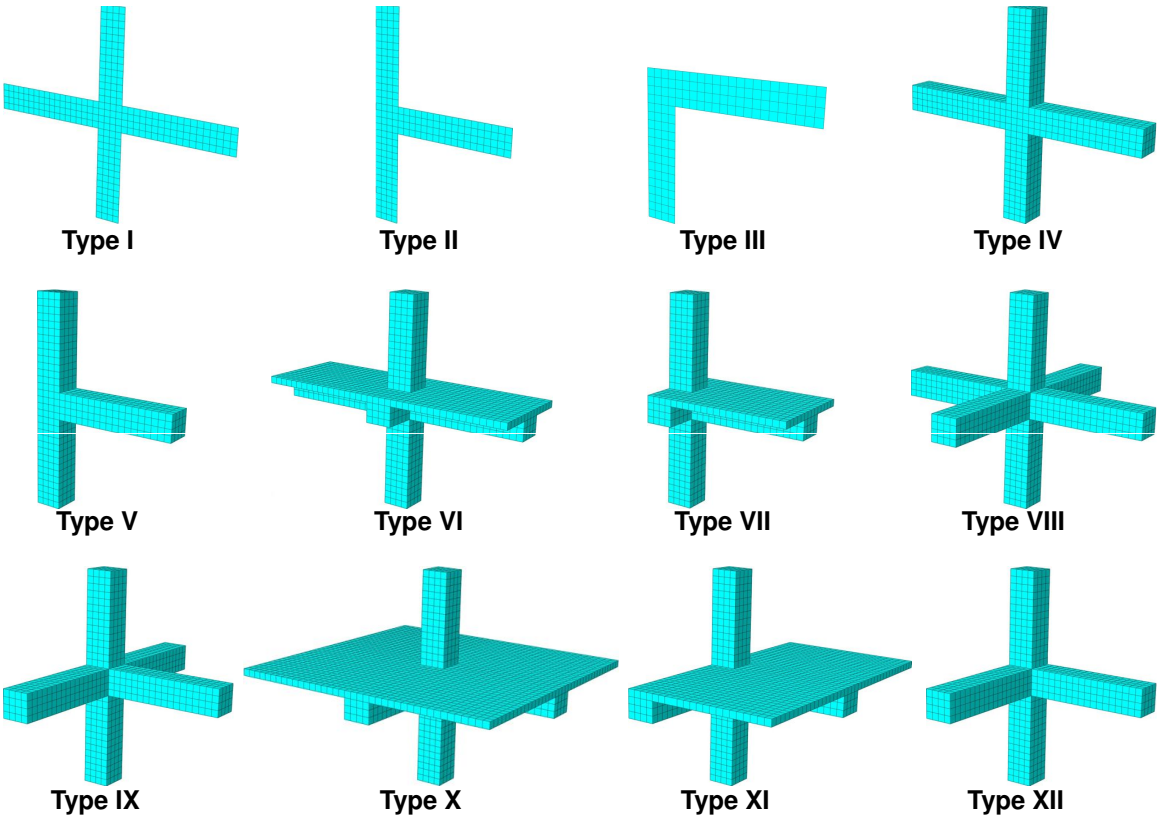

Figure 2.2: Representative Joint Finite Element Models from Literature

finite element models appearing in the literature is given in Figure 2.2. This classification system does not represent a catalog of all possible joint configurations, but only those appearing in the studies cited above; visual characteristics and dimensions are approximate. Scrutiny of Table 2.1 yields the following observations:

- *Software:* The majority of studies used specialized software developed for nonlinear analysis of reinforced concrete, such as DIANA, ATENA (previously SBETA), VECTOR2, MASA, or WCOMD, but several successful efforts were reported using more general purpose finite element software such as ANSYS and ABAQUS. Many simulations relied on software that the authors developed, such as the Noguchi prototype or material models implemented in larger packages by user subroutine.

- *Model geometry:* Based on the mesh classification system in Figure 2.2, it is evident that the majority of previous studies have focused on planar (one-way) interior

and exterior joints simulated under unidirectional loading, only one of which incorporated the influence of transverse beam stubs, integral slab, and cyclic loading. Of the remaining (all of which were two-way joints), only four efforts considered the presence of both transverse beams and integral slab. Only two studies evaluated eccentric joints.

- *Loading:* The majority of simulations evaluated joint response subjected to unidirectional monotonic or cyclic loading. Of the five studies simulating two-way joints simulated under bi-directional loading, only two considered the combination of cyclic load and both transverse beams and integral slab [162, 9]. Only one study considered dynamic loading (base excitation) [186]; in all other studies, loading was applied quasi-statically.

- *Joint design philosophy and failure modes:* Successful simulations were conducted of joints both with and without transverse reinforcements, demonstrating the ability of the applied techniques to capture both ductile and non-ductile failure modes including diagonal joint shear cracking, development of plastic hinges in beams, and extensive bond slip displacements due to inadequate anchorage. Precise data regarding the joint design and failure process was not available for all studies and was inferred from limited descriptions.

2.4.2 Joint Modeling Recommendations

The relative successes of the efforts reviewed in this report provide insight towards best practices for modeling reinforced concrete beam-column joints. The key recommendations are summarized as follows:

- *Concrete elements:* Analysis using three-dimensional solid elements was widely recommended over the use of plane stress elements, allowing for the spatial placement of reinforcement throughout the joint region and a more accurate representation of confinement provided by transverse reinforcement; in a plane-stress analysis, the uniaxial compressive response must be augmented to account for confinement using a relationship such as the modified Kent-Park model [177]. The use of solid modeling is clearly necessary for consideration of more realistic, biaxially loaded joints.

- *Crack modeling:* A review of the cracking models showed that a rotating smeared crack model captures the joint shear cracking process better than fixed crack models [209, 129, 192]. Good results were achieved for fixed smeared crack models, however, if the formulation allowed for multiple, non-orthogonal cracks to form at a point [121, 41]. Microplane models also successfully captured joint shear response [167]. Tension stiffening had an insignificant effect on predicted joint response, but improved convergence characteristics in the post-cracking regime [113]. In early studies, discrete cracks were modeled using gap elements; this approach is only appropriate when crack locations are known *a priori*.

- *Compression failure:* The most commonly employed failure surfaces were the two-parameter Drucker-Prager [45] and three- and five-parameter Willam-Warnke models [232]; an associated flow rule was typical. While the Willam-Warnke models provide a more refined representation of the failure surface under triaxial stress conditions, the simpler Drucker-Prager model may be advantageous as it requires calibration of fewer material constants (for which data may not be available) and has been shown adequate under moderate hydrostatic stress levels [36]. Models

based on the Modified Compression Field Theory have also been employed successfully by numerous researchers to capture the shear-critical failure in beam-column joints [173, 129, 106, 192].

- *Steel material modeling:* Reinforcements were modeled as elasto-plastic, often with the von Mises failure criterion. Incorporation of strain hardening not only improved accuracy but also increased numerical stability. Several studies characterized incorporation of the Bauschinger effect as critical for simulating cyclically loaded joints [64, 81, 194], since the modified unloading/reloading curves may allow cracks to close more easily during load reversals and thus improve the compression zone performance. Commonly-used steel models incorporating the Bauschinger effect include the Menegotto-Pinto [142] and Seckin [198] models. Nonetheless, many studies which simply employed an elastic perfectly plastic model satisfactorily represented the hysteretic joint response on a macro-level.

- *Bond slip:* The studies which neglected bond slip consistently overestimated the joint stiffness and ultimate capacity of the specimen, although the inclusion of bond slip led to numerical instability in some instances. The most commonly used bond slip laws were the Eligehausen et al. [54], CEB-FIP Model Code 90 [30], and Morita-Kaku [151] models. Typically, nonlinear bond slip of longitudinal reinforcement was incorporated via link/spring elements such as the one proposed by Ngo and Scordelis [155]. Bond slip of transverse reinforcement was consistently ignored. The numerical instability arising from bond slip may be improved by only specifying bond link elements for longitudinal reinforcements in the region near the joint [192].

- *Anchorage:* Modeling longitudinal reinforcements using truss elements with a one-dimensional bond slip law is insufficient to capture the anchorage behavior in the

joint region where hooks terminate. Researchers accounted for anchorage in several ways: providing perfect bond at the end node of longitudinal reinforcements [192], connecting the end node of reinforcements to concrete using a spring calibrated to pull-out tests of hooked bars [53], and introducing an additional truss strut element in the hook region [194].

- *Cyclic load history:* In most experimental studies used for model validation, multiple load cycles were repeated at each incremental drift level. Numerical simulations, however, often approximated this by either applying only monotonic load or neglecting repeated cycles at each drift level to decrease computation time. Depending on the hysteretic definition employed in the constitutive framework—such as the effect of prior tensile damage on compression response—these simplifications may result in an inability of the model to capture accumulation of damage and resulting strength and stiffness degradation in the joint.

- *Solution methods:* While many efforts successfully simulated the cyclic response of joints using an incremental-load tangent stiffness approach such as the Newton-Raphson method, many researchers cited difficulty in obtaining a converged solution in the post-peak regime due to extensive joint shear cracking and bond slip displacements. Studies showed that the difficulties arising from reversed cyclic loading may be reduced by using the arc-length and line-search methods [109, 182] or a total-load secant-stiffness algorithm [192].

- *Other simplifying assumptions:* In many studies the simulated material properties were artificially enriched in beam and column regions away from the joint, either by increasing the concrete strength or assuming elastic behavior, improving computation time and convergence characteristics without ill effect on global response accuracy. This approach alleviated a challenge faced in some studies where an inaccurately simulated local failure occurred near load and support conditions.

2.4.3 Gaps in the Literature

This review suggests that techniques to model planar beam-column joints are well established at this time; many researchers have accurately simulated key mechanisms such as joint shear failure, excessive bond slip, and accompanying strength and stiffness degradation under reverse cyclic loading.

Despite this progress in continuum modeling of reinforced concrete beam-column joints, though, there remain several areas where the applicability of such a modeling approach has not been fully evaluated.

- *Slab and transverse beams:* Some researchers have claimed that a one-way exterior joint with three exposed joint faces represents the condition most vulnerable to failure during cyclic load by minimizing the confinement provided by adjoining beams. However, previous experimental studies have demonstrated significant difference between behavior of one-way joints without slab or transverse beams with two-way joints with slab present. The presence of the slab may significantly increase the positive moment capacity of the system, accelerate yielding of beam bottom bars, increase the torsion in beams due to the shear condition at the beam-slab connection, and increase negative moment to the joint through incorporation of slab reinforcement as top steel [116, 67]. Inclusion of the slab and transverse beams will also lead to a more realistic representation of joint confinement. Simulation of such systems by continuum finite element analysis has not been widely validated and requires further research.

- *Eccentric beam-column joints:* On a related note, joints containing eccentric beams have not been simulated under the full range of feasible eccentricities and non-ductile joint reinforcing details. The ability of finite element analysis to reliably capture the resulting force transfer mechanism, particularly the influence of torsion, on joint failure requires investigation.

- *Bidirectional cyclic loading:* The effect of biaxial loading of realistic exterior joints with transverse beams has been experimentally shown to result in a joint shear demand significantly greater than that predicted by uni-directional models [60]. The ability of available constitutive frameworks to satisfactorily capture this complex, three-dimensional failure process has not been systematically confirmed. Furthermore, simulation of non-symmetric biaxial cyclic loading of joints has only been considered in two studies to date [162, 9].

- *Cyclic column axial load:* A building subjected to a lateral cyclic ground motion will experience an overturning effect which will result in cyclic axial loading of columns near the building exterior. Many researchers have evaluated the effect of column axial load experimentally or numerically where a cyclic lateral load is applied to a joint subassemblage under a parametrically varied constant axial load, but this condition is physically unrealistic. To investigate this effect, a coupling of the beam cyclic load to a cyclic column axial load can be determined wherein cyclic column axial forces are applied in a fixed ratio to cyclic lateral loads; joint performance needs to be further evaluated when subjected to these coupled cyclic loads. Sagbas [192] and Akgüzel [9] have attempted to simulate this effect, documenting the difficulty in determining appropriate column load levels without *a priori* knowledge of the experimental joint response.

- *Joint transverse reinforcement:* Parametric evaluations of one-way joints indicated that increasing joint transverse reinforcement improves joint shear capacity, but only to a limiting value at which point additional transverse reinforcement was detrimental. Further investigation under more realistic joint confinement conditions and bidirectional loading may lead to more rational design methods for joint transverse reinforcement.

- *Construction joints:* Only one study in this review accounted for the presence of a

construction joint adjacent to the beam-column joint, a typical detail in gravity-load-designed buildings. Johansson [92] considered the presence of a construction joint by introducing a weak plane in the finite element mesh. Further research regarding the fracture characteristics of construction joints needs to be conducted to identify best practices for modeling beam-column joints with this deficiency.

- *Indeterminate systems:* Two prior studies simulated the response of plane frames [186, 106] and only one simulated the response of a three-dimensional frame [162]. This three-dimensional case is the only published account of nonlinear simulation of a joint subjected to torsion in the context of a larger building laterally loaded eccentric to its center of rigidity. More studies are needed to investigate the response of indeterminate two-way frames in order to gain confidence in the utility of nonlinear finite element analysis for evaluating existing structures.

- *Dynamic analysis:* In all but one of the studies included in this review, quasi-static loads were applied to joint subassemblages. The applicability of time history finite element analysis of joints subjected to random seismic excitations has not been considered. In realistic structures subjected to seismic loading, constitutive modeling may require incorporation of strain rate effects. Future applications of the finite element method for blast and impact simulations will exhibit even greater rate dependence. Current constitutive models need to be evaluated against available experimental results for dynamically loaded systems.

- *FRP-repaired joints:* Several studies have investigated the response of FRP-strengthened beam-column joints. Simulation of externally bonded FRPs requires careful representation of complex debonding characteristics and local failure within the concrete cover. Simulation strategies for debonding of externally bonded FRPs is an ongoing area of research, and the complex mechanisms necessary to account for debonding in a biaxially loaded exterior beam-column joint subjected to torsion

and shear have not been reliably established to date. Furthermore, the contribution of externally bonded FRPs to joint shear resistance needs to be investigated.

2.5 Synopsis

A comprehensive review of prior efforts to simulate reinforced concrete beam-column joint behavior using the finite element method has been presented in this chapter. This review led to identification of best practices for nonlinear simulation of beam-column joints and constitutes a critical appraisal of the state of the art.

Based on this review, a clear precedent exists for the nonlinear finite element analysis of reinforced concrete planar beam-column joints subjected to unidirectional cyclic loading. The extension of available modeling strategies and constitutive laws to a general suite of joints under more realistic conditions has not been adequately established by previous researchers.

To this end, a research effort to validate a modeling strategy for an exterior corner slab-beam-column joint embodying nonseismic detailing subjected to bidirectional reverse cyclic loading was undertaken and is presented in subsequent chapters.

CHAPTER III

CONCRETE CONSTITUTIVE MODEL

3.1 Objective

In this chapter, a constitutive framework for plain concrete is systematically identified which will be suitable for nonlinear finite element analysis of non-seismically detailed reinforced concrete exterior beam-column joints. The theoretical background of the constitutive models is presented. The model is validated with experimental data for cyclic concrete compression and tension response, and parameter studies are conducted to determine the sensitivity of the model to various material properties.

3.2 Requirements for Beam-Column Joint Analysis

The behavior of reinforced concrete beam-column joints is complex, and the required behaviors an analytical joint model must capture are numerous. A nonseismically detailed joint may exhibit a combination of failure mechanisms such as diagonal joint shear cracking, flexural cracking and hinging of beams, yielding of reinforcement, and excessive bond slip resulting in loss of anchorage of beam longitudinal bars.

Investigation of reinforced concrete beam-column joints accounting for such behaviors via the finite element method has been the focus of numerous research efforts. The earliest efforts in FEA-based nonlinear beam-column joint analysis approached the problem by manually updating material properties normal to detected cracks [231] or through the specification of discrete cracks via crack-link springs [157, 165]. Limitations with such approaches—such as the requirement for *a priori* knowledge of crack locations—motivated researchers to adopt continuum-based elasto-plastic fracture models.

The Drucker-Prager plasticity model has been commonly paired with a multidirectional non-orthogonal fixed crack model to effectively capture the reversed cyclic response of building beam-column joints [206, 121, 120]. Microplane models have been employed successfully by various researchers to simulate one-way joint response under similar conditions [81, 52, 203]. The five-parameter Willam-Warnke plasticity model has been used in conjunction with a smeared rotating crack model to simulate more realistic joints incorporating slabs, transverse beams, and bidirectional loading [158, 163]. Smeared rotating crack models along the lines of the Modified Compression Field Theory have also been employed successfully by numerous researchers to capture the shear-critical response of reinforced concrete beam-column joints [173, 129, 106, 192]. A detailed review of these studies was provided in Section 2.4.

3.3 Software and Constitutive Theory Selection

The selection of an appropriate constitutive theory was governed by those behaviors deemed most important for characterizing the failure of shear-critical beam-column joints. To this effect, the following biases led the selection of constitutive theory.

Simplicity was favored over complexity. Complex plasticity-based constitutive models require extensive material parameter calibration. Since limited material property data (beyond concrete compressive strength and steel yield stress) is often available from experimental reports, a complex plasticity theory requiring specification of many parameters defining the failure surface is not widely applicable since many values must be inferred. A simpler model may also prevent the overfitting of data to a specific scenario, resulting in a more broadly applicable simulation strategy.

Constitutive theories exhibiting a more softened response were favored relative to those exhibiting a stiffer response. A frequent deficiency in simulation of deficient beam-column joints is an overestimation of both the stiffness and strength, as is clearly evidenced from the plots cataloged in Appendix A. This factor is also important because

of practical limitations regarding mesh refinement due to model size and computational cost.

Finally, constitutive theories inherently demonstrating more hysteretic pinching were favored over those exhibiting greater energy dissipation. Deficient beam-column joints exhibit shear-critical failure which leads to a highly pinched response. Numerical analysts have struggled repeatedly to capture adequate pinching of the hysteresis loops, again evident in the examples cataloged in Appendix A. Thus, models erring on the side of lower energy dissipation were favored.

Based on the integration of multiple constitutive frameworks for concrete failure, steel plasticity, and bond simulation, in addition to its frequent success in simulating highly nonlinear problems in the literature, the finite element software DIANA Release 9.4.4 [4] was chosen for this study. The finite element code Abaqus was also evaluated.

Between these two software packages, four constitutive frameworks were evaluated for use in this research. A summary of each constitutive theory considered is as follows:

1. A plastic damage model originally developed by Lubliner et al. [128] and later extended by Lee and Fenves [114]. This model captures the failure of concrete by representing the evolving strength of concrete using a hyperbolic approximation of the Drucker-Prager failure surface coupled with a continuum damage mechanics approach for stiffness degradation. This model is available in Abaqus.

2. A pairing of de Borst and Nauta's non-orthogonal multidirectional fixed smeared crack model [41] to represent tensile failure together with the Drucker-Prager plasticity model [45] to capture compression response. This model is available in DIANA [4].

3. An elasto-plastic damage model based on the constitutive theories of Maekawa et al. at the University of Tokyo [133, 134, 135]. This framework couples a damaged elasticity model with a fixed, rotating, or non-orthogonal smeared crack model.

This model is available in DIANA [4].

4. A rotating smeared crack model based on the Modified Compression Field Theory (MCFT), following the formulation from Selby and Vecchio [201, 200]. This model is available in DIANA [4].

These were each used for simplified verification examples in order to evaluate their efficacy in the prediction of beam-column joint failure processes. Frameworks 1–3 were eventually eliminated due to either (a) difficulties in obtaining numerical convergence or (b) overestimation of the energy dissipation capacity of the evaluated subjects. Due to the high level of pinching in the hysteretic response of non-ductile beam-column joints, a model capable of adequately capturing brittle, shear-dominated failure was critical. This factor led to the selection of the Vecchio and Selby total strain rotating smeared crack model, implemented in DIANA Release 9.4.4 [4].

3.4 Total Strain Rotating Crack Model

The concrete constitutive model chosen is based on the theory proposed by Selby and Vecchio [201, 200], an orthotropic, nonlinear elasticity model based on the Modified Compression Field Theory (MCFT), originally developed by Vecchio and Collins [226]. The implemented formulation represents the extension of the MCFT for the analysis of three-dimensional solids, accounting for lateral expansion and the evolution of concrete strength due to confinement and/or transverse cracking. The following section summarizes the constitutive theory. The full theoretical formulation for the model is presented in the DIANA material library reference manual [4].

The total strain rotating crack model is a hypoelastic constitutive model where orthogonal cracks are represented by a coaxial stress-strain concept. The constitutive relationships are always evaluated in the principal directions of the strain tensor. The model is called a *rotating crack model* because crack directions are allowed to continuously reorient with the principal directions of the strain tensor. Prior to cracking, the behavior in

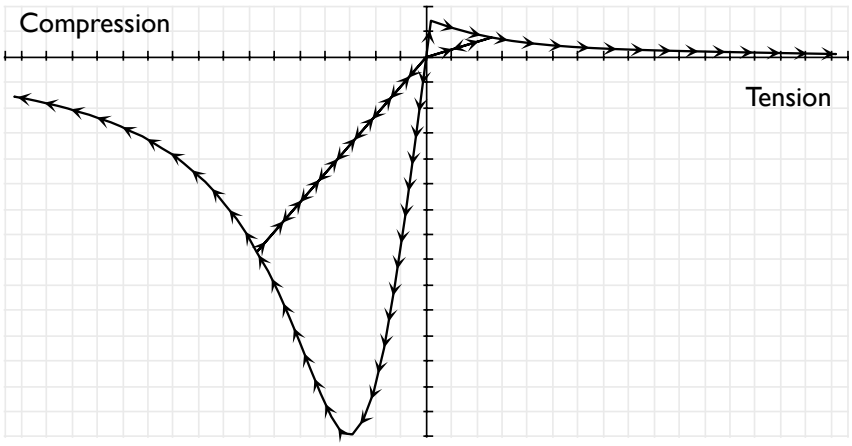

Figure 3.1: Hysteresis Rule for Concrete Response with Secant Unloading/Reloading

compression is similarly evaluated in a rotating system. While such an approach possesses less physical meaning than fixed crack models (where crack directions are not allowed to change after cracking occurs), rotating crack models have been successfully applied to simulate reinforced concrete failure for several decades. For such problems dominated by shear failure, a rotating crack model is advantageous over a fixed crack model since specification and validation of a shear retention factor is not required, although a limitation of this approach is the assumption that principal stresses and strains remain coincident. The components of the constitutive response in the principal directions are governed by uniaxial stress-strain curves for tension and compression, described later in Sections 3.5 and 3.6, respectively.

Deterioration of concrete material due to cracking and crushing is monitored with internal damage variables which track the maximum (tensile) and minimum (compressive) strains reached at each integration point. Damage recovery is not possible, thus internal damage variables—and therefore degradation of stiffness—can only increase. Unloading and reloading is modeled using the secant modulus, determined by the maximum and minimum strain in each crack direction. A typical uniaxial cyclic stress-strain curve is shown in Figure 3.1.

In an incremental-iterative solution scheme, the constitutive model must provide a

stiffness matrix such that equilibrium between the internal force vector and the external load vector can be achieved. In the rotating crack model, the tangent stiffness is formulated in the cracked coordinate system prior to transformation into a consistent global system for assembly. The stiffness matrix possesses nonzero, unsymmetric off-diagonal terms because of coupling due to lateral strain effects in the computation of principal stresses. These terms are partial derivatives of the stress-strain fields in the crack orientation. The stiffness components of the coupling terms between the normal and shear strain are equal to zero.

The Poisson effect governs the lateral deformation of a specimen subjected to uniaxial loading. When such deformations are constrained, a passive lateral confinement will result, an important effect in three-dimensional simulation of reinforced concrete. Selby and Vecchio [200] incorporated this effect in their constitutive model through a pre-strain concept wherein the lateral expansion effects are represented by an equivalent external loading on the structure. This concept is extended to the nonlinear rotating crack model by evaluating the stress vector in the principal coordinate system in terms of the equivalent uniaxial strain vector, not the principal strain vector.

After cracking occurs, the Poisson effect ceases because elongation in a cracked direction no longer produces lateral contraction. This effect is incorporated in the nonlinear rotating crack model using an orthotropic representation of the Poisson effect, in which Poisson's ratios are reduced at the same rate as the secant modulus after cracking.

Concrete exhibits a pressure-dependent response wherein strength and ductility increase when subjected to compressive isotropic stress. To simulate this effect, the compressive stress-strain function, described in Section 3.5, is modified according to a failure function which depends on the computed stresses in the lateral directions. The evolution of compressive strength due to lateral confinement is represented via the four-parameter plasticity model proposed by Hsieh, Ting, and Chen [86]. The failure surface possesses curved meridians and a noncircular cross-section.

In the case of compression with no lateral confinement, the response follows the base uniaxial stress-strain curve. The initial stiffness follows the elastic modulus, with increasing confinement producing a gradual increase in concrete strength, following the recommendations of Selby and Vecchio [200]. In a fully triaxial state of stress, the failure surface may not be reached and a linear elastic response is possible. Increased ductility due to confinement is modeled by a linear adaptation of the descending branch of the uniaxial compression curve.

Compressive behavior is also influenced by lateral cracking, in which case the compressive strength is reduced when large tensile strains perpendicular to the principal compression direction occur. Thus, the compressive strength depends not only on the internal damage variable in the direction of the compressive strain, but also on the internal variables monitoring lateral tensile damage. The model from Vecchio and Collins [227] is used to model the reduction in compressive strength due to lateral cracking.

The above constitutive framework depends on the specification of uniaxial concrete response curves for tension and compression, and any available models from the literature may be used in conjunction with the total strain rotating crack model. The following sections summarize the characteristics and validation of the various models chosen to define the uniaxial response of concrete in compression and tension.

3.5 Uniaxial Compression Response

The uniaxial compressive response of concrete is highly nonlinear, with the onset of inelastic deformation occurring at approximately 30% of the compressive failure stress. After the peak compressive stress, the stress will decrease until the crushing failure strain is reached.

Models commonly utilized to represent the uniaxial compressive response of unconfined concrete include the Popovics [185], Smith-Young [98], Saenz [191], Hognestad [83], and Thorenfeldt [217] models. Models with post-peak response incorporating the

effect of confinement include the Mander [139, 138], Kent-Park [105], Hoshikuma et al. [85], and Saenz-Spacone [191] models. Since the prototype constitutive framework is capable of modifying the failure surface of concrete in compression based on internally-computed lateral confinement, a uniaxial compression curve directly incorporating the effect of confinement is not necessary in the present study.

The uniaxial compression response chosen for the prototype model[1] follows the expression proposed by Thorenfeldt [217], in which the stress-strain relationship and associated parameters are given as

$$\sigma = f'_c \left(\frac{\epsilon}{\epsilon_0}\right) \frac{n}{n - 1 + \left(\frac{\epsilon}{\epsilon_0}\right)^{nk}} \tag{3.1}$$

$$n = 0.80 + \frac{f'_c}{17} \tag{3.2}$$

$$k = \begin{cases} 1.0 & \epsilon_0 > \epsilon \\ 0.67 + \frac{f'_c}{62} \geq 1.0 & \epsilon > \epsilon_0 \end{cases} \tag{3.3}$$

In this equation, f'_c is the reported compressive strength and ϵ_0 is the strain corresponding to the maximum compressive value, which Thorenfeldt [217] specifies as

$$\epsilon_0 = \frac{f'_c}{E_c} \cdot \frac{n}{n - 1} \tag{3.4}$$

Unless experimental values are reported for a particular set of experimental data, the elastic modulus for concrete is evaluated according to the ACI [7] equation as

$$E_c = 4700\sqrt{f'_c} \qquad \text{(MPa)} \tag{3.5}$$

The general shape of Thorenfeldt's uniaxial compression model is illustrated in Figure 3.2, in which the analytical expression from Equation 3.1 is verified with DIANA's implementation of the model.

The uniaxial compression model was validated against experiments conducted by Karsan and Jirsa [98] and Sinha, Gerstle and Tulin [207].

[1] Unless otherwise noted, all expressions are presented in SI units of N, mm, and MPa.

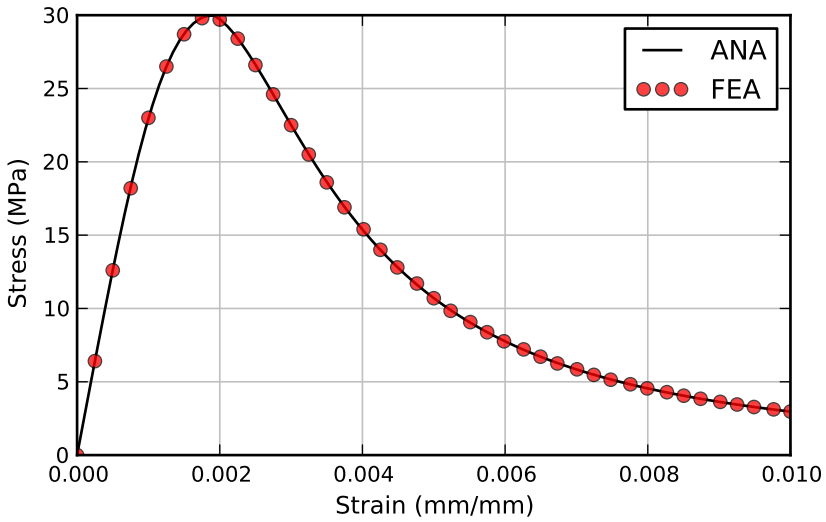

Figure 3.2: Thorenfeldt [217] Compression Analytical Curve and DIANA Verification

3.5.1 Verification with Karsan and Jirsa [98]

Karsan and Jirsa [98] tested a series of concrete prisms subjected to uniaxial cyclic compression loading. The test specimens were short rectangular columns with cross-section dimensions of 76.2 × 127 mm (3 × 5 inches) at the critical section, while the ends of the specimens were flared and reinforced in order to confine failure to the critical section. A sufficiently rigid loading frame was used to capture the response in the unstable portion of the stress-strain curve. The strain response was measured over a 165 mm (6.5 inch) gage length.

Specimen AC3-10 was modeled in this study, which possessed a compressive strength of 34.5 MPa (5010 psi). The finite element model consisted of a single truss element with compression response defined according to Equations 3.1–3.5. The monotonic response is shown in Figure 3.3. The cyclic response is evaluated in Section 3.5.4.

Good agreement was observed between computed and observed response. The prototype model follows the experimental model closely until a strain of approximately 0.0035 mm/mm at which point the numerical model underestimates the response. The initial stiffness is slightly underestimated, although the peak compressive stress and peak compressive strain are accurately captured.

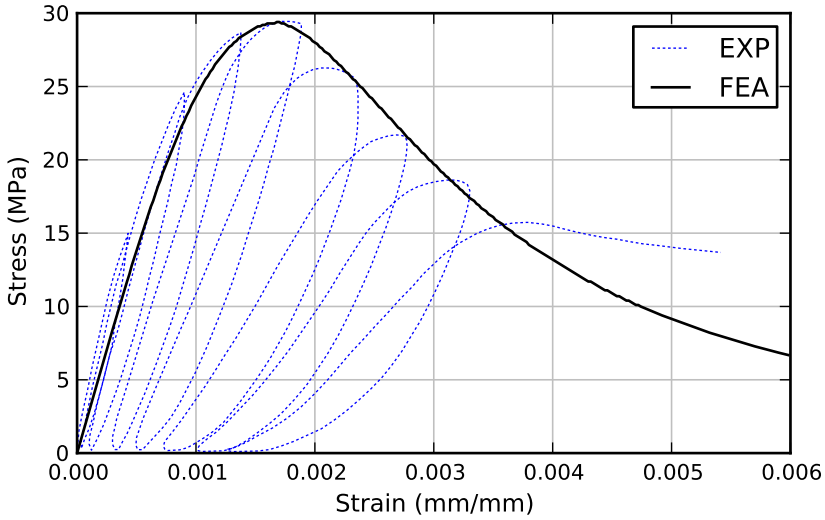

Figure 3.3: Uniaxial Compression Response for Karsan and Jirsa [98]

3.5.2 Verification with Sinha et al. [207]

The uniaxial compression model was also validated against experiments conducted by Sinha, Gerstle and Tulin [207]. Sinha et al. tested a series of concrete cylinders subjected to uniaxial cyclic compression loading.

Cylinder #1 was modeled in this study, which possessed a compressive strength of 25.9 MPa (3750 psi) at a peak strain value ϵ_0 of 0.0025 mm/mm. The cylinder had dimensions 76.2 $\times$ 152.4 mm (3 $\times$ 6 inches). As with the model for Karsan and Jirsa, the finite element model consisted of a single truss element with compression response defined according to Equations 3.1–3.5. The monotonic response is shown in Figure 3.4. The cyclic response is evaluated later.

The prototype model follows the experimental model closely until the peak strain is reached. At this point, the response is slightly underestimated up to a strain value of approximately 0.005 mm/mm, at which point the strength is overestimated.

3.5.3 Compression Response Parameter Sensitivity

From figures 3.3 and 3.4, it is evident that the Thorenfeldt curve provides a reasonable representation of the envelope of the cyclic compression response of concrete.

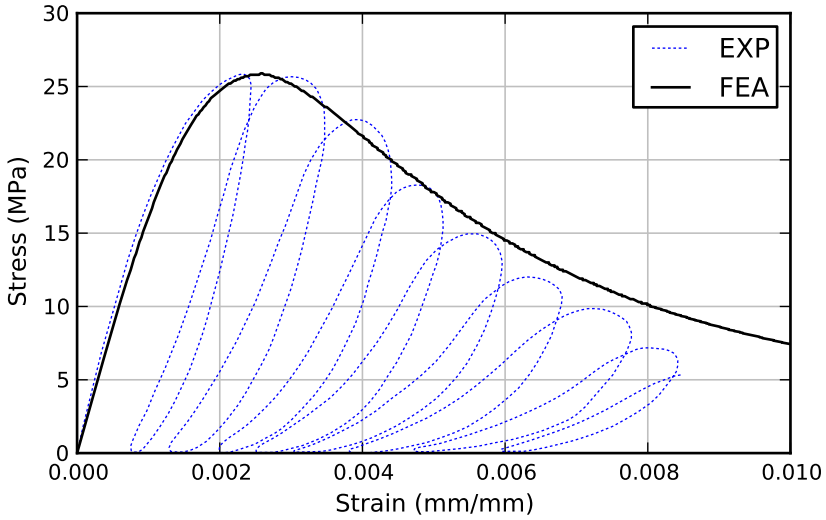

Figure 3.4: Uniaxial Compression Response for Sinha et al. [207]

The only derived input parameter employed in the Thorenfeldt uniaxial compression curve is the concrete modulus of elasticity, typically computed from the compression strength of the specimen using the ACI equation (unless otherwise noted). A parameter study was performed to evaluate the sensitivity of the compression response to Young's modulus. For both compression tests by Karsan and Jirsa [98] and Sinha et al. [207], the prototype model was used with modulus of elasticity varied by $\pm 10\%$.

The results of this study are presented in Figure 3.5 for both experimental programs. The effect of changing the modulus of elasticity is to shift the curve along the horizontal axis. The effect of increasing or decreasing the elastic modulus produced a marginal change in the response up to the peak value, while for larger strains the experimental response was bounded by the varied responses, with the prototype model producing the overall best representation considering both Karsan and Jirsa [98] and Sinha et al. [207].

3.5.4 Cyclic Compression Response

The models of tests by Karsan and Jirsa [98] and Sinha et al. [207] were also subjected to cyclic compression loading in order to evaluate the unloading-reloading rules in the total strain rotating crack model.

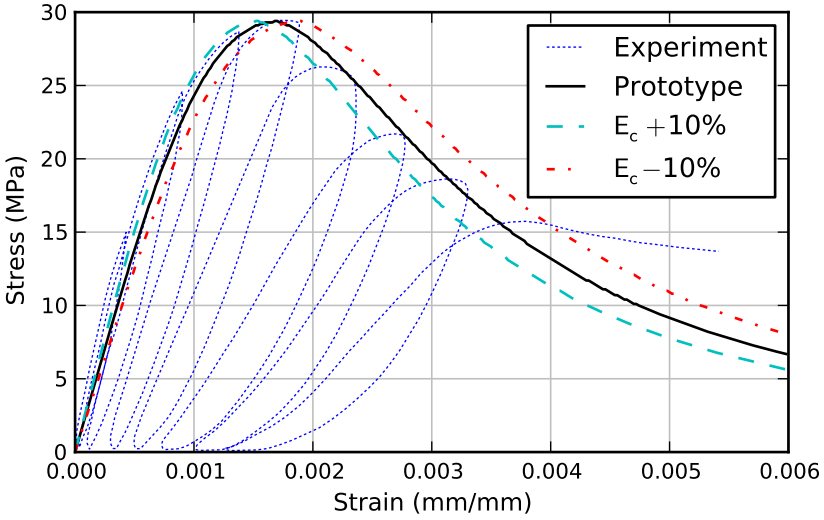

(a) Karsan and Jirsa [98]

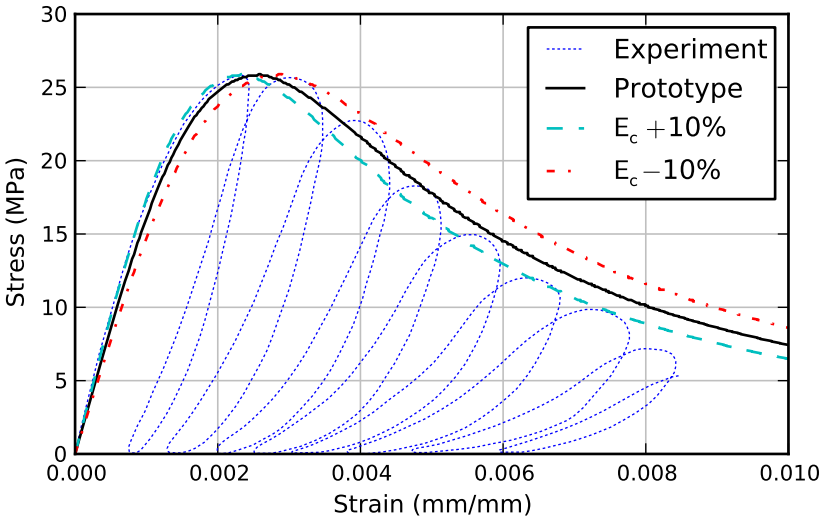

(b) Sinha et al. [207]

Figure 3.5: Sensitivity of Compression Response to Concrete Elastic Modulus (E_c)

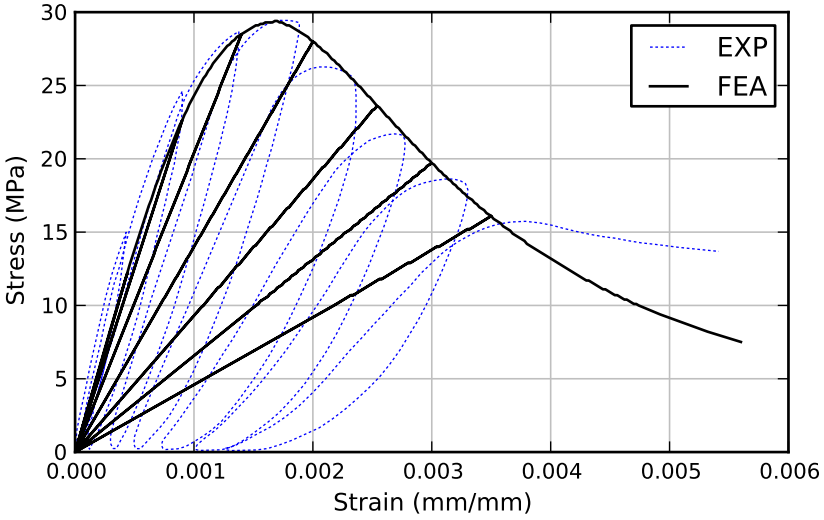

(a) Karsan and Jirsa [98]

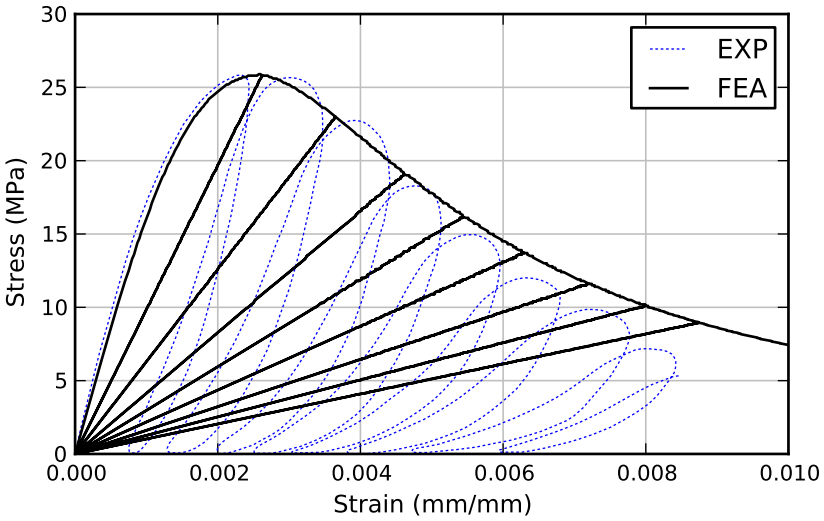

(b) Sinha et al. [207]

Figure 3.6: Uniaxial Cyclic Compression Response

When subjected to cyclic compression, the limitations of secant unloading and reloading are evident, as shown in Figure 3.6. The degradation of stiffness in the numerical models progressed more rapidly than the experimental data indicated, an effect more pronounced in the Sinha et al. [207] model. In both cases, the inability of the model to capture permanent, inelastic strains is obvious. Considering the intended use of this model (to capture the highly pinched response of nonseismic beam-column joints), however, this assumption is considered reasonable and will be evaluated in the context of its intended function in subsequent chapters of this thesis.

Additionally, the unloading-reloading rules of the total strain rotating crack model are judged more appropriate than the primary competing framework in DIANA—Drucker-Prager plasticity—wherein the initial elastic modulus is used for unloading regardless of the strain level. In this case, the unloading-reloading stiffness and permanent inelastic strains are uniformly overestimated at all levels of strain, resulting in an overestimation of the energy dissipation.

3.6 Uniaxial Tension Response

One of the most fundamental nonlinearities in the response of concrete structures is tensile cracking. While the tensile capacity of concrete is often neglected after tensile failure occurs for design purposes, experimental evidence suggests that concrete actually continues to contribute to the tensile response of reinforced concrete in the post-peak tensile region [25]. This behavior is known as tension softening.

The total strain rotating crack model requires specification of a uniaxial tension response curve. Depending on how reinforcements are modeled, either a tension softening or tension stiffening curve is required. Tension softening is needed when reinforcements are non-uniformly distributed and simulated with bond-slip interface elements, while tension stiffening is appropriate in regions with uniform reinforcement under the assumption of perfect bond. A more detailed discussion of tension stiffening is provided

in Section 3.6.5.

In the prototype model, the uniaxial tension response follows the softening law proposed by Hordijk [84], expressed as

$$\sigma_{cr} = f_t \left[\left(1 + \left(c_1 \frac{\epsilon_{cr}}{\epsilon_{ult}} \right)^3 \right) e^{\left(c_2 \frac{\epsilon_{cr}}{\epsilon_{ult}} \right)} - \frac{\epsilon_{cr}}{\epsilon_{ult}} (1 + {c_1}^3) e^{-c_2} \right] \tag{3.6}$$

$$\epsilon_{ult}^{cr} = 5.136 \frac{G_f}{h f_t} \tag{3.7}$$

with $c_1 = 3$ and $c_2 = 6.93$. The strain ϵ_{ult}^{cr} represents the maximum inelastic strain value for which tensile stresses are developed, which depends on the mode-I fracture energy G_f and tensile strength f_t. The crack bandwidth h is a characteristic length providing mesh objectivity with respect to the fracture energy G_f. When concrete is modeled using solid elements, the crack bandwidth is taken as $\sqrt[3]{V}$ where V is the volume of the element [4]. For beam and truss elements, the default value of h is taken as the length of the element. The tensile strength f_t is computed according to the CEB-FIP Model Code 1990 [30] as

$$f_t = 0.3 \, (f_c')^{\frac{2}{3}} \tag{3.8}$$

while the fracture energy G_f is computed according to the equation proposed by Remmel [189] as

$$G_f = 0.065 \cdot \ln \left(1 + \frac{f_c'}{10} \right) \qquad \text{(N/mm)} \tag{3.9}$$

The general features of Hordijk's uniaxial tension model are illustrated in Figure 3.7, in which the analytical expression from Equation 3.6 is verified with DIANA's implementation of the model.

The Hordijk tension softening model with the above material parameters was validated against concrete specimens tested in uniaxial cyclic tension by Gopalaratnam and Shah [68] and Reinhardt [188].

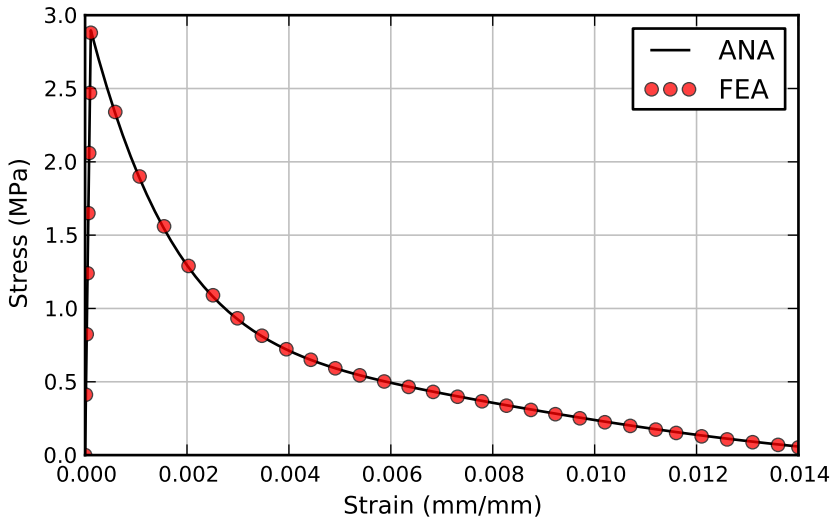

Figure 3.7: Hordijk [84] Tension Softening Analytical Curve and DIANA Verification

3.6.1 Verification with Gopalaratnam and Shah [68]

Gopalaratnam and Shah [68] tested a series of rectangular prism specimens in uniaxial cyclic tension. The specimens were loaded using wedge-type frictional grips designed to ensure failure of the prism away from the load application points, controlled using a closed-loop testing machine which insured a stable post-peak response. The specimens were cycled in tension between uniformly increasing displacement values and the zero stress condition.

A plain concrete specimen with dimensions 76 $\times$ 19 $\times$ 305 mm (3 $\times$ 0.75 $\times$ 12 in) was modeled in this study. Strain was measured over an 83 mm (3.25 in) gage length. The specimen had a tensile strength of 3.53 MPa (512 psi) which was reached at a tensile strain of 118×10^{-6} mm/mm, and a fracture energy of 0.0564 N/mm (0.433 lb/in). The finite element model consisted of a single truss element with tension response defined according to Equation 3.6. The monotonic numerical response is shown in Figure 3.8. The cyclic response is discussed in Section 3.6.4.

Good agreement was observed between computed and observed response. The initial stiffness and tensile failure point were accurately represented. The softening curve overestimated the capacity for strain values between approximately 0.0001 and 0.00025

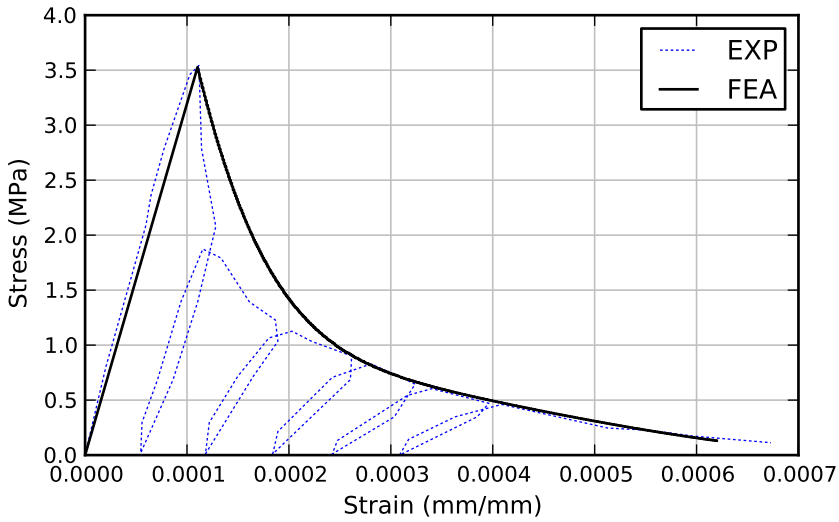

Figure 3.8: Uniaxial Tension Response for Gopalaratnam and Shah [68]

mm/mm, at which point the numerical and experimental responses became effectively indistinguishable.

3.6.2 Verification with Reinhardt [188]

The uniaxial tension model was also validated against experiments conducted by Reinhardt [188]. Reinhardt also tested a series of concrete prisms subjected to uniaxial cyclic tension loading, under similar conditions as that of Gopalaratnam and Shah.

The specimen modeled in this study was 250 mm long, 60 mm wide, and 50 mm thick (9.8 × 2.4 × 1.9 inches). A 5 mm × 5 mm (0.2 × 0.2 in) saw cut on each side reduced the effective cross-section to 50 × 50 mm^2 (1.9 × 1.9 in^2). The specimen was cycled in tension between increasing displacement values in tension, returning each cycle to a value of 5% of the tensile strength. The concrete had a measured compressive strength of 47.1 MPa (6830 psi) and a tensile strength of 3.2 MPa (464 psi). Strain was measured over a 35 mm (1.4 in) gage length. As with the model for Gopalaratnam and Shah, the finite element model consisted of a single truss element with tension response defined according to Equations 3.6–3.9. The monotonic numerical response is shown in Figure 3.9. The cyclic response is discussed later.

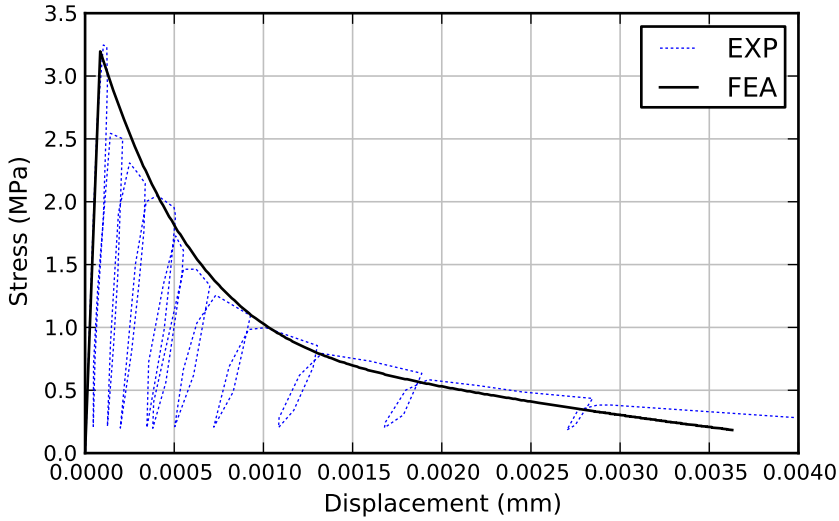

Figure 3.9: Uniaxial Tension Response for Reinhardt [188]

Excellent agreement was observed between computed and observed response. The initial stiffness and tensile failure point were accurately represented. In contrast to the Gopalaratnam and Shah model, the initial descending portion of the post-peak curve showed excellent agreement, while the numerical response underestimated the tensile strength for strain values above 0.001 mm/mm.

3.6.3 Tension Response Parameter Sensitivity

Figures 3.8 and 3.9 demonstrate that the Hordijk tension softening curve provides a reasonable representation of the envelope of the cyclic tension response of concrete. However, because the tension response depends upon multiple material parameters, a sensitivity study was conducted to better understand the impact of variation in computed material properties. Input material parameters investigated include modulus of elasticity E_c, concrete tensile strength f_t, concrete fracture energy G_F, and mesh objectivity based on the crack bandwidth parameter h. In each case, the parameter was varied from the prototype model by $\pm 10\%$. Each response is compared with the experimental response from both Gopalaratnam and Shah [68] and Reinhardt [188].

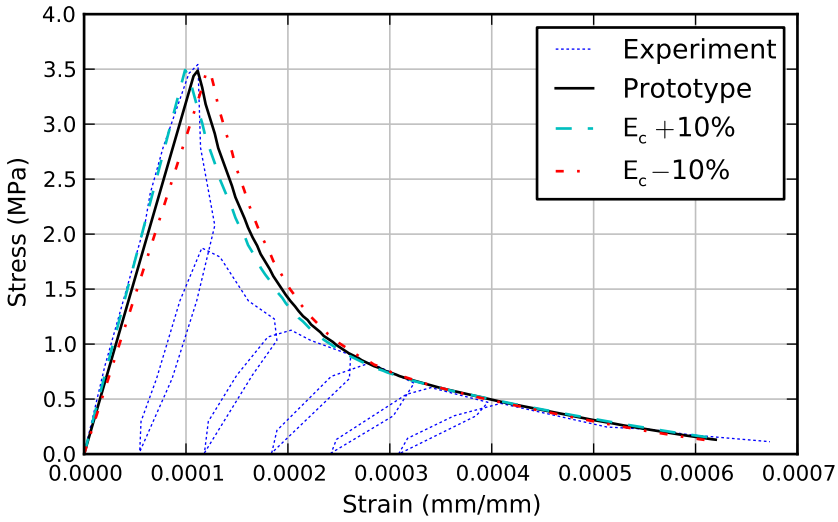

(a) Gopalaratnam and Shah [68]

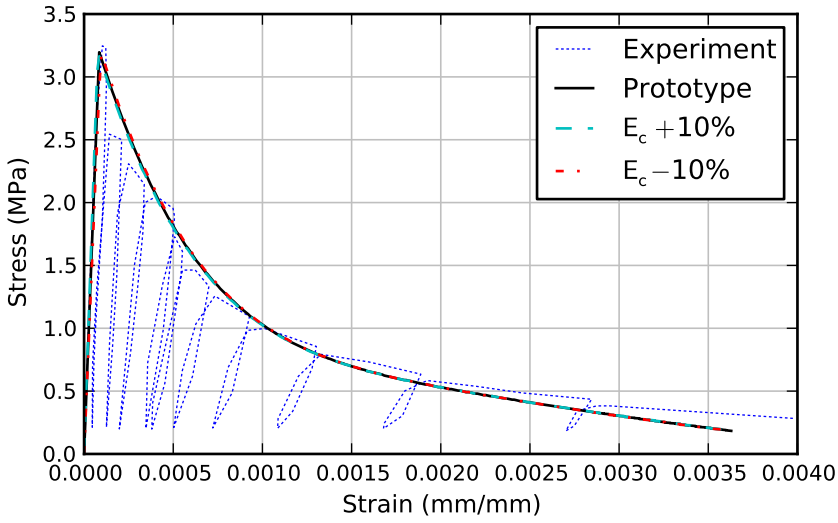

(b) Reinhardt [188]

Figure 3.10: Sensitivity of Tension Response to Concrete Elastic Modulus (E_c)

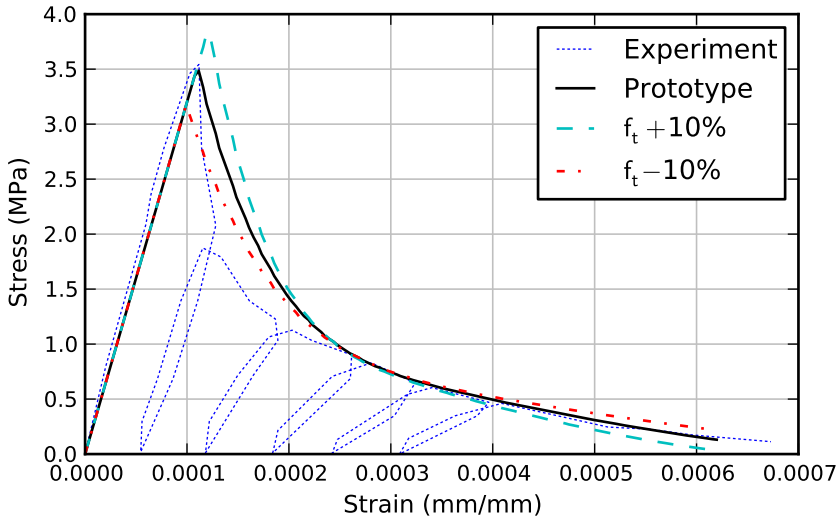

(a) Gopalaratnam and Shah [68]

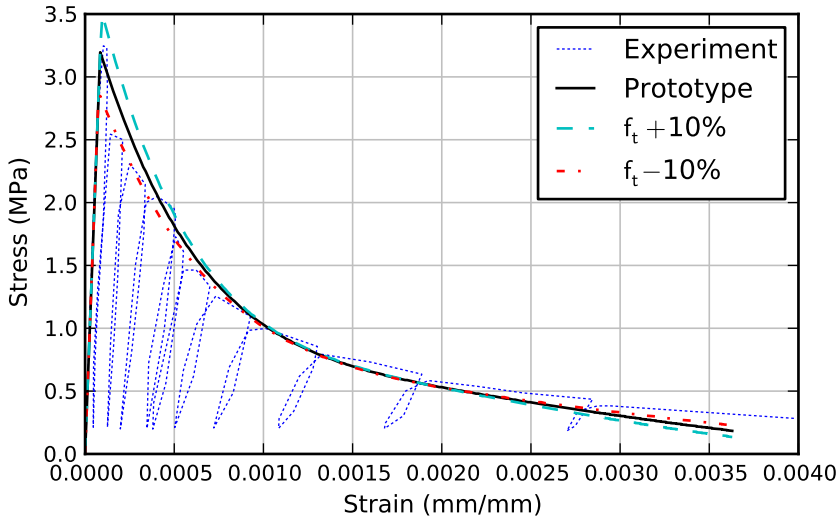

(b) Reinhardt [188]

Figure 3.11: Sensitivity of Tension Response to Concrete Tensile Strength (f_t)

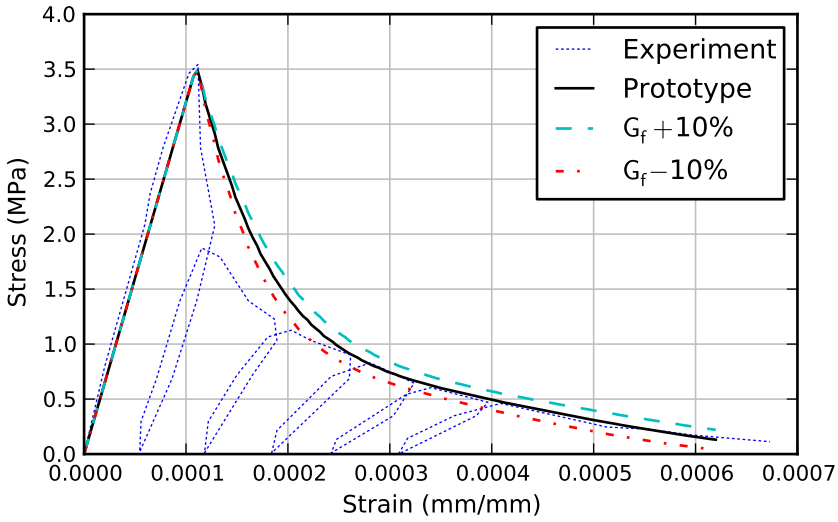

(a) Gopalaratnam and Shah [68]

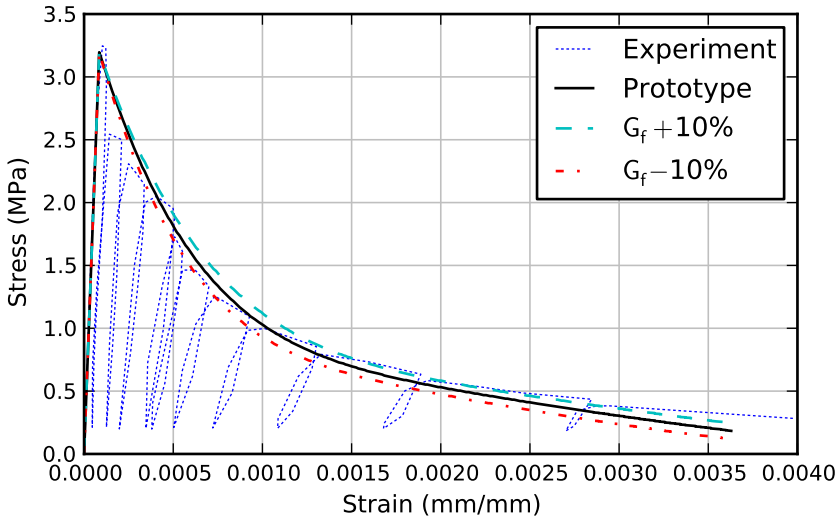

(b) Reinhardt [188]

Figure 3.12: Sensitivity of Tension Response to Concrete Fracture Energy (G_f)

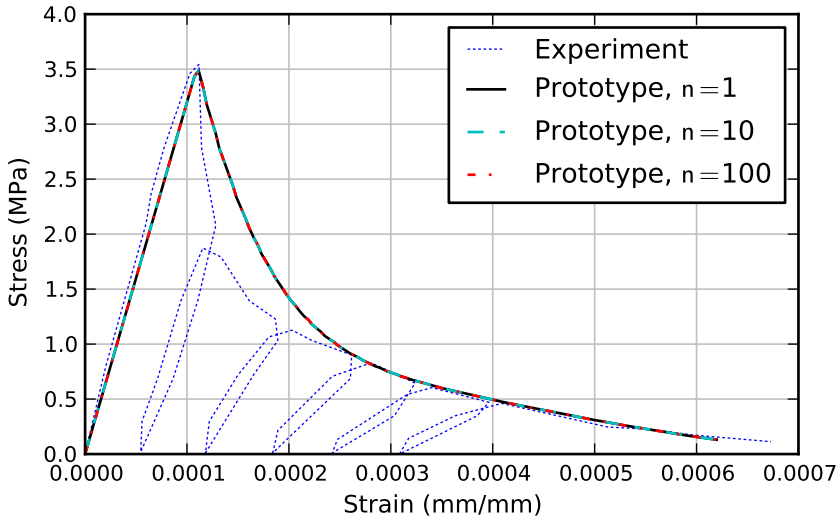

(a) Gopalaratnam and Shah [68]

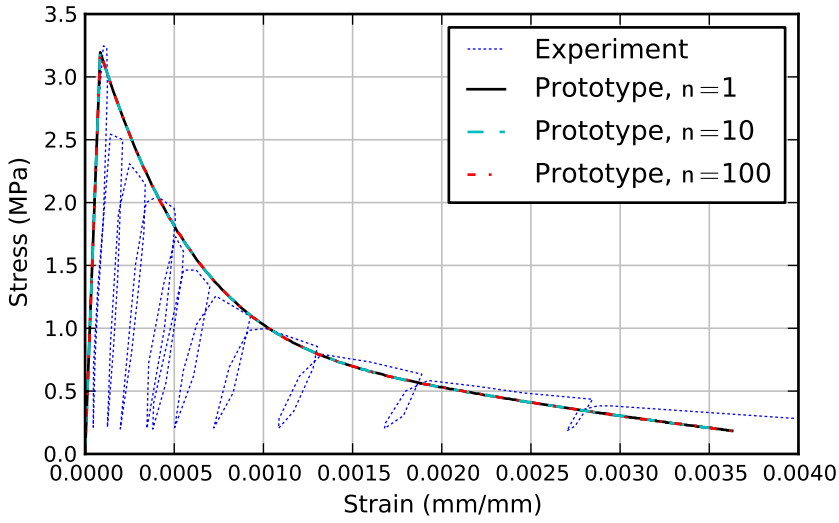

(b) Reinhardt [188]

Figure 3.13: Mesh Objectivity of Tension Response via Crack Bandwidth h

Figure 3.10 shows the sensitivity of the tension response to the concrete elastic modulus E_c. While the change in response is more visible in the Gopalaratnam and Shah model due to the differing magnitude of the strain scale, only the elastic loading branch and initial descending portion of the softening branch are influenced by modifying the modulus of elasticity 10%; the same input variation produced no visible difference in the model of Reinhardt's test.

Figure 3.11 shows the sensitivity of the tension response to the concrete tensile strength f_t, computed using the CEB-FIP Model Code 1990 [30] equation in the prototype model. For both models, the initial loading follows the elastic modulus until the maximum tensile stress is reached. From this point, unloading is governed by the Hordijk curve[84], and the rate of decay and maximum strain depend on the fracture energy and tensile strength, based on Equation 3.7. Thus, the maximum stress will vary by 10%, and the shape of the softening will decay from the peak value such that the energy released is constant. Thus, a reduction in ultimate strain is observed for the case where the tensile strength increases, and an increase in ultimate tensile strain is observed when the tensile strength decreases. For either case, the variation in post-peak response is marginal and the prototype response remained the best representation in comparison with both experimental studies.

Figure 3.12 shows the sensitivity of the tension response to the concrete mode-I fracture energy G_f, computed using the Remmel [189] equation in the prototype model. Fracture energy is only relevant after the cracking failure criterion has been detected in the finite element model, resulting in no influence during the ascending portion of the tensile response. Since fracture energy directly influences the area under the softening curve, increasing G_f will serve to shift the softening strain response by increasing ϵ_{ult}^{cr}, while reducing G_f will produce the opposite response. For either case, the result does not significantly alter the post-peak behavior, and the prototype response remained the best representation in comparison with both experimental studies.

Figure 3.13 shows the sensitivity of the tension response to the final parameter evaluated: the crack bandwidth h. The crack bandwidth provides mesh objectivity by normalizing the concrete fracture energy with respect to element size, resulting in the same energy release during the fracture process regardless of the number of elements (and therefore element size) representing a concrete specimen. Thus, specification of the appropriate crack bandwidth value should produce a response without mesh dependence, as was shown in this figure where, as the element size was systematically reduced by increasing the number of elements n, each model produced an indistinguishable response.

3.6.4 Cyclic Tension Response

As with the cyclic compression response, the limitations of the assumption of secant unloading and reloading are evident in Figure 3.14, where the cyclic response of the prototype model is compared with experimental data from Gopalaratnam and Shah as well as from Reinhardt. In this figure, where the specimen is cycled only in tension, the predicted stiffness degrades remarkably faster than that observed in both experimental studies, and permanent inelastic deformations are not captured. However, the response improves when the cycling loading process includes compression excursions.

To this effect, comparison was made with another experiment conducted by Reinhardt [188] where an identical specimen was subjected to cyclic tension-compression loading; the specimen was loaded in compression to a value equal to the magnitude of the tensile strength. A comparison of the numerical and experimental response is shown in Figure 3.15. In this case, while the numerical response clearly under-predicts the energy dissipation characteristics, the reloading stiffness in tension of the numerical model shows much improved agreement with that of the experiment. Furthermore, it is worth noting that the assumption of no permanent inelastic deformation may be of less consequence in tension because the magnitude of the maximum stresses attained is much smaller ($\approx$10x) than that observed in the compression response. As with the

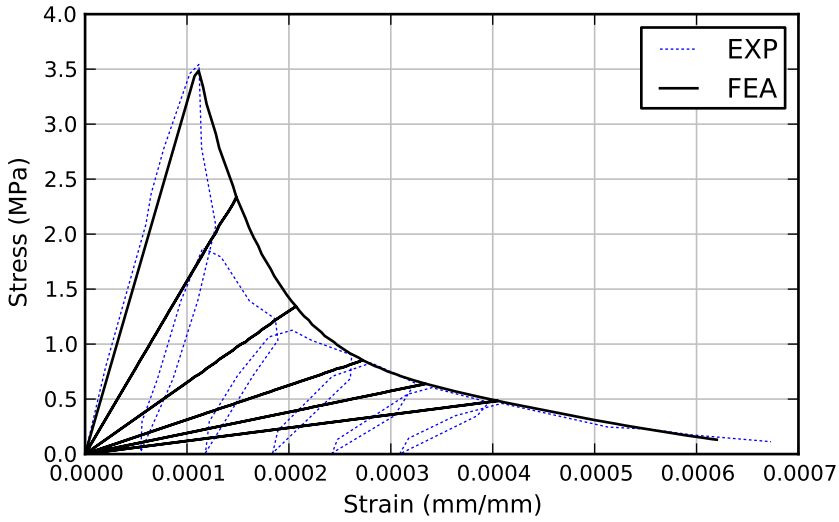

(a) Gopalaratnam and Shah [68]

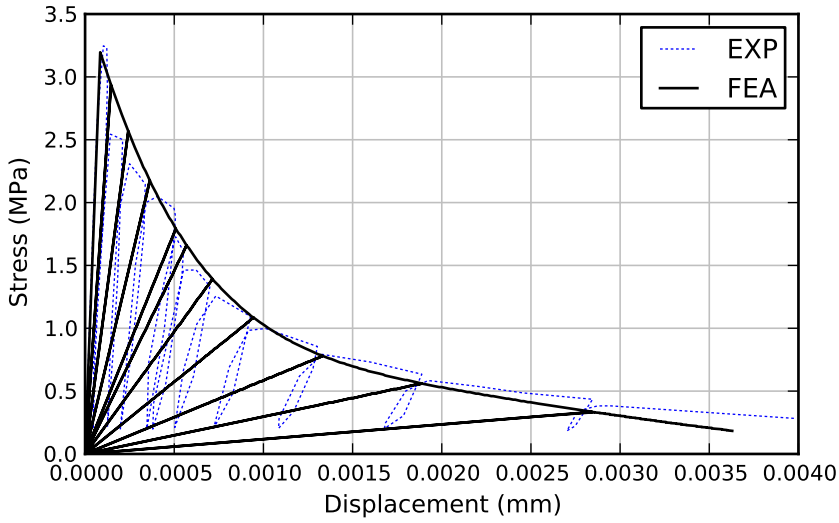

(b) Reinhardt [188]

Figure 3.14: Uniaxial Cyclic Tension Response

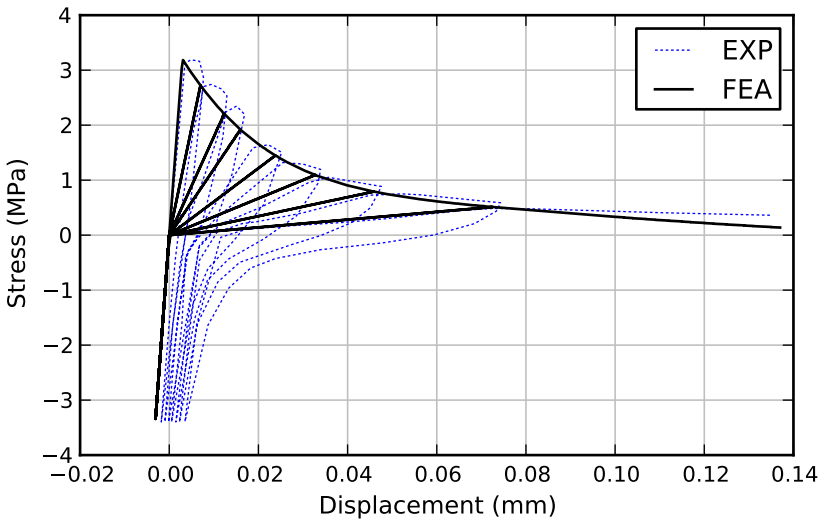

Figure 3.15: Uniaxial Reversed Cyclic Tension Response for Reinhardt [188]

cyclic compression response, the implications of these assumptions must be further investigated when the prototype model is applied to the case of a nonseismically detailed beam-column joint.

3.6.5 Tension Stiffening

Another important behavior of *reinforced* concrete subjected to tension is demonstrated in Figure 3.16a: for a uniaxially loaded reinforced concrete tensile specimen, the member response is shown to be stiffer than that of the bare reinforcing bars, despite the formation of tensile cracks in the concrete. This increase in stiffness (exhibited by the difference between the member and bar response) is known as tension stiffening. While tension stiffening is only applicable for reinforced concrete, it is included in this chapter since it must be specified as a component of the concrete constitutive model.

In this scenario, steel reinforcement transfers all force across cracks. Between cracks, however, the uncracked concrete engages in tensile stress and effectively resists deformation of reinforcing bars, provided adequate bond exists. A comparison of force and distributions for the concrete and steel between two cracks is shown in 3.16b.

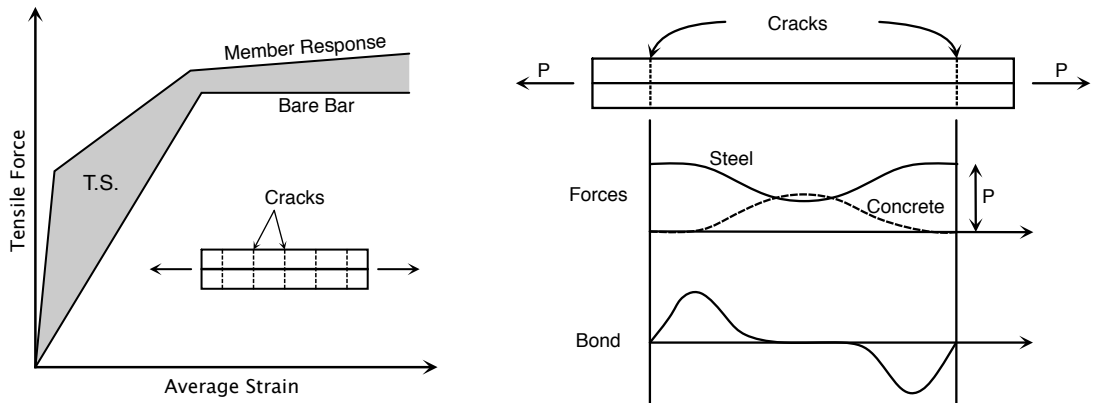

(a) CEB-FIP Model Code 1990 [30] (b) Belarbi and Hsu [25]

Figure 3.16: Tension Stiffening Effect

The tension stiffening effect can be incorporated via a post-peak concrete stress-strain curve for uniaxial tension. In regions containing a uniform distribution of orthogonal reinforcement with perfect bond, the tensile response is simplified to account for the effect of tension stiffening using the equation by Vecchio and Collins [225].

$$\sigma_1 = \frac{f_t}{1 + \sqrt{200\varepsilon_1}} \tag{3.10}$$

In this equation, σ_1 refers to the principal average concrete tensile stress, f_t is the tensile cracking strength, and ε_1 is the principal tensile strain as measured over a gauge length sufficient to span several cracks. The tensile behavior of reinforced concrete is assumed linear elastic until the onset of tensile cracking. In DIANA, this curve must be specified via the material keyword `MULTLN`.

The general characteristics of the Vecchio and Collins tension stiffening model are demonstrated and contrasted with the Hordijk tension softening model in Figure 3.17.

Tension stiffening is generally suitable in finite element models where reinforcing bars are simulated with perfect bond and sufficient development/anchorage is present to prevent relative translations of bars with respect to host concrete elements [3]. The tension stiffening response is discussed further in the context of the cyclic shear panel analyses presented in Section 4.5.

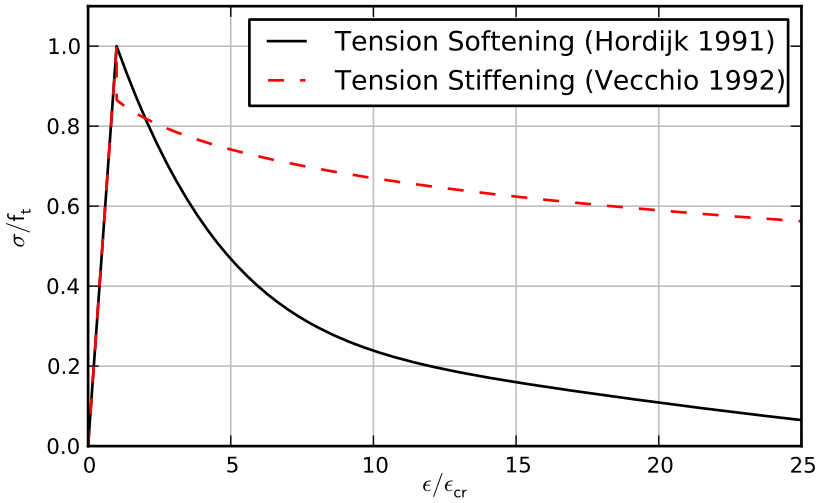

Figure 3.17: Tension Softening vs. Tension Stiffening Models

3.7 Summary

In this chapter, a concrete constitutive model suitable for the reversed cyclic analysis of nonseismically detailed beam-column joints was identified. The constitutive theory underlying the total strain rotating crack model in DIANA 9.4.4 was presented. Response models for uniaxial compression and tension were presented and successfully validated against experimental data. The sensitivity of each model to various material parameters was investigated.

The following chapter presents the extension of this framework to model the response of reinforced concrete, including the effects of steel plasticity, steel-concrete interface behavior, the response of anchored bars, and cyclic shear failure. The final prototype constitutive model is summarized in Section 4.6.

CHAPTER IV

EXTENSION TO REINFORCED CONCRETE

4.1 Objective

In Chapter 3, a constitutive model describing the response of plain concrete was described and validated against experimental data. In this chapter, the additional components necessary to simulate reinforced concrete are determined and validated against experimental data, ensuring that steel reinforcing bar response, bond-slip and anchorage response, and the failure of reinforced concrete in shear can be reproduced. The components of this "prototype model" are finally summarized in Section 4.6.

4.2 Steel Reinforcement Model

The response of beam-column joints is dependent on the nonlinear cyclic response of reinforcing bars. The Bauschinger effect—wherein the reinforcing bars exhibit premature yielding during load reversals—has been argued by some as critical for simulation of cyclically loaded joints [64, 81, 194], since the modified unloading/reloading curves allow cracks to close more easily during load reversals and thus improve the compression zone performance. Commonly-used steel models incorporating the Bauschinger effect include the Menegotto-Pinto [142], Monti-Nuti [148] and Seckin [198] models. Nonetheless, many analytical beam-column joint studies which simply employed an elastic-perfectly-plastic reinforcing bar response satisfactorily represented the hysteretic joint response on a macro level. These studies were reviewed in detail in Chapter 2.

In DIANA, reinforcing bars may be modeled using either the `L6TRU` truss element or the `L13BE` beam element. As the following discussion only considers uniaxially loaded

specimens, truss elements were specified in the following verification studies. The appropriateness of truss versus beam elements for reinforcing bar simulation are evaluated in Section 4.4, which addresses anchorage of hooked reinforcing bars.

Analytical models for reinforcing bar response in this study were validated against experimental data from Ma, Bertero, and Popov [131], wherein cyclic tests of steel reinforcing bars were performed as part of a larger effort to characterize the hysteretic response of reinforced concrete rectangular and T-beams. The Bauschinger effect is evident in the curved unloading/reloading response in this experimental data.

4.2.1 Menegotto-Pinto Model

Menegotto and Pinto [142] proposed an analytical model capable of respresenting the hysteretic behavior of steel reinforcing bars exhibiting the Bauschinger effect together with isotropic strain hardening. The Menegotto-Pinto model is available in DIANA 9.4.4 for embedded reinforcements [4].

In this model, the constitutive response consists of one-dimensional stress-strain relations for branches between two subsequent load reversal points, and is expressed in terms of dimensionless stress σ^* and strain ϵ^* as

$$\sigma^* = b\epsilon^* + \frac{(1-b)\epsilon^*}{(1+\epsilon^{*R})^{\frac{1}{R}}} \tag{4.1}$$

where b is the ratio of the strain hardening to initial modulus and R is the curvature parameter controlling the shape of the unloading-reloading cycles, defined as

$$R = R^0 - \frac{A_1 \xi_p^{max}}{A_2 + \xi_p^{max}} \tag{4.2}$$

In this equation R^0 is the initial curvature parameter and ξ_p^{max} is the maximum plastic excursion during a previous half-cycle. Isotropic hardening is represented by the equation

$$\frac{\sigma_{sh}}{\sigma_{y0}} = A_3 \cdot \left(\frac{\epsilon_{max}^t}{\epsilon_{y0}} - A_4 \right) \tag{4.3}$$

where σ_{y0} and ϵ_{y0} are the initial yield stress and corresponding strain, ϵ^{t}_{max} is the maximum absolute total strain at the instant of strain reversal, and σ_{sh} is the stress shift in the linear yield asymptote for isotropic hardening. A_1–A_4 are material constants which require experimental determination.

A parameter study, together with recommendations from the literature [142, 148], led to a selection of these parameters as $b = 0.002$, $R^0 = 22.0$, $A_1 = 18.5$, $A_2 = 0.15$, $A_3 = 0.15$ and $A_4 = 0.0$. The cyclic response of this model is compared with data from Ma et al. [131] in Figure 4.1.

As shown in Figure 4.1, the Menegotto-Pinto model shows good agreement with the experimental hysteretic response of reinforcing bars subjected to cyclic load. However, this model possesses an important limitation in the current version of DIANA due to its inability to be combined with bond-slip interface elements. Inclusion of bond-slip is critical for analysis of seismically deficient beam-column joints, thus other plasticity-based models for cyclic steel response were investigated.

4.2.2 Von Mises Plasticity

The Von Mises plasticity model has been commonly employed to simulate the response of steel reinforcing bars in nonlinear reinforced concrete finite element models. Previous researchers have applied Von Mises plasticity using the elastic-perfectly-plastic condition, isotropic hardening (wherein the yield surface expands), kinematic hardening (wherein the yield surface is shifted), and mixed isotropic/kinematic hardening. Each of these cases was investigated using DIANA 9.4.4 [4].

In the Von Mises plasticity model, the yield function is represented by the equation

$$f(\boldsymbol{\sigma}, \boldsymbol{\eta}, \kappa) = \sqrt{3J_2} - \bar{\sigma}(\kappa) = \sqrt{\frac{1}{2}(\boldsymbol{\sigma} - \boldsymbol{\eta})^T \mathbf{P} (\boldsymbol{\sigma} - \boldsymbol{\eta})} - \bar{\sigma}(\kappa) \tag{4.4}$$

This failure surface, shown in Figure 4.2, is a cylinder in the principal stress space centered about the hydrostatic axis ($\sigma_1 = \sigma_2 = \sigma_3$) if there are no back stresses $\boldsymbol{\eta}$ present

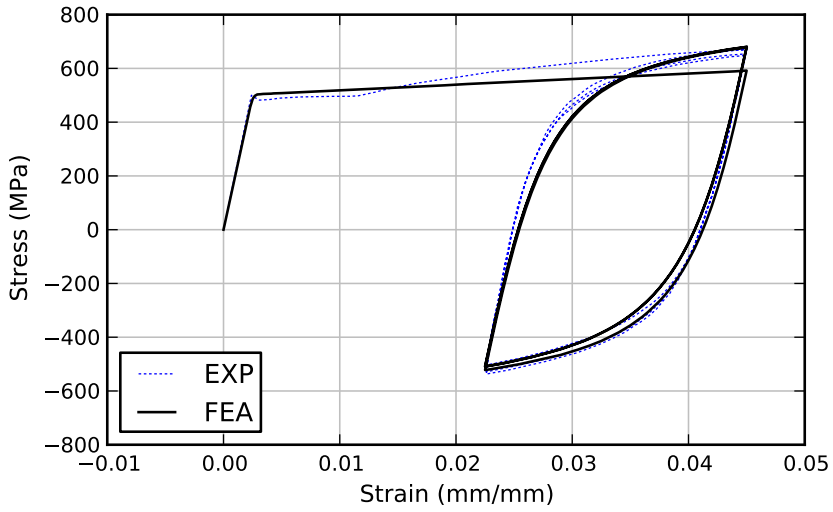

(a) Specimen 1

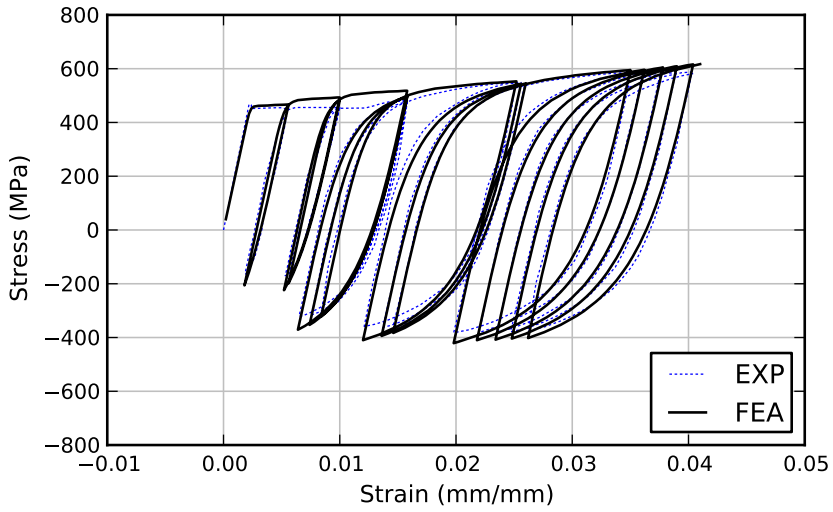

(b) Specimen 2

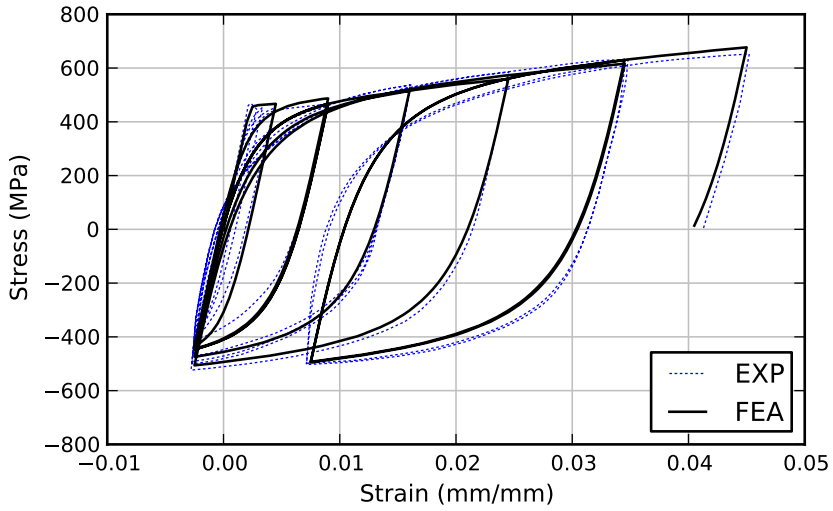

(c) Specimen 3

Figure 4.1: Reinforcing steel response – Menegotto-Pinto Model

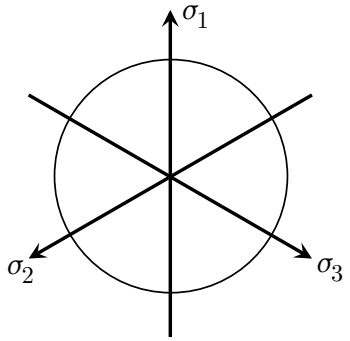

Figure 4.2: Von Mises Yield Surface in π-plane

(which would cause a shift in the location of the centroid of the cylindrical failure surface). The projection matrix $\mathbf{P}$ is used to compute the second deviatoric stress invariant J_2 and is given as

$$\mathbf{P} = \begin{bmatrix} 2 & -1 & -1 & 0 & 0 & 0 \\ -1 & 2 & -1 & 0 & 0 & 0 \\ -1 & -1 & 2 & 0 & 0 & 0 \\ 0 & 0 & 0 & 6 & 0 & 0 \\ 0 & 0 & 0 & 0 & 6 & 0 \\ 0 & 0 & 0 & 0 & 0 & 6 \end{bmatrix} \tag{4.5}$$

The flow rule assumes associated plastic flow which corresponds to the strain rate vector

$$\dot{\epsilon}^p = \dot{\lambda}\frac{\mathbf{P}(\boldsymbol{\sigma} - \boldsymbol{\eta})}{2\bar{\sigma}} \tag{4.6}$$

The back stresses $\boldsymbol{\eta}$ evolve according to

$$\dot{\boldsymbol{\eta}} = \frac{2}{3}(1-\gamma)\frac{\partial\bar{\sigma}}{\partial\kappa}\dot{\lambda}\frac{\mathbf{P}(\boldsymbol{\sigma} - \boldsymbol{\eta})}{2\bar{\sigma}} \tag{4.7}$$

where $0 \leq \gamma \leq 1$ is a scalar parameter governing the mixture of isotropic and kinematic hardening. Specifying $\gamma = 1$ results in isotropic hardening only; specifying $\gamma = 0$ results in kinematic hardening only. A mixture of isotropic and kinematic hardening is achieved by an intermediary value of γ between 0 and 1.

The relation between the internal state variable κ and the plastic process is given in the principal space by the following hardening hypothesis in the case of strain hardening.

$$\dot{\kappa} = \sqrt{\frac{2}{3}\left(\dot{\epsilon}_1^p\dot{\epsilon}_1^p + \dot{\epsilon}_2^p\dot{\epsilon}_2^p + \dot{\epsilon}_3^p\dot{\epsilon}_3^p\right)} = \dot{\lambda} \tag{4.8}$$

Here, $\dot{\lambda}$ is a plastic multiplier restricted by the standard Kuhn-Tucker conditions.

For the prototype model, a bilinear, uniaxial stress-strain law was specified via the multilinear input option. This law must be manually converted into equivalent stress $\bar{\sigma}$ and equivalent plastic strain κ. The plastic strain is given by

$$\epsilon_1^p = \epsilon_1 - \epsilon_1^e \tag{4.9}$$

with the uniaxial strain rate igiven by

$$\dot{\epsilon}_1^p = \dot{\lambda}\frac{\sigma_1}{\bar{\sigma}} = \dot{\lambda} \tag{4.10}$$

considering that the uniaxial stress and equivalent stress are equal ($\sigma_1 = \bar{\sigma}$) together with Equation 4.8. Thus, a multilinear stess-strain law σ-ϵ with n-points is converted to a multilinear equivalent stress-equivalent plastic strain law $\bar{\sigma}$-κ as follows for each point $i \in (1, n)$.

$$\bar{\sigma}_i = \sigma_i \tag{4.11}$$

$$\kappa_i = \epsilon_i - \frac{\sigma_i}{E} \tag{4.12}$$

Since the model follows a bilinear strain hardening diagram, the multilinear stress-strain law may be defined solely on the basis of the yield stress σ_y and the strain hardening ratio

$$b = \frac{E_{sh}}{E} \tag{4.13}$$

where E represents Young's modulus for steel, and E_{sh} is the modulus in the strain hardening branch. Depending on the specification of isotropic vs. kinematic strain hardening—as well as the range of strain values over which the model is intended to be applied—a different value of the strain hardening ratio b may be needed to achieve agreement with experimental data.

For the case of isotropic hardening, the yield surface expands according to the hardening specification. Back stresses $\boldsymbol{\eta}$ are not developed, so a shift in the failure surface is not observed. Thus, a reinforcing bar which is cycled will exhibit increasing stress

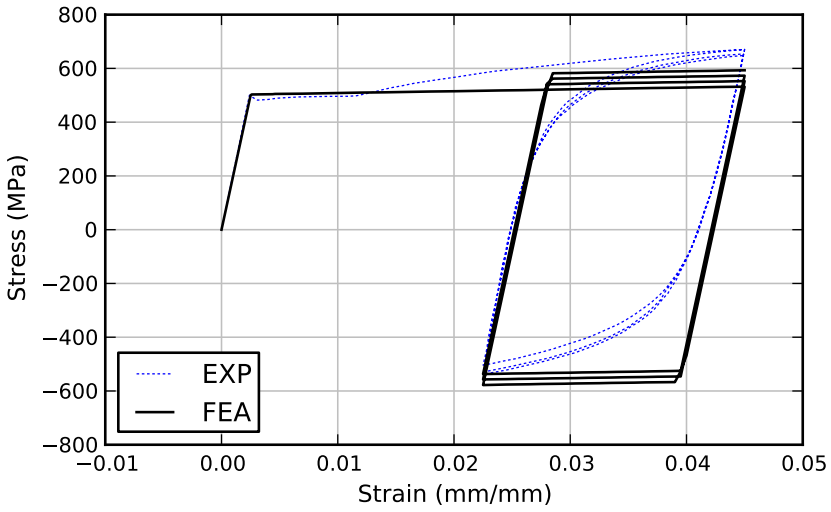

(a) Specimen 1

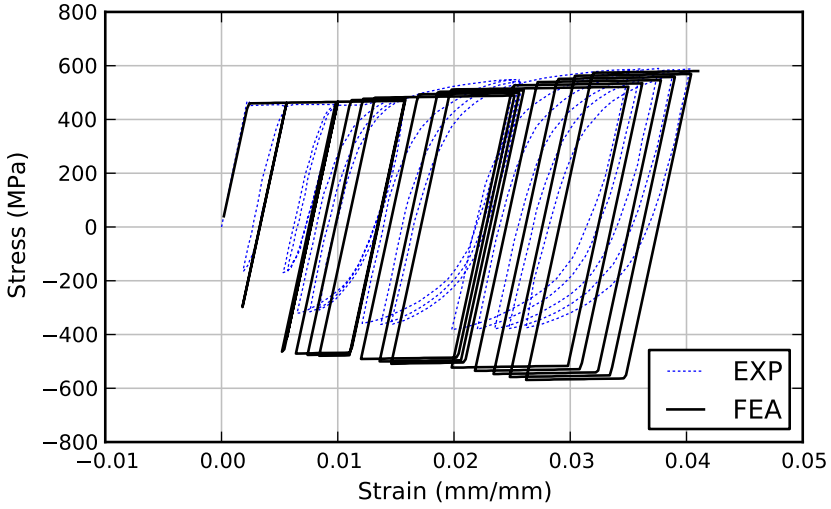

(b) Specimen 2

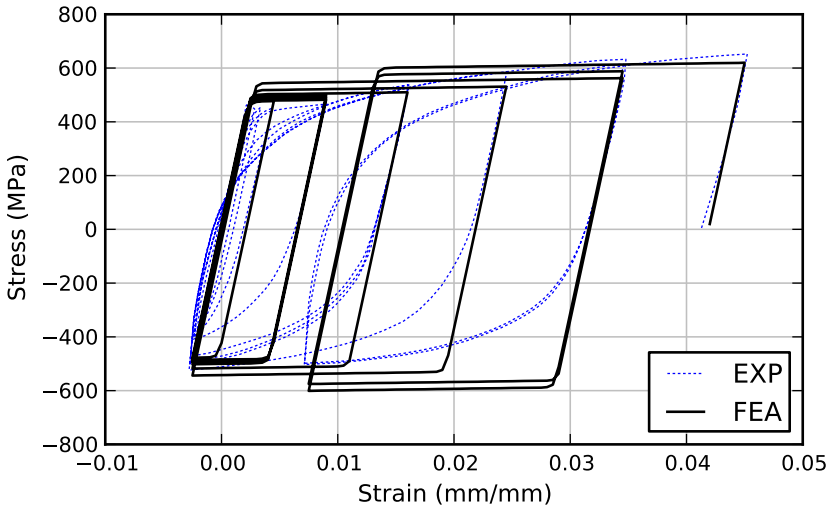

(c) Specimen 3

Figure 4.3: Reinforcing steel response – Von Mises with Isotropic Hardening

values when subjected to reversed cyclic loading in both tension and compression. This effect is illustrated in Figure 4.3, wherein the Von Mises model with isotropic strain hardening ($b = 0.001$) is compared to experimental data from Ma et al. [131]. For positive stress values, the increasing response due to isotropic hardening is reasonable, but in the negative stress regime, the experimental data appear to exhibit primarily kinematic hardening, such that the predicted and observed responses diverge.

For the case of kinematic hardening, the yield surface shifts according to the hardening specification. A parameter study was conducted to determine the optimum value of the hardening ratio b for kinematic hardening. The results of the study are illustrated in Figure 4.4 using data from Ma et al. [131]; the backbone of the response was most closely followed when $b = 0.02$. Using this value, the cyclic performance of the system was compared to data from Ma et al. [131] and is shown in Figure 4.5.

The cyclic prediction using kinematic hardening was significantly better than the response using isotropic hardening. For all three test specimens, especially specimens 2 and 3, the cyclic envelope showed good agreement with experimental data.

4.2.3 Prototype Steel Model

While the Menegotto-Pinto reinforcing bar model follows the nonlinear steel response more closely due to its representation of the Bauschinger effect, the inability to pair this model with line-to-solid bond interface elements in the current version of DIANA resulted in the selection of the Von Mises plasticity model with kinematic hardening for the prototype model. Based on the parameter study, a hardening ratio of $b = 0.02$ was selected to best represent the contribution of strain hardening in the range expected for beam-column joint simulation.

A potential limitation of this approach is that the energy dissipated by steel participation in the hysteretic reinforced concrete response will be over-predicted due to its neglecting the Bauschinger effect. However, since the concrete stiffness degradation

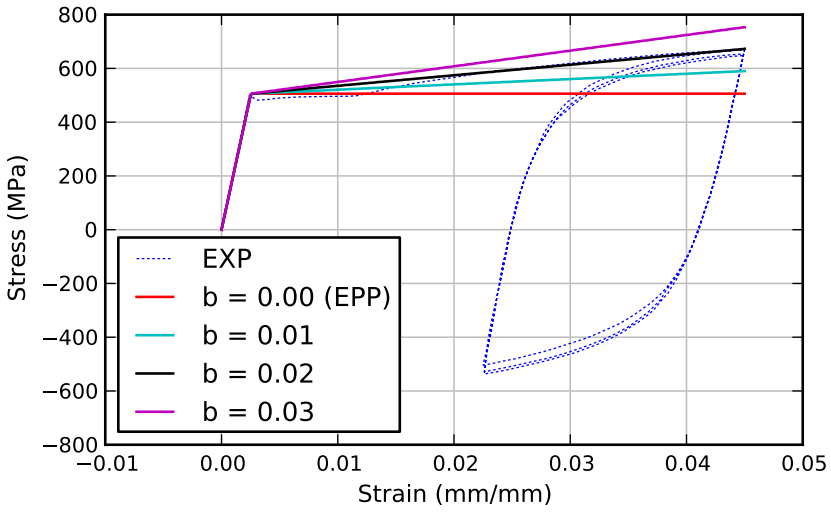

(a) Specimen 1

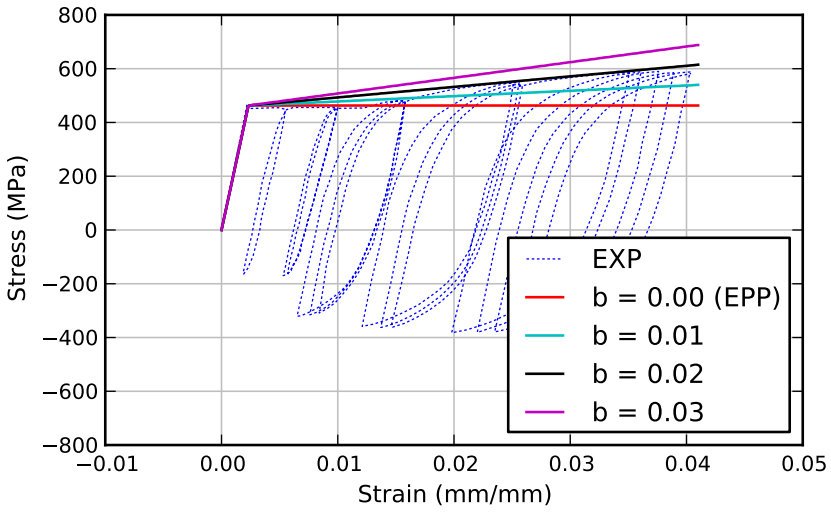

(b) Specimen 2

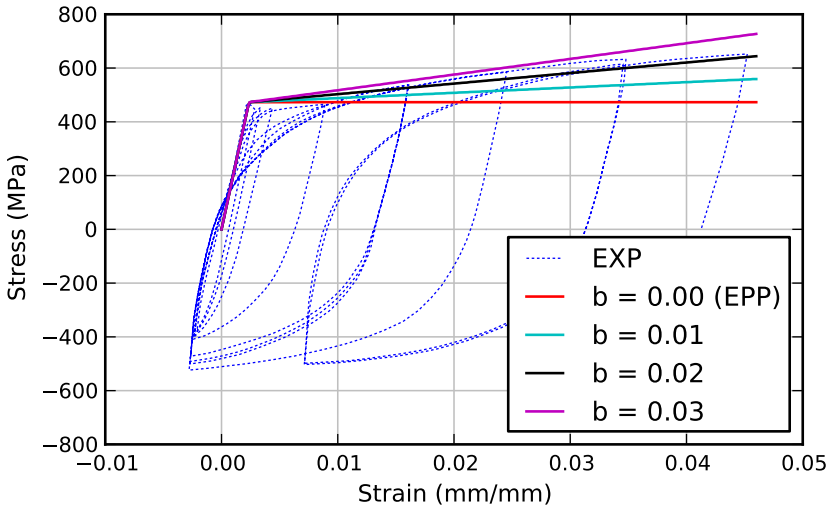

(c) Specimen 3

Figure 4.4: Sensitivity of Von Mises Model to Hardening Ratio b

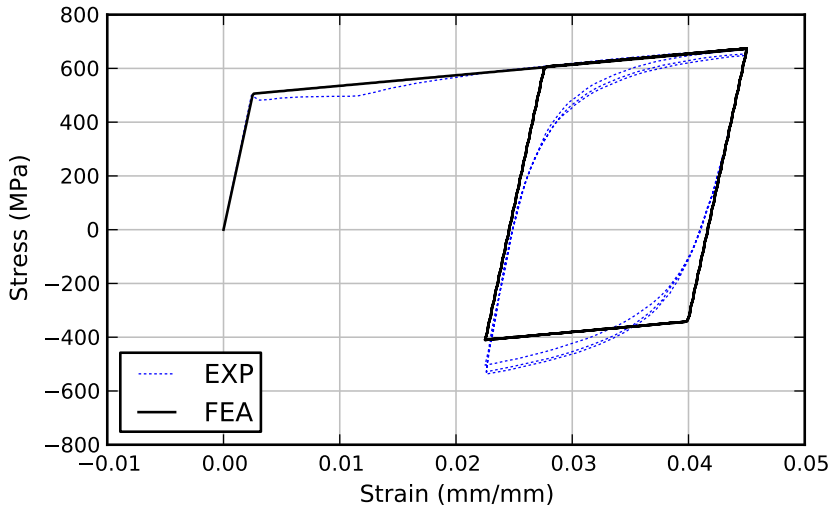

(a) Specimen 1

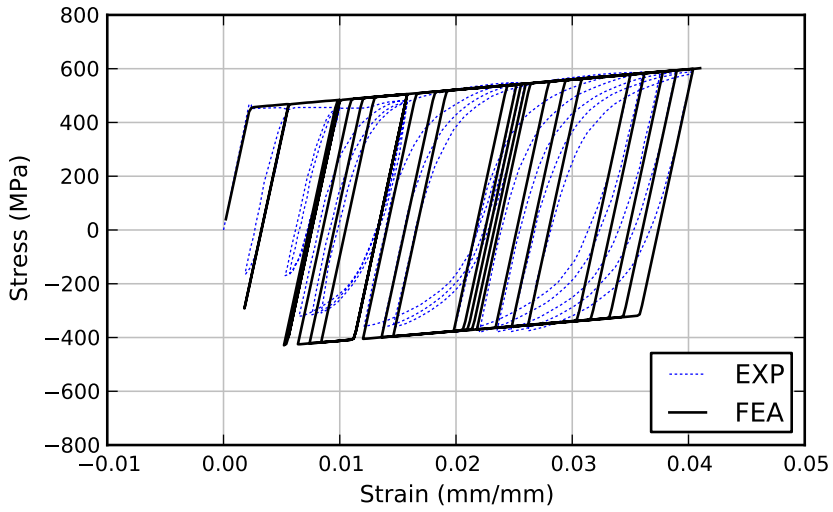

(b) Specimen 2

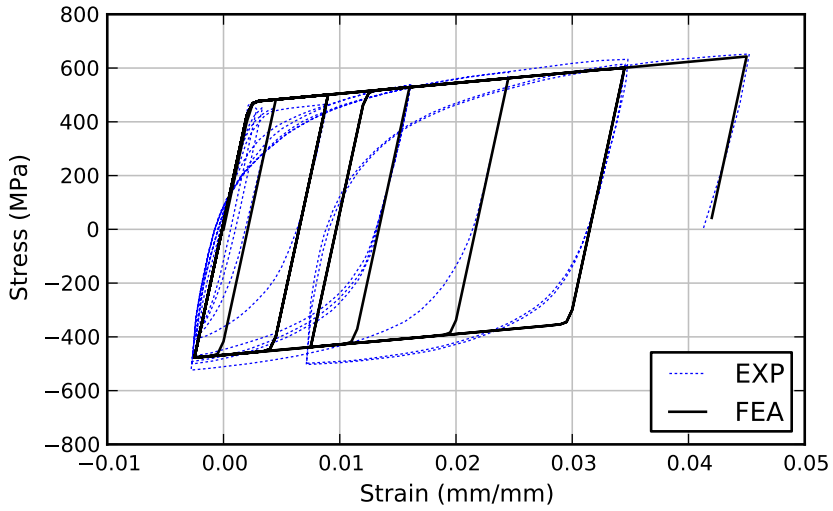

(c) Specimen 3

Figure 4.5: Reinforcing steel response – Von Mises with Kinematic Hardening

model does not allow for permanent inelastic strains (thus underestimating energy dissipation), a steel constitutive model which slightly overestimates energy dissipation may prove advantageous. A critical evaluation of this combination of concrete and steel constitutive models for global representation of energy dissipation in beam-column joint hysteretic response is provided in Section 5.6.

4.3 Bond-Slip Response

Bond-slip is an important component in the response of nonseismically detailed beam-column joints, especially when subjected to reversed cyclic loading. Some of the significant bond-related failure processes a deficient joint may exhibit include pull-out of longitudinal beam bottom reinforcements, degradation of column splices, and anchorage failure of hooked beam bars within the joint core.

4.3.1 Background on Bond-Slip Behavior and Simulation

Recent state-of-the-art reports by *fib* [2] and Joint ACI-ASCE Committee 408 (Development and Splicing of Deformed Bars) [8] provide in-depth treatment of the complex failure processes and prior research on cyclic bond performance and available models. Only the key characteristics of cyclic bond performance are described herein.

The types of failure modes exhibited in bond behavior can be divided into two categories: (a) failure by splitting of concrete, and (b) pull-out failure by shearing of concrete between reinforcing bar ribs. The former is common in unconfined concrete where bearing forces lead to high radial tensile stresses, while the latter is typical of pull-out failure in confined concrete, where sufficient cover and transverse reinforcement prevents propagation of splitting cracks [8].

Cyclic load arising from seismic excitation is categorized as low-cycle high-amplitude fatigue, wherein the system is subjected to a low number of cycles of large stress or slip

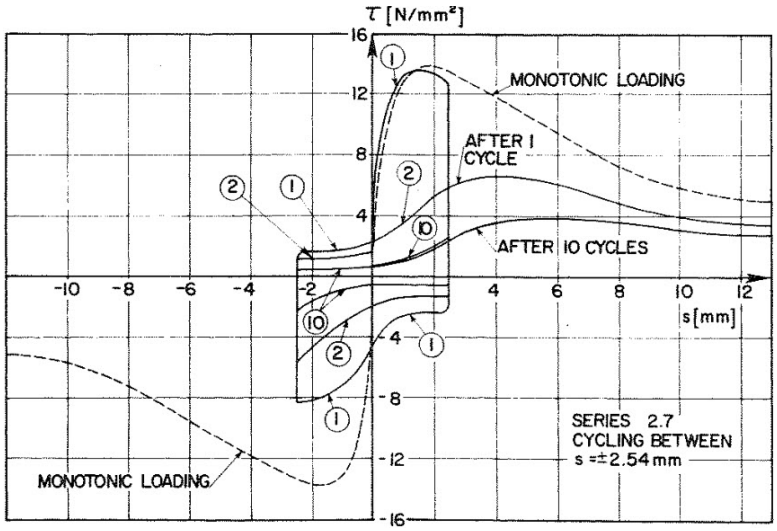

Figure 4.6: Cyclic Bond Deterioration from Eligehausen et al. [54]

levels at low strain rates [2]. In this case, the bond-slip performance is significantly reduced below that observed in monotonic loading of the same specimen, and further deterioration of the bond strength is observed with increased number of cycles. This process has been repeatedly observed in experimental campaigns such as those completed by Eligehausen et al. [54] and Viwathanatepa et al. [228], who tested the cyclic pull-out response of reinforcing bars embedded in concrete blocks. To illustrate this concept, a figure from Eligehausen et al. [54] is reproduced in Figure 4.6. For this configuration, the bond strength reduced by about 50% after the first cycle, and by about 60% between the first and tenth cycles.

Numerous factors affect the deterioration of bond strength under cyclic loading. Recent guidelines from ACI Committee 408 identify several of the most important factors as concrete compressive strength, concrete cover, bar size and transverse rib geometry, anchorage length, the yield stress of the reinforcing bar, confinement due to transverse reinforcement, and the type and rate of cyclic loading [8].

The contributing interactions of these and other factors is complex, and currently no single unifying theory is available to describe all possible combinations of bond condition. However, hysteretic bond stress-slip models incorporating various aspects of these

contributing factors have been developed. Several of the more sophisticated bond-slip models formulated specifically for simulation of reversed cyclic behavior are summarized in *fib* Bulletin no. 10 [2]. These models include the work of Morita and Kaku[151], Tassios [215], Viwathanatepa, Popov, and Bertero [228], Ciampi, Eligehausen, Bertero, and Popov [37], Eligehausen, Popov, and Bertero [54], Hawkins, Lin, and Jeang [76], Pochanart and Harmon [184], and Balàzs [20]. A simplified model based on that of Eligehausen et al. [54] is presented in the CEB-FIP Model Code 1990 [30] which, despite its simplicity, has been successfully used in many analytical studies of beam-column joint failure.

When applied in the context of a finite element simulation, these models have typically been used in conjunction with the element proposed by Ngo and Scordelis [155], whereby reinforcing bars are connected to host concrete elements via a series of nonlinear springs.

4.3.2 Interface Behavior in DIANA

Prior to selection of an analytical function to represent bond-slip, a review of the capabilities for bond-slip simulation in DIANA Release 9.4.4 [4] was conducted.

In DIANA, reinforcements may be connected to host concrete elements using various methods, including that of perfect bond, no bond (as in the case of unbonded tendons), manually generated line-to-solid interface elements, or by so-called "bond-slip reinforcements" which automate the discretization of reinforcing bars, line-to-solid interface elements, connection to host concrete elements, and the association of relevant material properties. The final option was chosen for this study.

With bond-slip reinforcements, the stress-slip law is incorporated in the finite element model via line-to-solid interface elements, in which steel elements are connected to concrete continuum elements via orthogonal, nonlinear springs. Steel reinforcements

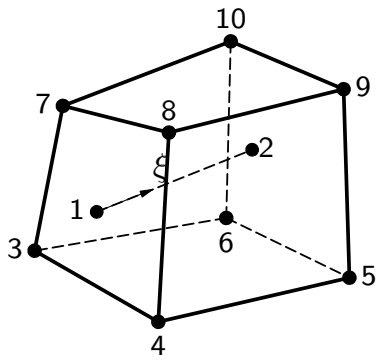

Source: DIANA [4]

Figure 4.7: Line-to-Solid Interface Element HX30IF

may be modeled with either truss or beam elements. A depiction of the line-to-solid interface element `HX30IF` is shown in Figure 4.7. Bond-slip reinforcements are invoked via the keyword `INTERF`.

A shear stress-slip relation is enforced along the longitudinal axis of the reinforcing bar, while a linear stiffness is specified in the two transverse directions. A multilinear bond-slip relationship of the user's choice may be specified by the material keyword `BONDSL` in the reinforcing bar material definition, while the initial values of the transverse linear stiffness values are specified according to the `DSTIF` keyword. Other available options for bond-slip reinforcements include the specification of end forces to simulate prestressing and tip stiffness to simulate, for instance, anchorage of a hooked bar to concrete via a nonlinear spring element.

The hysteretic rules governing loading-unloading-reloading behavior of bond-slip reinforcements in DIANA Release 9.4.4 [4] are summarized as follows[1]:

- A single shear stress-slip relation must be specified to represent the back-bone of the bond-slip response; this is the only user-defined input for bond behavior.
- The shear-slip relation is the same for positive and negative values of slip.

[1]TNO DIANA indicates several behaviors listed below will be improved in the upcoming DIANA 9.4.5 release.

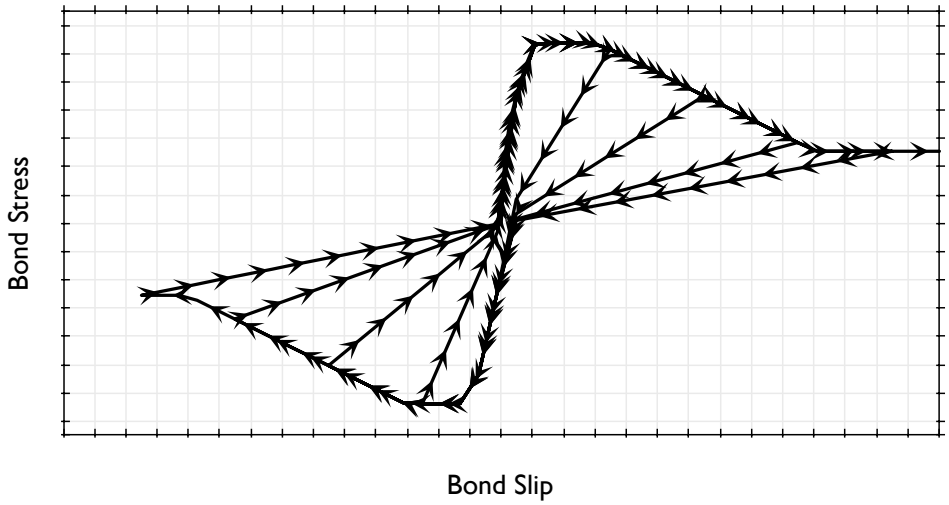

Figure 4.8: Hysteresis Rules for Bond Stress-Slip Response in DIANA

- Unloading follows the secant modulus back to the origin.
- When reversal of slip direction occurs, reloading always follows the full backbone curve in the opposite direction regardless of cycle number.
- Transverse effects—such as the influence of lateral confining pressure—cannot be considered.

These rules are qualitatively illustrated in Figure 4.8. There are several differences between these hysteretic rules and the experimental response from Eligehausen et al. [54]. Most importantly, whereas the experimentally-observed peak bond stress reduces during each cycle, the analytical response has no memory and will reach the full bond strength exhibited by the backbone curve in each subsequent cycle, even when very large values of slip have previously occurred. Also, although the experimental unloading stiffness is very high, the analytical model unloads according to the secant stiffness.

One potential solution to this problem was to use a so-called "phased" analysis and update the bond-slip law between load cycles. While this may have been viable for a single bond-slip interface spring, it cannot account for the non-simultaneous progression of bond failure not only throughout the entire specimen, but even along a single

bar with multiple steel-to-concrete connections.

Since use of a more sophisticated bond model capable of representing cyclic degradation of bond strength and stiffness (such as the Morita-Kaku or Eligehausen models) was not possible, a simpler alternative was necessary.

4.3.3 CEB-FIP Model Code 1990 Bond-Slip Models

The bond-slip model chosen for this study was based on that presented in the CEB-FIP Model Code 1990 [30] (MC90). The general case of the shear stress-slip relation is expressed as

$$\tau(s) = \begin{cases} \tau_{max}\left(\frac{s}{s_1}\right)^{\alpha} & 0 \leq s \leq s_1 \\ \tau_{max} & s_1 < s \leq s_2 \\ \tau_{max} - (\tau_{max} - \tau_f)\left(\frac{s-s_2}{s_3-s_2}\right) & s_2 < s \leq s_3 \\ \tau_f & s_3 < s \end{cases} \tag{4.14}$$

The various parameters in Equation 4.14 depend on the quality of the bond condition as well as the level of confinement present at the location of the bond interface. The values for each case are cataloged in Table 4.1.

The designation "unconfined" refers to cases where failure occurs by splitting of concrete, while the designation "confined" refers to cases where failure occurs by shearing of the concrete between the ribs (pull-out). Based on the quantity of transverse reinforcement and level of confining pressure, the parameter values may be linearly interpolated between the confined and unconfined cases. The MC90 acknowledges the wide scatter in experimental data for bond-slip and recommends this scatter be "taken into account." Note also that each curve represents the monotonic response; a reduction of bond strength at increasing cycles and slip values is needed in order to match the cyclic envelope of experimental bond results.

The general characteristics of the CEB-FIP Model Code 1990 [30] bond-slip laws are illustrated in Figure 4.9. Verification that DIANA output was accurately representing the multilinear analytical functions expressed in Equation 4.14 is demonstrated in

Table 4.1: Bond Parameters from CEB-FIP Model Code 1990

Confinement	Unconfined	Unconfined	Confined	Confined
Condition	Good	Other	Good	Other
s_1	0.6 mm	0.6 mm	1.0 mm	1.0 mm
s_2	0.6 mm	0.6 mm	3.0 mm	3.0 mm
s_3	1.0 mm	2.5 mm	Clear rib spacing	Clear rib spacing
α	0.4	0.4	0.4	0.4
τ_{max}	$2.0\sqrt{f_{ck}}$	$1.0\sqrt{f_{ck}}$	$2.5\sqrt{f_{ck}}$	$1.25\sqrt{f_{ck}}$
τ_f	$0.15\tau_{max}$	$0.15\tau_{max}$	$0.40\tau_{max}$	$0.40\tau_{max}$

Source: CEB-FIP Model Code 1990 [30]

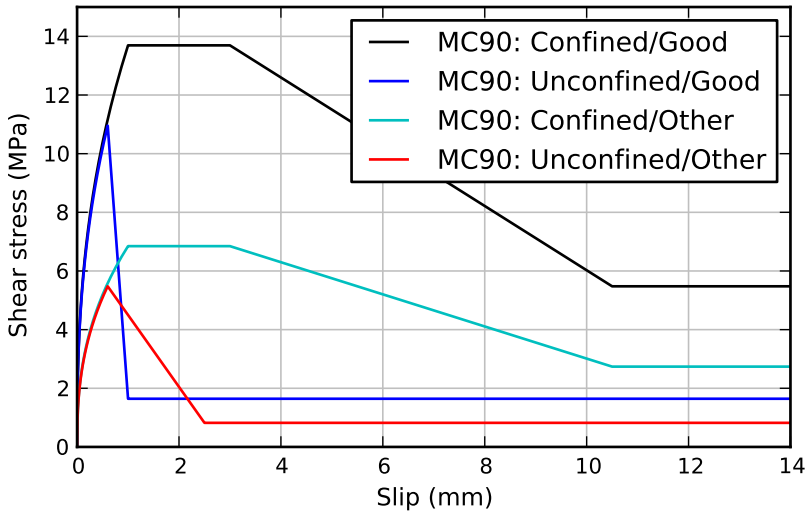

Figure 4.9: Bond-slip Laws from CEB-FIP Model Code 1990 ($f'_c = 30$ MPa)

Figure 4.10. This result was generated by simulating pull-out of a bar with very high stiffness connected to an equally stiff host element by interface elements with bond-slip following the MC90 relation for good bond condition and confined concrete.

4.3.4 Verification with Viwathanatepa et al. [228]

In order to better understand the implications of the previously described bond-slip simulation capabilities in DIANA, a finite element model was developed to simulate the response of cyclic pull-out experiments conducted by Viwathanatepa, Popov, and Bertero [228].

Viwathanatepa et al. [228] tested seventeen specimens where reinforcing bars embedded in column stubs were subjected to either cyclic push-pull or monotonic pull

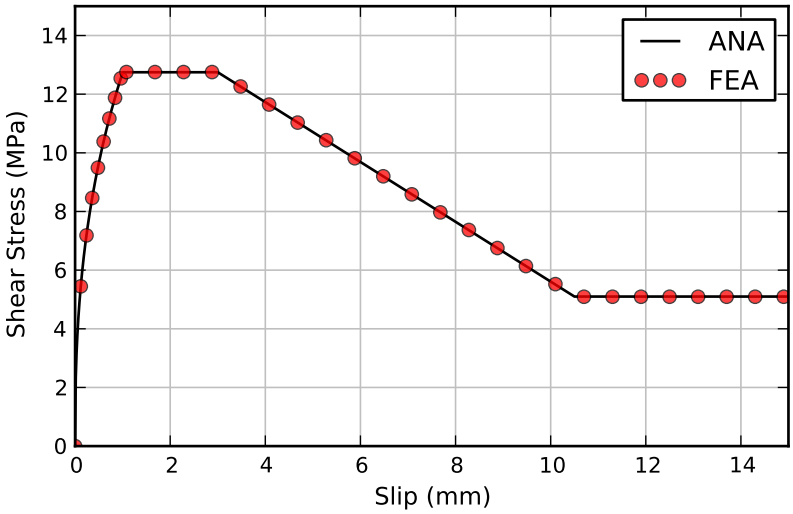

Figure 4.10: CEB-FIP Bond-Slip Analytical Curve and DIANA Verification (for confined concrete, good bond condition

loading, designed to simulate the conditions present for a longitudinal beam bar within an interior beam-column joint of a moment resisting frame. The specimens were well-confined by adequate transverse reinforcement and a constant axial load. A diagram of the experimental setup is shown in Figure 4.11.

Specimen No. 14 was chosen for numerical verification in this study; full specimen dimensions and detailing are shown in Figure 4.12. The primary longitudinal bar in this specimen was an M25 (#8) embedded in a $1168 \times 635 \times 254$ mm ($46 \times 25 \times 10$ in) concrete block. Vertical reinforcements were M22 (#7) bars while transverse reinforcements were M13 (#4) bars. The concrete had a measured compressive strength of 32.7 MPa (4740 psi) and tensile strength of 3.52 MPa (510 psi). M13 and M22 bars had a yield strength of 496 MPa (72 ksi) while the primary M25 bar had a yield strength of 468 MPa (68 ksi).

A finite element model of the specimen was constructed based on the components of the prototype model described thus far, shown in Figure 4.13. The concrete column stub was modeled using 880 solid elements. The primary longitudinal bar subjected to cyclic load (displayed in red in Figure 4.13) was modeled as a bond-slip reinforcement,

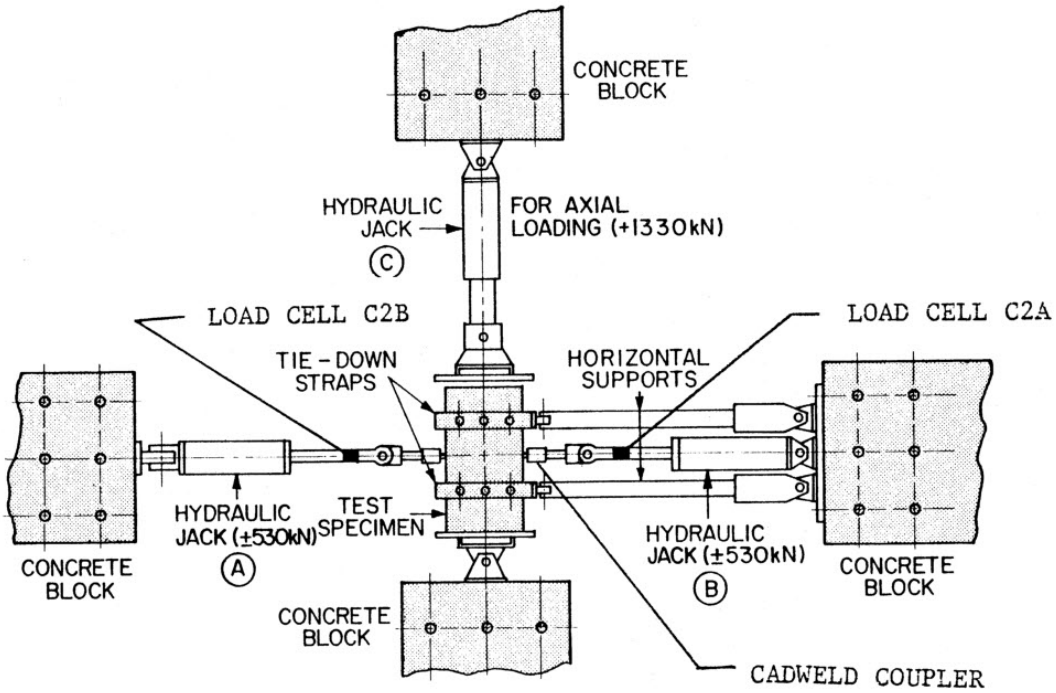

Source: Viwathanatepa et al. [228]

Figure 4.11: Experimental Setup for Viwathanatepa Specimen

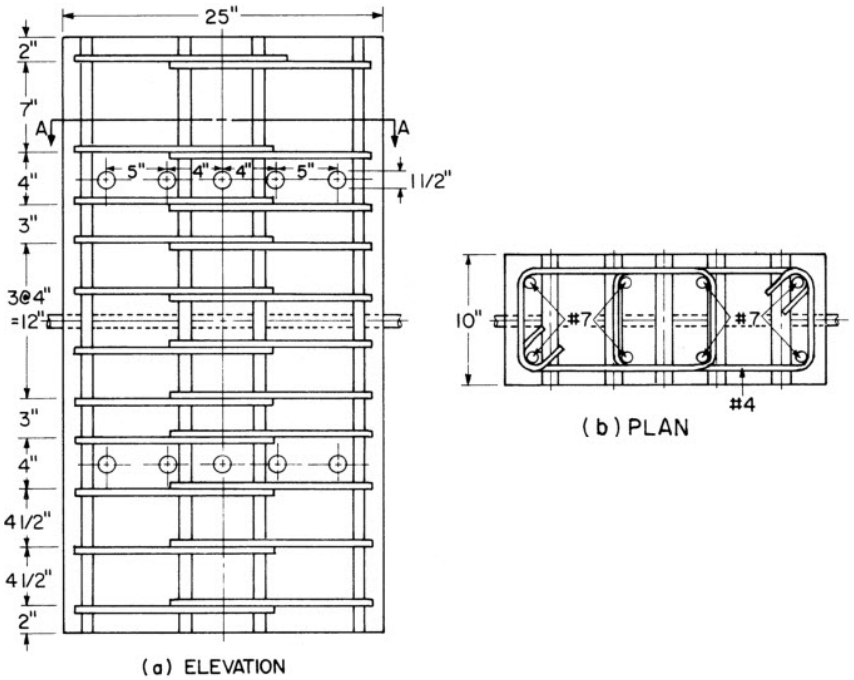

Source: Viwathanatepa et al. [228] (1.0 in = 25.4 mm)

Figure 4.12: Dimensions and Detailing for Viwathanatepa Specimen

internally discretized using beam elements and connected to the host concrete elements using line-to-solid interface elements. All other reinforcements (vertical reinforcing bars and ties) were modeled under the assumption of truss behavior and perfect bond.

The experimental boundary conditions were simulated as follows. All nodal degrees of freedom at the base of the column stub were restrained. Additionally, all x-direction translations at nodes located along the perimeter of the mesh at the location of the centroid of the lateral tie-down straps were restrained. A constant axial pressure equal to 25% of the column axial capacity was applied and held constant throughout the analysis. The finite element mesh, reinforcement elements, boundary conditions, and applied loads are shown in Figure 4.13.

Cyclic loads were applied simultaneously to each end of the embedded bar in displacement control. The precise displacement history from the experiments was not applied numerically; instead, the displacement amplitude was increased by ± 1.0 mm during each cycle until the maximum value reached experimentally was simulated.

The bond-slip relationship was simulated using all four cases from the CEB-FIP Model Code 1990 [30] (MC90) provisions considering confined/unconfined condition and good/other bond condition. The purpose of evaluating all four cases was simply to better understand the implications of the chosen bond stress-slip model parameter values for slip and bond strength. Initially, the response was modeled under monotonic load for comparison with the envelope of the cyclic response, the results of which are shown in Figure 4.14. The envelope of the experimental response was bounded by the confined/good and unconfined/good designations.

For the MC90 designation confined/good, the cycled reinforcing bar yielded prior to bond failure, which occurred near the peak bond stress in the experiment. The extension of this case to cyclic loading is shown in Figure 4.15a. The cyclic response was effectively elastic perfectly plastic. The inability of the bond stress-slip hysteresis to degrade with increased cycles was apparent in this (and all subsequent) cases. Since bond

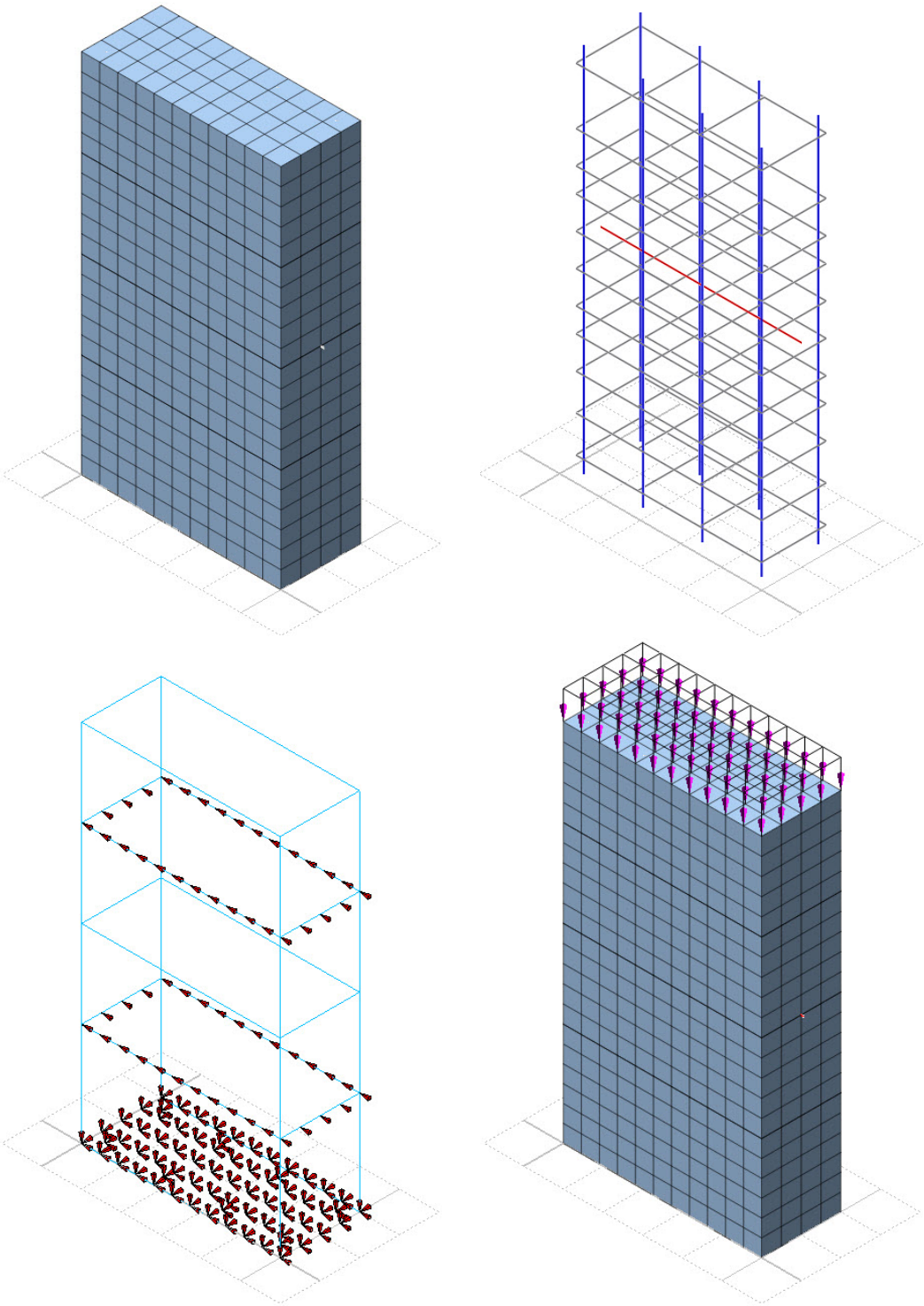

Figure 4.13: Finite element mesh, reinforcements, boundary conditions, and load for Viwathanatepa Specimen

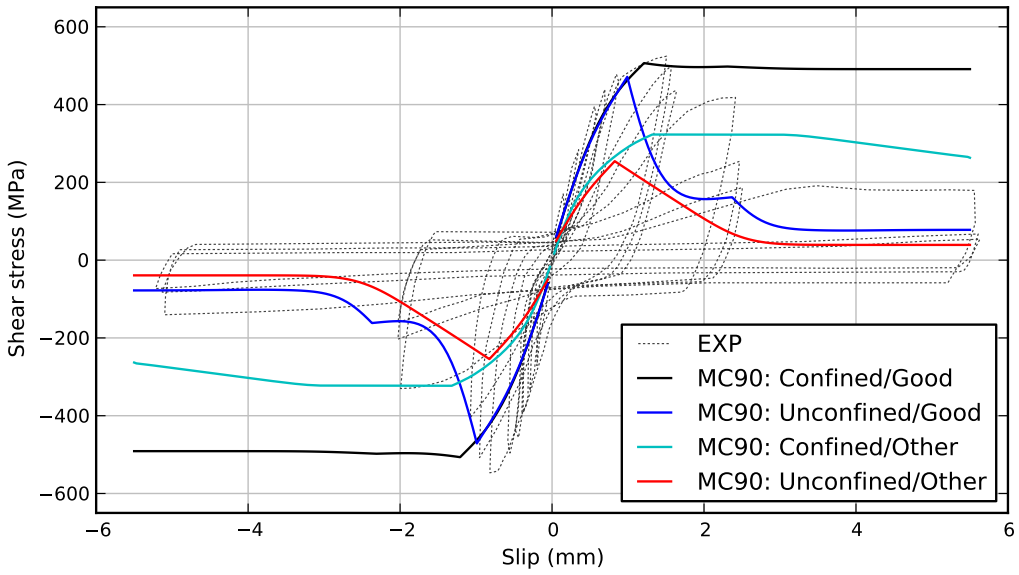

Figure 4.14: Monotonic Numerical Response for Viwathanatepa Specimen

failure was not achieved, the envelope of the cyclic experimental pull-out response is overestimated at all values greater than 1.0 mm.

The best overall agreement with the backbone of the experimental curves was achieved with the designation unconfined/good, shown in Figure 4.15b. The response was reasonable in the initial cycles up to a slip value of 1.0 mm, but in subsequent cycles the bond strength was significantly overestimated at low slip values and underestimated at large slips ($>$ 2.0 mm in this case). Figures 4.15c and 4.15d illustrate the response for the designated "other" bond condition; the confined case underestimated the bond strength initially but failed to degrade as slips occurred, while the unconfined case significantly underestimated the initial stiffness of the bond interface in early cycles but provided a reasonable estimate during more advanced cycles at large slip values.

A failure process commonly observed in pull-out tests such as this one is that of a cone formation at the face of the specimen where pull-out occurs. This effect is illustrated by photographs in Figure 4.16. The finite element model captured this response, also shown in the same figure.

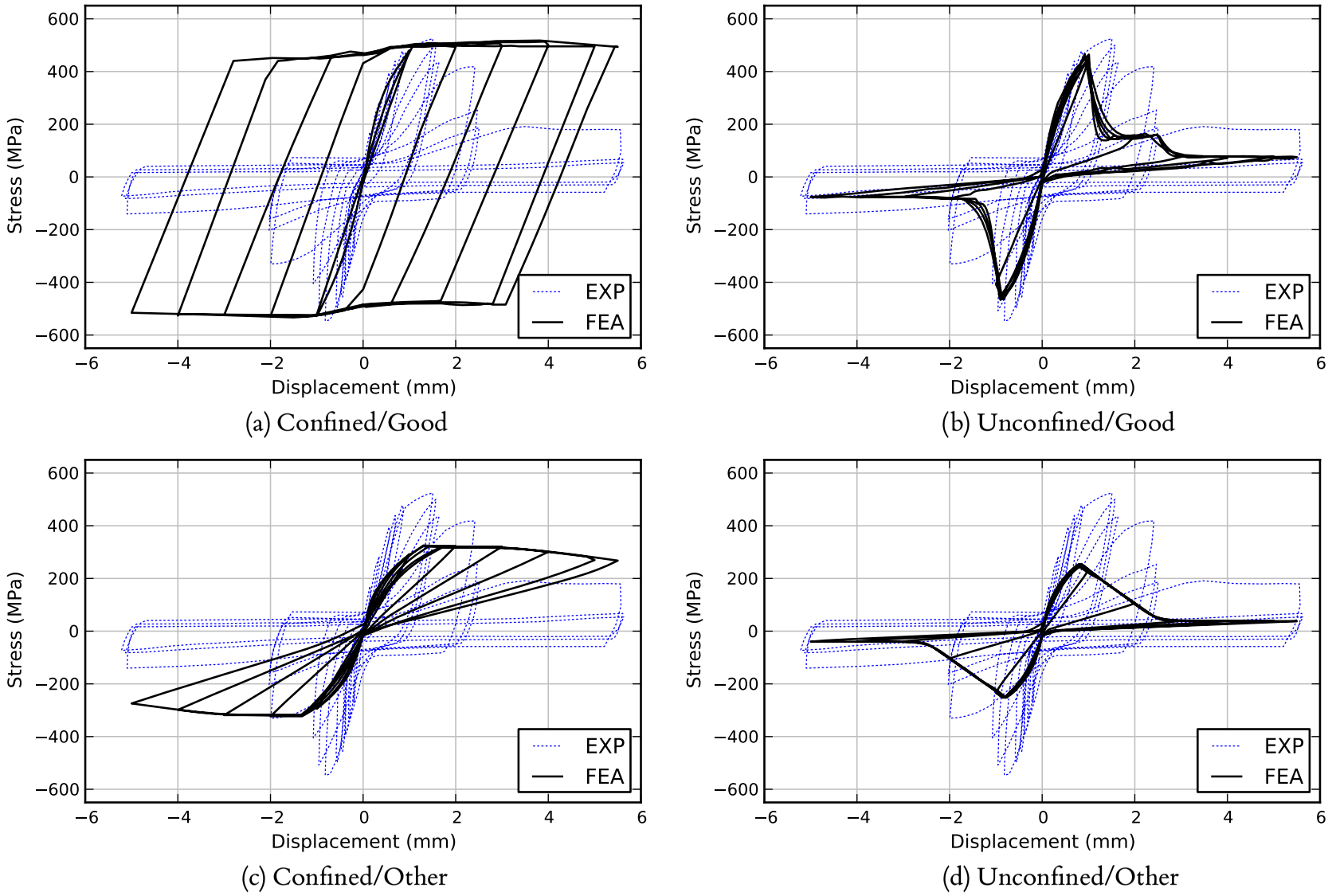

Figure 4.15: Viwathanatepa [228] vs. CEB-FIP MC90 [30] Bond Models

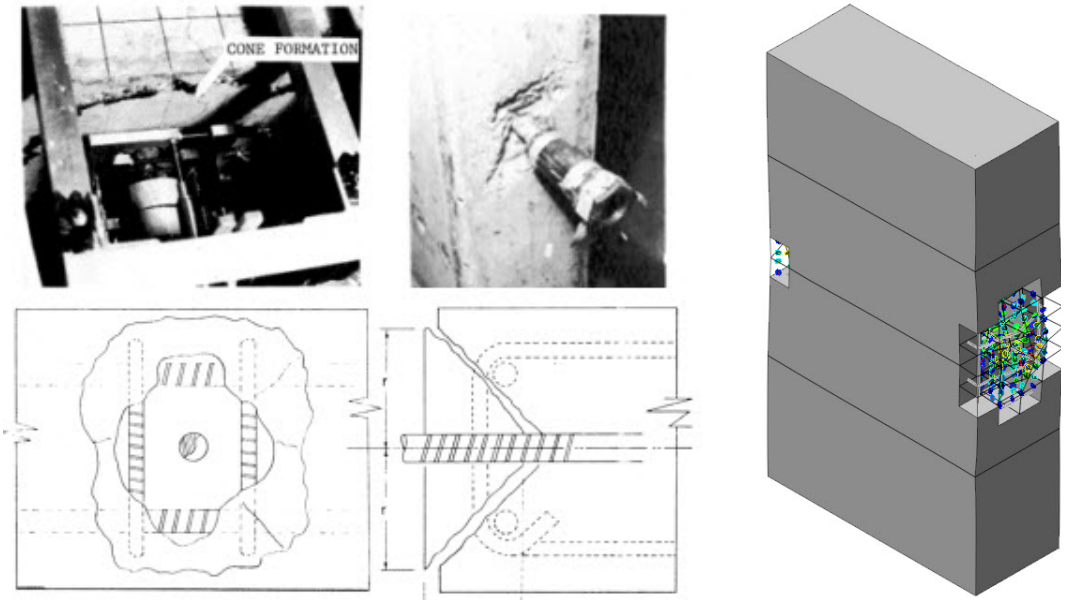

Source: Viwathanatepa et al. [228]

Figure 4.16: Simulation of Cone Formation Mechanism During Pull-Out Failure

The conclusions from the numerical verification of the bond response with experimental data from Viwathanatepa et al. [228] are as follows. The slip parameters corresponding to the designation "unconfined/good" yielded the best overall agreement with the experimental envelope, although matching the envelope was not a sufficient criterion considering the model's over-prediction of the bond strength in later cycles. Furthermore, a reduction of bond strength at increasing cycles and slip values is needed in order to match the cyclic envelope of experimental bond results—the MC90 parameters associated with the designation "unconfined" most closely produced this response.

No attempt was made to develop general recommendations for bond-slip law parameter selection beyond the guidelines of the CEB-FIP Model Code 1990 [30] because of the limitations of the bond-slip hysteresis rules in DIANA. Appropriate bond parameters for beam-column joint simulation must be independently evaluated for each subsequent study depending on the level of confinement, bond condition, and loading characteristics.

Also, the significance of the various factors affecting bond-slip response for analysis

of beam-column joints will depend on the magnitude of slips which occur during reversed cyclic loading. If anchorage of bars is sufficient to prevent large relative slips, the influence of the cyclic bond-slip response may not prove significant. An example of this is provided in the following section, where the limitations of the cyclic bond model do not adversely affect the numerical response of a well-anchored, hooked bar subjected to cyclic loading.

Finally, a critical reassessment of the bond performance following successful cyclic analysis of seismically deficient beam-column joints is later presented in Section 5.6.

4.4 Anchorage Response

Beyond the case of bond-slip for straight bars, an important aspect in the behavior of reinforced concrete beam-column joints is the anchorage of beam longitudinal bars which are terminated in the joint core with 90° or 180° hooks.

4.4.1 Background on Anchorage Simulation

The anchorage response of hooked bars has been studied experimentally by numerous researchers, including Jirsa et al. [93, 144, 90], Eligehausen, Bertero and Popov [51], and Hawkins, Lin, and Ueda [220, 77, 122]. Detailed descriptions of the key characteristics of low cycle anchorage failure have been recently summarized by ACI Committee 408 [8].

Previously, numerical analysts have used various techniques to simulate the response of the end-condition of anchored bars. For each case, it is assumed that bond-link elements connect the reinforcing bars to the concrete host elements along the length of the reinforcements. The following approaches address how best to capture the contribution of the hook at the end of beam longitudinal reinforcements.

Sagbas and Vecchio [192] showed that if a hook is sufficiently confined in the joint core, the reinforcing bar may be modeled using a straight element with the restraint

of the hook simulated by connecting the end of the bar to the concrete elements with perfect bond. In the case of a nonseismically detailed joint, they recommended placing bond elements at the end of the bar instead. Eligehausen et al. [53] simulated the hook response using an additional elastic spring which connected the end of the bar to the host concrete element. The spring stiffness was numerically determined by comparison with the results of experimental pull-out data.

In each of these approaches, additional contributions from the hooked bar to the joint response beyond the longitudinal restraint of the beam bar cannot be considered. More specifically, such approaches may (a) underestimate additional confinement provided to the joint core by the hooks, (b) alter the bearing action and resulting force-transfer mechanism developed between the curved hook and the joint core, and (c) fail to capture prying action from bars with non-negligible bending stiffness when beam moments are transferred to the joint, which may accelerate spalling of the concrete cover.

Based on these factors, a methodology was sought which would better represent the physical geometry of hooked bars. The prototype response chosen used an additional vertical bar at the end of a beam longitudinal bar to represent a 90° hook. Both bar segments were connected to each other as well as to the concrete via line-to-solid interface elements. While this approach does not capture the radius of curvature of the hook, it addresses the issues of confinement of the joint and prying action of the beam longitudinal bars, provided the reinforcing bars are simulated using beam elements and thereby embodying flexural stiffness.

In DIANA, bond-slip interface elements are composed of orthogonal springs with stiffnesses D11 and D22, specified with keyword `DSTIF`. The linear stiffness D11 controls the relationship between the normal traction and normal relative displacement between concrete and steel. The linear stiffness D22 controls the relationship between shear traction and shear relative displacement in the direction of bond-slip. If a nonlinear bond-slip curve is specified via keyword `BONDSL`, D22 is replaced by the initial stiffness of the

shear stress-slip curve. An initial value of D11 $= 10 \cdot$ D22 was assumed.

Based on this, the net stiffness provided at the end of the longitudinal beam reinforcement is governed by the bending stiffness of the element representing the hook, together with the normal traction-displacement interface provided along the hook element, governed by the linear stiffness D11. If reinforcements are modeled with truss elements, only the interface stiffness D11 contributes to the end stiffness.

4.4.2 Verification with Hawkins et al. [77]

Experimental data from Hawkins, Lin, and Ueda [220, 77, 122] was used to investigate the ability of the proposed bond-slip model to capture the response of anchored bars.

Hawkins et al. tested a series of idealized specimens designed to mimic the conditions in an exterior beam-column joint connection. Specimen B85 was chosen for numerical verification in this study. In this test, an M25 (#8) bar with 90° hook was embedded in a 1676 $\times$ 610 $\times$ 200 mm (66 $\times$ 24 $\times$ 8 in) concrete block. A coupler attached to the end of the anchored bar allowed for application of both tensile and compressive forces. The specimen was supported by six steel plates. Full specimen dimensions and detailing are shown in Figure 4.17. The concrete had a compressive strength of 22.8 MPa (3300 psi) and reinforcements had a yield strength of 468.9 MPa (68 ksi). The end of the anchored bar was subjected to multiple cycles of displacement-controlled loading. An inelastic response exhibiting strain hardening and the Bauschinger effect resulted.

A finite element model of the Hawkins et al. specimen was developed in DIANA. The mesh, reinforcements, and boundary conditions are shown in Figure 4.18. The prototype anchorage model consisting of two perpendicular, connected bar segments is illustrated in this figure. The model contained 564 solid elements.

The anchored bar was simulated using both truss and beam elements along with different levels of normal interface stiffness D11. The initial interface transverse stiffness D22 was taken as the initial stiffness of the bond-slip law, while D11 was evaluated for

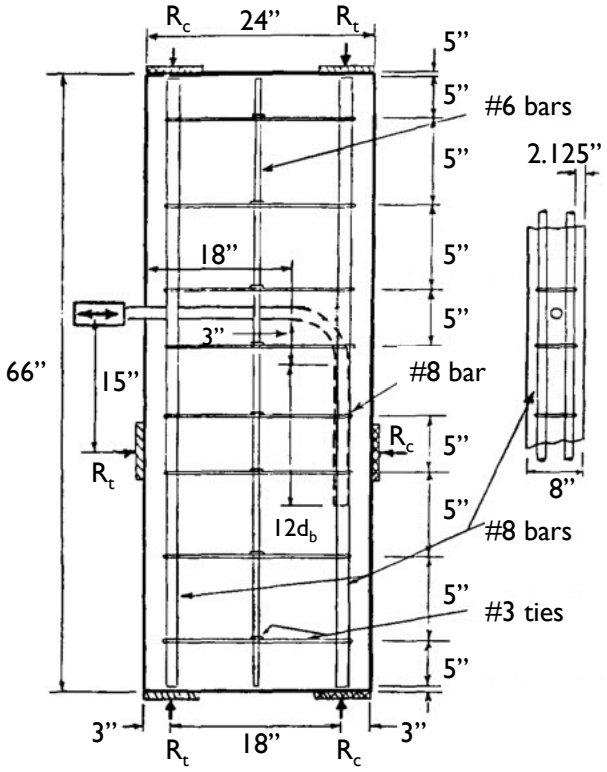

Source: Hawkins et al. [77] (1.0 in = 25.4 mm)

Figure 4.17: Anchorage Test Specimen Dimensions for Hawkins Specimen

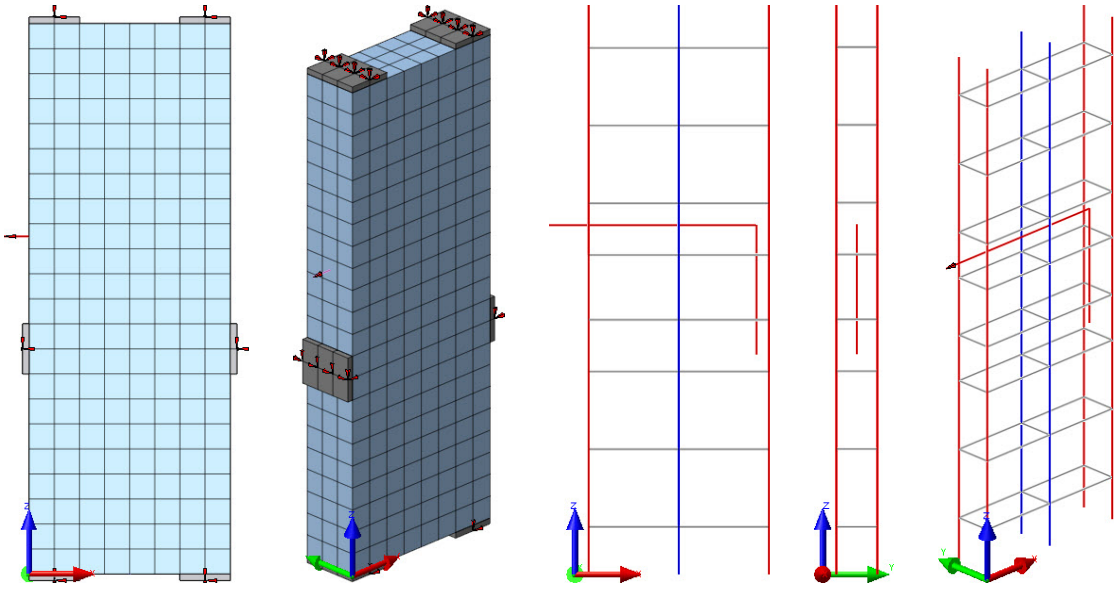

Figure 4.18: Finite Element Mesh, Boundary Conditions, and Reinforcing Bar for Hawkins Specimen

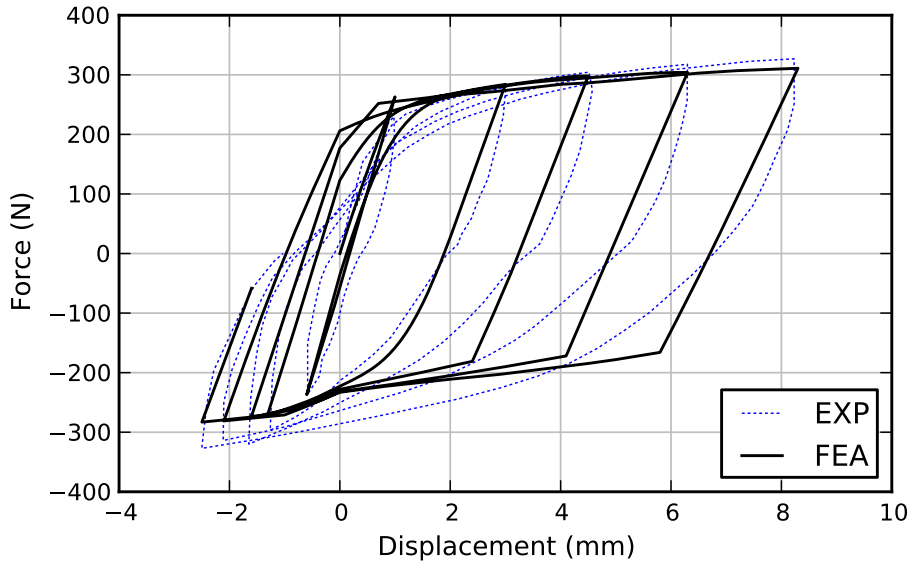

Figure 4.19: Prototype Anchored Bar Response for Hawkins Specimen (beam element / D11 = 10 · D22)

values of 1.0 · D22 and 10.0 · D22. The prototype steel reinforcement model (Von Mises plasticity with kinematic hardening) was used.

Good agreement was observed between computed and observed response. The response of the prototype model (reinforcements modeled using beam elements with D11 = 10 · D22) is shown in Figure 4.19. For loading in tension, the hardening response was closely followed, while the strength in compression was underestimated by approximately 13%. Similar to the comparison of the reinforcing bar response simulated by Von Mises plasticity with experimental data from Ma, Bertero, and Popov [131] (shown in Figure 4.5), the Bauschinger effect was not captured in the finite element model.

For the prototype model, the influence of the D11 parameter was evaluated by also simulating the response with D11 = D22, shown in Figure 4.20. Reducing the normal interface stiffness from 10.0 · D22 to 1.0 · D22 did not affect the capacity of the simulated anchorage response, but reduced the stiffness during unloading from tension to compression, a feature which became more pronounced as the system response became more inelastic.

The influence of simulating the anchored bar with beam vs. truss elements was also

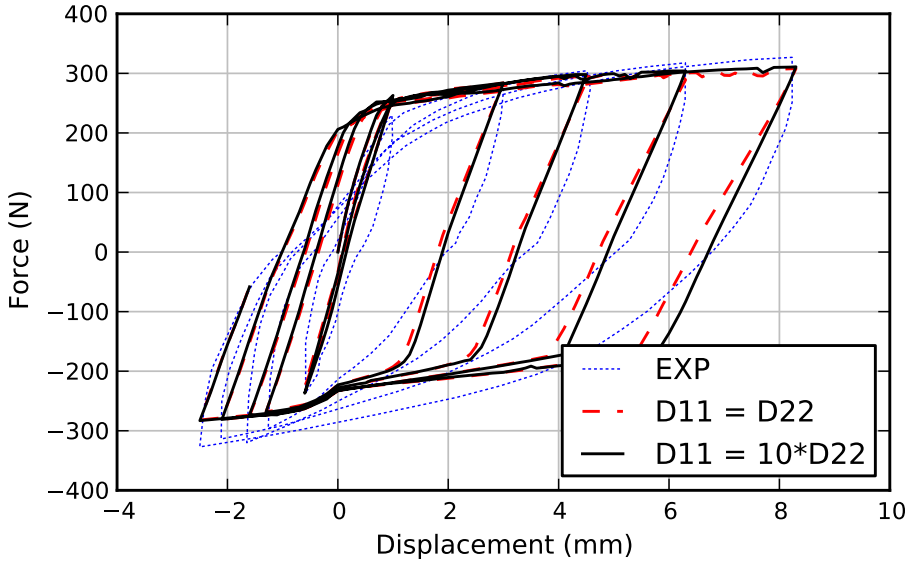

Figure 4.20: D11 Sensitivity for Anchored Bar Response for Hawkins Specimen (beam element)

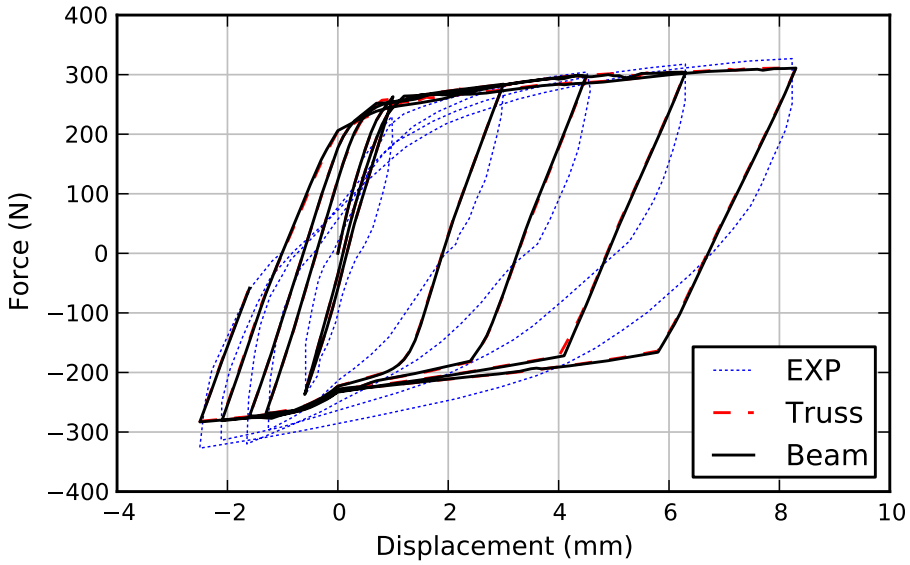

Figure 4.21: Truss vs. Beam Element Anchored Bar Response for Hawkins Specimen (D11 = 10 · D22)

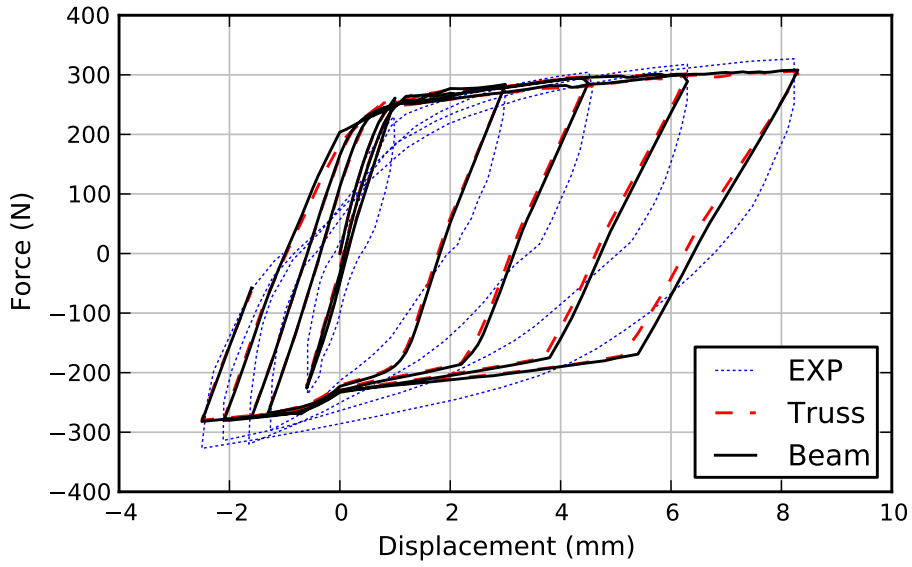

Figure 4.22: Truss vs. Beam Element Anchored Bar Response for Hawkins Specimen (D11 = D22)

evaluated for the case with D11 = 10 · D22, shown in Figure 4.21. For this value of normal interface stiffness, the response of an anchored truss bar was effectively identical to that of the beam bar. However, if D11 was reduced to 1.0 · D22, as shown in Figure 4.22, the truss bar showed a less stiff response during unloading from tension to compression than the beam bar exhibited. This indicates that for the case with D11 = 10 · D22, the normal interface stiffness dominates the influence from the flexural stiffness of the hook with the beam bar (a contribution clearly neglected with the truss bar).

Even though the difference in response was marginal for the cases evaluated, the use of beam elements is recommended over truss elements due to a more conceptually accurate representation of larger reinforcing bars, which possess non-negligible flexural stiffness. Furthermore, the effect of prying action at the exterior face of a beam-column joint may become more pronounced in a realistic configuration where the forces in the anchored bar are developed from a downward-displacing beam, instead of the simplified configuration of the experimental setup by Hawkins et al. [77].

Based on this study, the prototype constitutive model for bent-bar anchorage simulation consists of perpendicular beam elements connected to concrete elements with

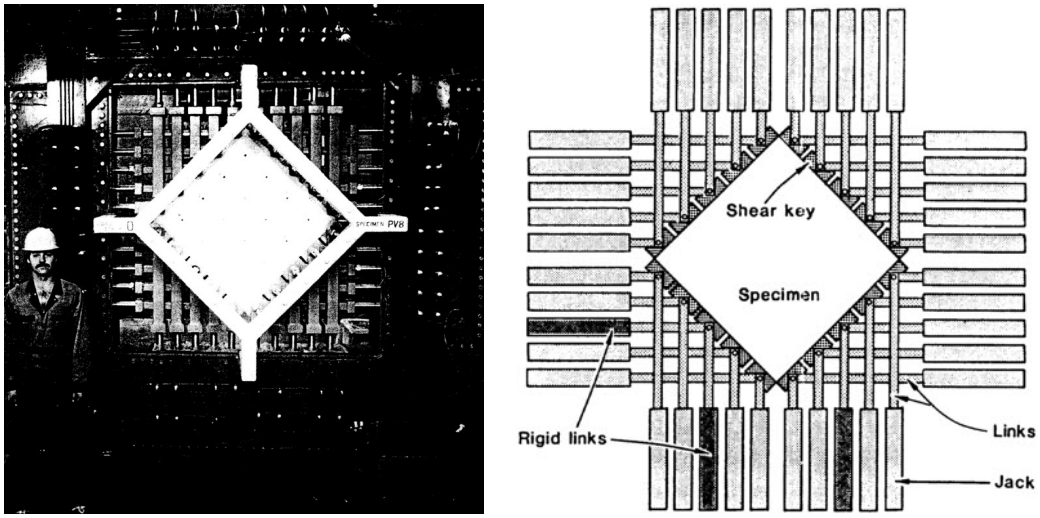

Source: Vecchio and Collins [226]

Figure 4.23: Toronto Panel Tester

interface stiffness D11 = 10 · D22 and D22 set to the initial stiffness of the bond-slip law.

4.5 Cyclic Shear Response

Diagonal joint shear cracking is one of the predominant failure mechanisms exhibited by nonseismically detailed beam-column joints subjected to reversed cyclic loads.

To evaluate the ability of the proposed model to capture shear-dominated failure processes in a three-dimensional model, simulations were conducted of cyclic shear panel tests reported by Vecchio [223]. Experiments such as these are valuable for model validation due to the simplicity of specimen geometry, applied loads, and boundary conditions.

A number of research campaigns involving shear panels have been conducted at the University of Toronto (and elsewhere), the most notable case being the original monotonic experiments by Vecchio and Collins [226] that led to the development of the Modified Compression Field Theory, a constitutive theory which has consistently proven capable of representing shear-critical response. A photograph and schematic of the Toronto panel tester is shown in Figure 4.23.

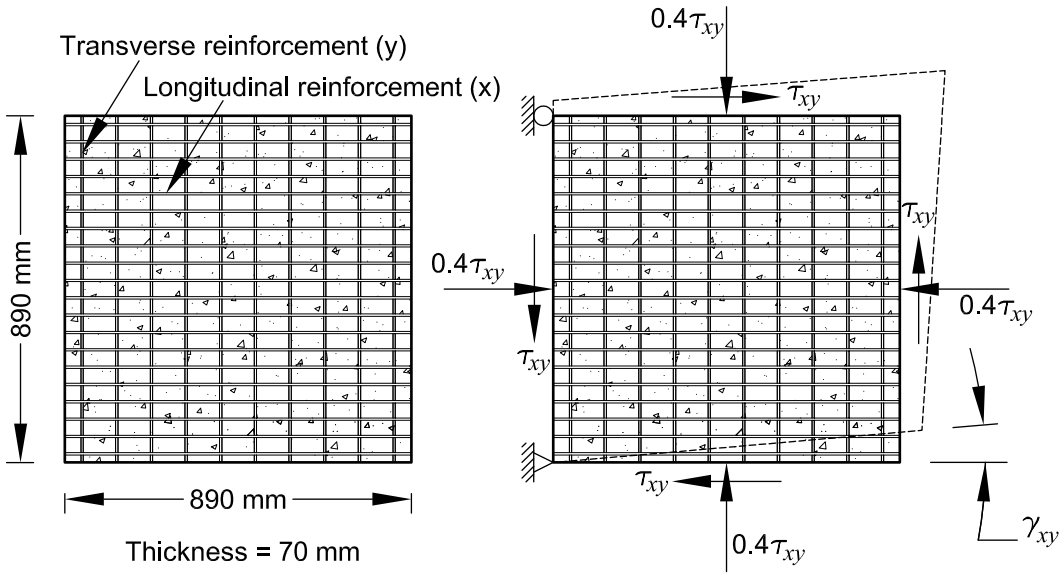

Figure 4.24: Geometry and Idealized Loading/Support Conditions for Vecchio Specimens

4.5.1 Description of Shear Panel Specimens

A series of panels reported by Vecchio et al. [223] was chosen for this study. All panels had dimensions 890×890×70 mm (35×35×2.75 in) and contained a longitudinal reinforcement ratio ρ_x of 1.82% and a transverse reinforcement ratio ρ_y of 0.91%. All reinforcing steel consisted of deformed D5 rebar, with a nominal diameter of 6.0 mm (0.24 in) and a yield stress of 282 MPa (41 ksi). Panel PDV1 had a compressive strength of 26.8 MPa (3890 psi) which corresponded to a strain value ϵ_0 of 1.62×10^{-3} mm/mm. Panel PDV2 had a compressive strength of 23.7 MPa (3440 psi) which corresponded to a strain value ϵ_0 of 1.63×10^{-3} mm/mm. Panel PDV3 had a higher compressive strength of 34.1 MPa (4950 psi) which corresponded to a strain value ϵ_0 of 1.69×10^{-3} mm/mm. The geometry of the panels is shown in Figure 4.24.

Panel PDV1 was subjected to monotonic load. Panel PDV3 was subjected to a cyclic load history (with unloading to zero between cycles), while Panel PDV2 was subjected to a reversed cyclic load history. In each case, the panels were loaded under a uniform, biaxial shear and compression condition with a fixed ratio of compression-to-shear of

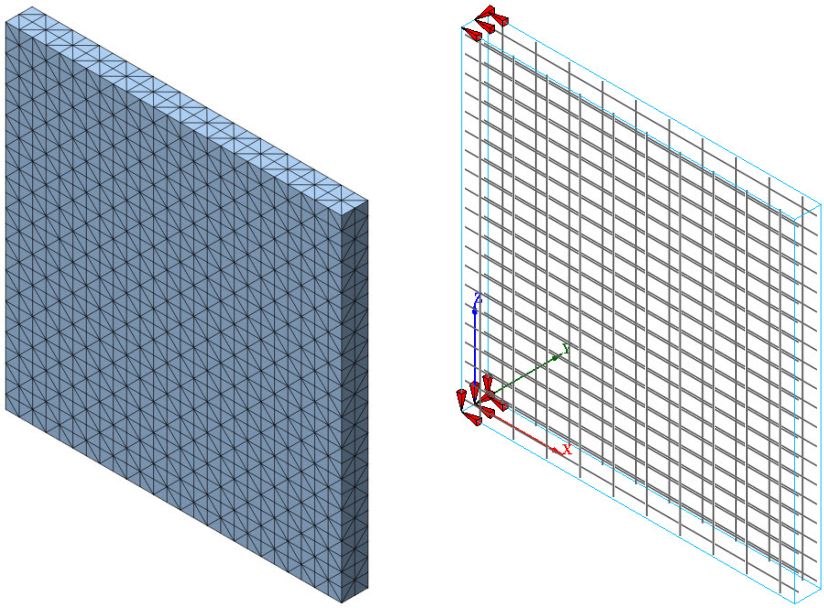

Figure 4.25: Finite element mesh for Vecchio Specimens

0.4, as shown in Figure 4.24. All panels failed in shear almost coincidently with yielding of longitudinal reinforcement; the transverse reinforcement had yielded prior to failure.

4.5.2 Description of Shear Panel Models

The shear panels were simulated using the constitutive approach described in Section 4.6 with minor modifications. The concrete mesh consisted of tetrahedral elements, as shown in Figure 4.25. Lower power elements such as these were reasonable since the shear panels were subjected to a near-uniform state of stress. Reinforcing bars were modeled using two layers of orthogonal truss elements. Since the specimens were uniformly reinforced, the model was simplified by specifying perfect bond in conjunction with the tension stiffening relationship from Equation 3.10.

The panel was supported along two corner edges as shown in Figure 4.25. Uniform shear and compression tractions were applied in fixed proportion (τ_{xy} and $0.4\tau_{xy}$) to the panel faces, following a force-control procedure. The shear strain γ_{xy} was computed from the displacement of the lower right corner of the panel, as indicated in Figure 4.24.

4.5.3 Prediction of Shear Panel Response

The shear stress-strain response of each panel is shown in Figure 4.26.

Excellent agreement was observed for specimen PDV1. The ratio of simulated to observed maximum shear stress was 0.998, and good overall agreement was observed with both the initial stiffness as well as the stiffness after the onset of cracking.

For the cyclic cases, the model followed the backbone curve from specimen PDV2 more closely than specimen PDV3, although the shear capacity for each specimen again showed excellent agreement. For specimen PDV2, the ratio of simulated to observed maximum shear stress was 0.987 for positive loading and 0.994 for negative loading. For specimen PDV3, the ratio of simulated to observed maximum shear stress was 0.994. Considering all panels, the mean ratio of predicted-to-observed shear capacity was 0.993 (CV 2.1×10^{-5}).

While the models showed excellent agreement with the maximum shear stress for each panel, an obvious limitation was the underestimation of permanent inelastic strains and energy dissipation. Since the concrete model assumes secant unloading in tension and compression, the only nonlinear component during unloading and reloading was characterized by the steel model, an effect with little influence in this example since longitudinal reinforcement did not yield until immediately prior to shear failure. More inelastic deformation was captured in panel PDV3 due to its higher compressive strength which allowed greater strains to develop in the reinforcement prior to failure.

A comparison of predicted and observed final crack patterns is shown for panel PDV1 in Figure 4.27. In the finite element model, the distribution of cracks was uniform due to the near-uniform application of load and distribution of reinforcement, together with the assumption of smeared cracking. The orientation of the predicted cracks showed good agreement with the experimental response.

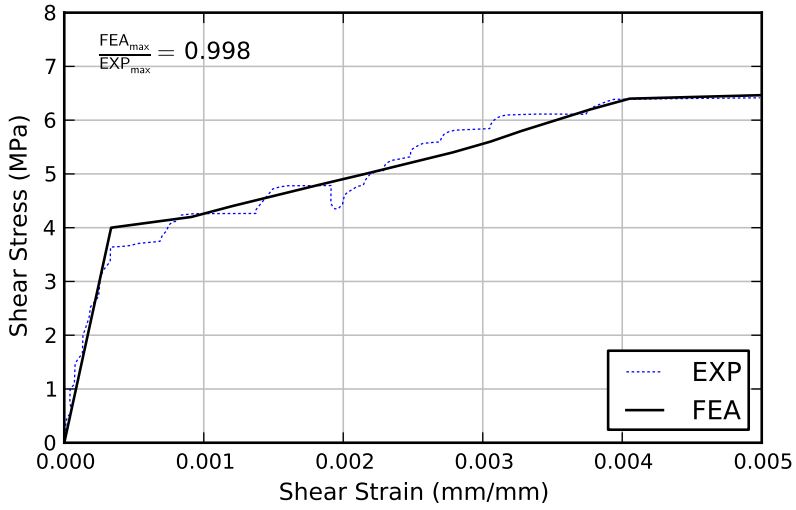

(a) Panel PDV1

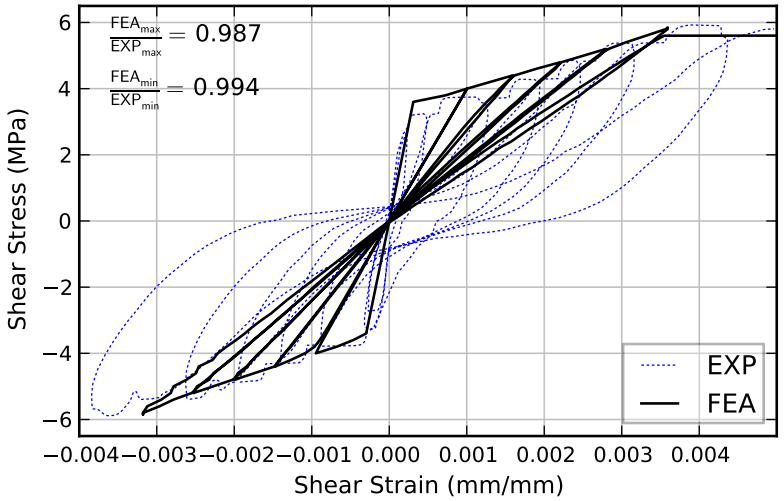

(b) Panel PDV2

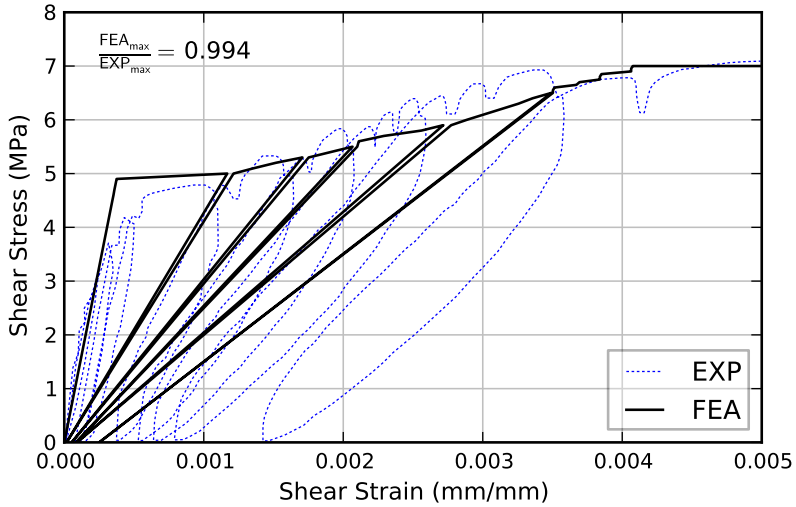

(c) Panel PDV3

Figure 4.26: Shear Stress-Strain Response for Vecchio Specimens

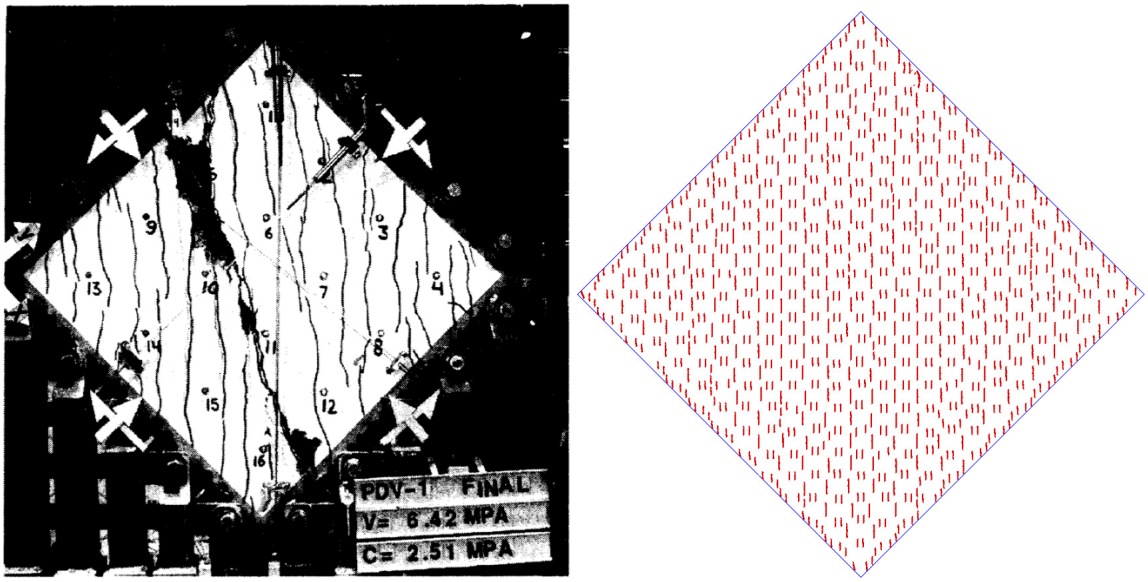

Source: Vecchio [223]

Figure 4.27: Observed vs. Predicted Crack Patterns for Shear Panel PDV1

Table 4.2: Prototype Constitutive Model

Type	Model Characteristic
Software	DIANA 9.4.4 [4]
Concrete framework	Total strain rotating crack model
Concrete constitutive theory	Selby and Vecchio [201, 200]
Tension softening	Hordijk et al. [84]
Tension stiffening	Vecchio [227]
Compression softening	Thorenfeldt [217]
Concrete Elastic Modulus	ACI Equation [7]
Concrete Tensile Strength	CEB-FIP Model Code 1990 [30]
Concrete Fracture Energy	Remmel [189]
Concrete element	HX24L
Steel framework	Von Mises plasticity
Hardening type	Kinematic
Hardening ratio	0.02
Steel element	L6TRU/L13BE
Bond Response	CEB-FIP Model Code 1990 [30]
Bond interface element	HX30IF
Bond normal stiffness	$D11 = 10 \cdot D22$
Nonlinear solution type	Quasi-newton, Broyden formulation
Force convergence criterion	0.01
Energy convergence criterion	0.0025
Max # iterations	1000 (20-30 iterations typical)

4.6 Summary of Prototype Model and Sample Material Input

Chapters 3 and 4 documented the systematic identification and experimental validation of a prototype constitutive framework for the simulation of reinforced concrete exterior beam-column joints with inadequate seismic detailing. This prototype model was developed by combining existing material models in a unique and novel way. The material models, parameter values, and elements chosen for the prototype model are summarized in Table 4.2. Unless otherwise noted, these properties were applied in all subsequent simulations reported in this thesis.

To illustrate specification of the prototype model for others who will use DIANA, a sample material definition using the prototype model is shown below for concrete with a compressive strength of 30 MPa (4350 psi) and reinforcing steel with a yield stress of 500.0 MPa (72 ksi). Material input definitions such as this one were generated using a Python script which has been provided in Appendix B.4.

inputs/prototype–material–input.dat

```
'MATERIALS'
:
: UNITS: Newton, mm, MPa
:
: PROPERTIES:
:    Compressive strength      Fcp = 30.0
:    Elastic modulus           Ec  = 25742.9602027
:    Poisson ratio             pr  = 0.2
:    Tensile strength          ft  = 2.89647143764
:    Fracture energy           Gf  = 0.0901091334728
:    Steel elastic modulus     Es  = 200000.0
:    Steel yield stress        sy  = 500.0
:    Steel poisson ratio       spr = 0.3
:
: MAT 1: Vecchio concrete plain
   1 YOUNG   25742.9602027
     POISON  0.2
     TOTCRK  ROTATE
     COMCRV  THOREN
     CNFCRV  VECCHI
     COMSTR  30.0
     TENCRV  HORDYK
     TENSTR  2.89647143764
     GF1     0.0901091334728
:
: MAT 2: Von Mises w/ strain hardening + Bond
   2 YOUNG   200000.0
     POISON  0.3
     YIELD   VMISES
     HARDIA  0.0 0.0
             500.0 0.0
             200495.0 98.997525
     DSTIF   1732.42790571 173.242790571
     BONDSL  3
     SLPVAL  0.0 0.0
             2.50507697944 0.0143153212983
             3.3890510651  0.0304749984115
             4.08857169547 0.0487166542542
             4.70777071004 0.0693085265765
             5.28515355849 0.0925534123147
             5.84005788524 0.118793120124
             6.38395761349 0.148413496566
             6.92446227568 0.181850099859
             7.46705417442 0.219594604626
             8.01595106185 0.262202031809
             8.57457762007 0.310298910081
             9.14584260005 0.364592488747
             9.73231144121 0.425881137619
             10.336319067  0.495066086797
             10.9600466776 0.573164678962
             11.6055759675 0.661325329086
             12.2749286964 0.760844411502
             12.9700964859 0.873185322678
             13.6930639376 1.0
             13.6930639376 3.0
             5.47722557505 10.5
             5.47722557505 100.0
:            Generated using:
:            alpha    =  0.4
:            s1       =  1.0
:            s2       =  3.0
:            s3       =  10.5
```

```
63   :            tmax_fac =  2.5
64   :            tf_fac   =  0.4
65   :
66   'GEOMET'
67      1 NAME   "ConcProp"
68      2 NAME   "EightBar"
69        CIRCLE  25.4
70        ZAXIS   1. 0. 0.
71        PERIME  79.8
72   'DATA'
73      1 NAME   "ConcPropData"
74      2 NAME   "DataEightBar"
75        INTERF BEAM
76   :
77   : End of prototype model input
```

CHAPTER V

ANALYSIS OF BEAM-COLUMN JOINTS

This chapter presents the application of the prototype constitutive model to simulate the response of four seismically deficient reinforced concrete beam-column joints subjected to reversed cyclic loading. Specimens analyzed include a one-way exterior joint tested by Pantelides et al. [174], a two-way exterior corner joint without slab tested by Akgüzel et al. [9], and a series of two-way exterior corner joints with slab, tested by Park et al. [179] and Engindeniz et al. [60].

5.1 Computation of Joint Response Quantities

The following section describes the response quantities computed for each beam-column joint analyzed. For each joint, only those quantities with an experimental counterpart available for comparison were computed.

5.1.1 Sign Convention

Four beam-column joints were analyzed in this study. In each of the source documents for these experiments, differing sign conventions and directional indicators were followed (cardinal directions and/or Cartesian systems). To craft a more consistent discussion, a common coordinate system was used in this document to describe the orientation of all beam-column joints as well as all computed results.

This convention is summarized as follows: The z-axis is taken as parallel to the column's longitudinal axis and directed upwards. In the case of a one-way, planar joint, the x-axis is taken parallel to the direction of the beam, directed from the column toward the beam end, while the y-axis is oriented orthogonal to the x- and z-axes such that a

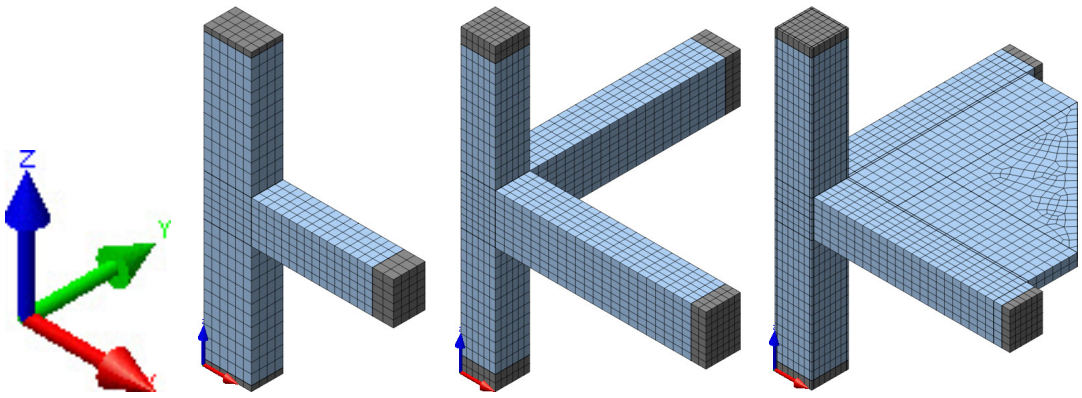

(x-axis: red y-axis: green z-axis: blue)

Figure 5.1: Sign Convention for Beam-Column Joint Models

right-handed coordinate system is formed.

In the case of a three-dimensional, two-way joint containing two beams, the z-axis is taken as parallel to the column's longitudinal axis and directed upwards. The x- and y-axes are placed parallel to the two beams and directed away from the column toward each beam end such that a right-handed coordinate system is formed.

This sign convention is illustrated in Figure 5.1. In all subsequent figures, the coordinate triad consistently represents the x-axis in red, the y-axis in green, and the z-axis in blue. Likewise, figures depicting model reinforcements show x-beam longitudinal reinforcements in red, y-beam longitudinal reinforcements in green, and column longitudinal reinforcements in blue. Transverse and slab reinforcements are shown in gray.

5.1.2 Drift Definition

The boundary conditions and method of load application vary among the prior work of beam-column joint subassemblage experiments. In some cases, the column top is cycled laterally while the beam end is roller-supported, while in other cases, the column is laterally supported at top and bottom while the beam is cycled vertically in displacement control. Both classifications are analyzed in this document.

When simulating experiments where a cyclic, lateral, displacement-controlled history was applied to the column top, the force-displacement response is presented in

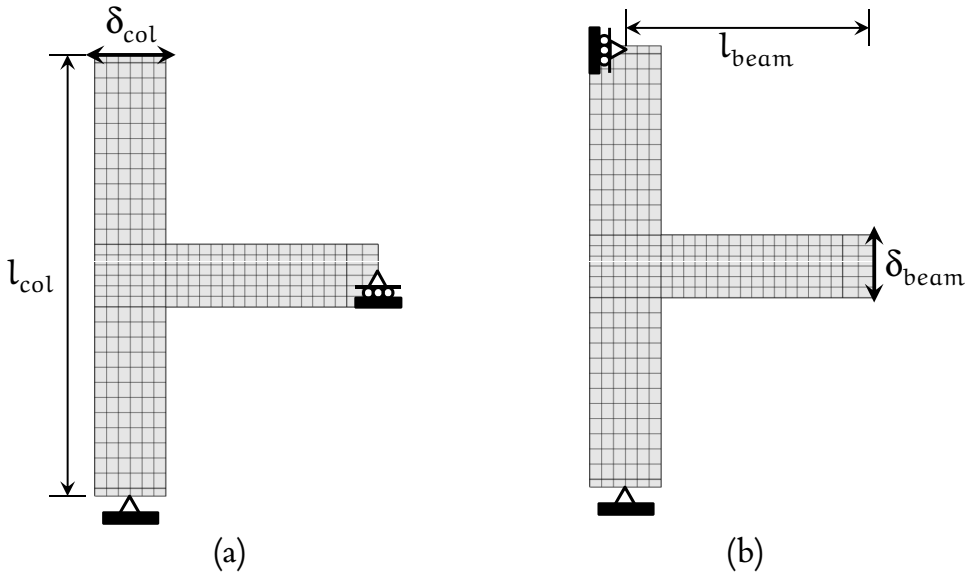

Figure 5.2: Story Drift and Beam Displacement Ratio Quantities

terms of *story drift*, taken as the ratio of the lateral column tip displacement δ_{col} to the unsupported length of the column l_{col}, shown in Figure 5.2a.

When simulating experiments where a cyclic, vertical, displacement-controlled history was applied to the beam end, the force-displacement response is presented in terms of *beam displacement ratio*, taken as the ratio of the vertical beam tip displacement δ_{beam} to the length from the centerline of the beam actuator to the centerline of the column l_{beam}, shown in Figure 5.2b.

5.1.3 Stiffness Degradation

Stiffness degradation was quantified on a per-cycle basis using peak-to-peak stiffness K_{pp}. Peak-to-peak stiffness is the slope of the line connecting the points of maximum and minimum force in the force-displacement response in a given cycle n, illustrated in Figure 5.3 and computed as

$$K_{pp_n} = \frac{F_{max_n} - F_{min_n}}{x_{F_{max_n}} - x_{F_{min_n}}} \tag{5.1}$$

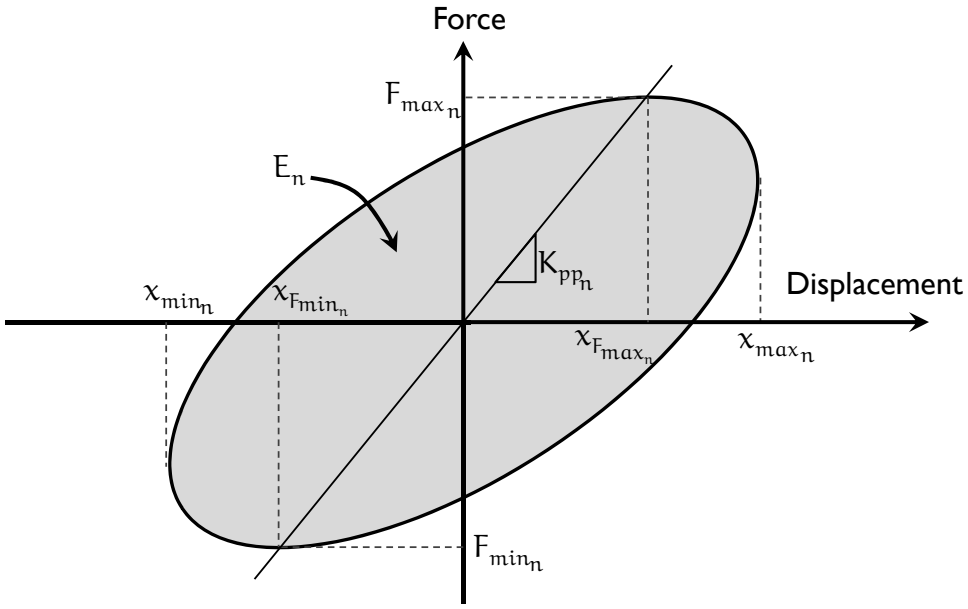

Figure 5.3: Metrics for Force-Displacement Cycle n

5.1.4 Energy Dissipation

Incremental energy dissipation was quantified by computing the area enclosed by the force-displacement response per cycle n, denoted E_n and also depicted in Figure 5.3.

Cumulative energy dissipation E_{cum_n} was computed as the integration of E_n over all cycles $1, \ldots, n$, including the contribution of both x- and y-direction beams for three-dimensional joint specimens. The value of E_{cum_n} corresponding to the final cycle of the analysis represents the total energy dissipated during the simulation.

5.1.5 Joint Shear Stress

The term *joint shear stress* is defined as the average shear stress acting on a horizontal plane at the mid-height of the joint.

Joint shear is often determined experimentally based on external reaction values at the column and beam ends [132]. Figure 5.4 shows the equilibrium of the beam-column joint subassemblage as well as equilibrium of the joint panel. The beam end force V_b generates a moment at the column face equal to $V_b \cdot l_b$, which can be replaced by the statically equivalent force-couple denoted by the equal forces C_b and T_b, separated by a

distance jd, according to

$$C_b = T_b = \frac{V_b \cdot l_b}{jd} \tag{5.2}$$

The internal moment arm jd is often assumed constant and taken as a factor of 0.875 of the effective depth, d. Following from this assumption, the horizontal shear force at the mid-height of the joint may be expressed as

$$V_{jh} = C_b - V_c \tag{5.3}$$

The joint shear stress is finally computed by dividing the joint shear force by the area of the joint mid-plane cross-section as

$$\tau_{jh} = \frac{V_{jh}}{h_b \cdot h_c} \tag{5.4}$$

where h_b is the beam height and h_c is the column width (measured in the y-direction in Figure 5.4). The joint shear stress is often normalized by the square root of the compressive strength of the concrete, expressed as

$$\tau'_{jh} = \frac{\tau_{jh}}{\sqrt{f'_c}} \tag{5.5}$$

5.1.6 Joint Shear Distortion

Joint shear distortion was computed from the displacements of the four corners $ABCD$ of the joint panel face, shown in Figure 5.4. The average shear distortion in the deformed configuration $ABCD'$ is computed as the average of the change of angle at each corner as

$$\gamma_{ave} = \frac{\Delta\angle ABC - \Delta\angle BCD + \Delta\angle CDA - \Delta\angle DAB}{4} \tag{5.6}$$

The experimental determination of joint shear distortion is highly sensitive to the placement of an LVDT array that may conflict with localized cracking or spalling of cover concrete in the joint region, which the numerical model may not explicitly capture (the strength of concrete is reduced due to corresponding damage). As such, disagreement between experimental and simulated joint shear distortion was expected, but evaluated nonetheless.

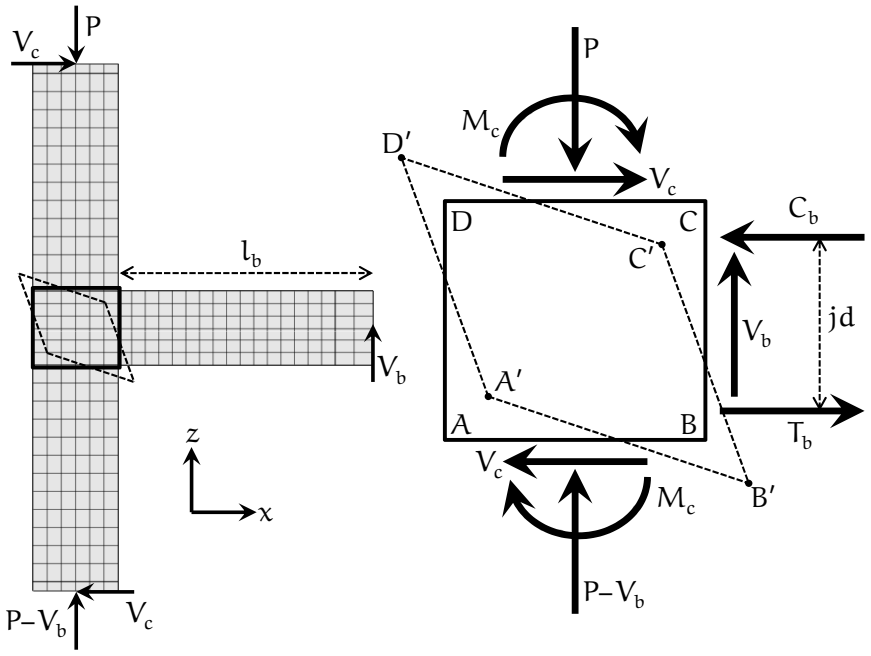

Figure 5.4: Joint Panel Equilibrium and Distortion

5.1.7 Visualization of Crack Patterns

For the total strain rotating crack model in DIANA, crack strains ϵ_{cr} are computed at each element integration point as

$$\epsilon_{cr} = \epsilon_{nst} - \frac{\sigma}{E} \tag{5.7}$$

where ϵ_{nst} are the principal stresses in the crack orientation nst and $\frac{\sigma}{E}$ represents the elastic strain [4]. The crack strain normal to the crack plane, ϵ_{nn}^{cr} is invoked in the DIANA post-processor via the result designation `EKNN`.

Crack patterns are visualized using disc plots. In such a graphic, a small disc is displayed parallel to the crack plane. In a plane-stress analysis, a disc plot decomposes to a series of straight line segments, but for a three-dimensional analysis, the disc shape may be more visible if cracks are no longer uniformly perpendicular to the screen axes.

Since the constitutive model depends on a smeared representation of cracks, visualized crack patterns will appear as bands of distributed cracks instead of single, localized cracks often seen in experiments.

5.2 One-Way Beam-Column Joint – Pantelides et al. [174]

An experimental program conducted by Pantelides, Clyde, and Reaveley [38, 174] was chosen to evaluate the ability of the prototype model to capture the nonlinear response of a seismically deficient one-way exterior beam-column joint subjected to unidirectional cyclic loading. This study consisted of a series of simulated seismic tests performed on four identically reinforced building joint subassemblages under two constant column axial load levels. While the failure processes exhibited in these experiments were complex, they represented a comparatively straightforward benchmark prior to modeling the more complicated two-dimensional bidirectionally loaded beam-column-slab joints presented later in this chapter.

5.2.1 Description of Experiments

The beam-column joints tested by Pantelides et al. possessed detailing consistent with typical reinforced concrete frame buildings designed according to ACI 318-63 [5], prior to the adoption of seismic guidelines. The specimens were constructed at one-half scale, with the reinforcement ratio in the beam increased to ensure shear failure of the joint. The joint possessed multiple seismic deficiencies: lack of transverse reinforcement in the joint core, poor anchorage of beam longitudinal bars in the joint core, inadequate column lap splice length, and insufficient confining reinforcement in the column and beam.

The specimen denoted test #2 was analyzed in the present study. The subassemblage geometry and reinforcing details are shown in Figure 5.5a. The concrete strength was reported as 46.2 MPa (6700 psi), while the yield strengths of beam, column, and ties were reported as 454.4, 469.5, and 427.5 MPa (65.9, 68.1, and 62.0 ksi), respectively. The 458 $\times$ 305 mm (18 $\times$ 12 in) column was reinforced with 8 M22 (#7) bars, corresponding to a reinforcement ratio of 2.54%, while the 406 $\times$ 305 mm (16 $\times$ 12 in) beam was reinforced with 4 M29 (#9) bars for both positive and negative reinforcement,

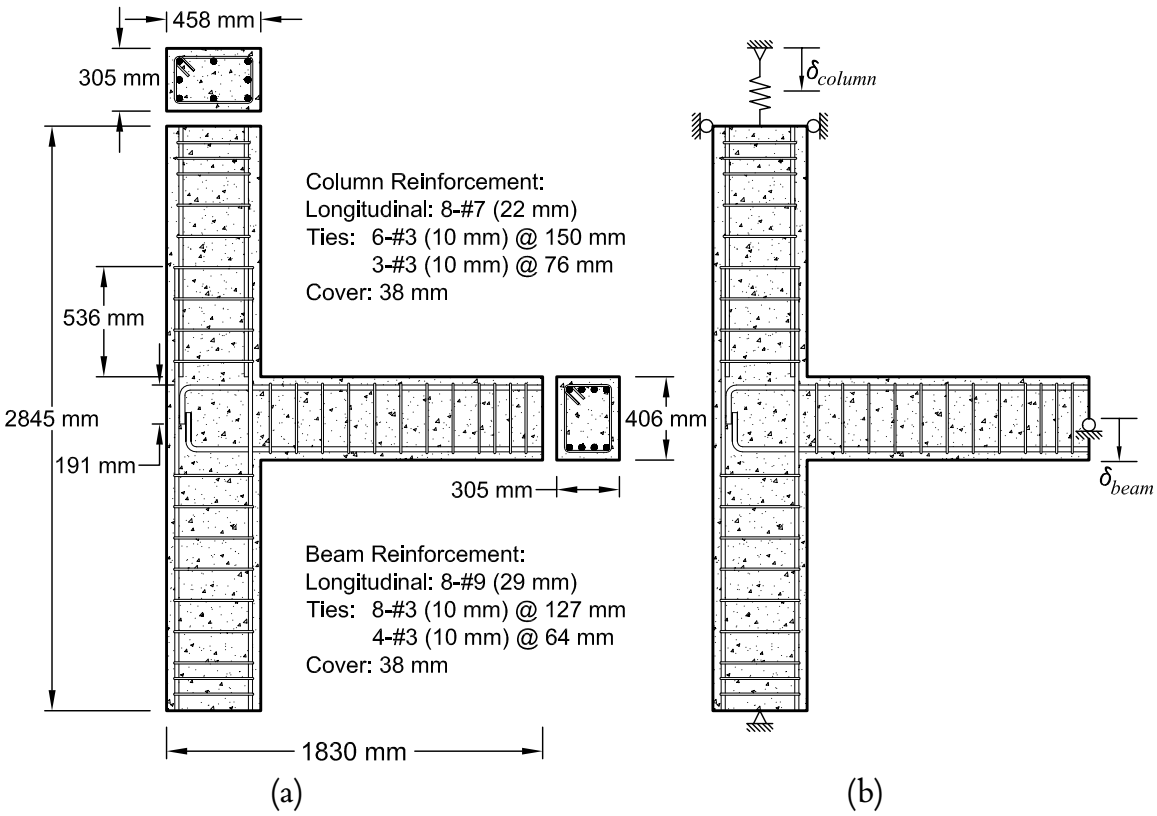

Figure 5.5: Joint Geometry and Idealized Boundary Conditions for Pantelides Specimen

corresponding to a reinforcement ratio of 2.47% for both top and bottom steel. Both top and bottom beam reinforcements were anchored with 191 mm (7.5 in) 90° hooks. Column longitudinal reinforcements were spliced a length of 536 mm (21 in) directly above the joint panel.

The column was mounted horizontally and roller-supported at both ends as shown in figure Figure 5.6. An initial axial load equal to $0.1f'_cA_g$ was transferred to the column through four threaded DWYDAG bars; this force was set at the onset of the test and left to change throughout the experiment. The variation in axial load was measured through strain gages attached to each rod.

The beam end was subjected to quasi-static cyclic loading via the loading collar shown in Figure 5.6. At each load step, three push-pull cycles were performed. The

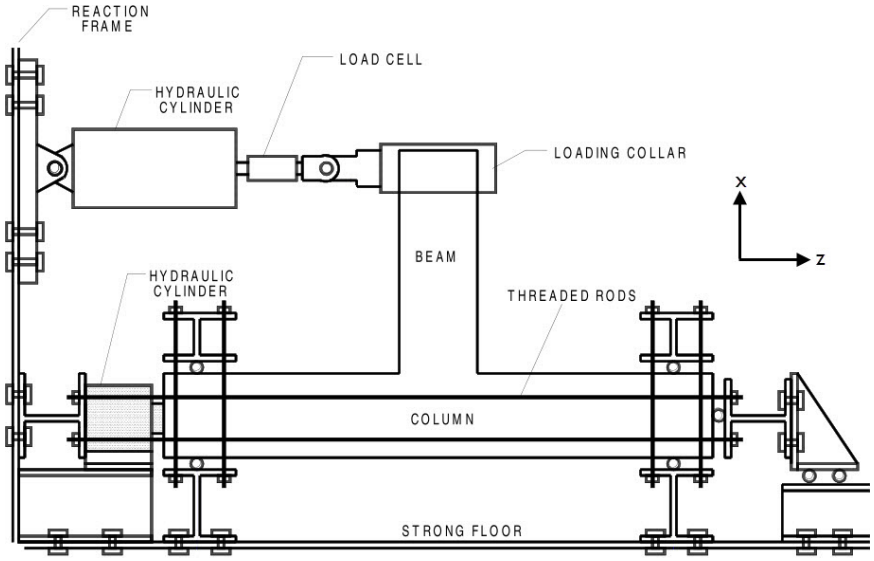

Source: Pantelides et al. [174]

Figure 5.6: Experimental Setup for Pantelides Specimen

first nine steps were administered in force control in increasing 22 kN (5 kip) increments until the first yield of reinforcements occurred, after which the test continued in displacement control. The test continued until the lateral load decreased below 50% of the peak value.

The predominant failure mode was shear failure of the joint panel. The first yield of longitudinal reinforcement occurred at approximately half the ultimate joint capacity. Hairline cracking was observed in the joint panel and beam in early cycles, which evolved into extensive diagonal joint shear cracking and propagated into the column after the peak beam end force was reached. Following strength degradation at higher displacement levels, concrete spalling occurred in the joint as well as the back surface of the column.

5.2.2 Finite Element Model

A detailed finite element model was developed to evaluate the response of test #2. Concrete was modeled using approximately 1700 eight-node solid elements; the mesh is

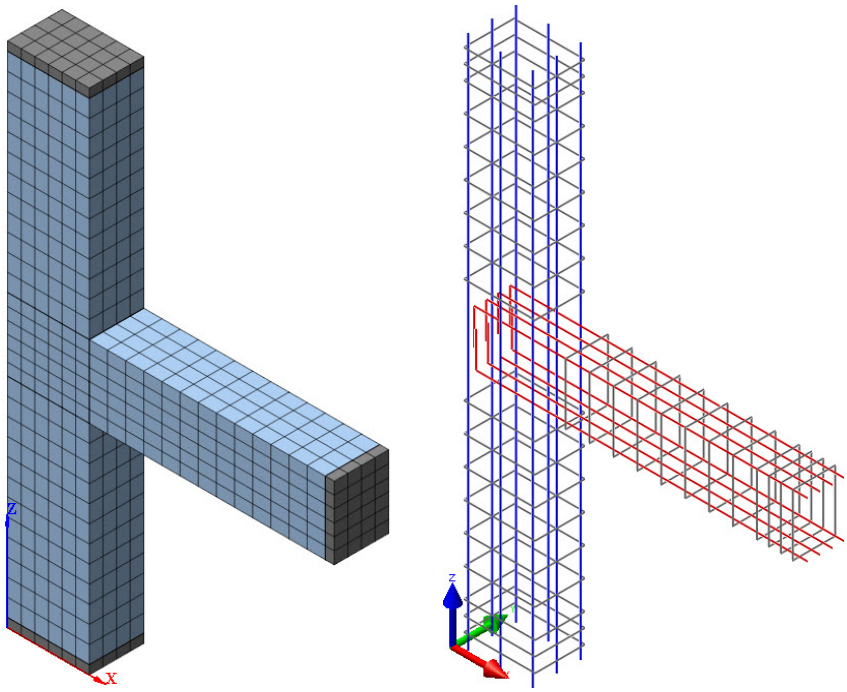

Figure 5.7: Finite Element Mesh for Pantelides Specimen

shown in Figure 5.7. The prototype constitutive model was applied to the entire concrete section, with the exception of a thin layer of stiff elements (1×10^7 MPa) at the column and beam ends to reduce stress concentrations and the possibility of material failure near the supports. No tension stiffening was specified due to the deficient reinforcing details in the system; the tensile response for all concrete elements followed the Hordijk [84] softening model. All reinforcements were discretely modeled using beam elements. All longitudinal and transverse reinforcing bars were connected to the concrete using interface elements to account for nonlinear bond-slip. The splice was not modeled since bond-slip was not observed in the splice region experimentally. The CEB-FIP Model Code 1990 [30] bond-slip law was specified with $s_1 = 1.0$ mm, $s_2 = 3.0$ mm, $s_3 = 5.0$ mm, $\alpha = 0.4$, $\tau_{max} = 2.0\sqrt{f_c}$, and $\tau_f = 0.40\tau_{max}$

The idealized boundary conditions for the model are shown in Figure 5.5b. Throughout the model validation process, the simulated response was shown to be highly sensitive to the boundary conditions, particularly the application of column axial load. The base of the column was pin-supported, while the top of the column was supported by

a roller allowing vertical translation. In early models, the column axial load was applied as a constant force acting at the top of the column, but this approach neglected the fluctuation in force due to the tendency of the beam end force to increase or decrease the deformation in the four threaded rods. Since the constitutive model is dependent on confining pressure and joint shear strength is sensitive to axial load level, a better representation was needed.

To solve this problem, the top of the column was supported by a vertical elastic support with a spring stiffness equivalent to that of the four threaded steel rods used to apply the column axial force experimentally. The spring stiffness of this elastic support K_{col} was computed as

$$K_{col} = \frac{nA_b E_s}{l_r} \tag{5.8}$$

where A_b is the area of each bar, E_s is the elastic modulus of steel, l_r is the unsupported length of the tension rods, and n is the number of rods. The diameter and length of the bars were not reported in the source documents, so they had to be visually estimated from figures. The rods were assumed to be 41.3 mm ($1\frac{5}{8}$") in diameter, 3490 mm (137.4") in length, and possessing elastic modulus $E_s = 200$ GPa (29,000 ksi), which resulted in a spring stiffness of $K_{col} = 306710$ N/mm (1741 lb/in). The elastic support was modeled by connecting the concrete mesh to an external support with the zero-length spring element `SP2TR`.

In the initial analysis step, the spring support was displaced a distance $\delta_{column} = -2.56$ mm (0.1 in), determined numerically from the final model to introduce a column axial force of $0.1 f'_c A_g = 689.4$ kN (155 kips). This external support displacement was held constant throughout the entire analysis, allowing the column axial force to change during subsequent loading cycles as the beam end force caused the spring to shorten or elongate. The beam tip was then cycled around this initial configuration in displacement control, with displacement levels δ_{beam} (Fig. 5.5) corresponding to the experimental load history.

Two large simulations were completed: one with all load cycles from the experiments reproduced, and another only representing a reduced number of load cycles. The purpose of this investigation was to determine whether reduced cycles may be appropriate for larger finite element models where computation effort becomes prohibitive.

The full analysis consisted of approximately 2900 load increments, which corresponded to a solution time of approximately eleven hours. The DIANA material definition for this model is provided in Section B.6.

5.2.3 Discussion of Results

The hysteretic force-displacement response for the beam-column joint model is shown in Figure 5.8, with peak values during each cycle listed in Table 5.1. Good agreement was observed between the computed and observed response. At the positive displacement level corresponding to the maximum experimentally observed beam end force (+1.8%), the ratio of simulated to observed beam end force was 1.021, although the numerical solution continued to show increasing strength until a displacement level of +2.4%, at which point the ratio of maximum predicted to maximum observed beam end force (at +1.8% displacement ratio) increased to 1.119. For negative loading, the experimentally observed peak beam end force occurred at a drift of −1.96%, while the computed peak beam end force occurred at a displacement level of −2.4%, with a ratio of simulated to observed peak beam end force of 0.985. For both positive and negative loading, the strength was overestimated after a displacement ratio of 1.8%, which may be attributed to the inability of the bond-slip model to adequately degrade as the number of cycles increased. The numerical response showed approximately the same strength for positive and negative loading, while experimental response showed higher capacity in the negative displacement regime. The mean predicted-to-observed strength ratio over all cycles was 1.141 (CV 0.070), although if only the 0.3–1.8% displacement

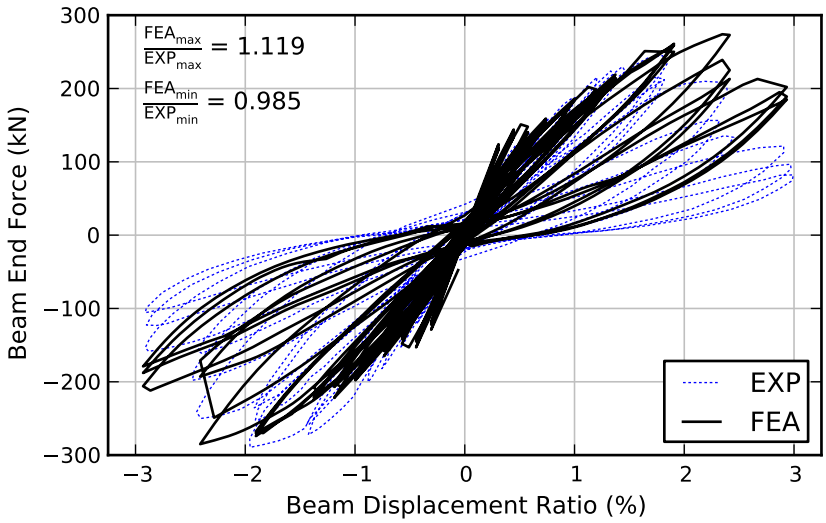

Figure 5.8: Force-Displacement Response for Pantelides Specimen

level cycles were considered, the mean predicted-to-observed strength ratio over all cycles improved to 1.043 (CV 0.013).

Stiffness degradation was quantified according to the peak-to-peak stiffness, computed for each cycle according to Equation 5.1 and shown in Figure 5.9. Good correlation was observed comparing experimental to numerical response. In early cycles, the finite element response was stiffer than the experiment, which may be due to initial microcracking of the specimen prior to testing which the model could not capture. Beginning in cycle #8, the model exhibited a more softened response than the experiment until the peak beam end force reached its maximum value at cycle #23, after which the model uniformly overestimated the stiffness of the system by about 1800 N/mm. The mean predicted-to-observed peak-to-peak stiffness ratio over all cycles was 1.106 (CV 0.073).

The energy dissipation response is presented in Figure 5.10, with the energy dissipated per cycle shown in Figure 5.10a and the cumulative (total) energy dissipated shown in Figure 5.10b. On a per-cycle basis, the numerical energy dissipation response showed excellent agreement with the experimental response except for cycles 19–27,

Table 5.1: Force-Displacement Metrics for Pantelides Specimen

			Peak Beam End Force						Peak Beam End Force		
Disp. ratio	Cycle	Dir	EXP (kN)	FEA (kN)	FEA/EXP	Disp. ratio	Cycle	Dir	EXP (kN)	FEA (kN)	FEA/EXP
0.3%	1	+	98.73	122.54	1.241	1.2%	1	+	216.75	202.84	0.936
		-	-94.70	-127.03	1.341			-	-230.52	-245.80	1.066
	2	+	98.33	118.10	1.201		2	+	212.07	197.66	0.932
		-	-94.38	-118.71	1.258			-	-227.21	-222.91	0.981
	3	+	96.33	115.14	1.195		3	+	209.80	196.18	0.935
		-	-94.06	-116.15	1.235			-	-224.57	-216.55	0.964
0.4%	1	+	125.15	142.15	1.136	1.3%	1	+	224.48	220.23	0.981
		-	-122.07	-151.21	1.239			-	-266.78	-223.86	0.839
	2	+	124.91	140.30	1.123		2	+	217.73	216.16	0.993
		-	-121.06	-142.33	1.176			-	-255.33	-221.32	0.867
	3	+	124.34	132.53	1.066		3	+	213.77	215.42	1.008
		-	-120.75	-136.93	1.134			-	-243.57	-215.59	0.885
0.6%	1	+	142.25	148.07	1.041	1.8%	1	+	245.24	259.82	1.059
		-	-153.74	-152.79	0.994			-	-289.35	-273.45	0.945
	2	+	140.76	139.19	0.989		2	+	216.34	257.23	1.189
		-	-143.91	-142.96	0.993			-	-252.15	-269.96	1.071
	3	+	139.06	138.46	0.996		3	+	212.67	249.83	1.175
		-	-138.20	-136.62	0.989			-	-235.62	-269.00	1.142
0.8%	1	+	159.75	159.54	0.999	2.4%	1	+	209.82	274.25	1.307
		-	-177.85	-165.16	0.929			-	-250.49	-284.78	1.137
	2	+	157.73	155.84	0.988		2	+	157.31	236.88	1.506
		-	-162.94	-157.87	0.969			-	-198.33	-247.59	1.248
	3	+	156.60	153.62	0.981		3	+	136.55	211.35	1.548
		-	-157.87	-156.60	0.992			-	-161.63	-191.57	1.185
1.0%	1	+	187.84	186.56	0.993	2.9%	1	+	121.48	211.72	1.743
		-	-215.91	-198.11	0.918			-	-159.76	-211.37	1.323
	2	+	186.03	185.08	0.995		2	+	96.65	193.59	2.003
		-	-197.47	-196.52	0.995			-	-124.71	-186.74	1.497
	3	+	183.80	184.34	1.003		3	+	82.40	183.60	2.228
		-	-193.98	-189.21	0.975			-	-106.86	-177.56	1.662

All Cycles: MEAN = 1.141 CV = 0.070

0.3-1.8% Cycles Only: MEAN = 1.043 CV = 0.013

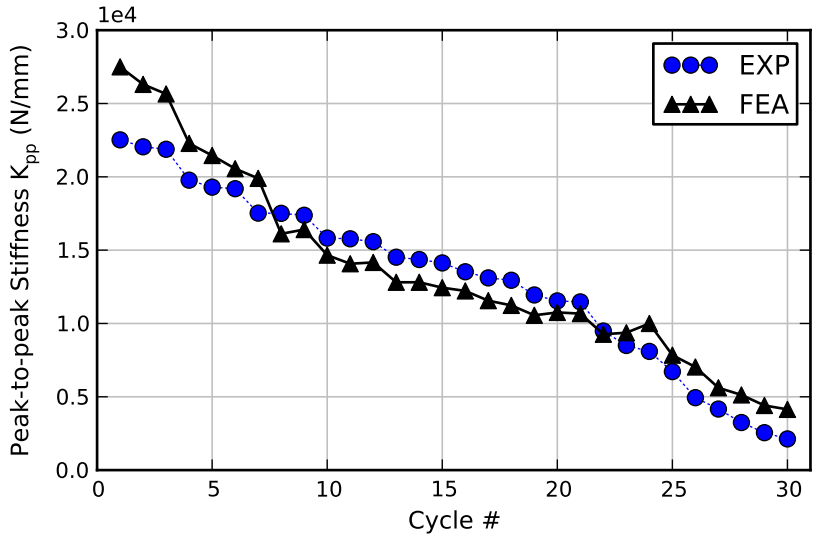

Figure 5.9: Stiffness Degradation Response for Pantelides Specimen

corresponding to the 1.8 and 2.4% beam displacement ratio levels during which the majority of material failure occurred. In these cycles, the constitutive model overestimated the degree of pinching in the hysteretic loops, also visible in the force-displacement response from Figure 5.8. Close agreement was achieved in the cumulative energy response until these same cycles were reached, at which point the difference in cumulative energy dissipated gradually increased until the final cycle, in which the cumulative energy dissipation for the entire simulation was underestimated by about 18%.

The joint shear stress-strain response is presented in Figure 5.11. The shear stress was computed from external reactions as described in Section 5.1.5. For positive joint shear distortion, the shear capacity was predicted within 5% of the observed response, while for negative shear distortion, the shear capacity was predicted within 7% of the experimental response. Good agreement was observed in predicted-to-observed joint shear distortion during the first 23 cycles. This corresponded to the point in the experiment where the peak force was reached and the model began over-predicting the peak-to-peak stiffness and under-predicting the energy dissipation. In the remaining cycles of the experiment, greater discrepancy was observed as permanent distortions began developing, evidenced by a shift of the experimental response toward increasing positive

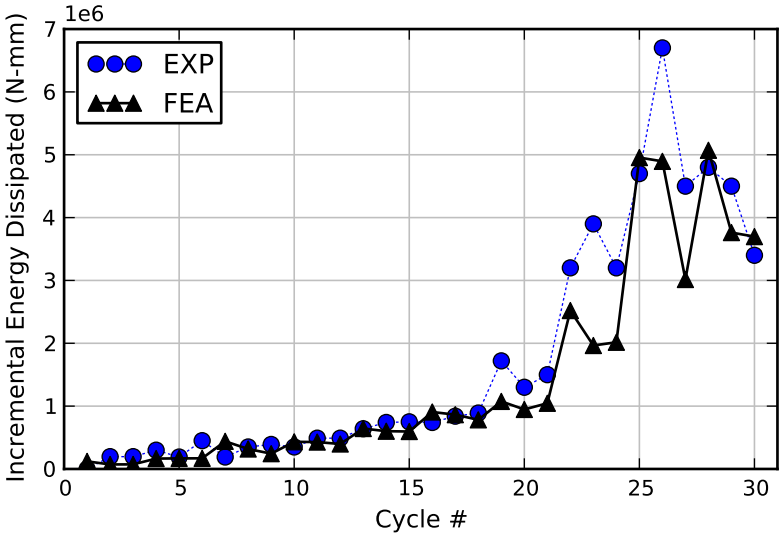

(a) Incremental

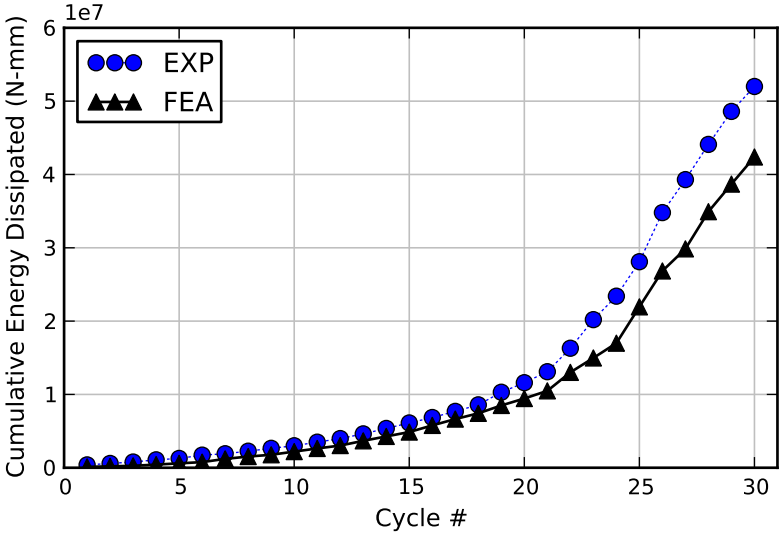

(b) Cumulative

Figure 5.10: Energy Dissipation for Pantelides Specimen

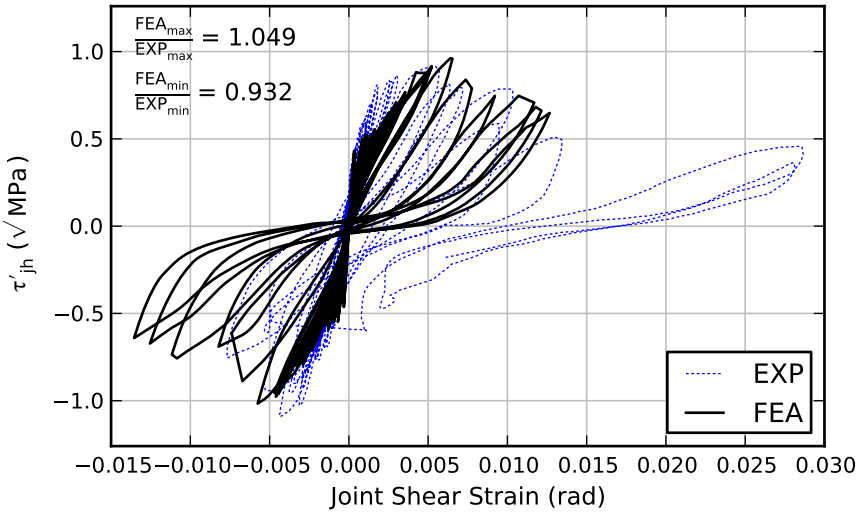

Figure 5.11: Joint Shear Response for Pantelides Specimen

(and decreasing negative) shear strain values. The numerical response, however, produced a nearly identical progression of degradation for positive and negative loading due to the secant constitutive model for the concrete. While this deviation was quite large, significant spalling had occurred in the experiment by this load level and, as such, close agreement of a local response such as joint shear distortion may be unrealistic.

The effectiveness of the column axial spring model in representing the condition developed by the four threaded rods was evaluated by comparing the force developed in the spring with experimental data, shown in Figure 5.12. In the experimental results, a degradation in column compression of approximately 10% was observed; in the simulation, the final compression force in the spring decreased by an additional 7%. Figure 5.12 shows general agreement for column compression vs. beam displacement ratio and beam end force. These results demonstrated that for both the experimental and analytical response, a positive beam end force increased the compression in the column, and that a negative beam end force also resulted in a similar, yet muted, increase in column axial force.

A comparison of the predicted crack pattern at the maximum displacement ratio of +3% during the final cycle with a photograph of the final damaged state of the joint

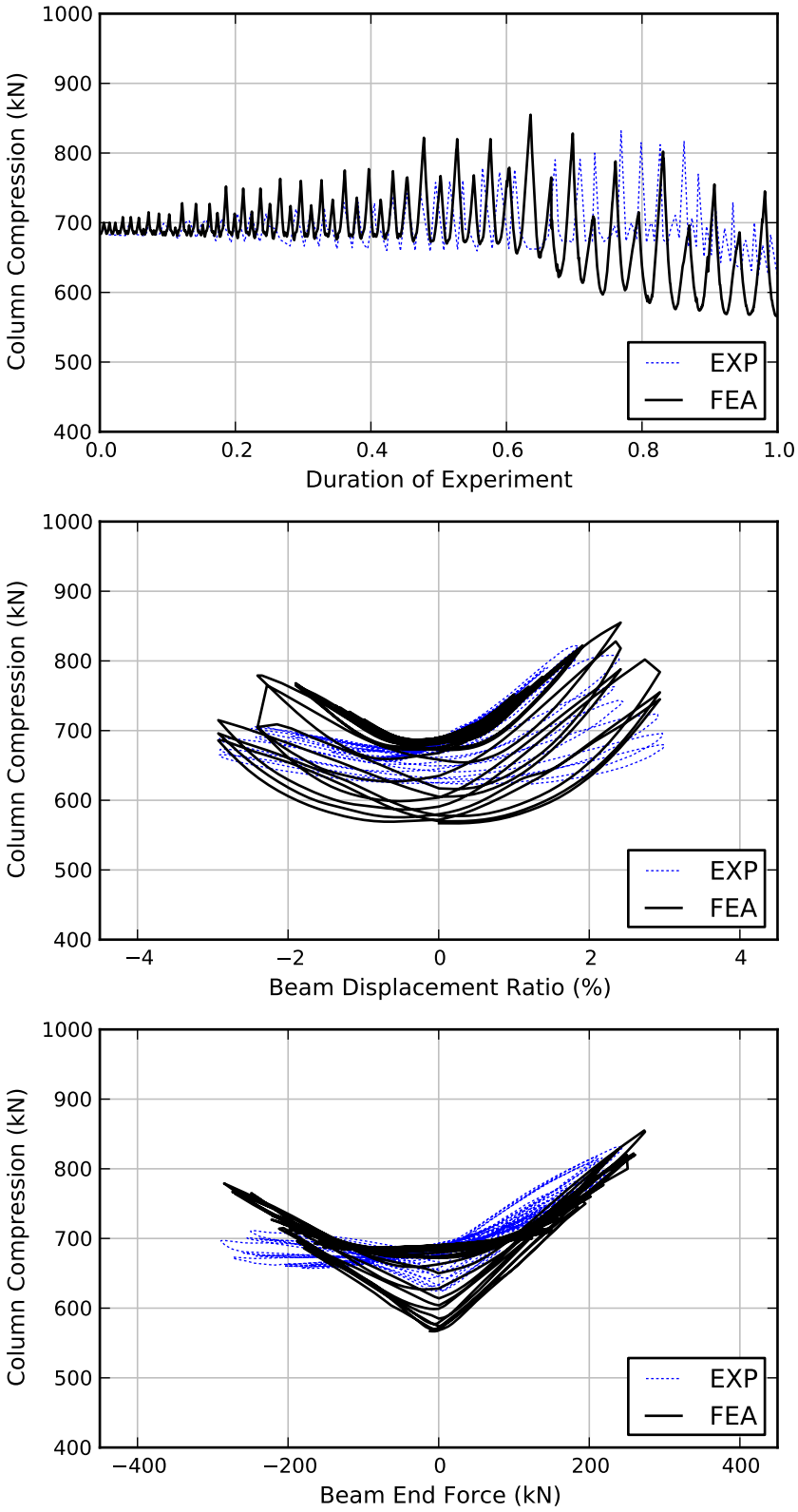

Figure 5.12: Variation of Column Compression for Pantelides Specimen

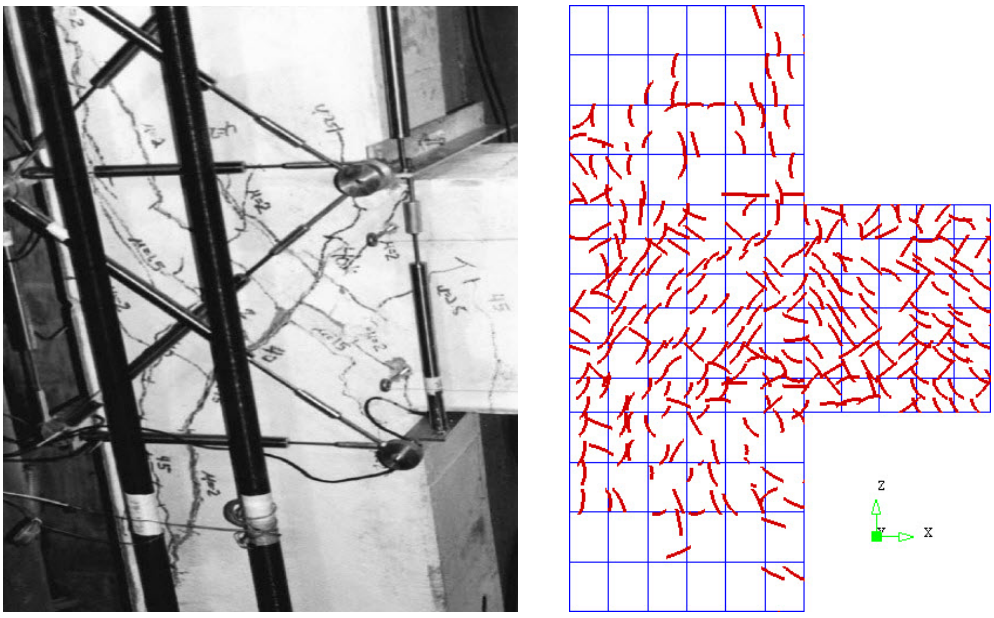

Source: Pantelides et al. [174]

Figure 5.13: Comparison of Final Crack Pattern for Pantelides Specimen

specimen is shown in Figure 5.13. Correlation was observed between the large diagonal crack propagating from the bottom left to the top right of the joint in the photograph and the band of similarly oriented smeared cracks in the analysis results. Since the response was simulated using a rotating crack model (in which crack orientations are permitted to rotate with the principal strain directions), only the final configuration of the crack directions was depicted.

In both the experimental program and the simulation described up to this point, the beam was cycled three times at each displacement level. To investigate means of reducing the computational cost of the simulation, the same model was executed with a reduced number of cycles. The simulation with reduced cycles only performed a single pass at each displacement level. A comparison of the force-displacement response with $n = 3$ and $n = 1$ cycles is shown in Figures 5.14a and 5.14b, respectively. The envelope of the reduced cycle response followed the envelope of the full simulation closely, with only marginal differences observed between peak strength values, peak-to-peak stiffness, and energy dissipation on a per cycle basis (not cumulative) between the two

models, implying that the response was more dependent upon maximum prior displacement level reached than the number of repeated cycles at a given displacement level. While the full simulation was completed in approximately eleven hours, the relatively small size of the model and simplicity of the loading history implied that a much larger three-dimensional model with transverse beams, integral slab, and alternating bidirectional cyclic load history would require significantly higher computational effort. This example seems to indicate that reducing the number of repeated cycles per load level is a justifiable means of reducing the total solution time in more complex beam-column joint models which may otherwise be prohibitive or impossible to simulate on available hardware, without compromising the ability to capture the key characteristics of the response and failure mechanisms exhibited by the system.

5.3 Two-Way Beam-Column Joint – Akgüzel et al. [9]

An experimental campaign conducted by Akgüzel and Pampanin at the University of Canterbury in Christchurch, NZ [10, 9, 11] was chosen to evaluate the ability of the prototype model to simulate a two-way exterior corner beam-column joint subjected to bidirectional cyclic loading. This simulation was a logical next step following the analysis of the one-way joint tested by Pantelides et al. [38, 174] since it introduced an additional transverse beam and a more complex multiaxial cyclic load history.

5.3.1 Description of Experiments

Akgüzel and Pampanin [10, 9, 11] evaluated a series of one- and two-way, nonseismically detailed and FRP-retrofitted beam-column joints subjected to simulated seismic loading. The joints were subjected to both bidirectional and varying axial load. The reinforcing details in both one- and two-way joints were nominally identical so that the influence of unidirectional vs bidirectional loading protocols could be investigated. Specimen 3D1 was analyzed in the present study.

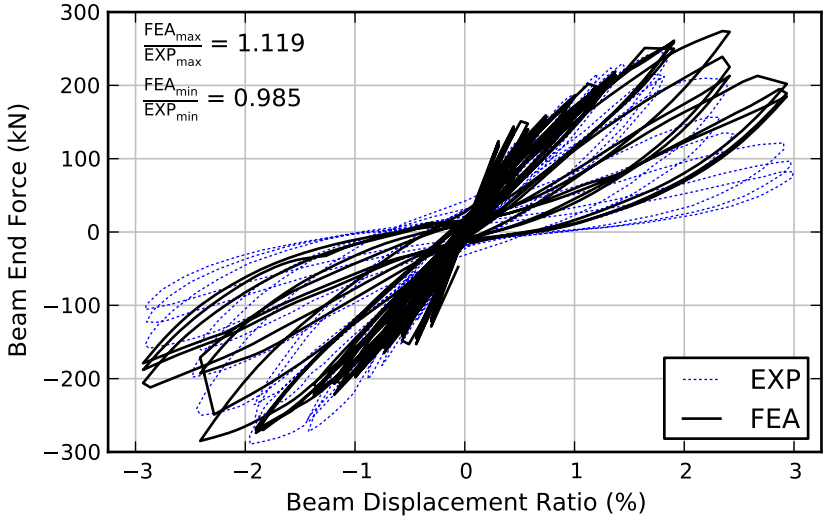

(a) 3 cycles at each displacement level

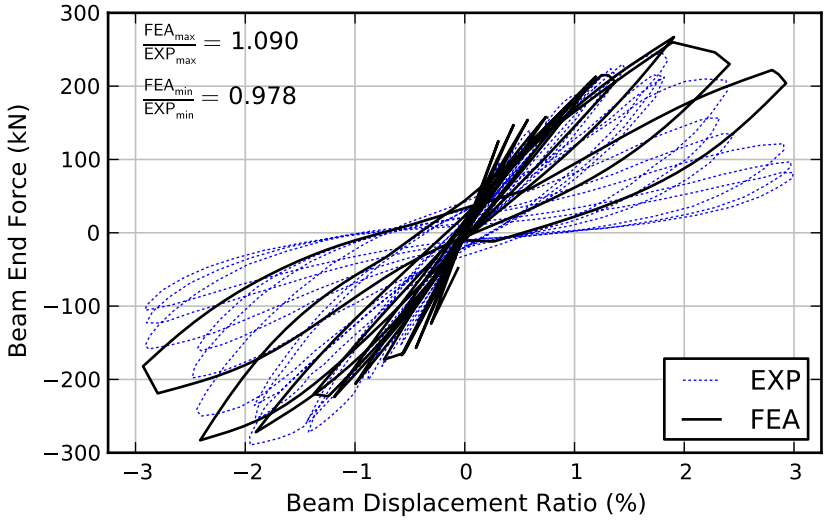

(b) 1 cycle at each displacement level

Figure 5.14: Influence of Repeated Cycles on Joint Simulation Response

Specimen 3D1 represented an "as-built" corner beam-column joint subassemblage consisting of a column and two orthogonal transverse beams; there was no slab present. The specimen was designed to mimic the behavior of a first-story corner joint in a mid-rise residential building designed only for gravity loads according to the 1955 New Zealand standard [1]. The lengths of the column and beams were chosen to correspond to the contraflexure points under lateral load, assumed to occur at the mid-height and mid-span of the frame. The specimen was constructed at two-thirds scale.

The dimensions and reinforcing details of the specimen are shown in Figure 5.15. The joint core contained no transverse reinforcement. Beam longitudinal bars were anchored in the joint with 180° hooks. The column had a 230 × 230 mm (9 × 9 in) cross-section, and the beam was 230 mm wide × 330 mm deep (9 × 13 in). The beams contained four R10 (10 mm diameter) Grade 300 smooth bars on both the top and bottom surfaces. The column contained six R10 Grade 300 smooth bars, three on each face parallel to the yz-plane. Transverse reinforcements in the column and beams were R6 (6 mm diameter) Grade 300 plain round bars. On the day of testing, the concrete had a compressive strength of 17.4 MPa (2520 psi) and a tensile strength of 2.20 MPa (320 psi). The yield strengths of the R10 and R6 bars were 340 and 408 MPa (49 and 59 ksi), respectively.

The experimental setup is shown in Figure 5.16. The beam ends were roller-supported, allowing translation in the x- and y-directions. The base of the column was supported by a universal joint which allowed rotation about the x- and y-axes. Bidirectional lateral load histories were applied to the top of the column via displacement-controlled hydraulic actuators. A series of Macalloy bars were also used in conjunction with a servo-controlled actuator to apply compressive force at the top of the column. Restrainers were used to prevent significant out-of-plane displacement and rotation of the beams.

In order to investigate a wide range of potential displacements which can occur in

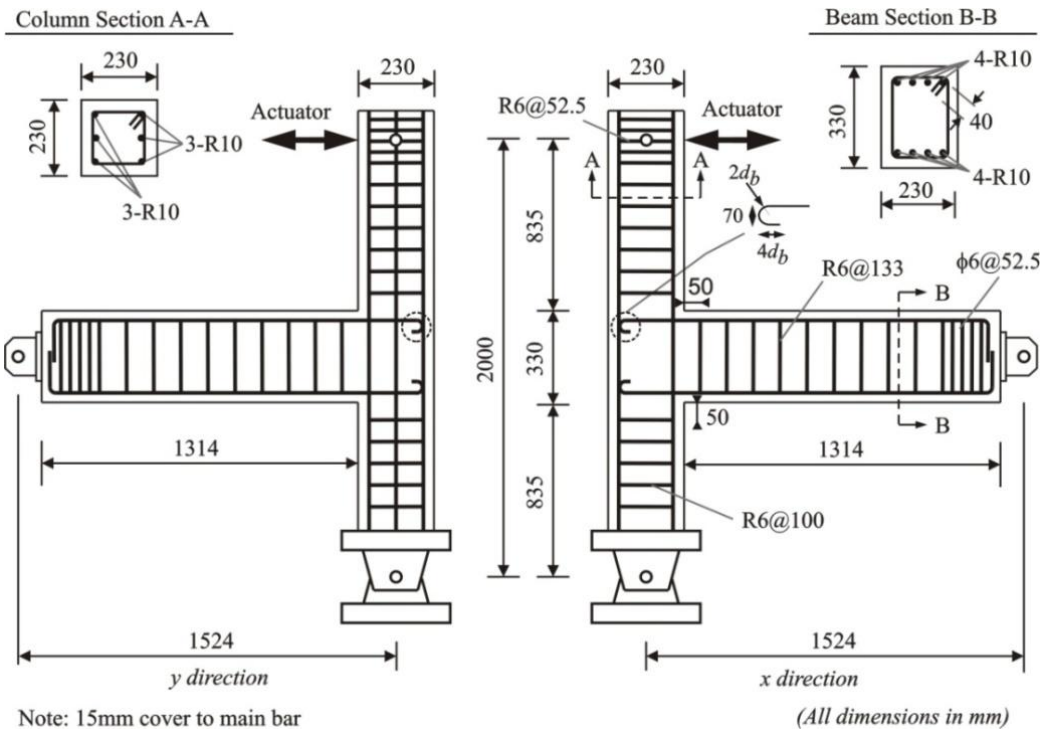

Source: Akgüzel [9]

Figure 5.15: Specimen Dimensions for Akgüzel Specimen

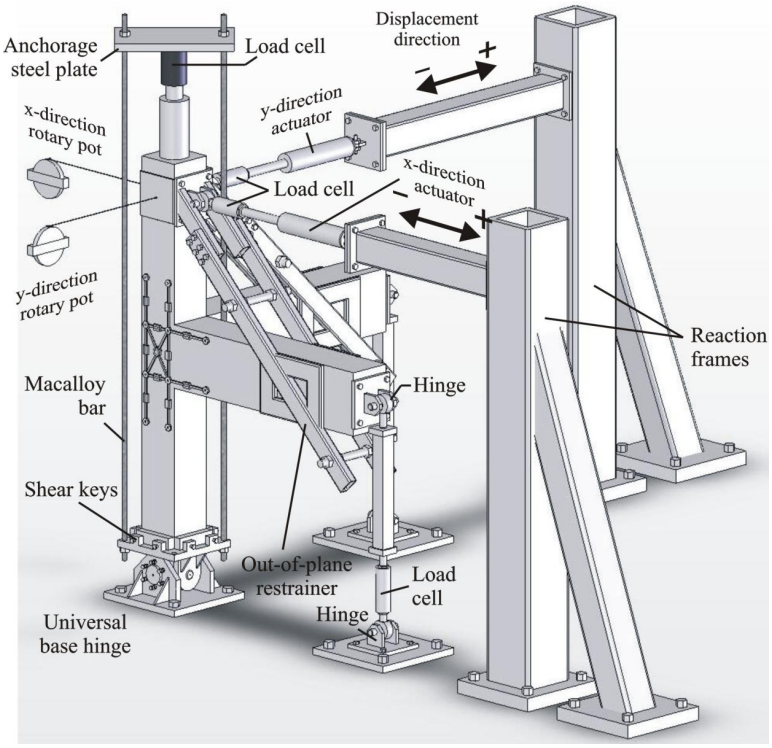

Source: Akgüzel [9]

Figure 5.16: Experimental Setup for Akgüzel Specimen

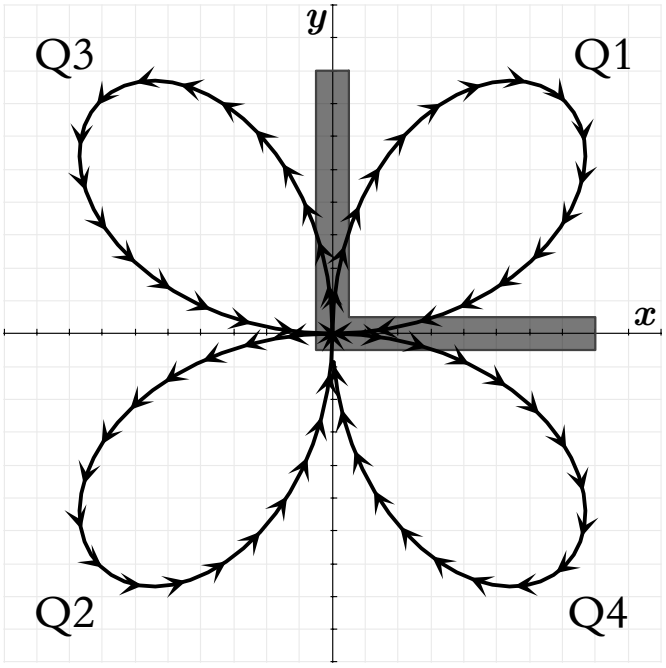

Figure 5.17: Bidirectional Cloverleaf Lateral Load Pattern for Akgüzel Specimen

a building depending on the direction of earthquake acceleration, a bidirectional cyclic lateral load history following a cloverleaf pattern was applied to the column top at increasing drift levels. At each drift level, the x- and y-displacements were applied according to the function

$$x(\theta) = R\sin(2\theta)\cos(\theta) \qquad y(\theta) = R\sin(2\theta)\sin(\theta) \tag{5.9}$$

where θ was the angle measured with respect to the x-axis in the xy-plane and R is the magnitude of the maximum displacement reached per cycle, measured at $\theta = 45°$, 135°, 225°, and 315°. The directions of the displacement history per cycle were followed in the order of the four quadrants as labeled in Figure 5.17. Note that a consequence of the cloverleaf pattern is that two full cycles are performed in the x- and y-directions at each drift level. This pattern was repeated at story drift levels of 0.1, 0.2, 0.5, 1.0, 1.5, 2.0, 2.5, and 3.0%. The conversion between lateral displacement and story drift was a factor of 20 mm per 1% drift, derived from the height of the column.

In a building subjected to a lateral ground acceleration, the axial force in exterior

columns will increase or decrease according to the direction of lateral load and subsequent overturning effects. Akgüzel accounted for this effect experimentally by varying the column axial force in a fixed proportion to the computed reaction forces at the column top, V_{cx} and V_{cy}, according to the equation

$$N = N_g - \alpha_x V_{cx} - \alpha_y V_{cy} \tag{5.10}$$

The initial value of column axial force, N_g, was estimated as the gravity load in the prototype building tributary area as 115 kN. The proportionality constants α_x and α_y were taken as 2.35. Thus, when both V_{cx} and V_{cy} were positive (Quadrant 1), the axial force decreased, while negative values of V_{cx} and V_{cy} resulted in an increase in column axial force (Quadrant 2). Thus, the experiment depended on a real-time feedback loop between measured column lateral forces and the applied axial force history. The column axial load varied between $0.06–0.21 A_g f'_c$.

The failure of the joint was dominated by joint shear cracking and formation of a concrete wedge mechanism. Initial cracking of the joint core occurred at a drift of 0.5%, resulting in a sudden drop in strength and energy dissipation capacity. In later cycles, a "shear hinge" mechanism formed in the joint panel, and the experiment was halted during the 3% drift cycle when failure of the joint core resulted in loss of stability in the column.

Akgüzel also analyzed specimen 3D1 using the nonlinear finite element analysis code MASA. This analysis was previously described in Section 2.3.5, and the finite element mesh and force-drift hysteretic response is shown in Figure A.59 on page 253.

5.3.2 Finite Element Model

A finite element model was developed to simulate the response of specimen 3D1. The concrete mesh contained 3600 eight-node continuum elements. The prototype constitutive model was applied to the entire concrete mesh except for regions near the supports at the column and beam ends, which were modeled with high elastic stiffness

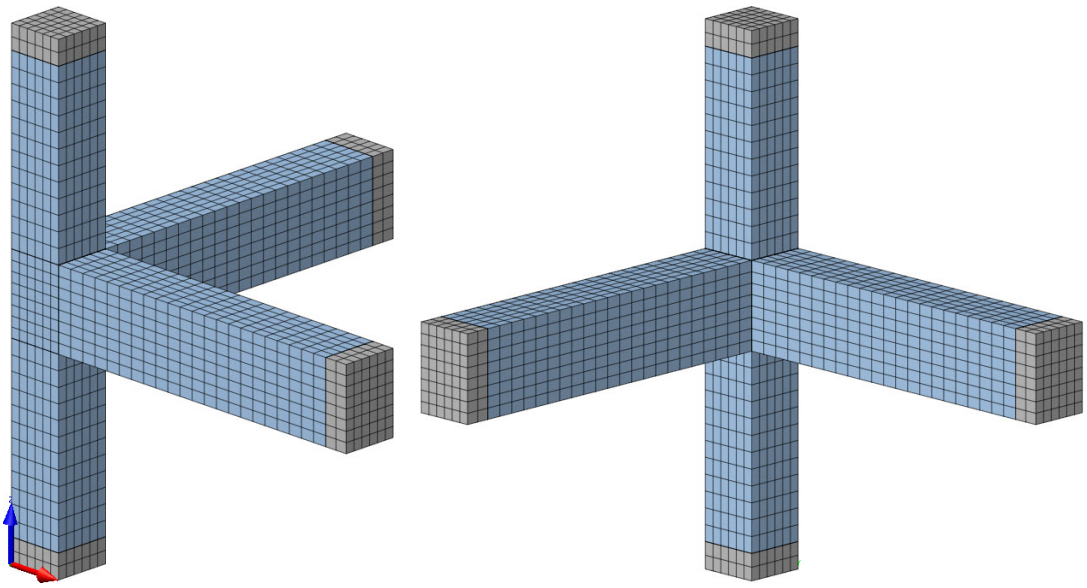

Figure 5.18: Finite Element Mesh for Akgüzel Specimen

(1×10^7 MPa) to better distribute concentrated effects arising from support reactions and applied loads into the system. The finite element mesh is shown in Figure 5.18, with the stiffened regions shown in dark gray.

The distribution of reinforcement in the model is shown in Figures 5.19 and 5.20. All longitudinal reinforcements were modeled using beam elements with bond-slip interface elements, while transverse elements were modeled as truss elements with perfect bond. The 180° hooks were modeled as three orthogonal beam elements, illustrated in the joint detail in Figure 5.19. Since smooth reinforcing bars were used, the bond-slip law was significantly reduced according to the recommendations in CEB-FIP Model Code 1990 [30] for smooth bars with good bond condition.

Boundary conditions were specified as follows. At the center node of the column base, all translations were constrained (pin supported). The beam ends were supported at the center node of the free end, preventing vertical and out-of-plane displacements but allowing free translation in the direction of each beam's longitudinal axis.

The application of the cyclic bidirectional and column axial load histories at the top of the column was the most challenging aspect of the simulation. Lateral loads had to

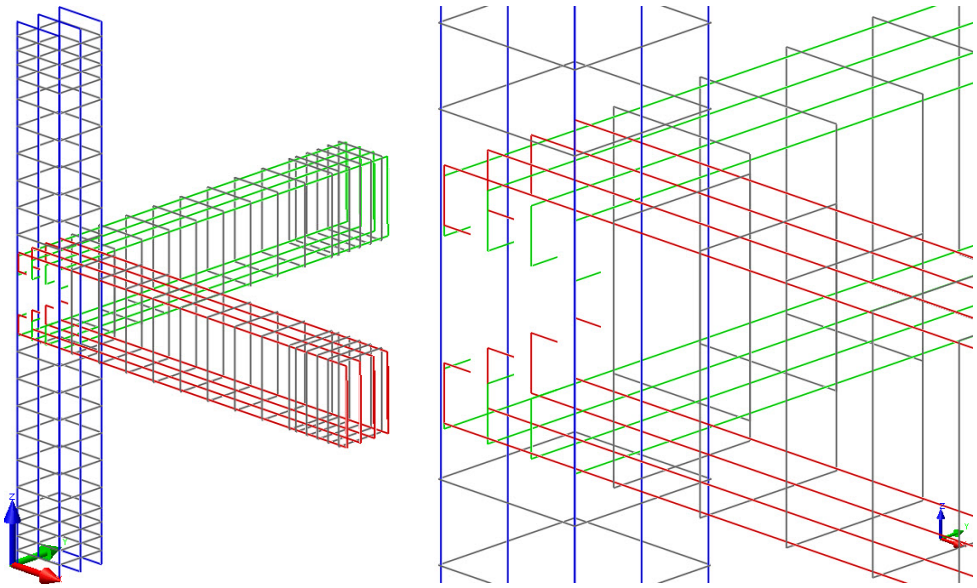

Figure 5.19: Reinforcing Bar Mesh for Akgüzel Specimen – Isometric View and Joint Detail

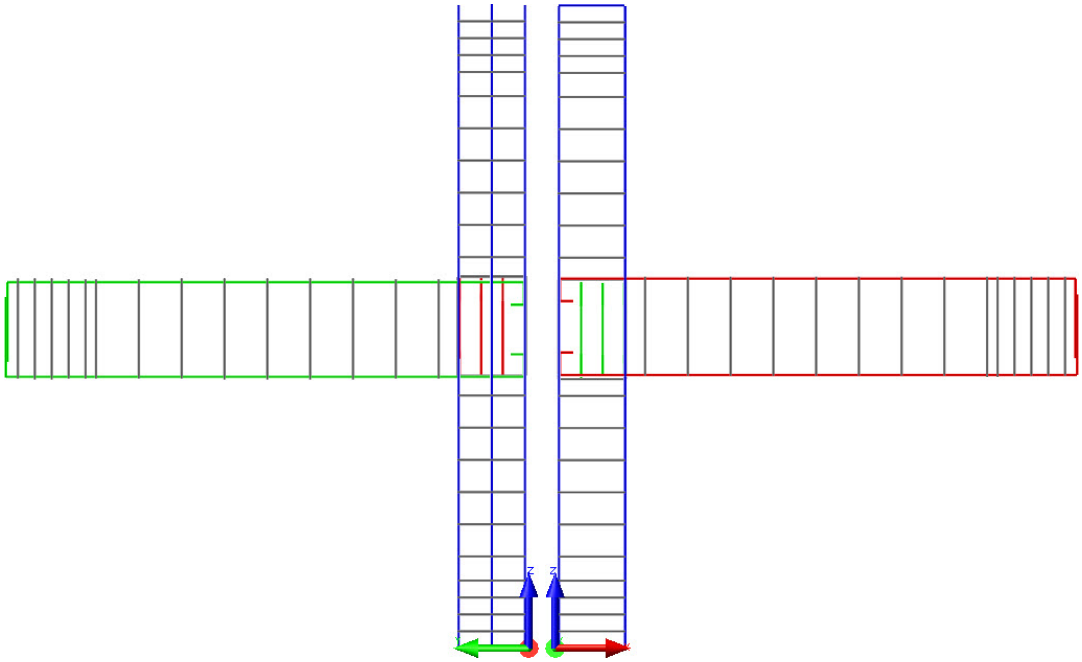

Figure 5.20: Reinforcing Bar Mesh for Akgüzel Specimen – Elevation View

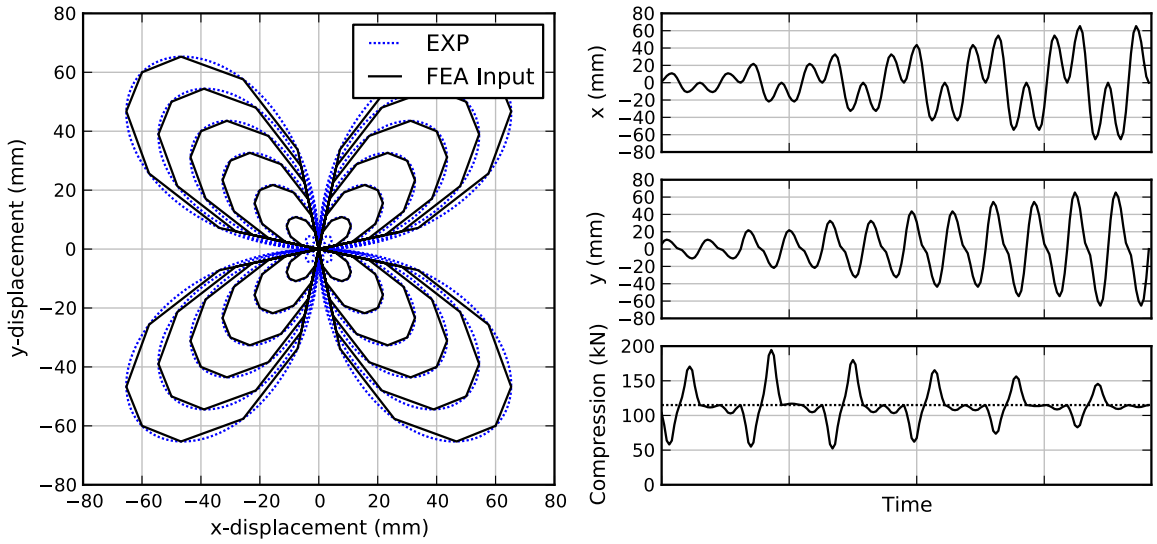

Figure 5.21: Simulation Load History for Akgüzel Specimen

be applied in displacement control, while the vertical column axial force was applied in force control. A Python script was developed to generate a piecewise linear representation of the cloverleaf load history and corresponding DIANA input for each drift level's displacement history in the x- and y-directions. Due to the high computational effort required to simulate this experiment, not all experimentally applied drift levels were considered in the simulation (the 0.1 and 0.2% drift levels were neglected). A visualization of the resulting numerically-applied cloverleaf load history is given in Figure 5.21a, with displacement directions following the sequence illustrated in Figure 5.17.

The column axial force history was generated as follows. In the experiments, the column axial force was updated in real-time from the measured column shears according to Equation 5.10. In the finite element model, however, there was no way to simultaneously apply a column force level as a fixed proportion of the computed lateral force reactions. Thus, the peak column axial force levels reported by Akgüzel for each drift level (and corresponding quadrant) were simultaneously applied with a ramp function in each cyclic excursion, cycled around a base column axial force level of 115 kN. The influence of column axial force can be visualized in 2D in Figure 5.21b, or in 3D in

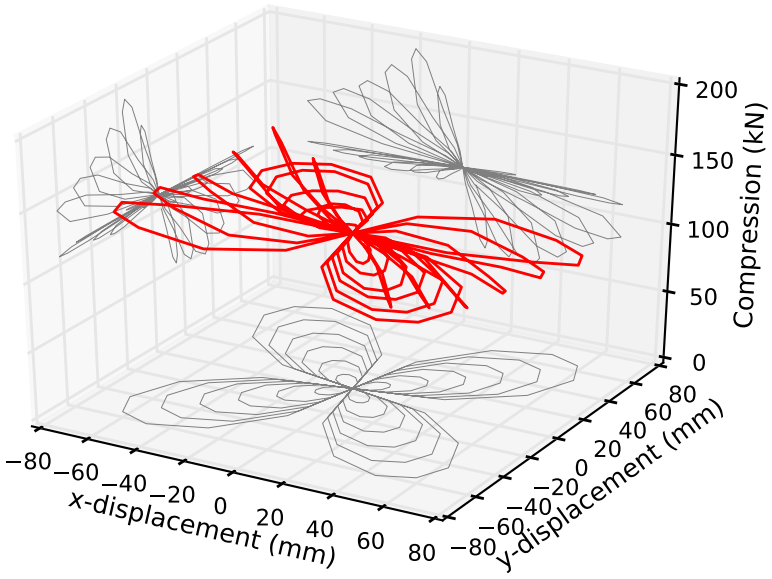

Figure 5.22: Simulation Load History for Akgüzel Specimen – 3D Visualization

Figure 5.22 (with column axial compression force corresponding to the vertical axis). From this figure, it is evident that the column axial force is at a minimum in Quadrant 1 of the load history when both column shear forces are positive, while it reaches its maximum value in Quadrant 2 when both column shear forces are negative.

The Python code used to generate the load history input for DIANA is documented in Section B.7.1, along with the input displacement and axial force levels for each excursion in the bidirectional cloverleaf pattern.

The analysis consisted of approximately 2000 load increments, which corresponded to a solution time of approximately twenty hours. The DIANA material definition for this model is provided in Section B.7.2.

5.3.3 Discussion of Results

The x-direction hysteretic force-drift response for the beam-column joint model is shown in Figure 5.24a. Good overall agreement was observed with the experimental envelope. For positive drifts, the ratio of predicted-to-observed lateral force capacity was 0.986

at a drift level of +1%, while for negative drifts, the ratio of predicted-to-observed lateral force capacity was 1.057, again at a drift level of −1%. For positive drift ratios, the capacity was overestimated in both cycles at the +2.5 and +3% drift levels. For negative drifts, the capacity was overestimated for the first cycle but underestimated for the second cycle at the −2.5 and −3% drift levels. The mean ratio of predicted-to-observed strength over all x-direction cycles was 1.143 (CV 0.281).

The y-direction hysteretic force-drift response is shown in Figure 5.24b. Again, good overall agreement was observed with the experimental envelope, especially for negative drift levels. For positive drifts, the lateral force capacity was overestimated by about 20% in the +1% drift cycle, and likewise overestimated the maximum force at subsequent drift levels. For negative drift levels, the response was much better. The ratio of predicted-to-observed lateral capacity at the −1% drift level was 0.937, and subsequent cycles followed the experimental response more closely than the equivalent cycles in the x-direction response.The mean ratio of predicted-to-observed strength over all y-direction cycles was 1.134 (CV 0.126).

Considering both x- and y-direction cycles, the mean ratio of predicted-to-observed strength over all cycles was 1.139 (CV 0.199). This metric was relatively high because of the overestimation of strength in the final three cycles, in some cases by a factor of two or more. If only cycles corresponding to 0.5–1.5% drift levels were considered, the mean ratio of predicted-to-observed strength over all cycles reduced to 0.980 (CV 0.042).

As reviewed in Chapter 2, Akgüzel also conducted numerical analysis of Specimen SP1 using the nonlinear finite element code MASA, which represents concrete failure using a microplane constitutive model [167]. Since this is the only other known simulation of any of the beam-column joints analyzed in the present study, the prototype model's previously described x-direction force-drift response was compared with

Table 5.2: Force-Displacement Metrics for Akgüzel Specimen

			Peak X-Direction Column Shear			Peak Y-Direction Column Shear		
Drift level	Cycle	Direction	EXP (kN)	FEA (kN)	FEA/EXP	EXP (kN)	FEA (kN)	FEA/EXP
0.5%	1	+	12.51	13.10	1.047	12.50	13.86	1.108
		-	-13.28	-15.88	1.196	-12.74	-15.10	1.185
	2	+	11.27	11.22	0.995	11.27	12.90	1.145
		-	-12.97	-12.90	0.994	-11.21	-11.39	1.017
1.0%	1	+	15.22	15.01	0.986	13.66	16.38	1.199
		-	-18.63	-19.69	1.057	-17.06	-15.98	0.937
	2	+	14.60	11.64	0.797	12.73	15.60	1.226
		-	-14.01	-11.09	0.792	-14.61	-10.81	0.740
1.5%	1	+	14.11	11.92	0.845	13.13	14.40	1.097
		-	-16.61	-18.40	1.107	-15.88	-14.41	0.907
	2	+	11.52	10.80	0.937	11.40	13.94	1.223
		-	-12.69	-6.19	0.488	-12.23	-6.08	0.497
2.0%	1	+	11.29	11.82	1.047	10.99	12.36	1.124
		-	-13.03	-13.40	1.029	-12.71	-12.14	0.955
	2	+	7.39	11.01	1.489	7.97	10.45	1.311
		-	-9.88	-4.55	0.460	-8.52	-5.06	0.594
2.5%	1	+	8.07	11.11	1.378	8.17	11.54	1.412
		-	-10.14	-13.44	1.326	-10.12	-12.11	1.197
	2	+	4.84	10.70	2.211	5.91	9.82	1.662
		-	-7.66	-4.65	0.607	-6.08	-5.50	0.905
3.0%	1	+	6.15	11.45	1.861	7.02	12.77	1.820
		-	-9.15	-13.40	1.464	-9.31	-12.30	1.322
	2	+	4.14	11.32	2.734	5.63	11.13	1.977
		-	-7.06	-4.15	0.587	-6.56	-4.37	0.666

X-Direction Cycles: MEAN = 1.143 CV = 0.281
Y-Direction Cycles: MEAN = 1.134 CV = 0.126
X- & Y-Direction Cycles (all): MEAN = 1.139 CV = 0.199
X- & Y-Direction Cycles (0.5-1.5% only): MEAN = 0.980 CV = 0.042

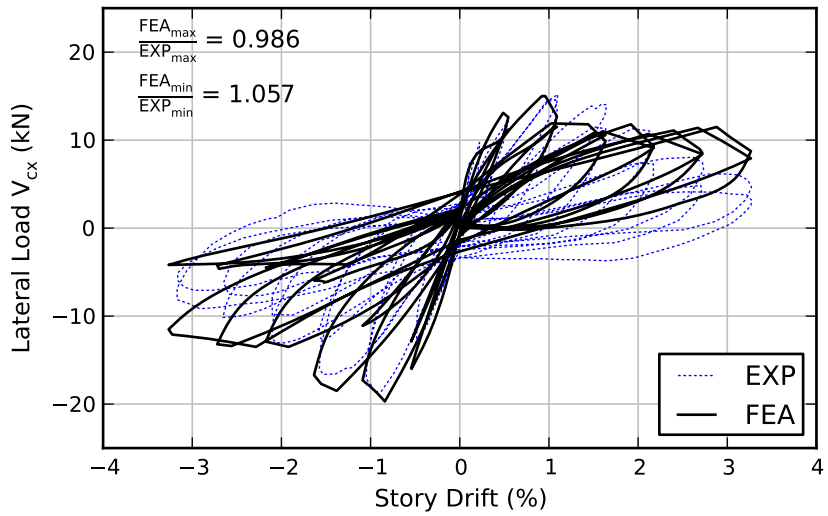

(a) X-direction

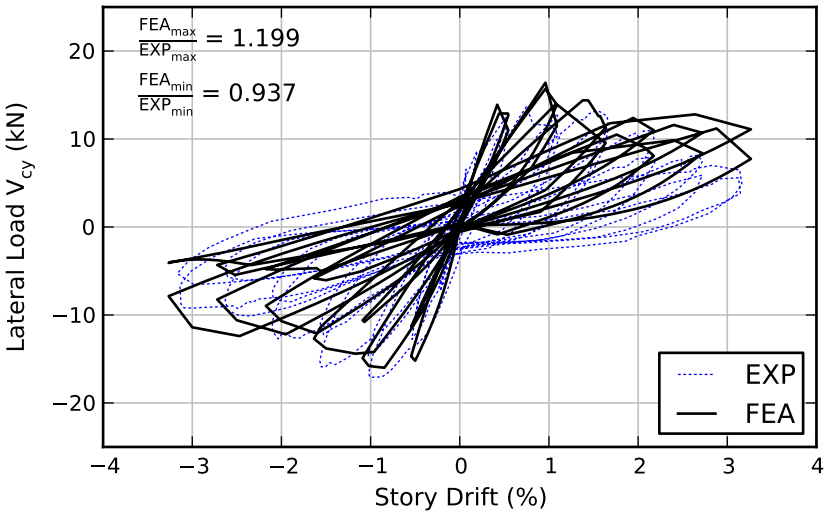

(b) Y-direction

Figure 5.23: Force-Drift Response for Akgüzel Specimen

Akgüzel's numerical response in Figure 5.24a-b; the y-direction response was not available. Akgüzel's simulation matched very well up to 0.5% drift in the pull direction, after which the response was underestimated by a margin of approximately 25%. Improved agreement in the push direction was observed up to a drift level of 2%. Numerical instabilities prevented Akgüzel's analysis from progressing beyond the 2% drift level. It is worth noting that Akgüzel simulated the initial 0.1 and 0.2% drift level cycles which the present study neglected in order to reduce computational cost. This may have contributed, together with selection of different constitutive models and mesh characteristics (Fig. A.59), to the differences in response between the prototype model response and Akgüzel's simulation.

A plot comparing the predicted bidirectional x- and y-direction lateral column shear forces with the experimental response is shown in Figure 5.25, clearly following the cloverleaf pattern of the prescribed displacement history. The response is somewhat symmetric about the line $V_{cx} = V_{cy}$. In Quadrant 1 (V_{cx} and $V_{cy} > 0$), the axial force decreased according to Equation 5.10, which reduced the joint confinement and lateral force capacity of the system. In Quadrant 2 (V_{cx} and $V_{cy} < 0$), the axial force increased according to Equation 5.10, which improved the joint confinement and lateral force capacity of the system. Both of these trends are evident in Figure 5.25.

The response quantities that follow were only reported by Akgüzel for the x-direction response in order to facilitate comparison with one-way joint tests. These include stiffness degradation, energy dissipation, and joint principal tension vs. joint shear distortion.

Stiffness degradation was quantified by peak-to-peak stiffness (K_{pp}) according to Equation 5.1. Two plots are shown: Figure 5.26a presents the peak-to-peak stiffness for the first cycle at each drift level (Quadrants 1–2), while Figure 5.26b presents the peak-to-peak stiffness for the second cycle at each drift level (Quadrants 3–4). Remarkable agreement was observed between predicted and observed response. Since the simulation

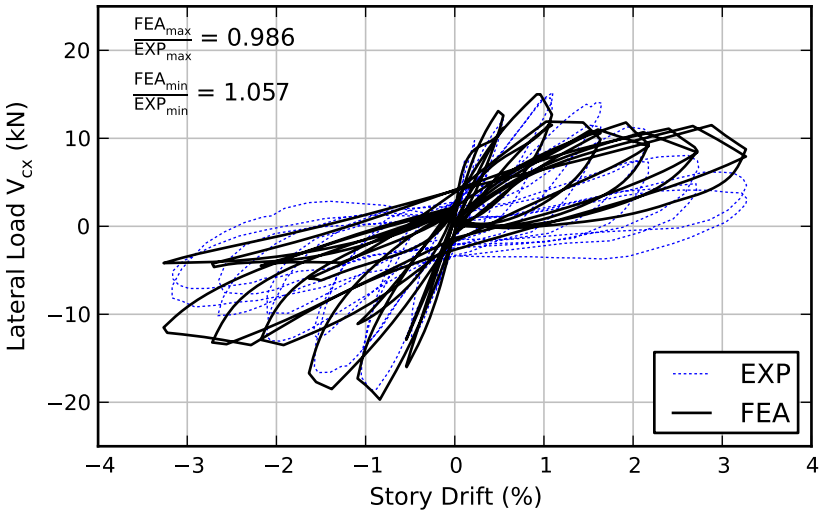

(a) x-direction force-drift response from present study

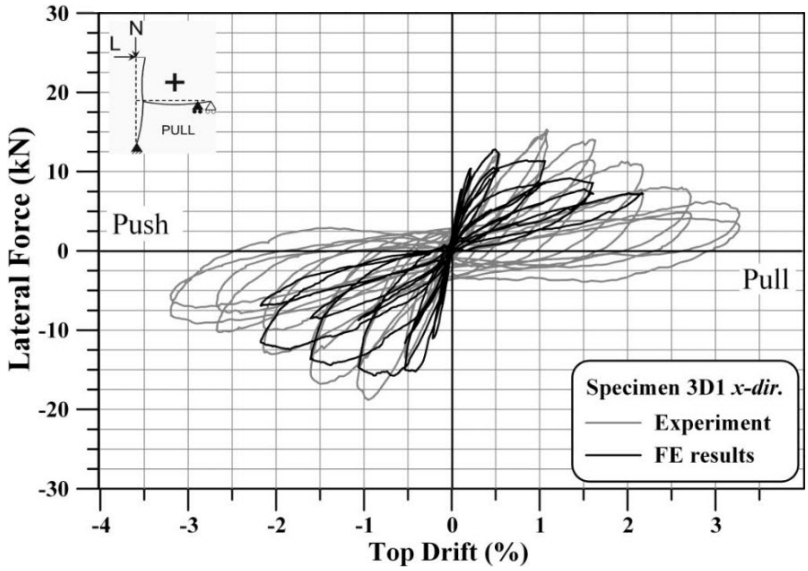

(b) x-direction force-drift response from FEA by Akgüzel et al. [9]

Figure 5.24: Comparison with FEA Conducted by Akgüzel

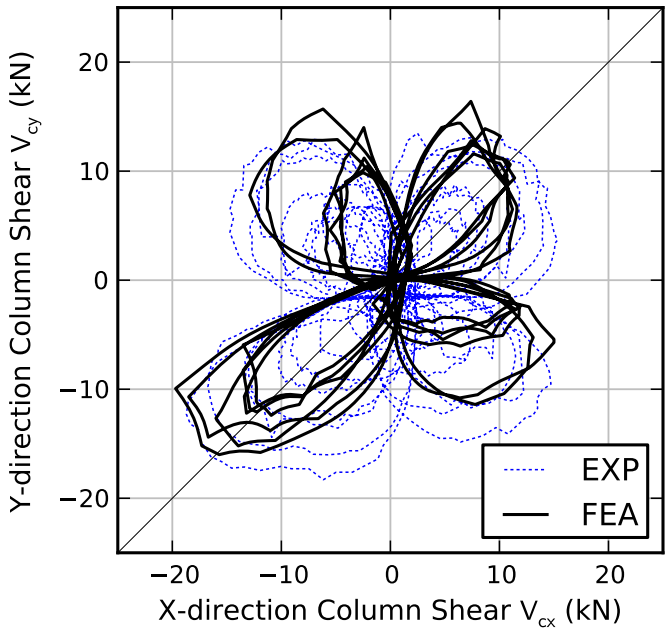

Figure 5.25: Column Shear Response for Akgüzel Specimen

did not include the 0.1 and 0.2% drift levels, the initial stiffness of the model was used to estimate K_{pp} at 0.1% for the first and second cycles.The mean ratio of predicted-to-observed peak-to-peak stiffness ratio over all x- and y-direction cycles was 1.139 (CV 0.199); this ratio is high primarily due to the overestimated stiffness during the initial and final cycles.

Energy dissipation was evaluated by computing the area enclosed by the force-drift hysteresis per cycle. Two plots are shown: Figure 5.27a presents the incremental energy dissipation for the first cycle at each drift level (Quadrants 1–2), while Figure 5.27b presents the incremental energy dissipation for the second cycle at each drift level (Quadrants 3–4). From these plots, it is evident that the simulation underestimated the energy dissipation in the system, particularly during the first cycles at the 1.0, 1.5, and 2.0% drift levels. The response was somewhat improved during the second cycles at each drift level, although the energy dissipation was underestimated during both cycles at 3.0% drift.

The cumulative energy dissipation in the system is shown in Figure 5.28. In this plot,

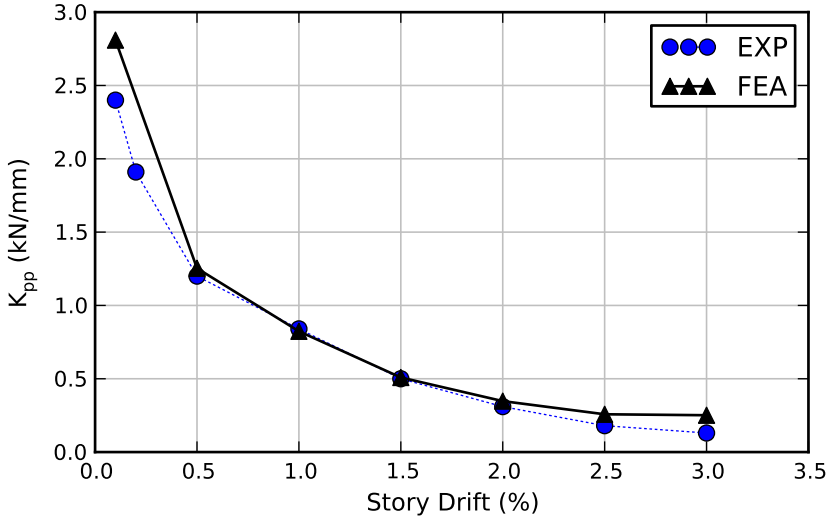

(a) First cycle response

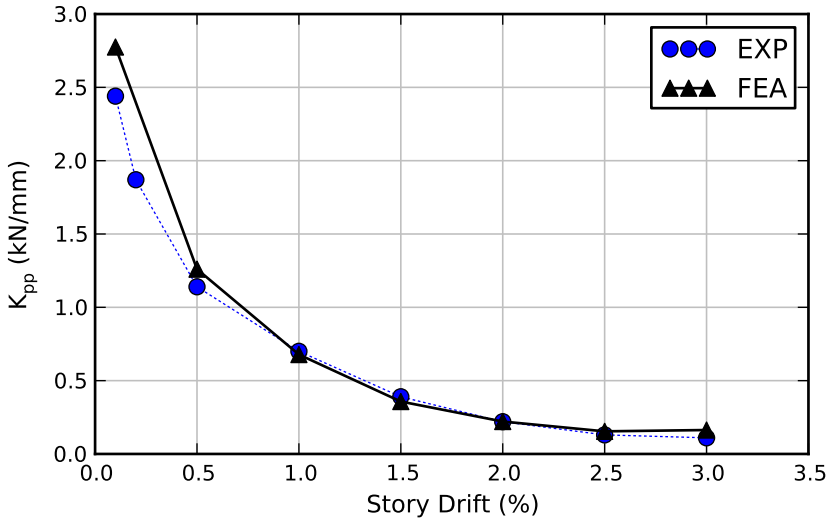

(b) Second cycle response

Figure 5.26: Stiffness Degradation (x-dir) for Akgüzel Specimen

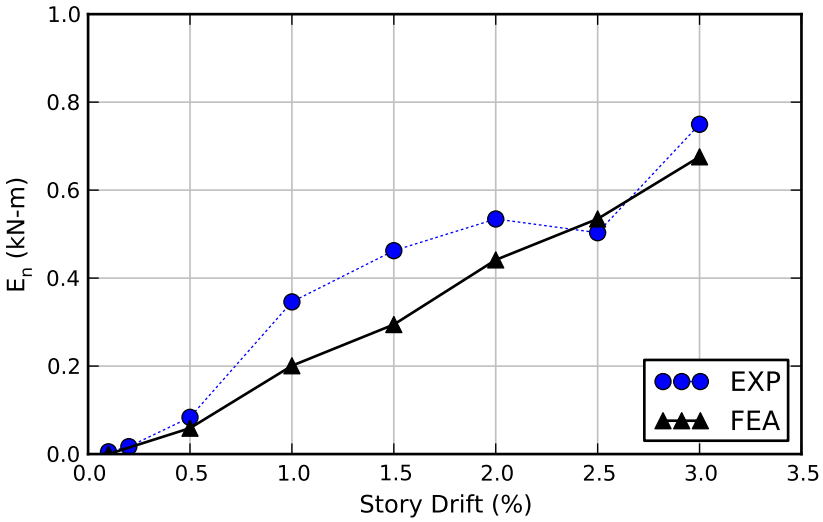

(a) First cycle response

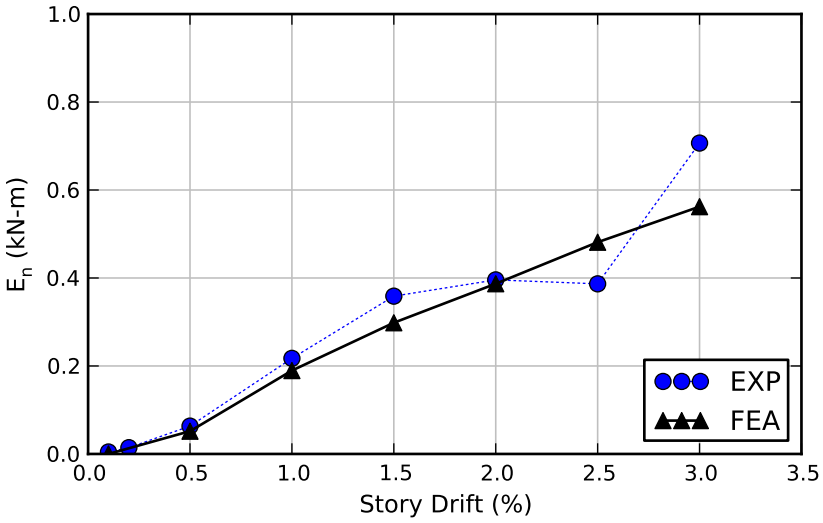

(b) Second cycle response

Figure 5.27: Energy Dissipation Per Drift Level (x-dir) for Akgüzel Specimen

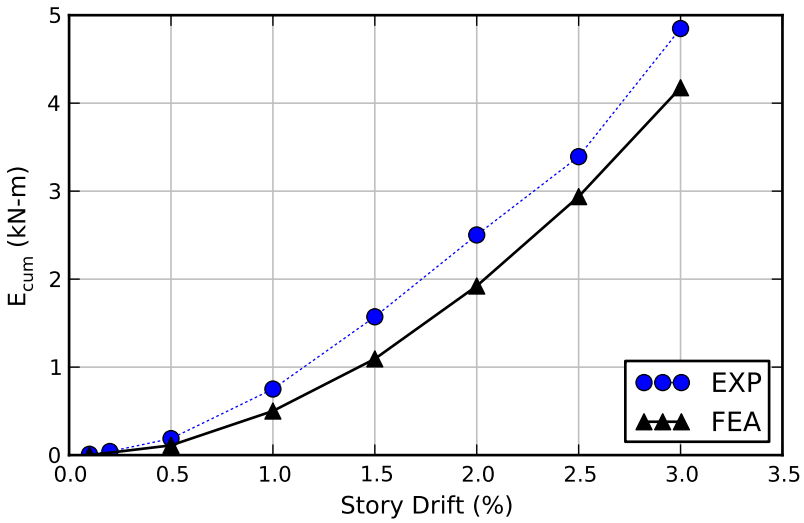

Figure 5.28: Cumulative Energy Dissipation (x-dir) for Akgüzel Specimen

the contribution of the full bidirectional load pattern is accounted for at each drift level (Quadrants 1–4). Thus, the total energy dissipated throughout the simulation can be compared with the experimental response by considering the final point at 3.0% drift. The ratio of predicted-to-observed total energy dissipation was 0.861, indicating good overall agreement considering the difference exhibited on a per-cycle, incremental basis. This estimate likely would have improved slightly had the 0.1 and 0.2% drift levels been included in the simulation.

The shear response of the joint was evaluated by comparing the principal tensile stress in the joint core with the joint shear distortion, following the procedure outlined by Akgüzel [9]. Joint shear distortion was computed using Equation 5.6. Principal tensile stress is derived from the column axial force and joint shear force. The nominal compressive stress in the column at the joint mid-height is computed as

$$f_v = \frac{N_v}{h_c b_c} \tag{5.11}$$

where N_v is the column axial force, b_c is the width of the column, and h_c is the width of the joint. The joint shear stress τ_{jh} is determined from Equation 5.4. Principal tensile

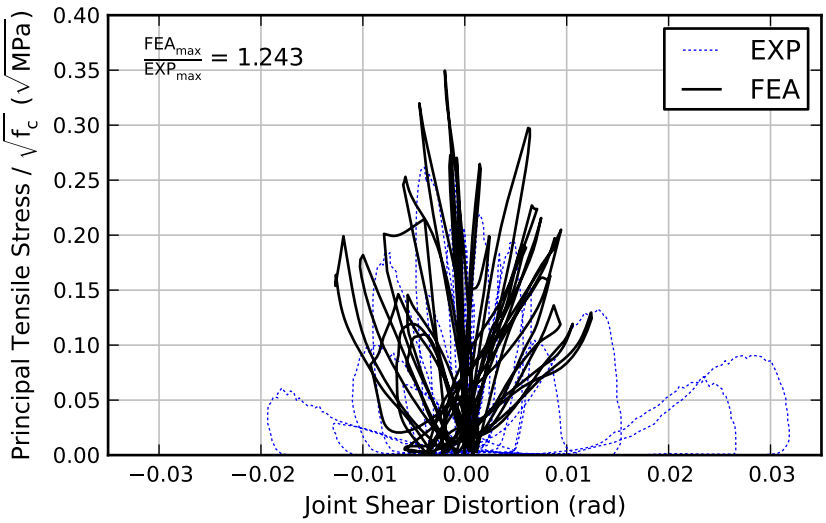

Figure 5.29: Joint Shear Response for Akgüzel Specimen

stress p_t is then computed using Mohr's circle as

$$p_t = -\frac{f_v}{2} \pm \sqrt{\left(\frac{f_v}{2}\right)^2 + \tau_{jh}^2} \tag{5.12}$$

and is often normalized by $\sqrt{f_c'}$. A plot of the normalized principal tensile strain vs. joint shear distortion is shown in Figure 5.29. The ratio of maximum predicted-to-observed principal tensile stress was 1.243. Reasonable agreement was observed for the predicted joint shear distortion values until the final four cycles were reached. During these final cycles as the joint exhibited excessive damage, the ratio of maximum predicted-to-observed joint shear distortion was 2.58.

Figure 5.30 presents a comparison of the final damaged state from the experiments with the crack pattern predicted by the finite element model corresponding to the final cycle at the maximum drift level of 3.0%. Good agreement was observed between the overall extent and concentration of damage, orientation of diagonal cracks within the joint core, and with the vertical bands of cracks which formed in the beams (particularly evident in the numerical response of the x-direction beam).

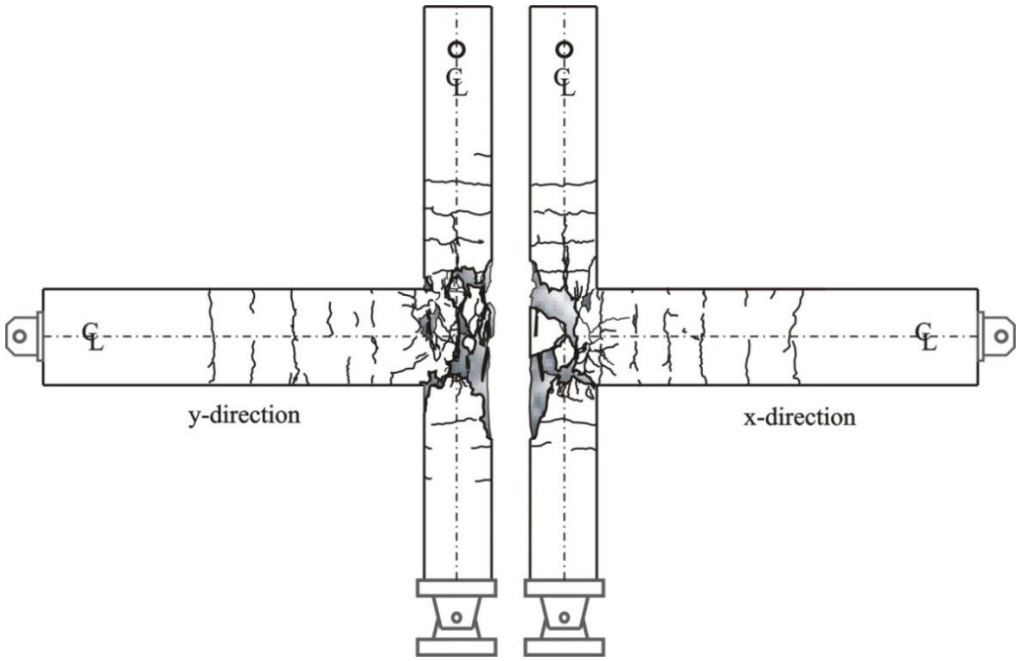

(a) Experimental Crack Pattern. *Source*: Akgüzel [9]

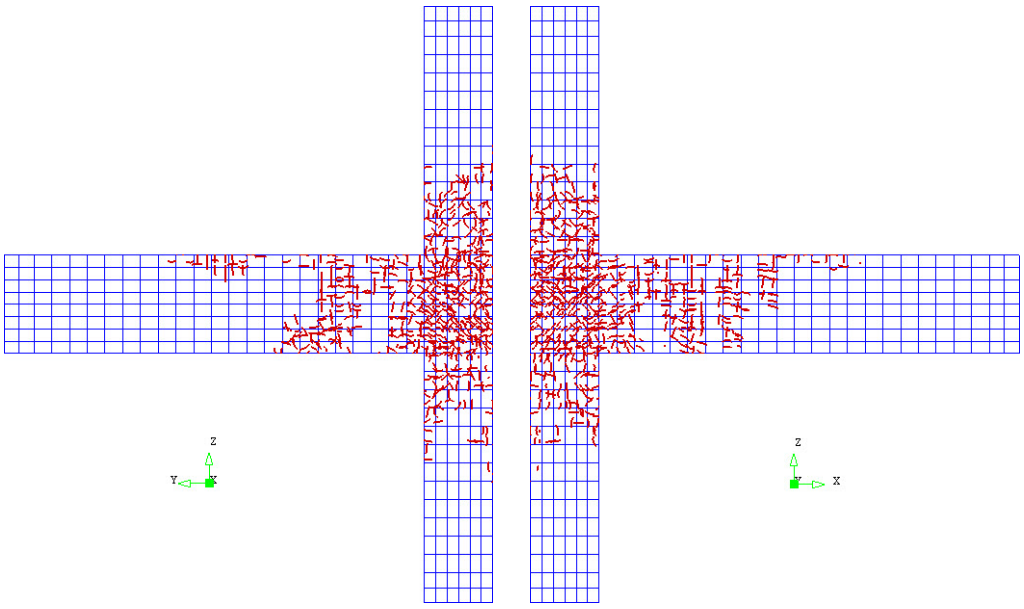

(b) Predicted Crack Pattern.

Figure 5.30: Predicted Crack Pattern for Akgüzel Specimen

5.4 Two-Way Beam-Column-Slab Joint – Park et al. [179]

An experimental program conducted by Park and Mosalam [179, 180] was chosen to evaluate the ability of the prototype model to simulate a nonseismically detailed reinforced concrete exterior corner beam-column joint with integral slab, subjected to bidirectional and cyclic axial loading. The introduction of the slab makes this a logical step after analyzing the joint tested by Akgüzel and Pampanin, described in Section 5.3.

This series of experiments was performed in the NEES laboratory at the University of California, Berkeley.

5.4.1 Description of Experiments

Park and Mosalam investigated the response of four full-scale reinforced concrete corner building joints which lacked transverse reinforcements as the primary seismic deficiency. Specimen SP2 was chosen for the present study.

The dimensions of specimen SP2 are shown in Figure 5.31. The system was designed according to the strong column/weak beam philosophy, with a ratio of column-to-beam flexural capacity of 1.9. The high beam reinforcement ratio was intended to generate shear failure in the joint core prior to yielding of beam longitudinal reinforcements. Column reinforcements were designed to remain elastic until after beam yielding occurred. The joint core had an aspect ratio of 1.0. The beam was reinforced with four M25 (#8) bars on the top surface and four M22 (#7) bars on the bottom surface. Both bottom and top beam longitudinal bars were anchored with 90° hooks. The column contained eight M32 (#10) bars equally spaced around the column perimeter. Both the column and beams were reinforced with M10 (#3) bars on 76 mm (3") centers; this high level of shear reinforcement was intended to prevent shear and torsion failures away from the joint. The slab was 152.4 mm (6") deep and was reinforced with M10 (#3) bars on 305 mm (12") centers. Top slab bars were anchored in the beam with 90° hooks, while bottom bars had a straight anchorage length of 152.4 mm (6"). The high

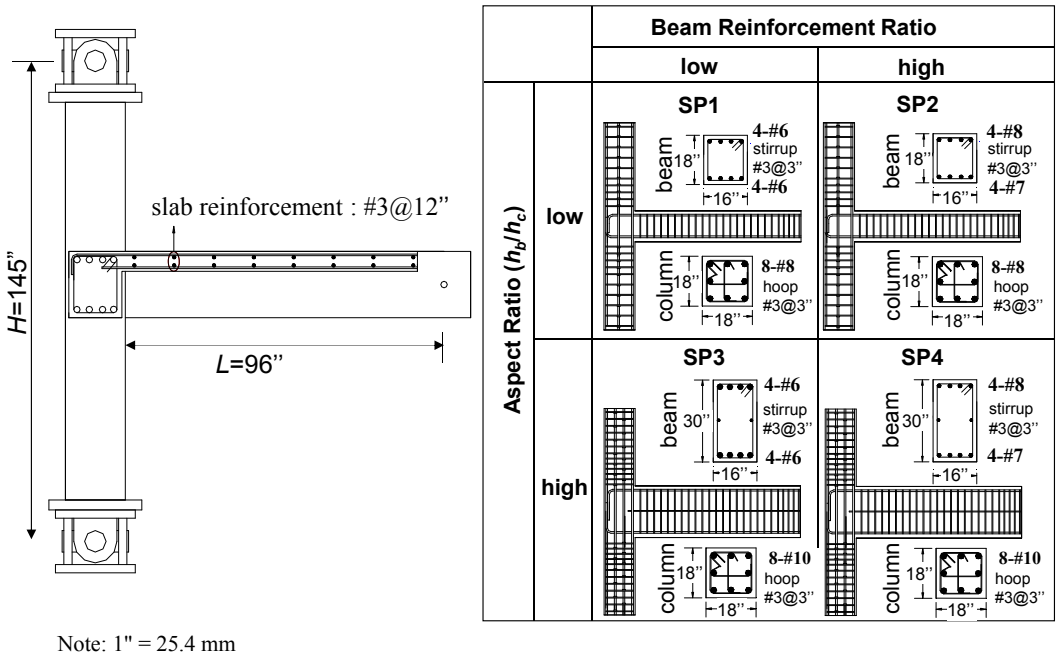

Source: Park [179]

Figure 5.31: Dimensions of Park Specimen

level of beam and column reinforcement resulted in a congested configuration in the joint core. The concrete had a measured compressive strength of 24.3 MPa (3530 psi) and a splitting tensile strength of 2.34 MPa (340 psi). The yield stress of the reinforcing bars ranged from 471–507 MPa (68.3–73.5 ksi).

An illustration of the experimental set-up is provided in Figure 5.32. The “lateral loads” were applied in displacement control at the beam ends, while the column axial load was applied in force control at the top of the column. Both the base and the top of the column were supported by bi-directional swivels which allowed rotation about the x– and y-axes. A lateral restraining frame was used to prevent lateral movement of the column top. Two 120-kip capacity actuators were used to load the beam ends, while two 360-kip capacity actuators were used to apply column axial force via a built-up box section located above the column.

A cyclic displacement-controlled loading history was applied to the beam ends. To simulate the initial gravity load configuration at the beginning of the experiment, both

beam ends were displaced downward a distance of $\Delta_0 = \frac{\Delta_y}{4}$, where Δ_y was the estimated displacement to cause yielding of the beam. This displaced configuration was the reference point about which cyclic displacement excursions were applied at a total of seven increasing displacement levels of 0.25, 0.5, 0.75, 1.25, 2.0, 3.125, and 4.813 times the displacement at first yield, Δ_y, which was 31.5 mm (1.24") for specimen SP2. At each displacement level, two full reversed cycles were applied to each beam separately while the other was held at constant displacement; the x-direction beam was cycled twice first, followed by the y-direction beam.

A cyclic column axial force history was determined to accompany the beam end load history with values which would be expected due to overturning effects in an earthquake. A nonlinear frame analysis was completed using the software OpenSEES to simulate the response of a prototype building with detailing consistent with the experimental joint subassemblages (the Van Nuys Holiday Inn building, damaged during the 1994 Northridge earthquake). This model was used to determine a relation between beam end shear forces and column axial load from a pushover analysis. Based on these results, the cyclic column axial force was applied according to the equation

$$P_{col} = 422.56 - 4V_{bx} - 4V_{by} \qquad \text{(kN)} \tag{5.13}$$

where P_{col} is the column axial force (positive for compression in this equation), and V_{bx} and V_{by} are the beam end forces in the x- and y-directions, respectively. Positive beam end forces resulted in a reduced column axial force, while negative beam end forces resulted in an increased column axial force. During the experiment, the values of V_{bx} and V_{by} were recorded in each load increment and used to automatically adjust the column axial force according to Equation 5.13.

The failure of the joint progressed as follows. The initial cycles resulted in flexural cracking in the beams and slab, as well as an initial splitting crack at the beam-joint interface. The first "x"-style diagonal cracking of the joint panel occurred during the 0.3–1.0% displacement cycles, and was immediately followed by first yielding of the

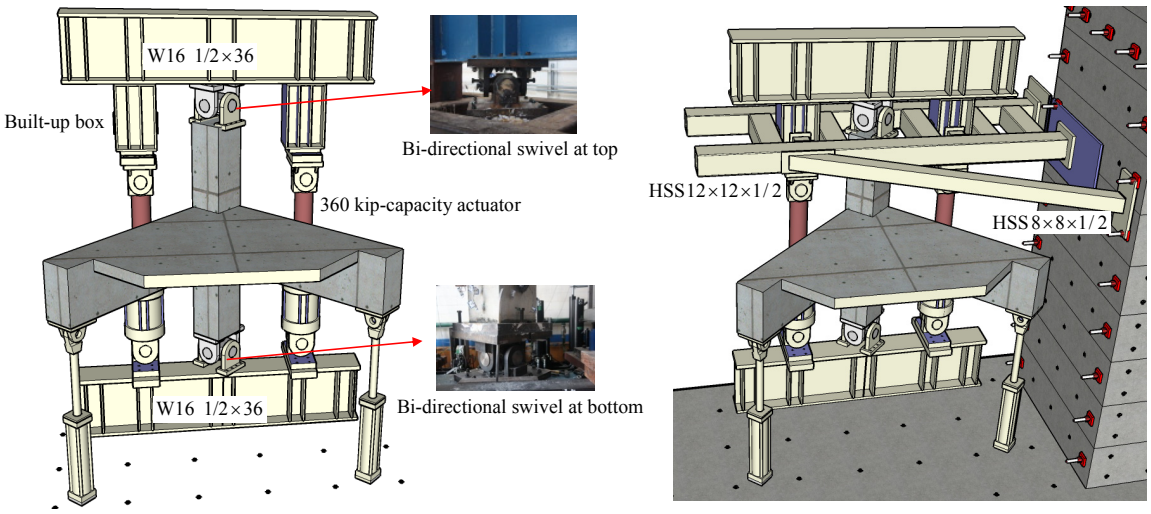

Source: Park [179]

Figure 5.32: Experimental Setup for Park Specimen

beam top and bottom reinforcements in the 1–2% displacement level range. The diagonal joint cracks continued to widen in each cycle until the 5% displacement level, at which point the joint cover began spalling. As localized damage increased in the joint core, flexural crack widths in the beams and slab reduced. Crushing of the joint core concrete occurred during the final cycles.

5.4.2 Finite Element Model

A detailed finite element model was developed to simulate the response of Specimen SP2 from Park and Mosalam [179]. The model contained approximately 5000 eight-node brick elements. The prototype constitutive model was applied to the entire concrete mesh except for regions near the supports at the column and beam ends, which were modeled with high elastic stiffness (1×10^7 MPa) to better distribute concentrated effects arising from support reactions and applied loads. The concrete mesh is shown in Figures 5.33–5.34. The column cross-section was discretized with an 8×8 element mesh, the beam with a 6×6 element mesh, and the slab with two layers of elements through the depth of the deck.

Reinforcements were modeled by approximately 550 reinforcing bar segments. All

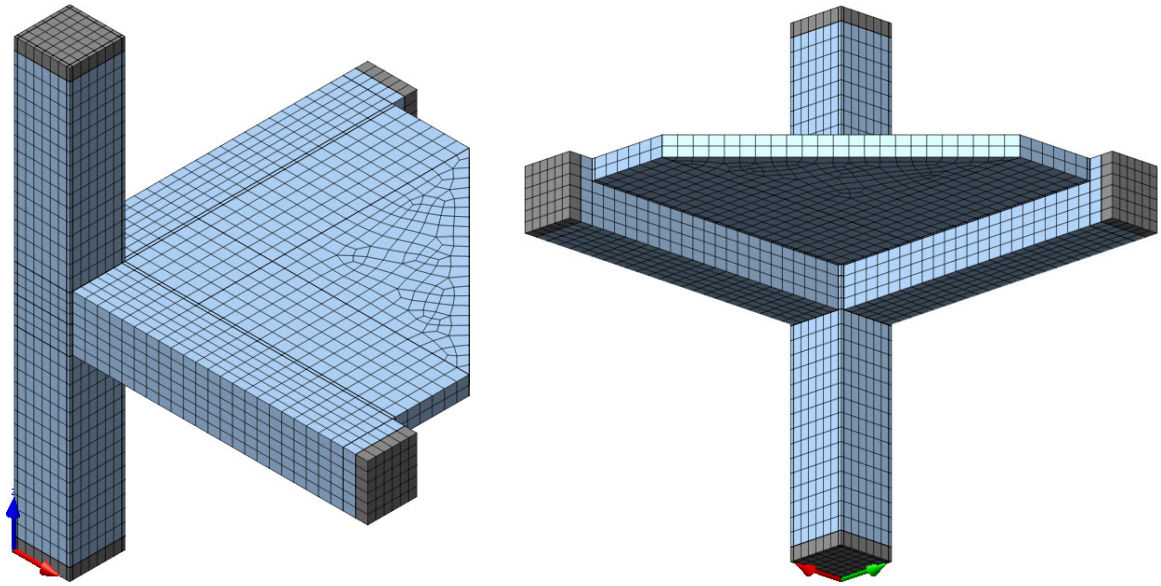

Figure 5.33: Finite Element Mesh for Park Specimen

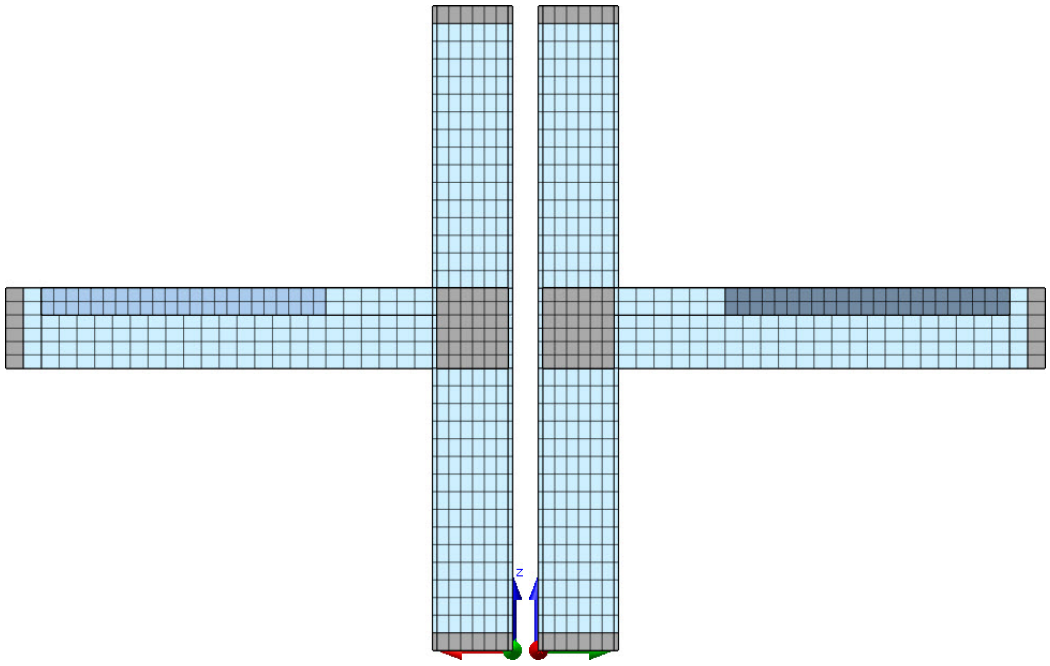

Figure 5.34: Finite Element Mesh for Park Specimen – Elevation Views

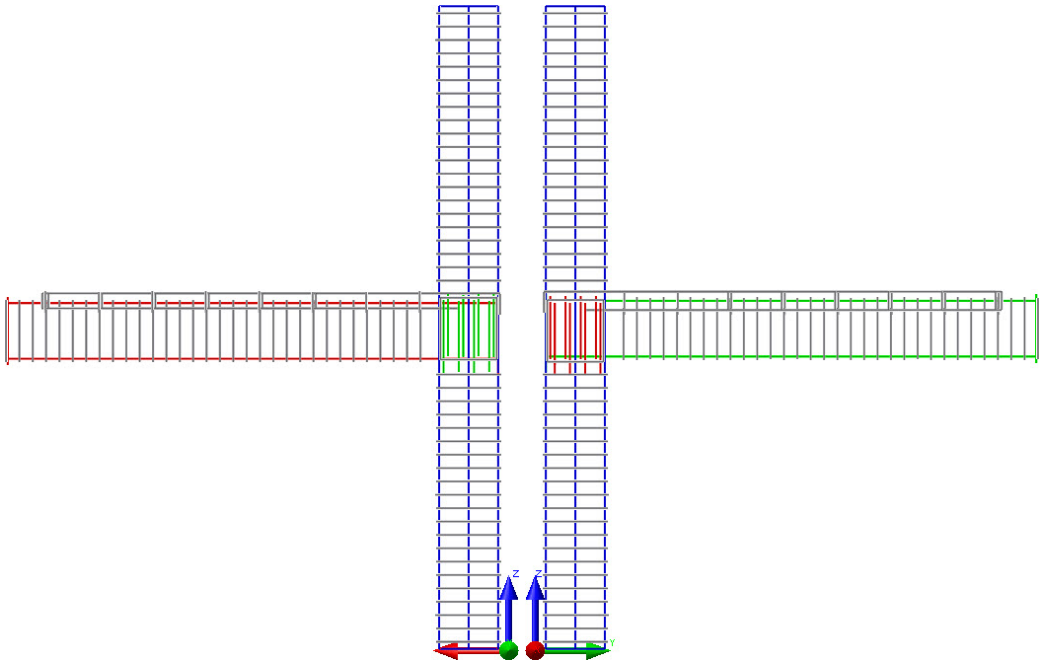

Figure 5.35: Reinforcing Bar Mesh for Park Specimen – Elevation Views

reinforcements were modeled using truss elements and were connected to the concrete mesh using nonlinear interface bond-slip elements. The bond-slip law followed the CEB-FIP Model Code 1990 [30] law for the classification "good/confined," due to the high level of confinement in the beams and column provided by transverse reinforcements. Care was taken to shift reinforcement locations to the exact locations they were placed experimentally due to congestion in the joint core. The configuration of reinforcing bars in the column, beams, and slab is shown in Figures 5.35–5.37.

The structure was supported at the ends of the column and beams at a single node at the centroid of the face of the member. The column base was free to rotate, but translations were restrained in all directions. The column top was free to translate vertically and rotate about any axis, but x- and y-direction translations were restrained. The beam ends were free to translate in the direction of its respective longitudinal axis, but out-of-plane translations were restrained together with the vertical translation (which was used to apply the beam cyclic load via vertical support displacements).

The beam ends were cycled in displacement control corresponding to the first cycle

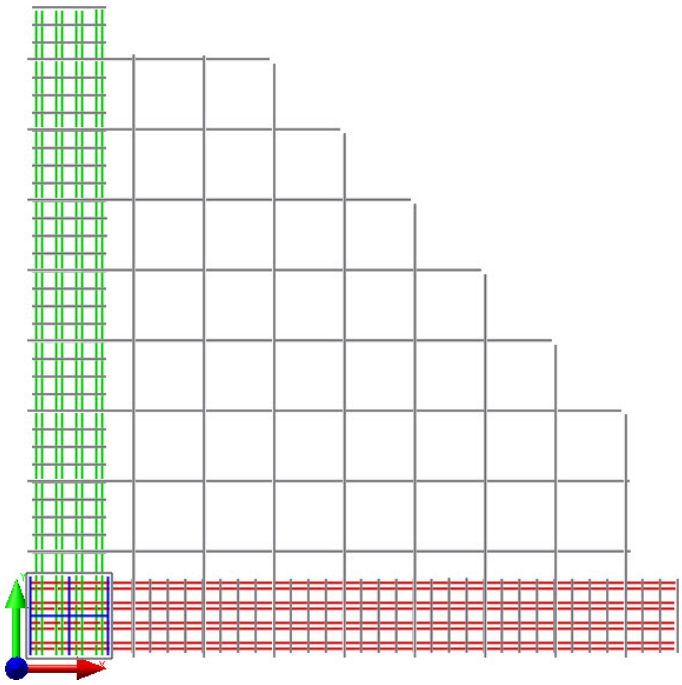

Figure 5.36: Reinforcing Bar Mesh for Park Specimen – Plan View

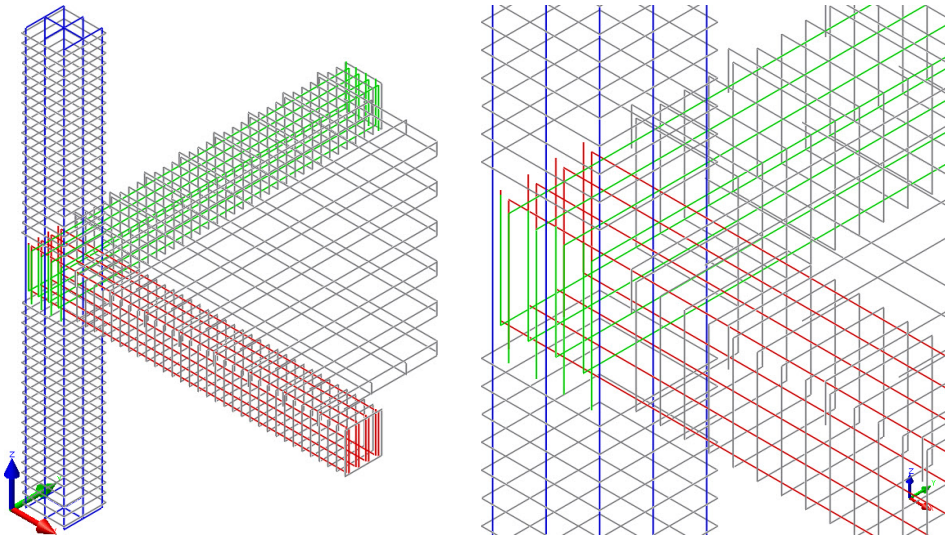

Figure 5.37: Reinforcing Bar Mesh for Park Specimen – Isometric View and Joint Detail

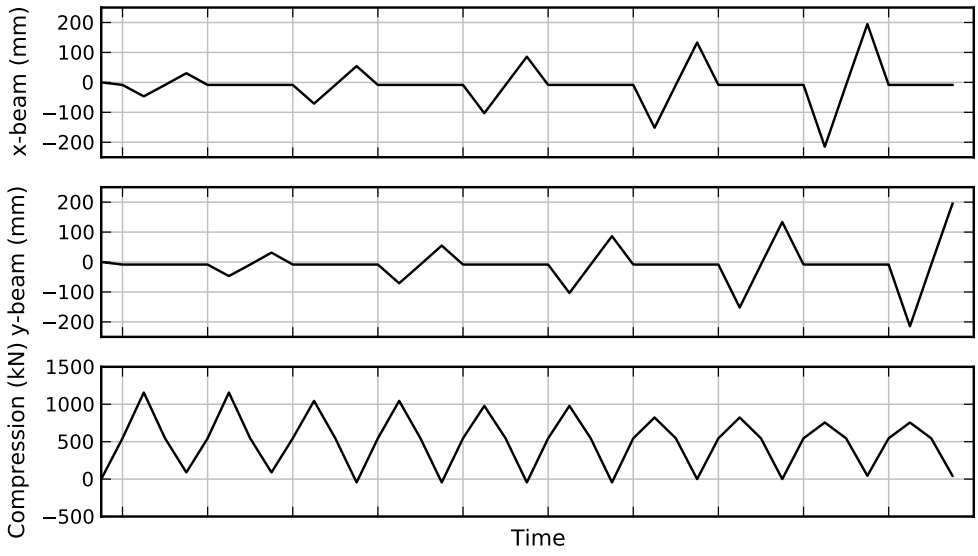

Figure 5.38: Loading History for Simulation of Park Specimen

of the last five displacement levels applied in the experiment; the second cycle at each level was neglected to reduce the computational cost. In the initial load case, the beam ends were displaced downward to the gravity configuration, and then the x- and y-direction beam ends were alternatingly cycled at increasing displacement levels for a total of five reversed cycles per beam while the other was held constant at the initial gravity datum.

Similar to the simulation of the joint tested by Akgüzel and Pampanin, there was no means to apply a column axial force as a function (Equation 5.13) of numerically-determined beam end forces during the analysis. As such, the measured peak axial forces obtained during each cycle of the experiment were used as input values for the cyclic column compression force. The DIANA load input was generated using a Python script, which is included in Section B.8.1. The resulting combined loading history including beam end displacements and column compression force is shown in Figure 5.38.

The analysis consisted of approximately 1300 load increments, which corresponded to a solution time of approximately nineteen hours. The DIANA material definition for this model is provided in Section B.8.2.

Table 5.3: Force-Displacement Metrics for Park Specimen

		Peak X-Beam End Force			Peak Y-Beam End Force		
Cycle	Direction	EXP (kN)	FEA (kN)	FEA/EXP	EXP (kN)	FEA (kN)	FEA/EXP
1	-	-160.00	-159.70	0.998	-168.03	-150.72	0.897
	+	106.10	92.99	0.876	101.92	88.45	0.868
2	-	-164.07	-167.03	1.018	-169.39	-164.65	0.972
	+	130.60	123.12	0.943	129.14	116.62	0.903
3	-	-162.70	-170.84	1.050	-150.40	-147.42	0.980
	+	137.77	126.61	0.919	125.59	99.65	0.793
4	-	-130.42	-114.38	0.877	-103.29	-56.40	0.546
	+	126.72	102.76	0.811	100.46	85.71	0.853
5	-	-87.20	-69.67	0.799	-76.53	-55.50	0.725
	+	106.40	91.36	0.859	83.05	78.89	0.950
		X-Direction Cycles:		MEAN = 0.915	CV = 0.007		
		Y-Direction Cycles:		MEAN = 0.849	CV = 0.018		
		X- & Y-Direction Cycles (all):		MEAN = 0.882	CV = 0.013		

5.4.3 Discussion of Results

The force-displacement response of the beam-column joint in the x- and y-directions is shown in Figures 5.39a and 5.39b. Good agreement was observed between the experimental and numerical response. The peak force values achieved in each cycle are reported in Table 5.3. For the x-direction beam, the ratio of peak predicted-to-observed beam end force for positive and negative displacement levels was 0.919 and 1.050, respectively, while for the y-direction beam, the ratio of peak predicted-to-observed beam end force for positive and negative displacement levels was 0.903 and 0.972. The mean ratio of predicted-to-observed strength over all x-direction cycles was 0.915 (CV 0.007). The mean ratio of predicted-to-observed strength over all y-direction cycles was 0.849 (CV 0.018), lower due to the overly degraded numerical response in the final negative cycles. Considering all x- and y-direction cycles, the mean ratio of predicted-to-observed strength over all y-direction cycles was 0.882 (CV 0.013).

A comparison of stiffness degradation between the model and experiment is presented in Figure 5.40. The peak-to-peak stiffness at each drift level shows excellent

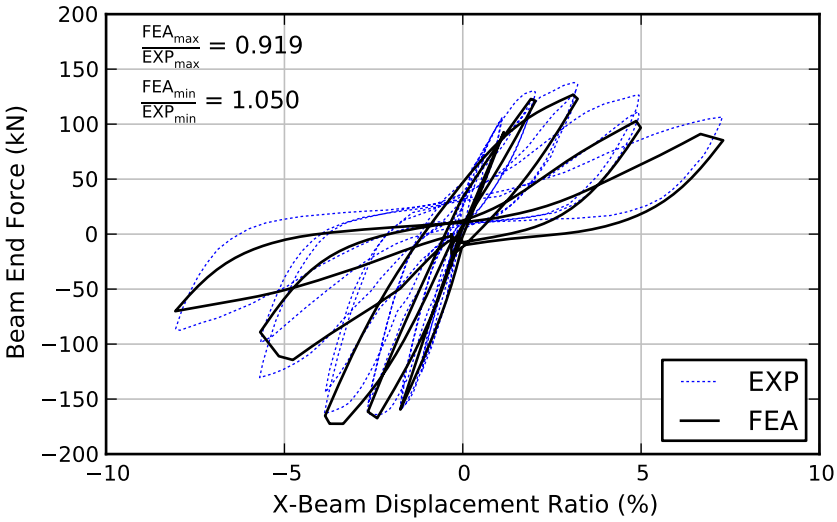

(a) X-direction

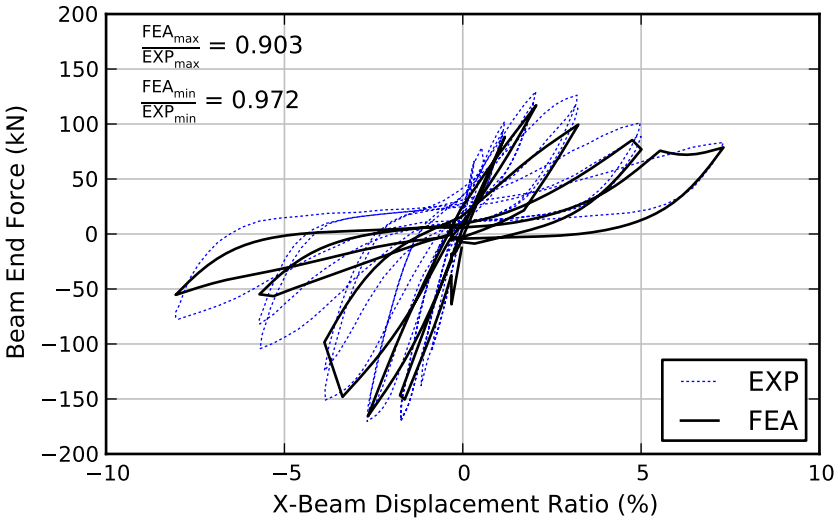

(b) Y-direction

Figure 5.39: Force-Drift Response for Park Specimen

agreement with experimental results. For x-direction cycles, the model slightly over- or underpredicted the stiffness depending on the cycle, resulting in a mean predicted-to-observed stiffness ratio of 0.974 (CV 0.008). For y-direction cycles, the model slightly underestimated the stiffness at all displacement levels, resulting in a lower mean predicted-to-observed stiffness ratio of 0.864 (CV 0.006). For both x- and y-direction cycles, the mean predicted-to-observed stiffness ratio was 0.920 (CV 0.011).

Energy dissipated per cycle is compared with the corresponding first-cycle values from the experiment in Figure 5.40. From this figure, it is evident that the model underestimated the energy dissipation during each cycle except for the cycle corresponding to a displacement ratio of 3.0%. The total effect of this underestimation is shown in Figure 5.41, which compares the cumulative energy dissipation from the numerical model with the cumulative energy dissipation from the experiment considering first-cycle values. At the end of the simulation, the ratio of predicted-to-observed total energy dissipation was 0.809, indicating the model underestimated the total energy by about 19%. As exhibited in the experiment, more energy is dissipated in x-direction cycles than in y-direction cycles in the analytical results, especially in the final two cycles in both directions.

Normalized joint shear stress τ'_{jh} was computed and compared with the experimental response in the x- and y-directions, shown in Figure 5.43. The ratio of predicted-to-observed joint shear stress for x-beam loading was 0.982 for downward beam displacement and 0.914 for upward beam displacement. The ratio of predicted-to-observed joint shear stress for y-beam loading was 0.947 for downward beam displacement and 0.853 for upward beam displacement. The prototype model showed good agreement with joint shear distortion during the first three cycles, but significantly overestimated distortion by as much as 2-3x in subsequent cycles, during which significant joint damage was accumulating.

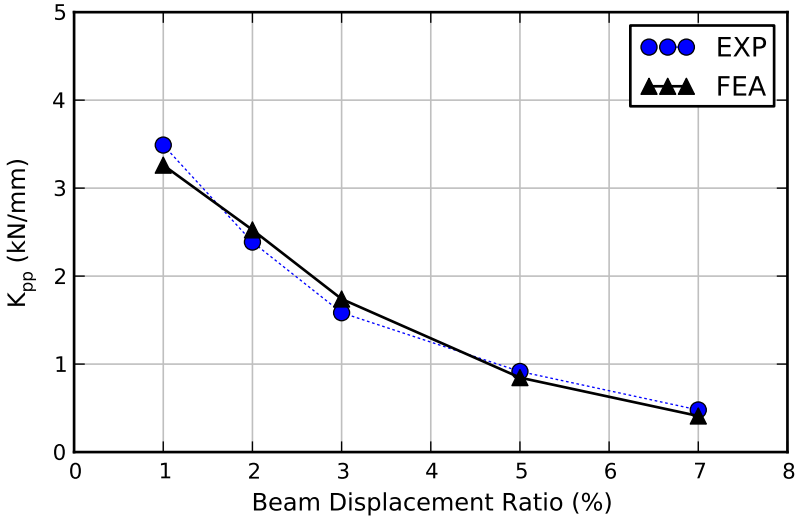

(a) X-direction (experimental 1st cycle only)

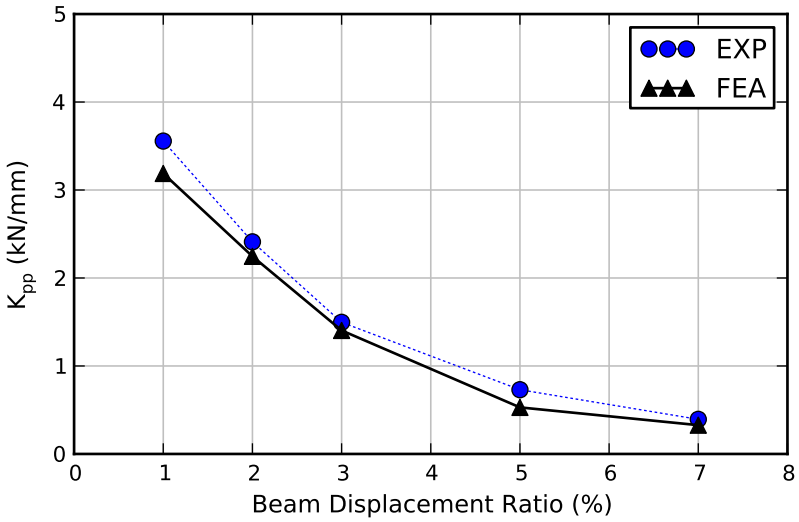

(b) Y-direction (experimental 1st cycle only)

Figure 5.40: Stiffness Degradation for Park Specimen

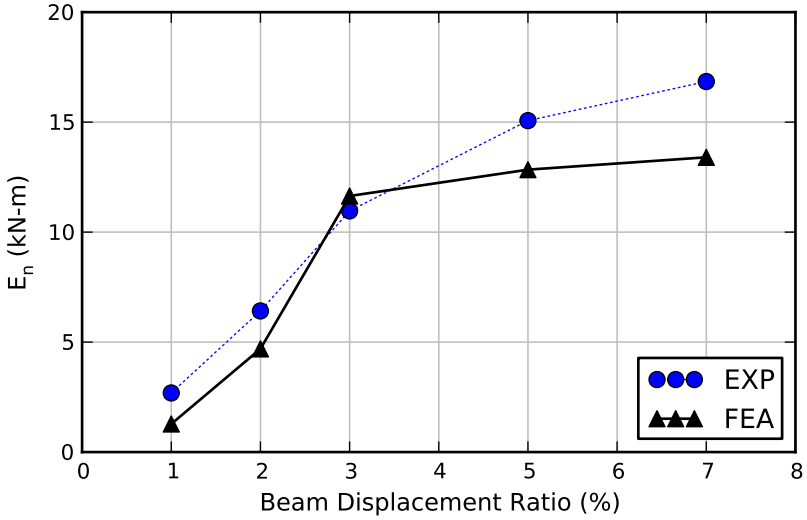

(a) X-direction (experimental 1st cycle only)

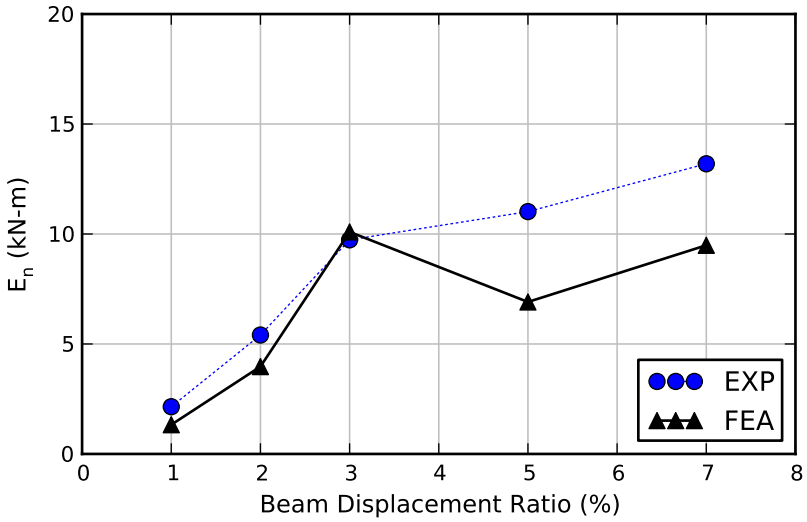

(b) Y-direction (experimental 1st cycle only)

Figure 5.41: Incremental Energy Dissipation for Park Specimen

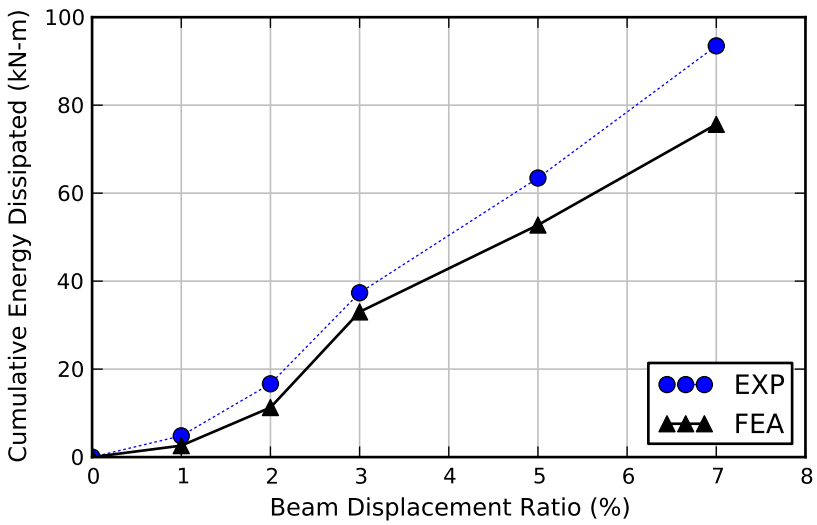

(experimental 1st cycle only)

Figure 5.42: Cumulative Energy Dissipated for Park Specimen

A comparison of predicted-to-observed crack patterns at different load levels is presented in Figures 5.44–5.48. These comparisons show that the response of the simulation was less localized than the failure processes in the actual joint. Figures 5.44 and 5.45 show the cracking on the xz- and xz-faces of the joint immediately prior to joint shear failure, for both downward and upward beam end loading. The trends of the primary diagonal shear cracks were reproduced in bands of smeared cracks from the models. The final crack patterns on the exterior faces of the beams are shown in Figure 5.46. Again, general agreement can be inferred for the diagonal beam longitudinal cracks, as well as for the concentration of damage at the beam-joint interface. Figure 5.47 depicts the cracking patterns on the surface of the slab as well as the slab-column interface. While the experiments showed a grid of cracks roughly parallel to slab reinforcements, the simulation predicted a uniform distribution of hairline cracks. The spalling of concrete in the column immediately above the slab was represented by a concentration of larger cracks in the model. Figure 5.48 shows the final configuration of the specimen after the test was concluded, with all loose concrete removed; the distribution of final cracks in the column and beams is not visible in this photograph. In the simulation, the largest

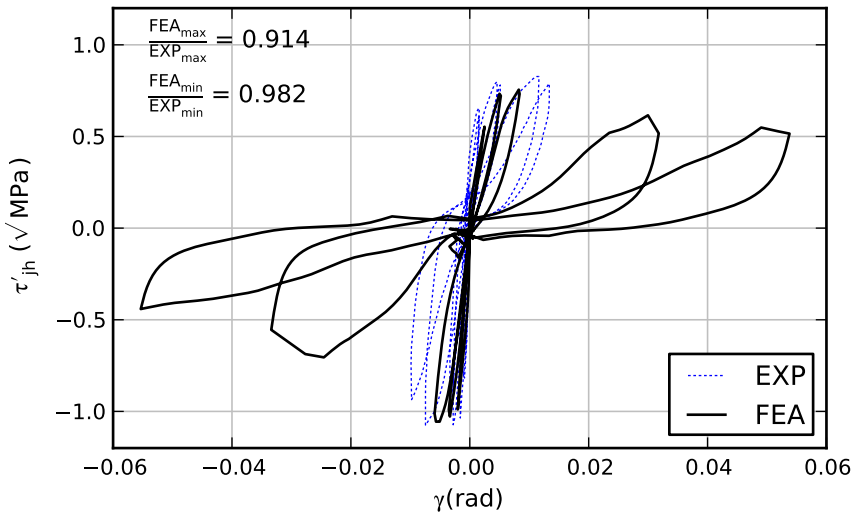

(a) X-direction

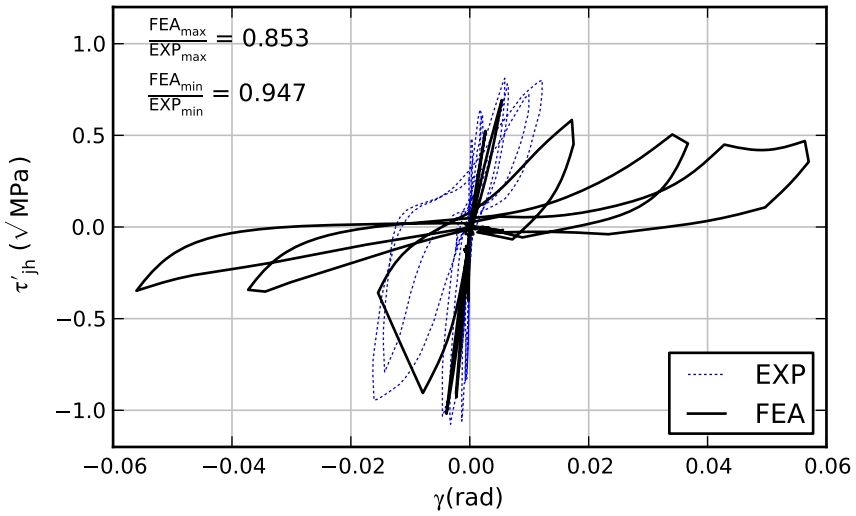

(b) Y-direction

Figure 5.43: Joint Shear Response for Park Specimen

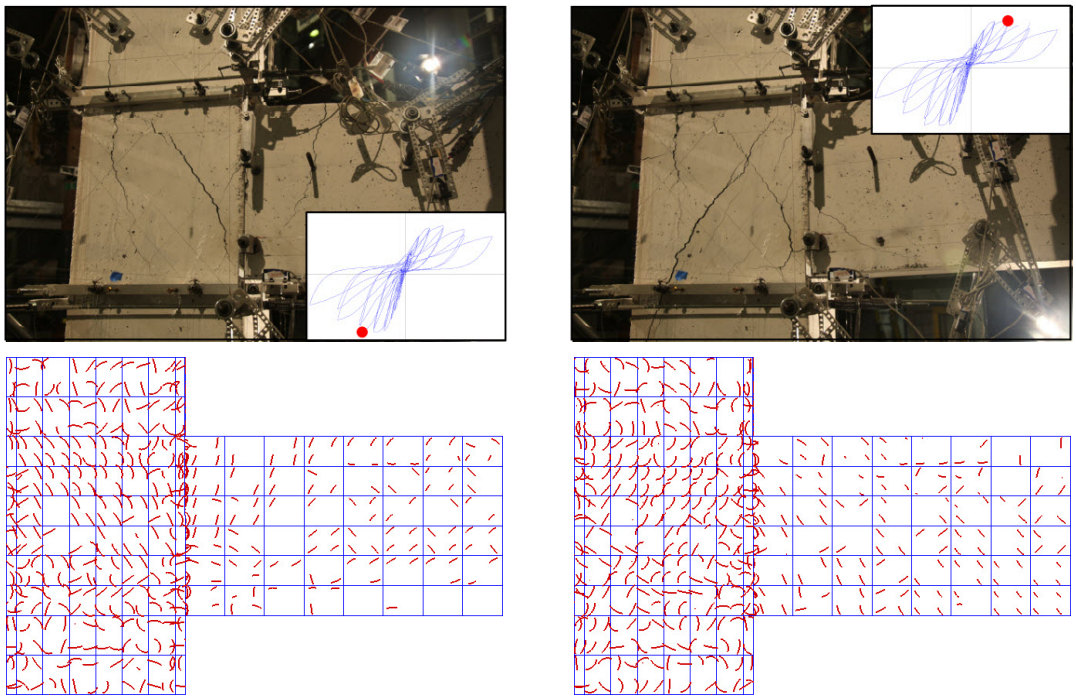

Figure 5.44: XZ-Face Joint Crack Pattern Prior to Failure for Park Specimen

crack strains occurred within the joint region, but the response was not as localized as in the experiment, evident by the continuation of cracking much further into the column.

5.5 Two-Way Beam-Column-Slab Joint – Engindeniz et al. [60]

The final beam-column joint chosen for analysis was selected from a suite of experiments conducted by Engindeniz, Kahn, and Zureick [60, 62] at the Georgia Institute of Technology Structures Laboratory. This joint was similar to the specimens investigated by Park and Mosalam in that it represented an exterior corner beam-column joint with integral slab subjected to bidirectional cyclic loading, but it possessed additional seismic deficiencies beyond those considered by Park, resulting in a significantly more complex and less ductile response. These seismic deficiencies amount to what may be considered a "worst-case" scenario for performance of a gravity load-designed joint subjected to lateral forces.

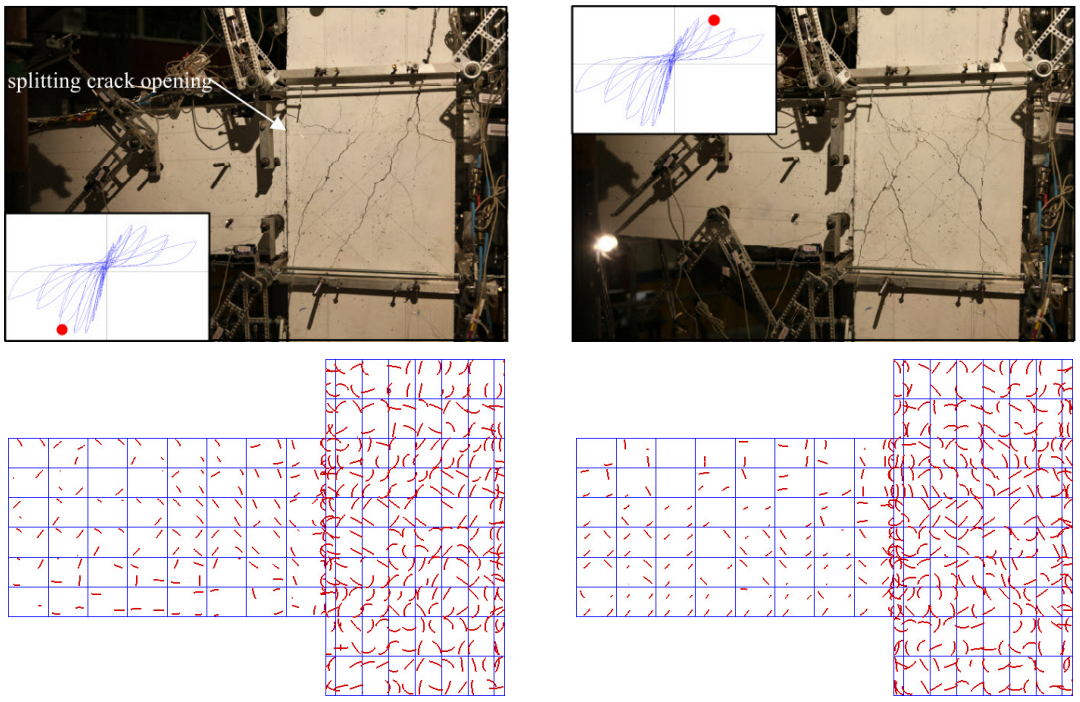

Figure 5.45: YZ-Face Joint Crack Pattern Prior to Failure for Park Specimen

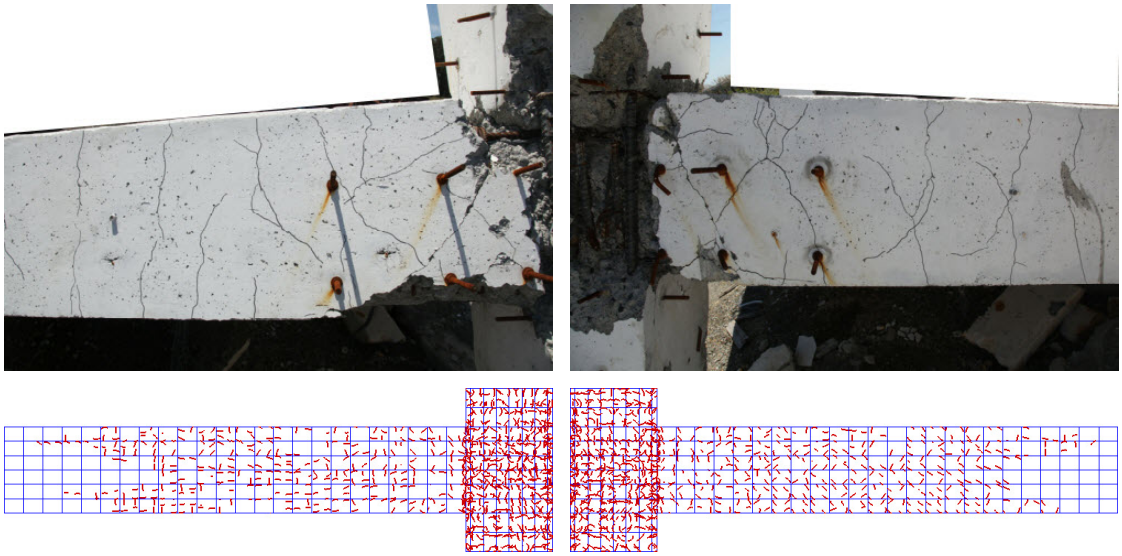

y-beam x-beam

Figure 5.46: Beam Final Crack Pattern for Park Specimen

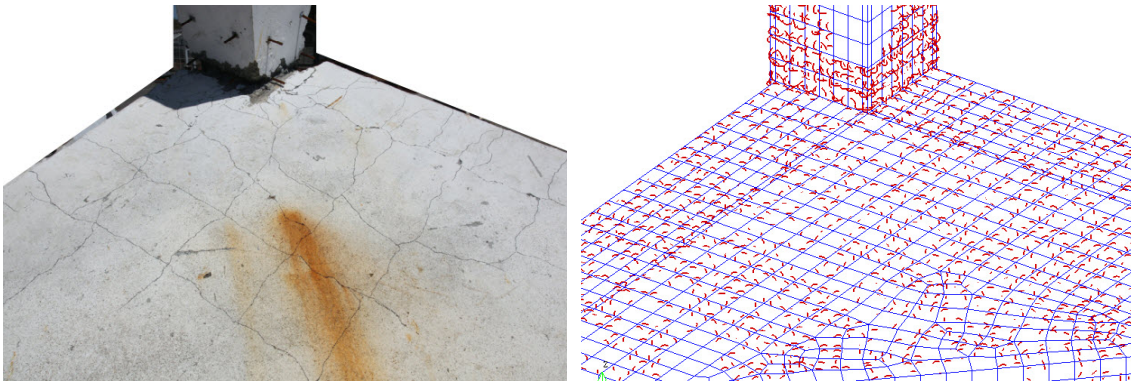

Figure 5.47: Slab Final Crack Pattern for Park Specimen

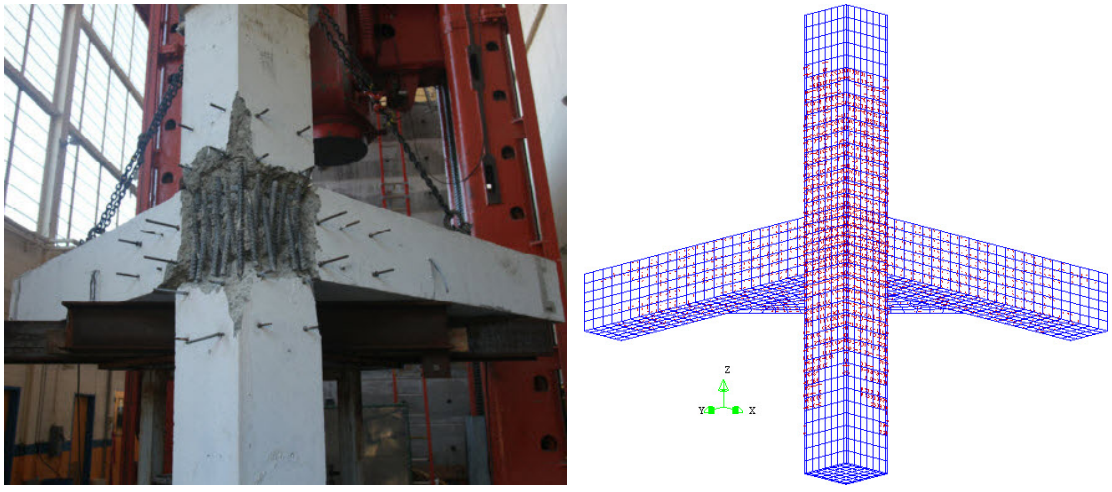

Figure 5.48: Joint Damage at End of Experiment for Park Specimen

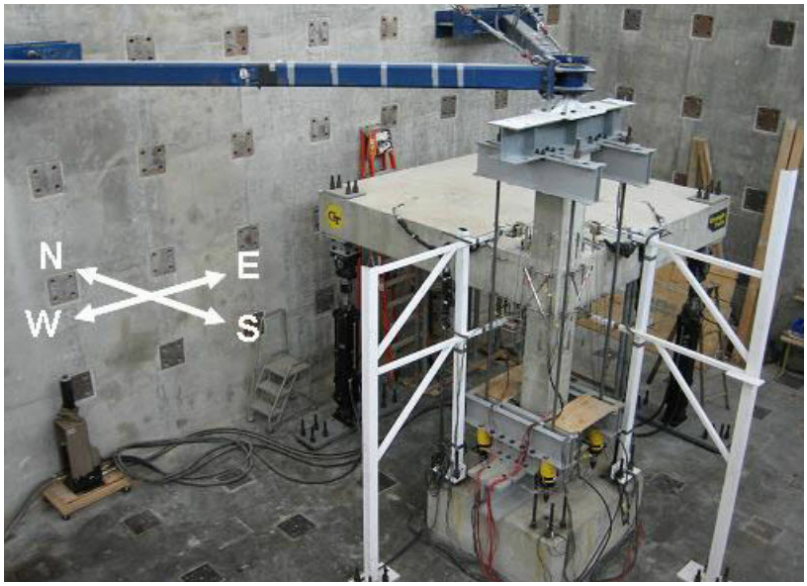

Source: Engindeniz [60]

Figure 5.49: Experimental Set-up for Engindeniz Specimen

5.5.1 Description of Experiments

Engindeniz tested a series of full-scale corner beam-column subassemblies under bidirectional cyclic loading. The specimens were designed to represent a corner region of a building with non-seismic detailing, isolated between two stories at the inflection points of the beams and columns with integral floor slab, as shown in Figure 5.49. Four specimens were subjected to six tests in which parameters varied included: (1) concrete strength, (2) various retrofit details utilizing carbon fiber reinforced polymers (CFRP), and (3) level of damage prior to retrofit. Specimen 1, which was tested to evaluate the adequacy of an as-built pre-1970 joint, was chosen for this analytical study.

The specimens were detailed in accordance with ACI 318-63 [5] and possessed significant seismic deficiencies. A strong column-weak beam criterion was intentionally violated using a column-to-beam moment strength ratio $\frac{\sum M_c}{\sum M_b}$ of approximately 0.9 in both primary directions. Other deficient details included a lack of transverse joint reinforcement, insufficient embedment of beam bottom bars within the joint core, and a column lap splice of inadequate length and confinement directly above the joint. All

specimens were nominally identical in dimensions and reinforcement details, and varied only by concrete properties.

The specimen dimensions and reinforcement details are shown in Figure 5.50. The column was 356 × 356 mm (14" × 14") and was reinforced at each corner by two bundled M16 (#5) bars; bars were spliced immediately above the joint region over a length of 320 mm (12.5"). The beams were 305 mm wide × 508 mm deep (12" wide × 20" deep) and reinforced with 6 M19 (#6) bars on the top surface and 3 M19 (#6) bars on the bottom surface. The top beam bars were anchored in the joint core with 90° hooks, while bottom beam bars were terminated in the joint core with a straight embedment of only 150 mm (6") in length. Both beams were nominally identical except for differing cover distances in the x- and y-directions to account for congestion in the joint region; x-direction beam reinforcements were located 19 mm (0.75") higher than y-direction beam reinforcements. All slab and transverse reinforcements were M10 (#3) bars. Top and bottom slab reinforcements were spaced at 305 mm (12") and 610 mm (24"), respectively.

The design strength of the concrete was 20.7 MPa (3000 psi), and Grade 40 reinforcing bars were specified. The actual properties achieved on the test day for Specimen 1 were as follows. The lower column, joint, beams, and slab had a strength of 25.8 MPa (3740 psi), while the upper column had a strength of 34.1 MPa (4950 psi). The M10, M16, and M19 bars had yield strengths of 367, 352, and 315 MPa (53.2, 51.1, and 45.7 ksi), respectively.

A photograph of the experimental set-up is shown in Figure 5.49. The top of the column was connected to a lateral reaction frame using a universal joint which simulated a three-dimensional pin, leaving the top of the specimen free to translate vertically and rotate about any axis. Beneath the universal joint was a built-up W16 section which was used in conjunction with four DWYDAG bars to apply axial force to the column. The column base connection simulated a fixed support; column reinforcements were welded

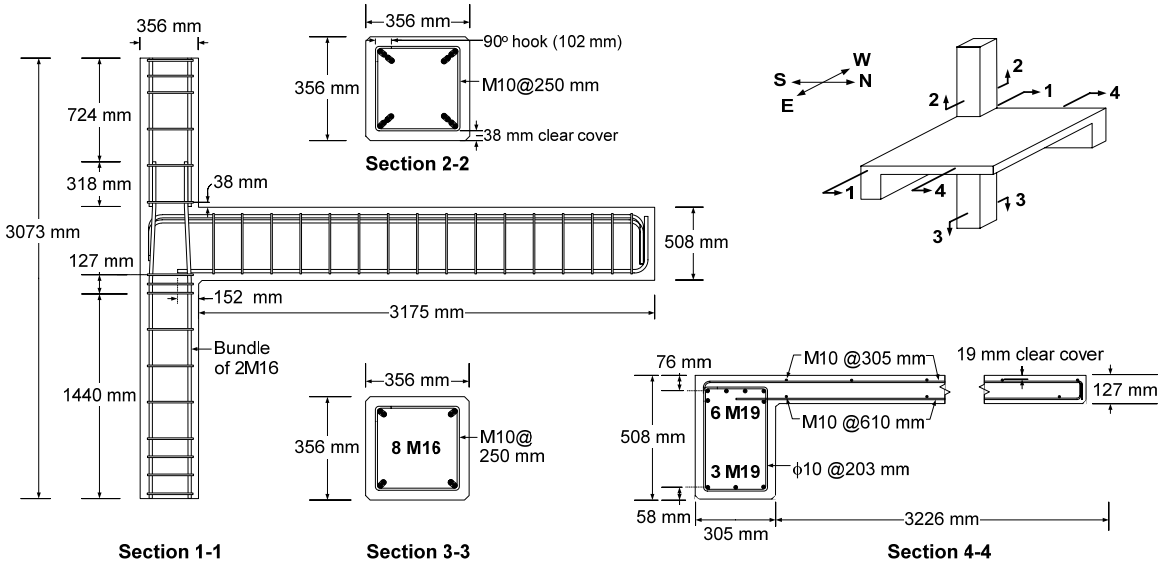

Source: Engindeniz [60]

Figure 5.50: Reinforcement Details for Engindeniz Specimen

to a steel plate which was post-tensioned to a strong floor via an intermediate steel beam and concrete block. The lower column was made longer so that the location of its inflection point matched the length of the upper column. Cyclic "lateral" forces were applied vertically to the beam ends using hydraulic actuators; the actuator-to-beam connection allowed for free rotation in the beam bending and torsional directions.

Gravity effects were modeled by applying a compressive column axial load of $0.10f'_cA_g$ at the beginning of the experiment through the four threaded rods using a hydraulic pump. The compressive force in the column was not modified during the experiment to simulate overturning effects, although variation due to the changing beam end forces was allowed. Beam ends were also displaced downward a distance required to generate negative beam moments comparable to those estimated to occur in the prototype frame under service load conditions. Cyclic lateral loads were then simulated around this deformed configuration by vertical quasistatic loading of the beam ends in displacement control. The cyclic load history is shown in Figure 5.51, and was comprised of cycles corresponding to 0.93, 1.40, and 1.87% beam displacement ratios. Unidirectional loadings were applied in the x- and y-directions prior to bidirectional loading. Slightly

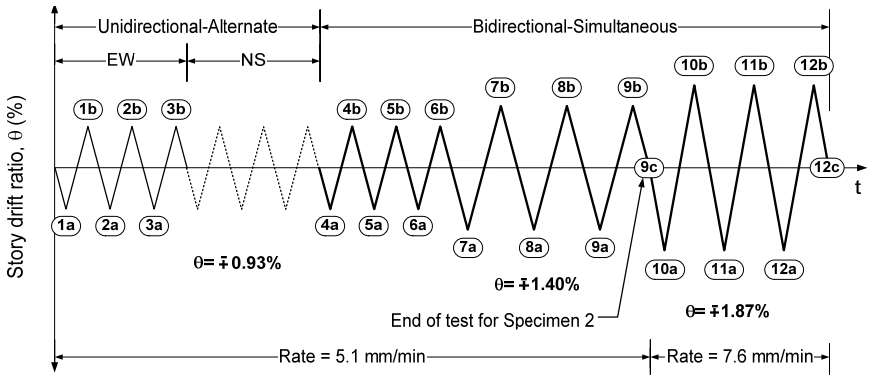

Source: Engindeniz [60]

Figure 5.51: Load History for Engindeniz Specimen

higher positive (and subsequently reduced negative) displacement levels were achieved in the x-direction response due to correction of the data arising from slip in the x-beam-to-actuator connection during load reversals (see Fig. 5.58a).

The hysteretic response of Specimen 1 in the x-direction is shown in Figure 5.52a, clearly exhibiting a non-ductile response. The damage modes varied between positive and negative directions of loading. For downward beam displacement, the behavior was characterized by yielding of upper column bars prior to yielding of beam top bars, joint shear cracking, and subsequent propagation of joint shear cracks into the upper column splice region. For upward beam displacement, the behavior was characterized primarily by loss of anchorage of the beam bottom bars and the subsequent inability of the beam to develop substantial positive moments at the column face. The final damaged state of Specimen 1 is shown in Figure 5.52b.

5.5.2 Finite Element Model

A finite element model was developed to simulate the response of Specimen 1. The mesh contained approximately 6700 solid elements. The prototype model was applied to two distinct concrete regions to account for the change in concrete compressive strength. The column mesh cross-section was six elements by six elements, the beam mesh cross-section was five elements wide by eight elements deep, and the slab had two layers of

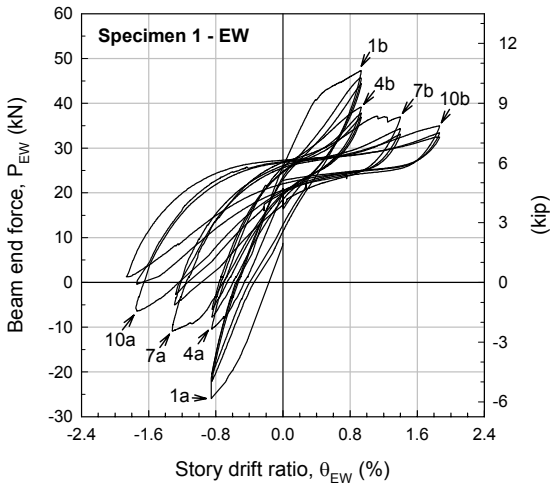

(a) Force-drift

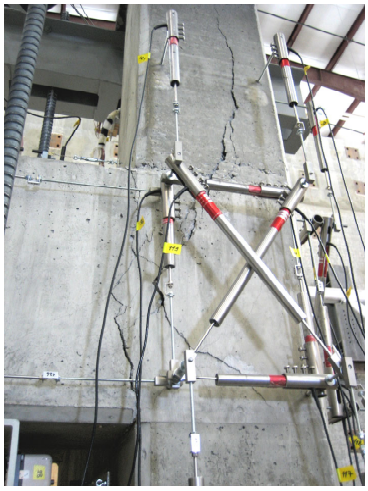

(b) Damaged state

Figure 5.52: Response of Specimen 1 from Engindeniz [60]

elements through the thickness. The regions near the supports at the column and beam ends were modeled as elastic to better distribute concentrated effects arising from support reactions and applied loads into the system without inciting localized failure mechanisms. The concrete mesh is shown in Figure 5.53a; the two concrete regions are shown in varying shades of blue, while the elastic support regions are shown in dark gray.

Reinforcements were modeled by approximately 350 reinforcing bar segments. All reinforcements were modeled using truss elements and were connected to the concrete mesh using nonlinear interface bond-slip elements. Reinforcements were carefully placed to correspond to the locations achieved in the experiments, accounting for differing cover distances and offsets to avoid intersection of reinforcements in the joint core. The column splice was explicitly modeled, shown in Figure 5.54. The bond-slip relationship was specified according to the "unconfined/other" designation per CEB-FIP Model Code 1990 [30], chosen based on the poor confinement bond performance reported in the experiments. The configuration of reinforcing bars in the column, beams, and slab is shown in Figures 5.53–5.56.

Initial trial runs indicated the model results were very sensitive to the boundary conditions, so the experimental supports were reproduced analytically as closely as possible.

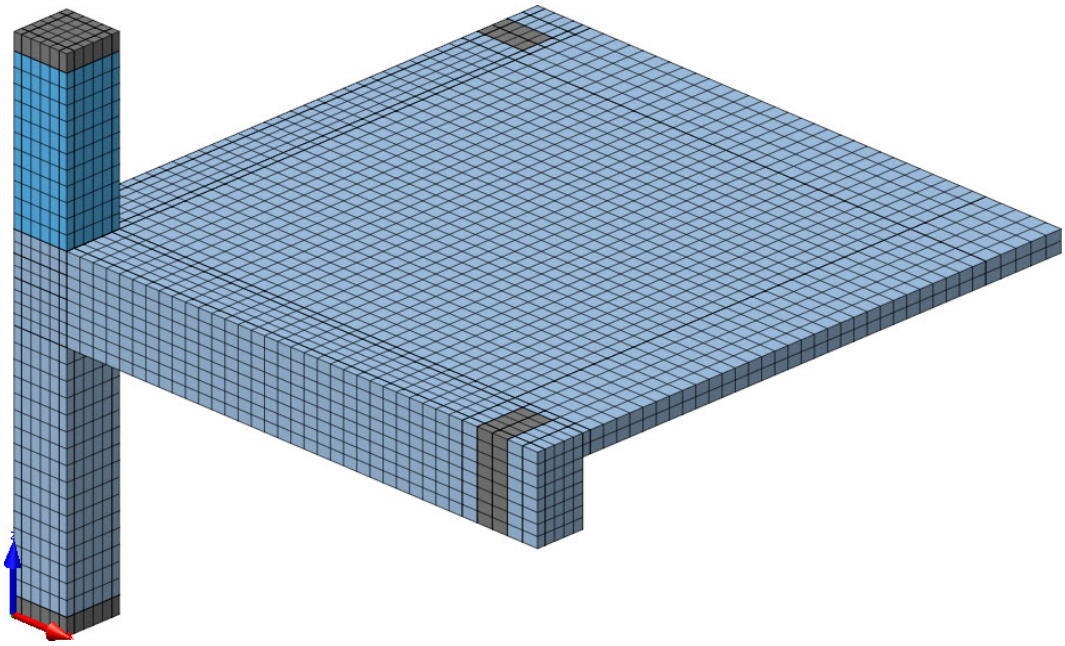

(a) Concrete Mesh

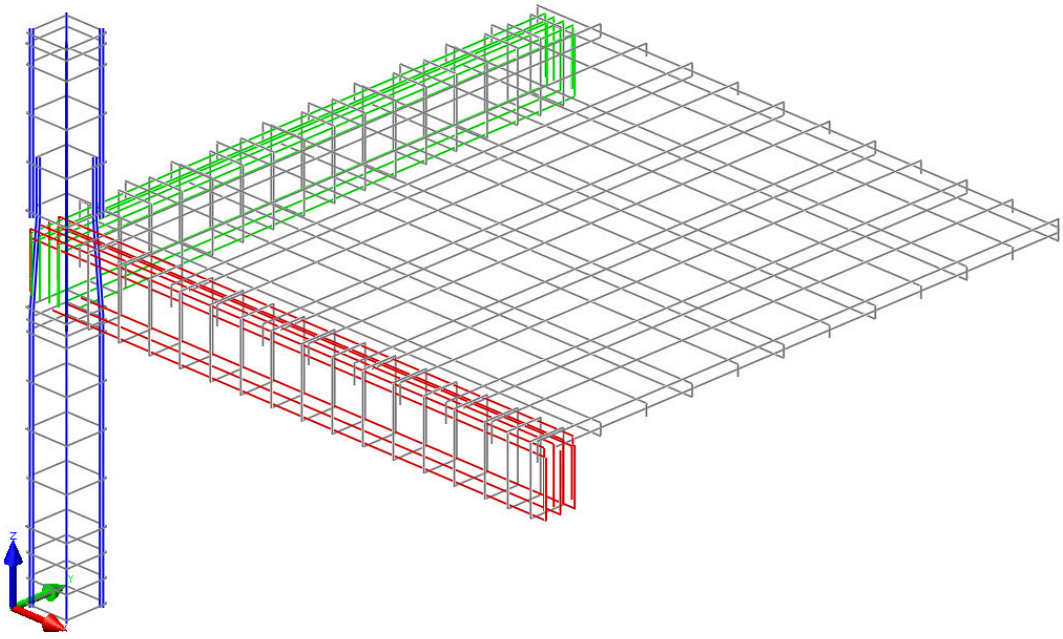

(b) Reinforcing Bar Mesh

Figure 5.53: Finite Element Mesh for Engindeniz Specimen

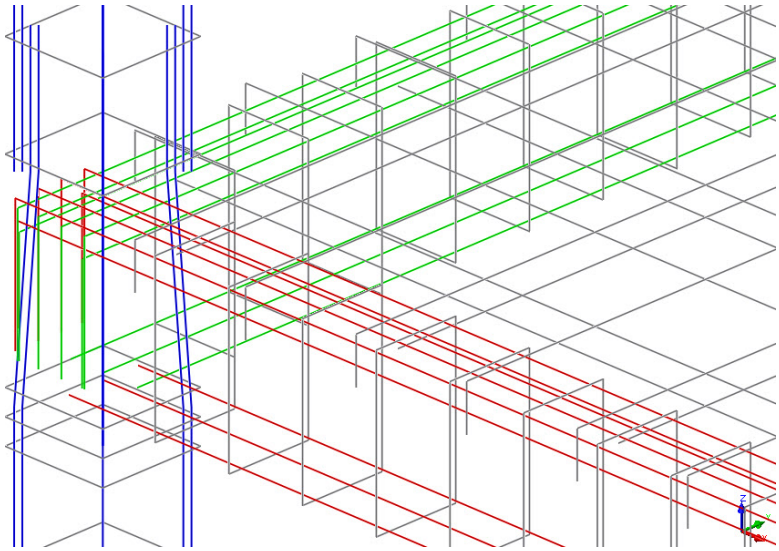

Figure 5.54: Reinforcement Element Joint Detail View for Engindeniz Specimen

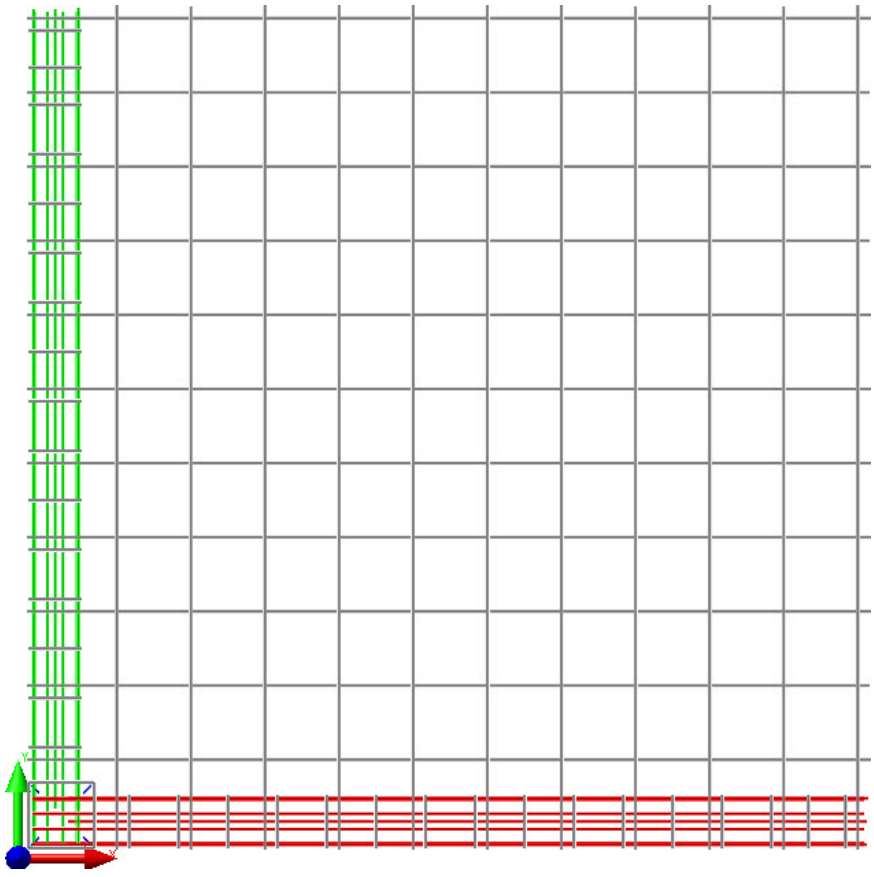

Figure 5.55: Reinforcement Element Plan View for Engindeniz Specimen

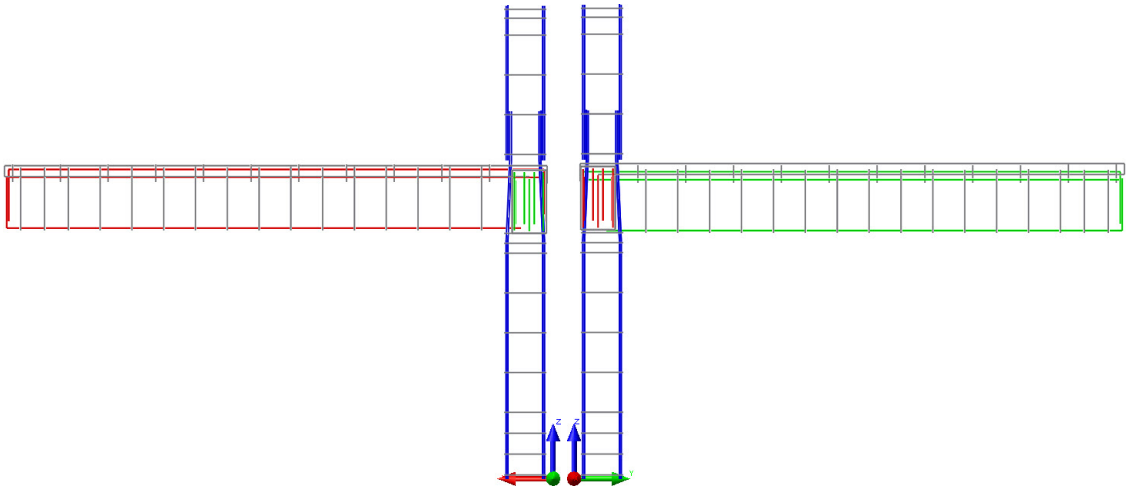

Figure 5.56: Reinforcement Element Elevation View for Engindeniz Specimen

The fixed condition at the base of the column was reproduced by four pin supports arranged in a 114 × 114 mm (4.5” × 4.5”) grid at the center of the column base, which together with the elastic layer of stiffened elements provided partial moment restraint, shown in Figure 5.57a. The condition at the top of the column is shown in Figure 5.57b, where the loading apparatus was recreated using space frame members, including the built-up W16 section (in red), the 150 mm (6”) diameter tube connecting the built-up section to the universal joint (in blue) and the 200 mm (8”) HSS members which formed the lateral reaction frame (in green). These members may be compared to the photograph in Figure 5.49 for reference.

The top of the column was supported by an elastic support which was calibrated to mimic the effect of the application of column axial force via four threaded rods. The spring stiffness for this elastic support was computed according to Equation 5.8, following the same procedure used for simulation of the cyclic column axial force response in the Pantelides specimen model, described in Section 5.2.2. Assuming four bars of diameter $d_b = 32$ mm (1.25”), $E = 200$ GPa (29000 ksi), and length $l_b = 3073$ mm (121”), the resulting column spring stiffness was $K_{col} = 206{,}086$ N/mm (1176.8 lb/in).

In the initial analysis step, the system was displaced into a configuration intended to

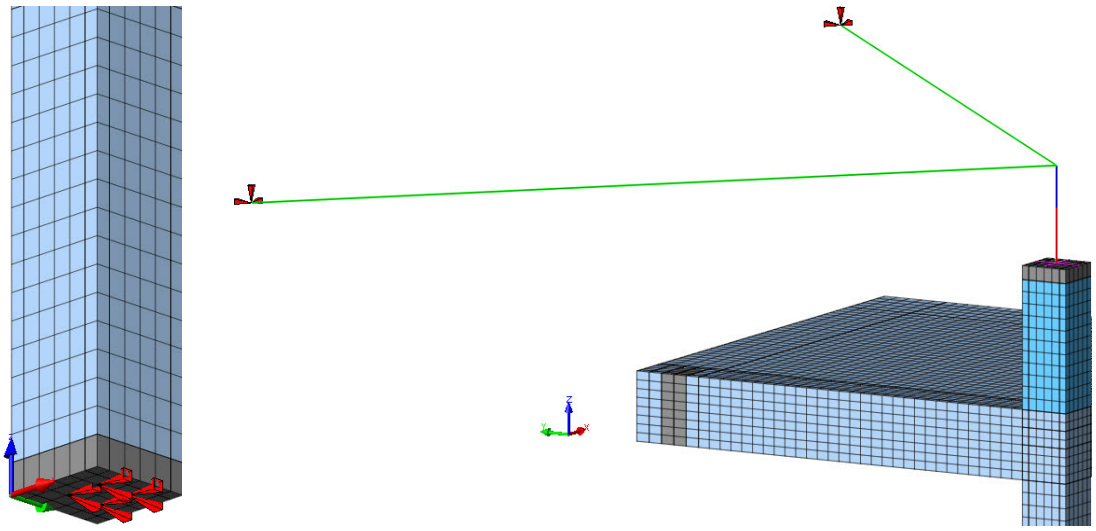

(a) (b)

Figure 5.57: Column Support Conditions for Engindeniz Specimen

represent the gravity condition. The column support was displaced a distance numerically determined from the model to induce a compression force in the column equal to 311.36 kN (70 kips), and the x- and y-direction beam ends were displaced upwards a distance numerically determined to induce shear forces equal to 8.718 kN (1.96 kips) and 12.188 kN (2.74 kips), respectively. These force values were chosen to match the initial values reported in the experimental data prior to cyclic loading. An upward displacement of the beam ends was necessary in order to offset the weight of the slab and produce double curvature of the beams.

Beam end loading was applied in displacement control using a vertical (z-direction) support at the centroid of the stiffened region near the beam ends, corresponding to the centroid of the hydraulic actuators used in the experiment, which was located 2870.0 mm (113”) from the column face. For the simulation, the load history from the experiments was reduced due to the high computational cost of the model; only one full cycle was applied at each specified displacement level instead of three, including each of the unidirectional cycles at the start of the test. Using the nomenclature from Figure 5.51,

this load path can be summarized as:

$$\underbrace{\text{0-1ax-1bx-0}}_{\text{x-dir}}\ \underbrace{\text{0-1ay-1by-0}}_{\text{y-dir}}\ \underbrace{\text{0-4a-4b-0-7a-7b-0-10a-10b-0}}_{\text{xy-directions}} \tag{5.14}$$

Thus, a total of four reversed cycles (one unidirectional, three bidirectional) were completed in each direction. Cycles 4, 7, and 10 were simultaneously applied in both the x- and y-directions. The Python code used to generate the load history input for DIANA is documented in Section B.9.1.

The analysis consisted of approximately 1090 load increments, which corresponded to a solution time of approximately seventeen hours. The DIANA material definition for this model is provided in Section B.9.2.

5.5.3 Discussion of Results

The hysteretic force-displacement response of the system in the x- and y-directions is shown in Figure 5.58. The peak force values achieved in each cycle are listed in Table 5.4. Good agreement was achieved between experimental and numerical responses. For the x-direction beam, the peak forces for both positive and negative displacement levels were slightly overestimated but within 5% of reported experimental values[1]. For the y-direction beam, the ratio of predicted-to-observed peak force was 0.922 for positive displacements and 1.233 for negative displacements. The mean predicted-to-observed strength ratio over all x-direction cycles was 0.951 (CV 0.039), while the mean predicted-to-observed strength ratio over all y-direction cycles was 1.078 (CV 0.042). Considering both x- and y-direction cycles together, the total mean predicted-to-observed strength ratio over all cycles was 1.015 (CV 0.042). In the experiment, the reduced capacity after the initial cycle for positive displacement levels was due to loss of beam bottom bar anchorage and resulted in significantly reduced positive moment capacity at the joint face. The close agreement in the force-displacement response for positive

[1] Ratio of predicted-to-observed force was computed using a reference force level of 20 kN since the beam was cycled around a non-zero initial configuration simulating gravity effects.

Table 5.4: Force-Displacement Metrics for Engindeniz Specimen

		X-Beam			Y-Beam		
Cycle	Direction	EXP	FEA	FEA/EXP	EXP	FEA	FEA/EXP
		kN	kN		kN	kN	
1A/1B	-	-25.73	-28.00	1.050	-17.71	-26.51	1.233
	+	47.27	48.27	1.037	50.69	48.31	0.922
4	-	-10.31	-13.12	1.093	-7.96	-20.18	1.437
	+	38.99	36.43	0.865	41.78	39.80	0.909
7	-	-10.71	-9.42	0.958	-8.45	-15.10	1.233
	+	37.07	35.71	0.920	40.74	40.20	0.974
10	-	-6.21	6.24	0.525	-4.64	-1.10	0.857
	+	34.91	37.35	1.164	37.92	38.91	1.055
		X-Direction Cycles:		MEAN = 0.951	CV = 0.039		
		Y-Direction Cycles:		MEAN = 1.078	CV = 0.042		
		X- & Y-Direction Cycles (all):		MEAN = 1.015	CV = 0.042		

displacement cycles above the 1% displacement level for both x- and y-direction cycles suggests this effect was accurately captured in the model.

While the strength of the specimen was closely represented, the force-displacement plots indicated that during many cycles, the numerical model exhibited a stiffer response than the experiments showed. This can be seen more effectively in Figure 5.59, which presents the stiffness degradation of the system using peak-to-peak stiffness (K_{pp}) per cycle. Even though peak strength values showed reasonable agreement, these values were reached at lower displacement levels in many cycles, resulting in increased K_{pp}. The x-direction stiffness response showed good agreement except for the initial cycle, but during the first three cycles of the y-direction response, the stiffness was uniformly overestimated. Considering both x- and y-direction cycles together, the total mean predicted-to-observed peak-to-peak stiffness ratio over all cycles was 1.189 (CV 0.043).

The per-cycle energy dissipation response of the simulation is compared with experimental data in Figure 5.60. For the x-direction response, the energy dissipated in the first three cycles showed close agreement with the experiment, although it was significantly underestimated in the final cycle. For the y-direction response, the energy

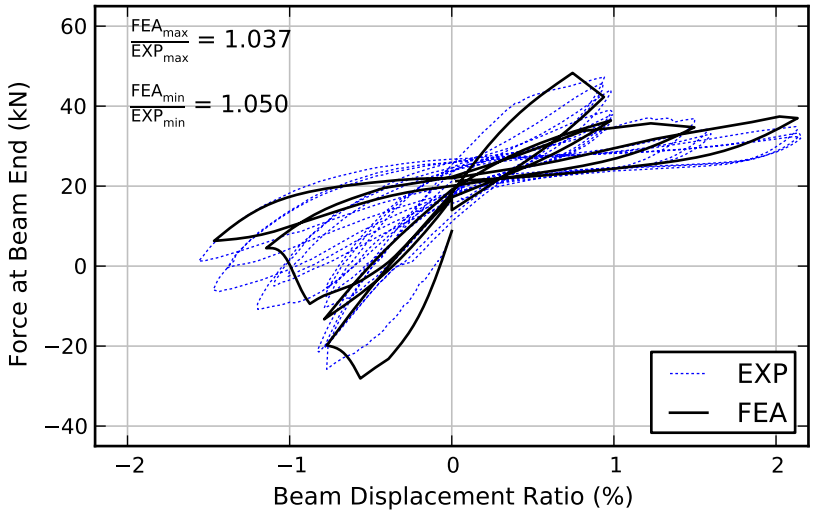

(a) X-direction

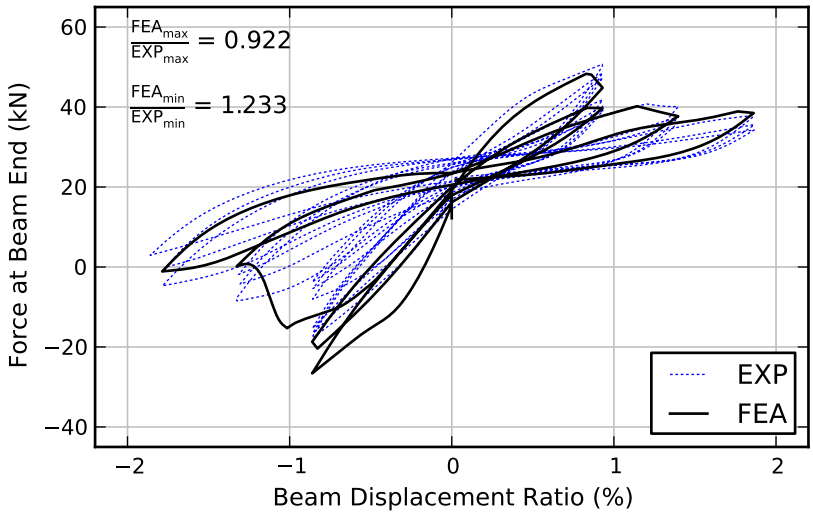

(b) Y-direction

Figure 5.58: Force-Displacement Response for Engindeniz Specimen

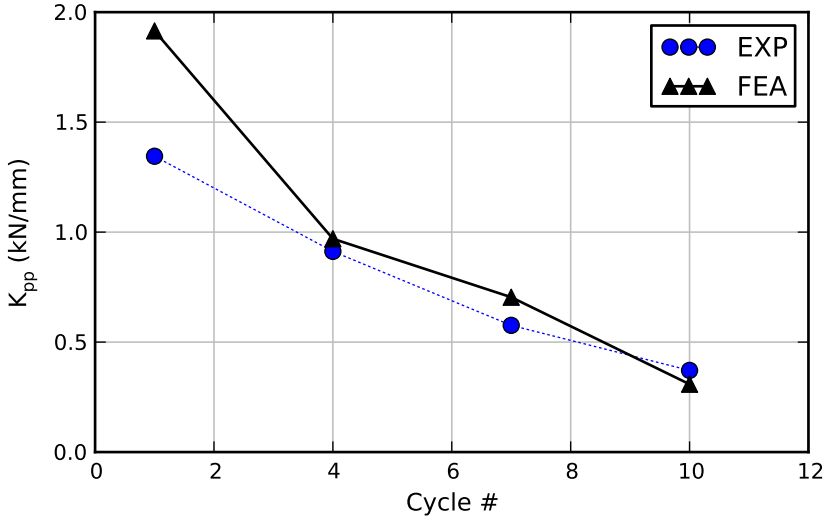

(a) X-direction

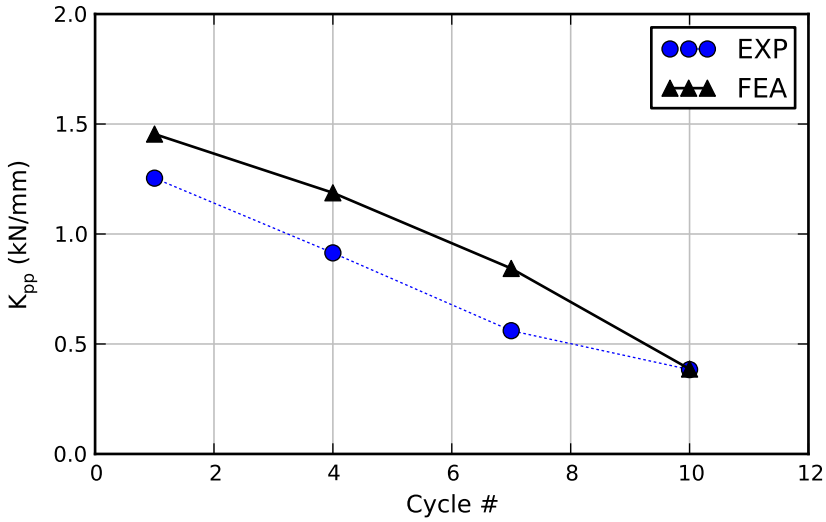

(b) Y-direction

Figure 5.59: Stiffness Degradation for Engindeniz Specimen

dissipated in the first two cycles showed close agreement, but was overestimated in the third cycle and (like the x-direction response) underestimated in the final cycle. The y-direction third-cycle response is also evident in the force displacement response in Figure 5.58b, indicated by the large hysteresis loop in the third cycle negative displacement regime. Despite the per-cycle fluctuations, good agreement was achieved for the cumulative energy dissipation response, shown in Figure 5.61 (considering experimental values only for simulated cycles). The ratio of predicted-to-observed total energy dissipated was 0.928.

The joint shear stress-distortion response of the system is presented in Figure 5.62. Significant degradation of joint shear capacity was observed for both upward and downward beam loading during increased cycles. The shear capacity during upward beam loading was significantly less due to pull-out of bottom beam bars, which reduced the shear forces at the joint face arising from positive beam moment. For x-direction loading, the peak predicted-to-observed normalized joint shear strength ratios for positive and negative loading were 0.917 and 0.989, respectively. The y-direction response was not as closely predicted, with peak predicted-to-observed normalized joint shear strength ratios for positive and negative loading of 0.854 and 1.118, respectively. The shear distortion response was represented better for the Engindeniz specimen than for the Pantelides, Akgüzel, and Park specimens. Fair agreement was observed in early cycles, although significant deviation from the experimental response was still observed during later cycles after extensive joint cracking had occurred, as has also been documented repeatedly for the previous joint simulations in this chapter.

The predicted final crack patterns in the joint regions are compared with photographs from the experiments in Figure 5.63. It is important to note that in this specimen, the typical "X"-pattern joint shear cracks did not form due to loss of anchorage of beam bottom bars which prevented transmission of large shear forces into the joint panel during

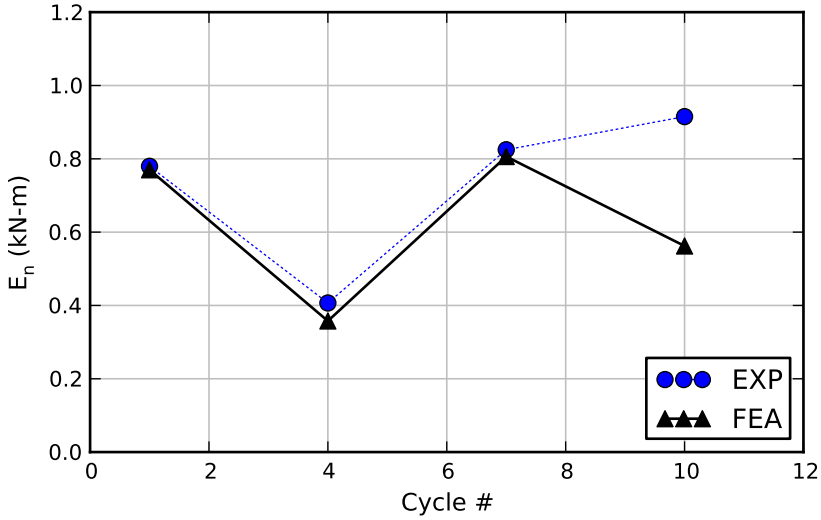

(a) X-direction

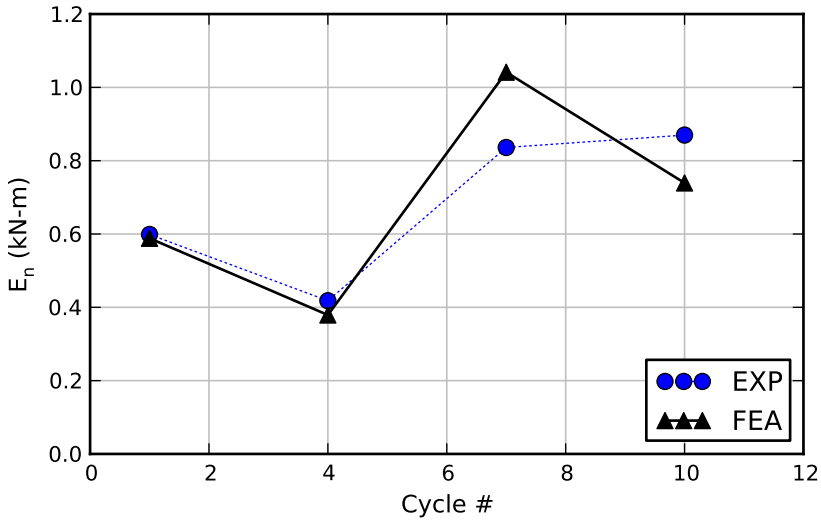

(b) Y-direction

Figure 5.60: Energy Dissipated per Cycle for Engindeniz Specimen

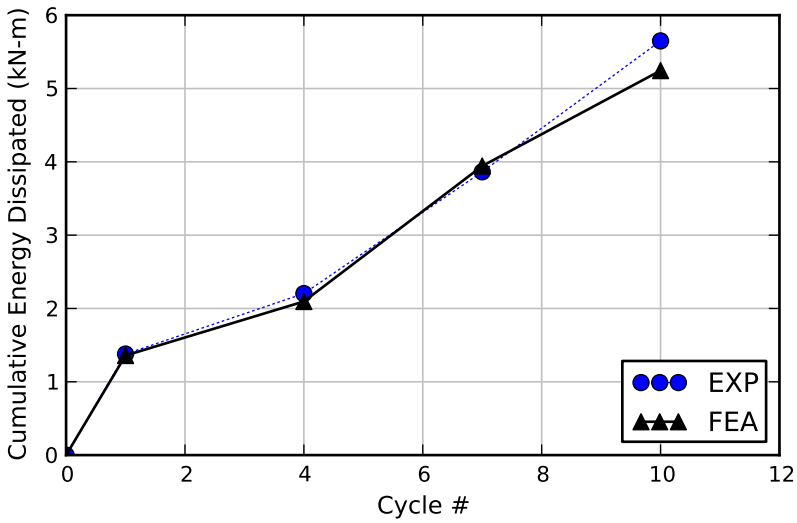

(Experimental 1st cycle values only)

Figure 5.61: Cumulative Energy Dissipation for Engindeniz Specimen

upward beam loading. The bands of predicted cracks were more distributed than the localized failures seen in the experiment. On both the xz- and yz-faces, the vertical crack at the bottom of the beam-joint connection, the diagonal shear cracks, and the progression of cracking into the column splice region was depicted. In the experiments, significant cracking and spalling occurred at the interior corner of the column immediately above and below the slab connection. Accumulated damage was observed in the predicted crack patterns in these regions, compared with photographs in Figures 5.64 and 5.65.

The progression of cracking on the top surface of the slab is shown in Figure 5.66 and agrees with the qualitative description provided by Engindeniz [60]. Figures 5.66a–e show the state at the peak negative displacement during both unidirectional cycles (1 & 2) and the three bidirectional cycles (4, 7, & 10), while Figure 5.66f shows the final state at the end of the simulation. During the initial downward displacement of the x-direction beam, a series of flexural cracks formed along the interface between the y-direction beam and the slab. A similar line of cracks developed at the x-beam-slab interface during downward displacement of the y-direction beam, along with a diagonal

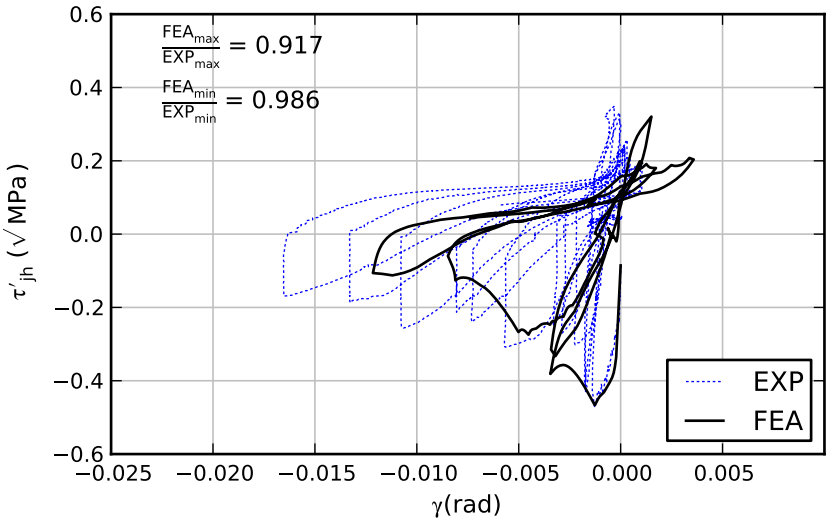

(a) X-direction

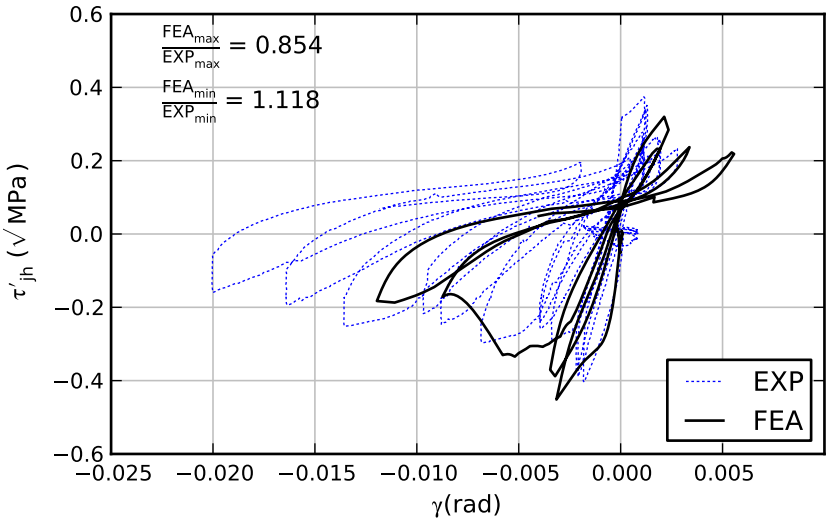

(b) Y-direction

Figure 5.62: Joint Shear Stress-Strain Response for Engindeniz Specimen

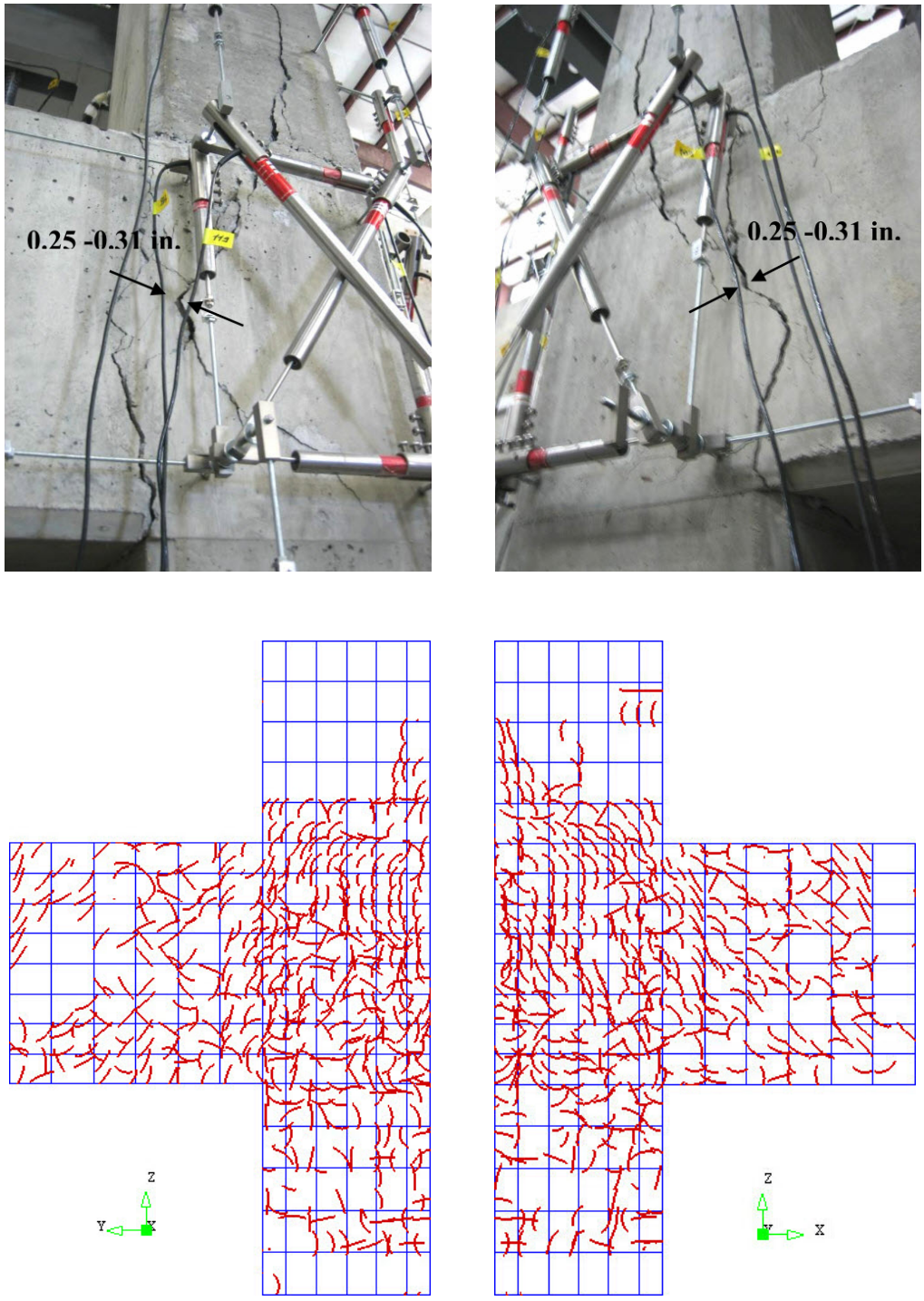

(a) yz-face (b) xz-face

Figure 5.63: Final Joint Face Damage for Engindeniz Specimen

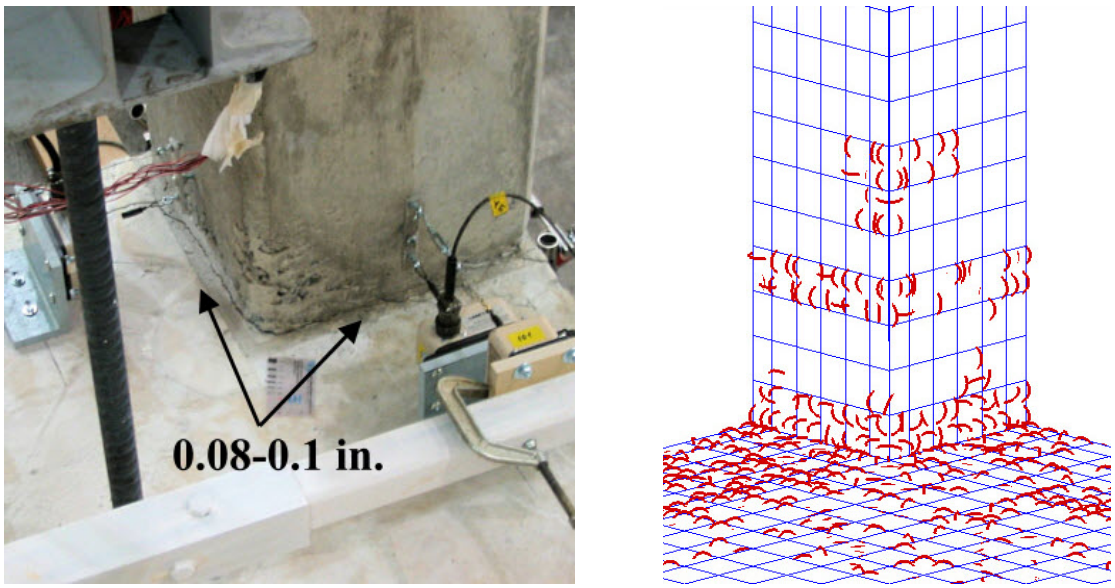

Figure 5.64: Damage at Upper Column Base for Engindeniz Specimen

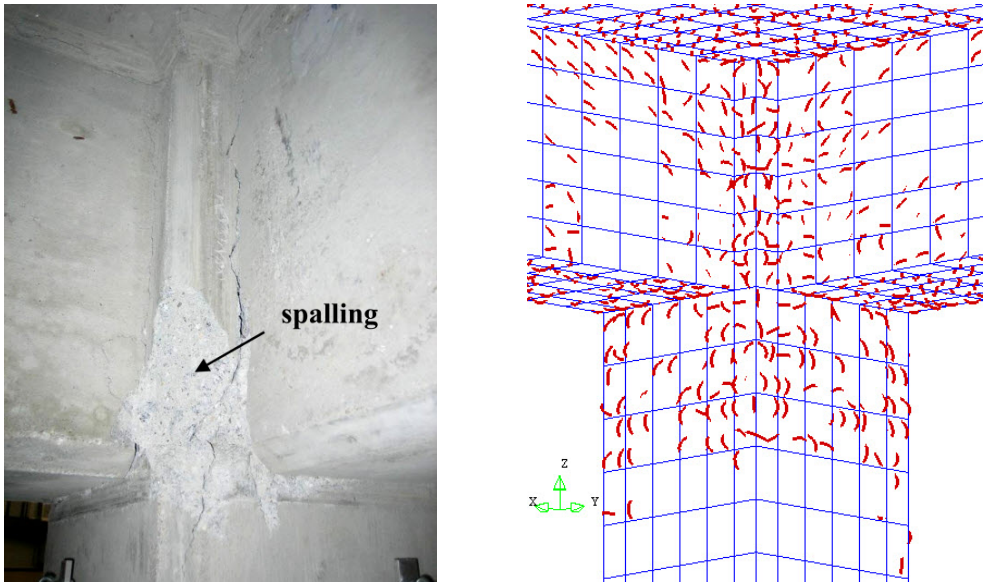

Figure 5.65: Spalling at Column Interior Corner Beneath Slab for Engindeniz Specimen

crack in the slab which began at the column and progressed toward the free corner of the slab. This diagonal crack is consistent with the expected location of yield lines in a continuous slab-and-beam floor [176]. The crack was skewed toward the y-direction beam because (a) the beams and slab had different moment capacities in the x- and y-directions due to different cover distances and (b) the bidirectional loading pattern meant the beams were not simultaneously loaded. After cycle 4, the cracks in the slab did not progress significantly due to localized failure in the joint region, which dominated the system-level response.

5.6 Critical Appraisal of Prototype Model for Joint Analysis

In this chapter, a series of beam-column joint subassemblages were successfully analyzed using the prototype model described in Chapters 3 and 4. The four specimens analyzed possessed varying degrees of seismic deficiency, but all exhibited failure processes common to gravity-load-designed frames, namely shear-dominated failure, rapidly degrading strength and stiffness, and a highly-pinched hysteretic response. The joints became progressively more complex throughout the chapter, beginning with a one-way exterior joint subjected to unidirectional cyclic loading (Pantelides specimen), followed by a two-way joint with two orthogonal beams subjected to cyclic bidirectional and column axial loading (Akgüzel specimen), and finally two beam-column joints with integral slab subjected to bidirectional reversed cyclic loading (Park and Engindeniz specimens).

To better facilitate a comparison of the performance of the prototype model across all beam-column joints presented in this chapter, mean ratios of predicted-to-observed response quantities from each simulation were compiled in Table 5.5. The overall weighted means and coefficients of variation listed in columns 6 and 7 of the table were computed taking into account the variation in numbers of cycles and directions of loading among the various simulations.

The mean ratio of predicted-to-observed peak force for each simulation is shown

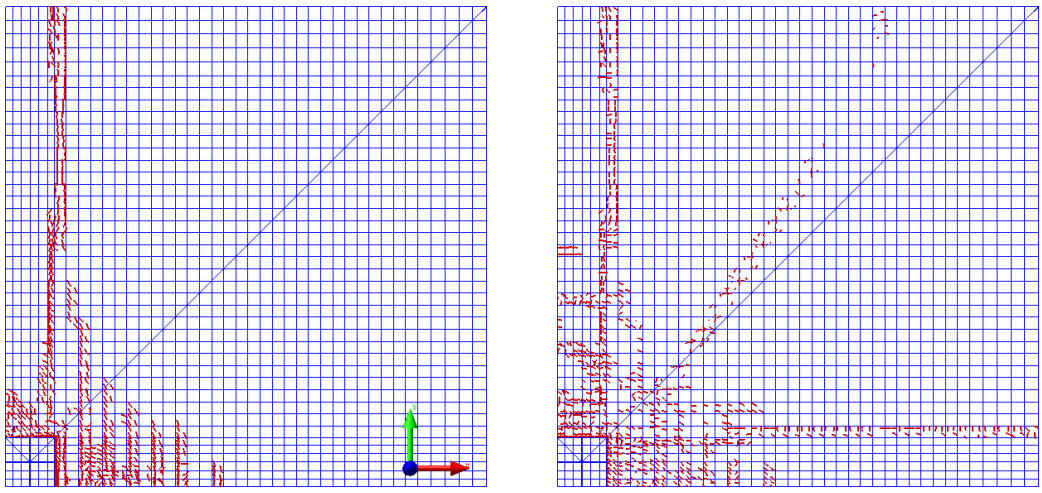

(a) 1a (down)

(b) 2a (down)

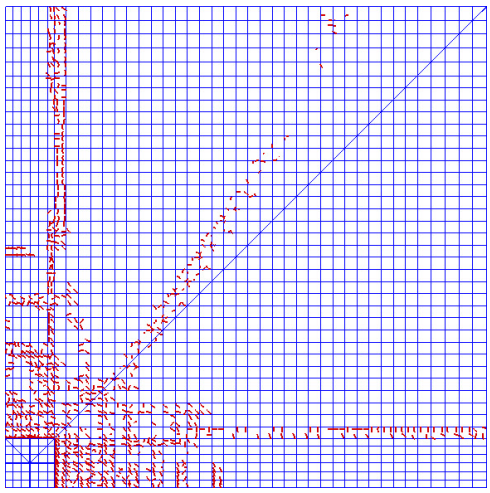

(c) 4a (down)

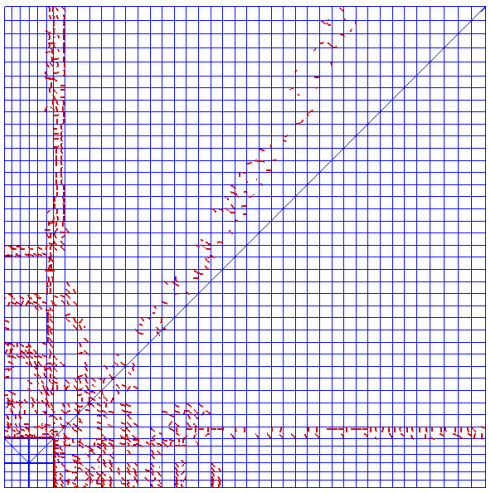

(d) 7a (down)

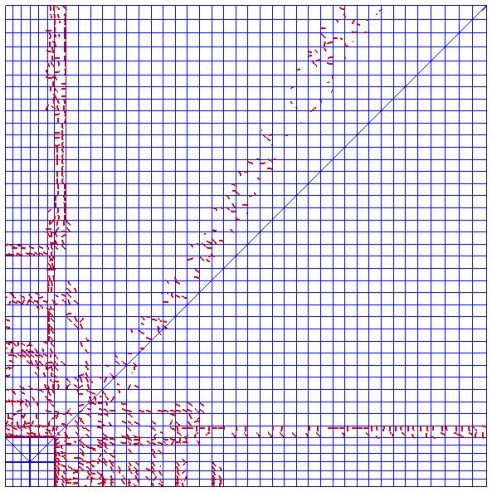

(e) 10a (down)

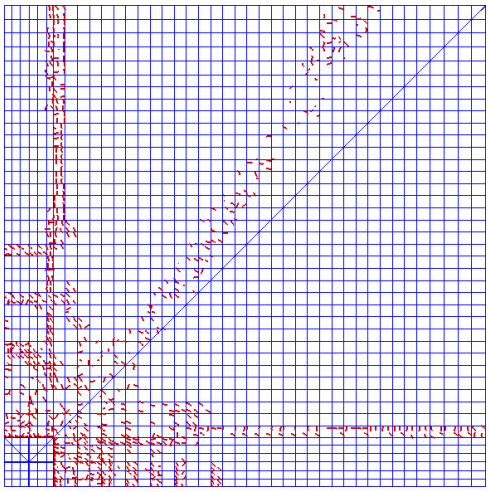

(f) Final

Figure 5.66: Progression of Top Surface Slab Cracks for Engindeniz Specimen (diagonal blue line is a member of the lateral reaction frame)

Table 5.5: Mean Ratios Comparing Predicted-to-Observed Response For All Simulations

Response Quantity	Pantelides	Akguzel	Park	Engindeniz	Mean[1]	CV[1]
Peak Force	1.052	1.045	0.961	1.061	1.026	0.010
Peak Force per Cycle	1.141	1.139	0.882	1.015	1.090	0.109
Peak-to-Peak Stiffness K_{pp}	1.106	1.179	0.920	1.189	1.103	0.066
Total Energy Dissipation E_{cum}	0.819	0.861	0.809	0.928	0.854	0.003
Joint shear strength	0.991	NA	0.924	0.969	0.955	0.007

1: Weighted according to number of cycles completed and directions of loading for each simulation.

in the first row of Table 5.5. The prototype model showed excellent agreement with experimental strength values, with a mean ratio of predicted-to-observed peak force per simulation ranging from 0.961 to 1.061. The peak force for all beam-column joint specimens was computed with a mean predicted-to-observed ratio of 1.026 (CV 0.010).

The mean ratio of predicted-to-observed peak force for individual cycles in each simulation is shown in the second row of Table 5.5; the determination of these values was shown previously in Tables 5.1–5.4. Overall agreement was closest for the Engindeniz specimen, a surprising result considering it possessed the most deficient detailing of all specimens evaluated. The Pantelides and Akgüzel specimen simulations both overestimated the strength over the full range of analysis by about 14%, while the Park specimen simulation underestimated the same quantity by about 12%. The accuracy of strength prediction decreased somewhat during post-peak cycles, resulting in a mean ratio of predicted-to-observed peak force for individual cycles over all simulations of 1.090 (CV 0.109).

The strength of the Park specimen per cycle was typically underestimated by the prototype model, the only case where this occurred. In this specimen, the beams and column possessed a significantly higher level of transverse reinforcement than the other three specimens, shown in Figures 5.31 and 5.37. The concrete constitutive model incorporates a pressure-dependent plasticity failure surface, intended to reflect increased

compressive strength due to lateral confinement; the details of the formulation are provided in the DIANA material library reference manual [4]. The underestimation of the strength of the Park specimen may indicate that the influence of lateral confinement was not sufficiently captured in the prototype simulation. No simplified validation cases with experimental data were conducted to investigate the response over a range of lateral confinement pressures (beyond the shear panel analysis in Section 4.5), but such an exercise may be valuable to future researchers using the prototype model for highly confined concrete.

Similar to confinement, accurate representation of boundary conditions was critical for close prediction of force-displacement response, particularly support conditions related to column axial load application. Both the Pantelides and Engindeniz specimens used threaded rods to apply an initial axial force into the column. The simulation of axial force for these specimens using an external elastic support displacement—with the spring stiffness and subsequent displacement computed to mimic the behavior of the four rods—was critically important to accurately represent the joint strength. The Akgüzel specimen, similarly, could not be accurately simulated without applying the full bidirectional, cloverleaf lateral displacements coupled with cyclic column loading; the multiaxial state of stress was too complex to generate using a simplified loading pattern. For the Engindeniz specimen, the lateral reaction frame and partially restrained base support had to be simulated to capture the system-level response.

Stiffness degradation was quantified by peak-to-peak stiffness K_{pp} throughout this chapter. The values listed in the third row of Table 5.5 indicate that the prototype model was generally more stiff than the experiments, although as previously explained, the error indicated by these ratios tended to be dominated by the first cycle initial stiffness. Over all simulation cycles, the peak-to-peak stiffness was overestimated by about 10.3% (CV 0.066). One factor that may have influenced the stiffness of the system was the fineness of the mesh. The mesh sizes used were inferred from similar successful simulations

reported in the literature. The high computational cost of the simulations made mesh refinement studies prohibitive, not because of the total computation time for the nonlinear solution, but because of the size of output database files which became too large for post-processing with the finite element code graphical user interface. High stress and strain gradients are anticipated during failure within the joint core, and it is likely that increasing the mesh density would positively influence the results, in particular the stiffness of the system.

Some researchers have hypothesized that simulating a lower number of cycles than were conducted experimentally may result in an inability to capture the full extent of strength and stiffness degradation in specimens like the ones studied in this research. The data in rows 1–3 of Table 5.5 does not seem to support this assertion. Recall that all experimental cycles were recreated in the Pantelides and Akgüzel specimen simulations, while only one-half of the Park specimen cycles and one-third of the Engindeniz specimen cycles were recreated analytically. By this argument, the Pantelides and Akgüzel specimens should have outperformed the Park and Engindeniz specimens for strength and stiffness metrics, but in fact there was no distinguishable trend. This is an important result because it (a) suggests a more favorable view of the prior body of beam-column joint FEA research where reduced cycles were used and (b) suggests that meaningful insights may be obtained by simulating cases near the limits of current computational power, such as seismic simulation of entire frames using continuum analysis, with reduced loading histories.

The energy dissipation response is compared in the fourth row of Table 5.5. Considering all simulation cycles, the mean predicted-to-observed total energy dissipated was 0.854 (CV 0.003). Comparison of the per-cycle, incremental energy dissipation plots throughout this chapter showed that good agreement was achieved until the peak force level was reached; after this point the model response typically exhibited more

hysteretic pinching than was observed experimentally. This behavior is clearly inherent to the total strain rotating crack concrete constitutive model, which always uses the secant modulus during unloading/reloading branches of the plain concrete stress-strain response. It was hypothesized in Chapter 4 that, given the inability of the concrete constitutive model to represent permanent inelastic strains, the Von Mises steel model may be preferable to a steel model capable of representing the Bauschinger effect, such as the Menegotto-Pinto model; this hypothesis appears valid. Comparison of Figures 4.1 and 4.5 showed that the Von Mises model with kinematic hardening followed the peak values of the experimental reinforcing bar closely, but overestimated the energy dissipated per cycle compared to the Menegotto-Pinto model. This suggests that while the Menegotto-Pinto model provides a much better response of a single reinforcing bar, had it been used with the prototype concrete constitutive model, the energy dissipation would have likely been even further underestimated. Thus, the exaggerated energy dissipation capacity inherent to the Von Mises reinforcement model made up for some of the deficit exhibited by the concrete constitutive model, although the total energy dissipated was still underestimated for all specimens. Thus, the capability to capture permanent concrete deformations is needed.

Joint shear stress predictions are quantified on the fifth row of Table 5.5. Good agreement was achieved with experimental data, with a mean predicted-to-observed joint shear stress ratio of 0.955 (CV 0.007). Note that joint shear stress ratios could not be computed for the Akgüzel specimen since normalized joint shear stresses, τ'_{jh}, were not directly reported from the experiments. Joint shear stress was determined from simulation results using the same method that is typically used experimentally—based on equilibrium of forces acting on the joint panel, inferred from external reaction forces as described in Section 5.1.5. Despite this approach's widespread use, improved understanding of the force transfer mechanism in the vicinity of the joint is needed, and a validated modeling strategy could play an important role in determining, for instance, a

realistic distribution of joint shear stresses throughout the joint panel, the role of specific bars in transferring beam and slab moments into the joint, and the influence of beam torsion on joint failure under multiaxial loading conditions. The preliminary results from this chapter show promise for use of the prototype model in this type of internal investigation of joint behavior, especially if based on element nodal forces which exhibit less mesh sensitivity than stress fields. The next step to this end would be a numerical scheme to directly compute the resultant force acting at the joint mid-height (V_{jh}), accounting for the influence of both the concrete continuum as well as shear forces carried by column reinforcements passing through the joint region.

Joint shear distortion predictions showed good agreement in cycles performed before the peak lateral load was reached, but were poorly represented in cycles after significant damage occurred in the joint core, such as spalling of the joint face concrete and loss of column cover on the back face of the joint. During post-peak cycles, the distortion was often under- or over-predicted by as much as one-half to three times the experimental values. Shear distortion was best captured in the Engindeniz specimen, shown in Figure 5.62, although the peak shear deformations were still underestimated. The difference between computed and observed response may be attributed to the fact that experimental determination of joint shear distortion is highly sensitive to the placement of an LVDT array that may conflict with localized cracking or spalling of cover concrete in the joint region.

Bond-slip is an important component in nonlinear simulation of concrete response. The use of automatically-generated bond-slip reinforcements in DIANA does not appear to currently allow for visualization of slip values along reinforcing bars. As such, the ability of the model to represent bond-slip failure was monitored using indirect measures. No attempt was made to develop general recommendations for bond-slip law parameter selection beyond the guidelines of the CEB-FIP Model Code 1990 [30] because

of the inherent limitations of the bond-slip hysteresis rules in DIANA, which were documented in Section 4.3.2. That said, the following statements can be made regarding bond performance in the prototype model.

That the overall response of four nonseismically detailed beam-column joints subjected to reversed cyclic loading was predicted as uniformly well as it was indicates that the lack of cyclic bond degradation did not play as prominent a role as expected.

In the Pantelides, Akgüzel, and Park specimens, beam longitudinal bars were anchored with hooks in the joint core; large bond-slip displacements were not expected along these bars. Regardless of whether large slips were mobilized, though, early trial simulations of the Pantelides specimen with perfect bond significantly overestimated the initial stiffness of the specimen, indicating that all longitudinal reinforcements should be simulated with interface bond elements to capture the true system stiffness. Overestimation of the force-displacement capacity in post-peak cycles in the Pantelides and Akgüzel specimen simulations may be attributable to the lack of cyclic bond degradation, but this explanation seems unlikely since the post-peak force-displacement capacity was not overestimated in the Park specimen analysis.

Pull-out failure (loss of anchorage) of beam bottom bars was one of the defining characteristics in the experimental response of the Engindeniz specimen. Experimental strain profiles indicated this effect had developed by the beginning of the bidirectional load cycles (cycle 4a). The prototype model's accurate prediction of the sudden reduction in positive beam end force values in cycles 4, 7, and 10 in Figure 5.58 indicates an adequate approximation of bottom bar pull-out was achieved. The inability of the joint to mobilize significant joint shear values during beam upward loading in Figure 5.62 further supports this claim.

Finally, crack patterns were compared with photos of specimen damage from the experiments at varying load levels. Although general agreement could be inferred, these visualizations offer limited insight into real behavior. In all cases, the predicted crack

patterns were distributed over broad regions of the model, and unable to closely track the precise locations or widths of actual, localized cracks observed experimentally. The distribution of damage was most accurately represented for the Akgüzel specimen, as shown in Figure 5.30. For the Engindeniz specimen, the progression of cracking in the slab closely followed the description of the experimental response.

Considering the good agreement with the many quantitative metrics and qualitative behaviors represented, the prototype model was judged a success in simulating the response of nonseismically detailed reinforced concrete exterior beam-column joints subjected to reversed cyclic loading.

CHAPTER VI

CONCLUSIONS

6.1 Summary of Research Outcomes

This research used nonlinear finite element analysis to investigate the behavior of reinforced concrete exterior beam-column joints with seismically deficient detailing when subjected to bidirectional reversed cyclic loading. Existing constitutive models were combined in a novel way, as described later in this section, to simulate the response of a nonseismically detailed reinforced concrete exterior corner joint with slab, which had not been previously analyzed.

This study began with a critical assessment of the state-of-the-art for constitutive modeling of beam-column joints which established the viability of the current investigation and suggested best practices for simulating failure mechanisms commonly exhibited in gravity-load-designed frames. This review led to the selection of a modeling strategy using the DIANA finite element software which was systematically validated against experimental data for a variety of behaviors, including concrete tension and compression post-peak softening, reinforcing bar plasticity, bond-slip mechanisms such as pull-out and anchorage behavior, and cyclic shear failure.

Four beam-column joint subassemblages possessing nonseismic detailing were successfully simulated under quasistatic reversed cyclic loading. Specimens analyzed include a one-way exterior joint tested by Pantelides et al. [174], a two-way exterior corner joint without slab tested by Akgüzel et al. [9], and a series of two-way exterior corner joints with slab, tested by Park et al. [179] and Engindeniz et al. [60]. The three-dimensional specimens were subjected to bidirectional cyclic loading, and the Akgüzel

and Park specimens also to cyclic column axial loads which simulated overturning effects in a building during an earthquake.

The principal findings of this research are as follows:

- The finite element method can be used to accurately simulate the response of three-dimensional reinforced concrete beam-column joints with insufficient seismic detailing.

- This research was the first known successful application of nonlinear finite element analysis to simulate the response of a nonseismically detailed reinforced concrete exterior corner joint with slab.

- The validated prototype model proved highly effective for joint simulation, closely reproducing the hysteretic characteristics and failure mechanisms observed experimentally.

- Recommended components for joint simulation are summarized as follows: Concrete response was simulated using the total strain rotating smeared crack constitutive model by Selby and Vecchio [201, 200], with the Thorenfeldt [217] compression and the Hordijk [84] tension softening models. Reinforcing steel was simulated using Von Mises plasticity with kinematic hardening, and bond-slip was simulated following the guidelines of the CEB-FIP Model Code 1990 [30]. All simulations were conducted using DIANA [4]. The full list of recommended constitutive laws and material parameters is provided in Section 4.6.

- The process of systematic model validation using appropriate, simplified experimental data proved highly effective and allowed for accurate analysis of much more complex systems without the tweaking of parameters to fit the data. Proper verification must be conducted for all component models which may play a prominent role in the expected failure mechanisms of the specimen being analyzed.

- The peak force for all beam-column joint specimens was computed with a mean predicted-to-observed ratio of 1.026. The accuracy of strength prediction decreased somewhat during post-peak cycles, resulting in a mean ratio of predicted-to-observed peak force for individual cycles of 1.090.

- The prototype model overestimated the initial stiffness of the joint, but typically showed good agreement after the onset of cracking. The ratio of predicted-to-observed peak-to-peak stiffness over all cycles was 1.103.

- Energy dissipation was underestimated for the beam-column joint specimens, with a mean predicted-to-observed ratio of 0.854. This difference was attributed to the use of the secant modulus for unloading-reloading in the concrete constitutive model. Nonetheless, this was judged an improvement over many simulations in the literature which were unable to capture sufficient pinching in the force-displacement hysteresis.

- Along these lines, the use of the Von Mises plasticity model with kinematic hardening for reinforcing bar response—which neglected the Bauschinger effect—did not not appear to introduce an adverse effect on the total energy dissipation characteristics of the system since the concrete model underestimated energy dissipation.

- The well-documented ability of the total strain rotating crack model to simulate shear failure was verified in this study. The joint shear capacity was closely predicted in all cases, with a mean ratio of predicted-to-observed maximum joint shear stress of 0.955.

- The prediction of joint shear distortion showed good agreement until the peak load was reached, after which the distortion was often under- or over-predicted by as much as one-half to three times the experimental values. This finding casts

doubt on the appropriateness of joint shear distortion as a parameter for joint characterization as well as on the reliability of its experimental determination.

- Joint response was simultaneously simulated under the multiaxial stress states arising from cyclic bidirectional lateral loading as well as cyclic column axial force. Correct modeling of the column axial force was essential for accurate prediction of the strength of the joint.

- The overall response in terms of capacity and total energy dissipation was best predicted for the Engindeniz [60] specimen, which possessed the most deficient detailing for resistance of lateral loads, suggesting the model validation process—intentionally optimized for shear-dominated failure—was a success.

- The simulation of the Engindeniz [60] specimen accurately reproduced the sudden loss of positive moment capacity and inability to mobilize significant joint shear strength under upward beam loading—both behaviors which were attributed to loss of beam bottom bar anchorage in the experiment—which confirmed the prototype model's ability to capture pull-out failure.

- The bond-slip formulation in DIANA did not appear to introduce a significant adverse effect on joint simulation results based on the overall agreement with experimental data. Nonetheless, no attempt was made to develop general recommendations for bond-slip law parameter selection for beam-column joint analysis beyond the general guidelines of the CEB-FIP Model Code 1990 [30], nor is such an attempt recommended until improvements are made to the cyclic bond formulation in DIANA.

- Even in cases where significant bond-slip is not expected, specification of bond-slip interface elements may be necessary to correctly represent the initial stiffness of a reinforced concrete structure.

- The capacity of the Park [179] specimen was uniformly underestimated, but was the only joint that exhibited this behavior. This specimen possessed a much higher quantity of transverse reinforcement in the beams and column than the Pantelides [174], Akgüzel [9], and Engindeniz [60] specimens, which suggests that the constitutive model may not have sufficiently captured the increased strength expected due to passive confinement. The response of the concrete constitutive model must be investigated over a range of well-defined confinement pressures before its use can be recommended for analysis of beam-column joints with modern confinement detailing.

- Model results were very sensitive to boundary conditions. Experimental support must be modeled at the precise location of resultant forces and with realistic stiffness, accounting for partial restraint. Depending on the relative stiffness of the supporting elements to the specimen, the flexibility of components such as reaction frames should be considered in the analysis.

- Reducing the number of cycles completed at each displacement level did not appear to have an adverse effect on the overall prediction of the strength and failure mechanisms of the joints analyzed.

- DIANA was found to be an extremely powerful tool for nonlinear analysis of concrete behavior, and its use is recommended for other researchers attempting to simulate failure processes in brittle materials. In no cases did an inability to achieve numerical convergence prevent the completion of a simulation using the previously described constitutive model for concrete cracking.

6.2 Recommended Future Research

The following research topics are suggested for future inquiry:

- *Slab contribution*. Now that the ability of the prototype model to represent the

global response of a corner joint with slab has been established, research is needed to more fully characterize: (a) the influence of the slab on load transfer from the floor system into the joint, (b) the influence of increased beam moment capacity due to the presence of the slab and the resulting decrease in the column-to-beam moment ratio, (c) the influence of the slab on the yielding and potential loss of anchorage of beam longitudinal reinforcement, and (d) the influence of torsion of transverse beams on joint shear failure.

- *Parametric studies of beam-column joint behavior.* Such factors requiring systematic inquiry for two-way exterior corner joints include: (a) the effect of concrete compressive strength, (b) the effect of column axial load ratio on joint shear failure, (c) the effect of various joint transverse reinforcement configurations, and (d) the influence of torsion due to beam eccentricities.

- *Analysis of FRP-repaired joints*. The success of the prototype model in simulating "as-built" pre-1970 joints suggests that it may be an appropriate tool to evaluate the efficacy of various rehabilitation methods, such as externally bonded fiber reinforced polymers (FRP), provided suitable models for debonding and delamination of the FRP can be identified and carefully validated.

- *Analysis of modern joints*. The present research identified a need to better understand the performance of the prototype model when high lateral confinement is provided by transverse reinforcements. Such an exercise would allow for evaluation of beam-column joints conforming to current design standards, and potential use of FEA more broadly during the development of future design codes.

The following topics are currently inhibited by high computational cost. Once advances in computing resources allow, the following topics should be evaluated.

- *Analysis of indeterminate frames*. The present study only simulated the response of

joint subassemblages which were isolated from the surrounding structure at assumed points of contraflexure. The force redistribution mechanisms which occur during failure of a three-dimensional indeterminate frame are significantly more complex, and evaluation of such frames using numerical analysis would provide valuable insights, especially if performed in conjunction with the following:

- *Dynamic analysis*. The simultaneous specification of cyclic lateral and cyclic column axial loading was an important step forward, but in all cases these were still simulated in a quasistatic context. Nonlinear time history analysis of a nonseismically detailed indeterminate frame subjected to appropriate ground motions—in conjunction with suitable experimental data for validation—would provide even further valuable insight into the failure of realistic joints during earthquakes.

- *Evaluation of mesh sensitivity*. In the current study, mesh density was increased as much as computational resources allowed, which prohibited in-depth mesh sensitivity studies. The prototype model needs to be evaluated considering (a) increased element density in the joint as well as regions in the beams and columns near the joint and (b) increased number of elements through the depth of the slab.

6.3 Recommended Improvements to DIANA

Based on the experience gained through this research, the following improvements are recommended for the DIANA finite element software:

- *Cyclic bond-slip degradation*. As detailed in Section 4.3.2, the current rules governing hysteretic bond behavior were unrealistic for the application at hand. Recommended changes to improve control of the cyclic bond response include implementation of the Eligehausen [54] or Morita-Kaku [151] cyclic bond models, the ability to specify a multi-linear stress-slip curve in conjunction with a Wöhler (S-N) diagram, and an unloading response with increased stiffness.

- *Plastic offsets in cyclic concrete behavior.* Despite the overall success of the total strain based smeared cracking constitutive model, a formulation for the unloading/reloading behavior of concrete which accounts for plastic offset strains, such as the Palermo model [169], would improve the energy dissipation characteristics of concrete structures simulated under cyclic load histories.

- *Menegotto-Pinto model for bond-slip reinforcements*. The current implementation of the Menegotto-Pinto model restricts its use to reinforcements with perfect bond. Extension of this model for use with so-called bond-slip reinforcements in DIANA (which generate both truss/beam elements for reinforcements and line-to-solid interface elements to represent bond), would allow for improved representation of the cyclic response of reinforced concrete and improve energy dissipation.

APPENDIX A

LITERATURE REVIEW VISUAL SUPPLEMENT

The following appendix complements the state of the art literature review presented in Chapter 2. From each paper, a representative finite element mesh and a graph comparing numerical results to experimental data is presented.

Since many studies investigated multiple joint configurations and response types, the following criteria were used to determine which mesh and sample results graphic to display. The response quantity chosen for this review was the first available from the following hierarchy: force-drift response, joint shear stress-strain response, moment-curvature response, then crack pattern. Three-dimensional meshes were chosen over two-dimensional ones. The results of non-seismically detailed joints were chosen over those with modern detailing or FRP upgrades. The results of cyclically-loaded simulations were chosen over monotonic results; likewise those with bidirectional load histories were chosen over those with unidirectional loading. For studies evaluating both reinforced and post-tensioned concrete, the reinforced concrete results were chosen. If analytical results were not graphically compared with experimental results in the source paper, only the mesh is shown.

Each study is reviewed in detail in Chapter 2. A summary of the software used, constitutive models employed, joint geometry, loading protocols, reinforcement characteristics, and other model parameters is given in Tables 2.1 and 2.2.

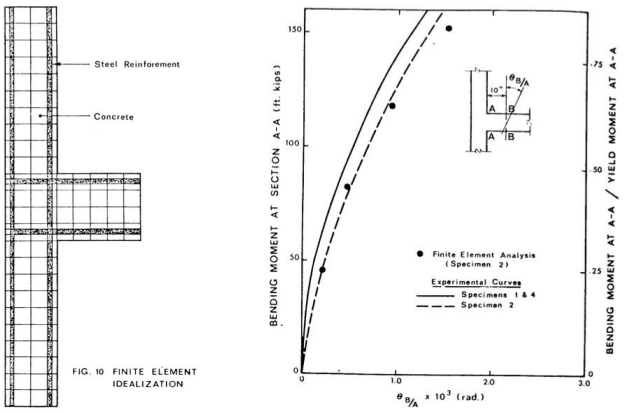

Figure A.1: Representative mesh and moment-rotation response—Will, Uzumeri, and Sinha 1972 [231]

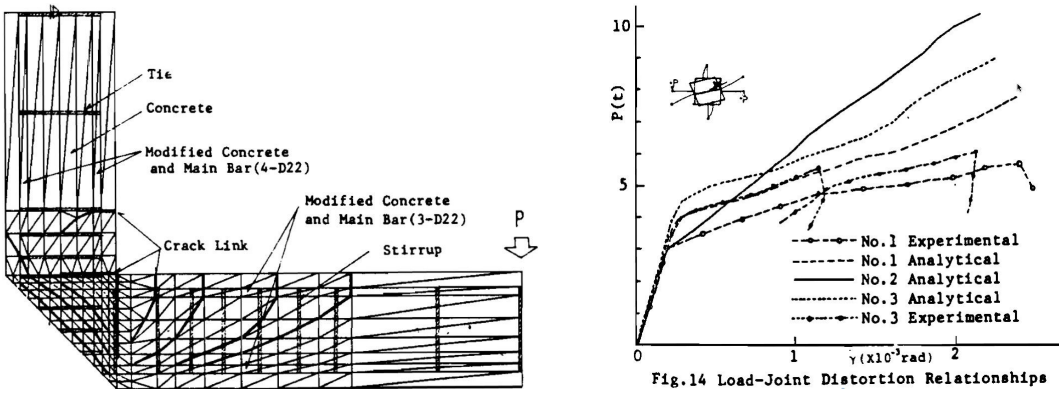

Figure A.2: Representative mesh and load-deflection response—Noguchi 1981 [157]

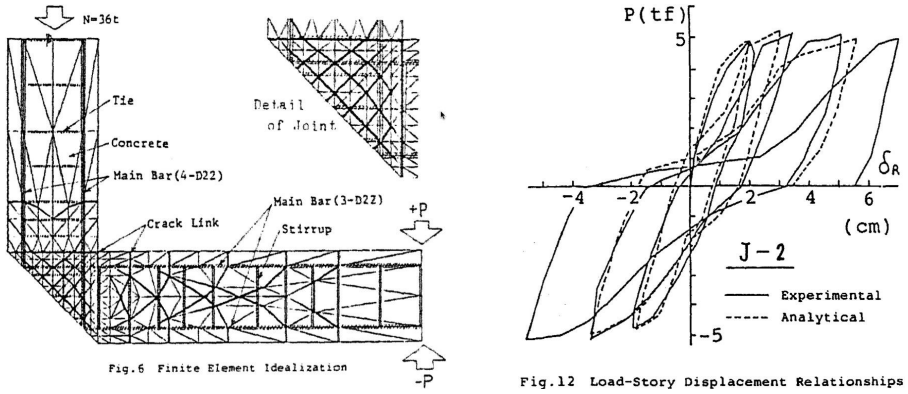

Figure A.3: Representative mesh and load-deflection response—Noguchi and Naganuma 1984 [165]

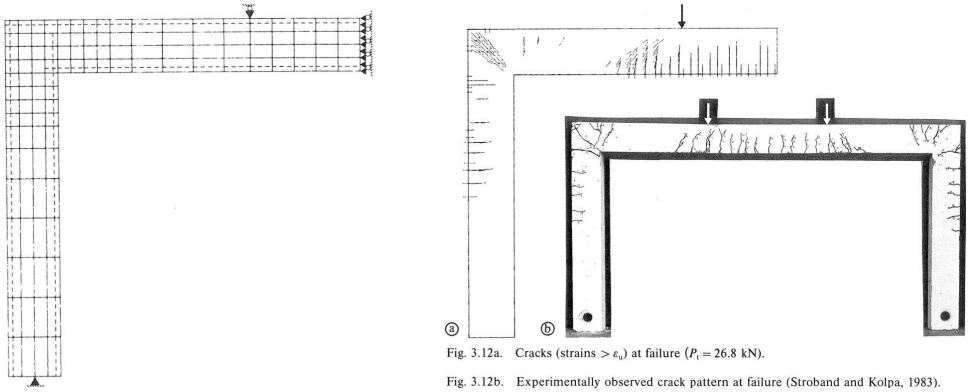

Fig. 3.12a. Cracks (strains $> \varepsilon_u$) at failure ($P_t = 26.8$ kN).

Fig. 3.12b. Experimentally observed crack pattern at failure (Stroband and Kolpa, 1983).

Figure A.4: Representative mesh and crack pattern response—Van Mier 1987 [222]

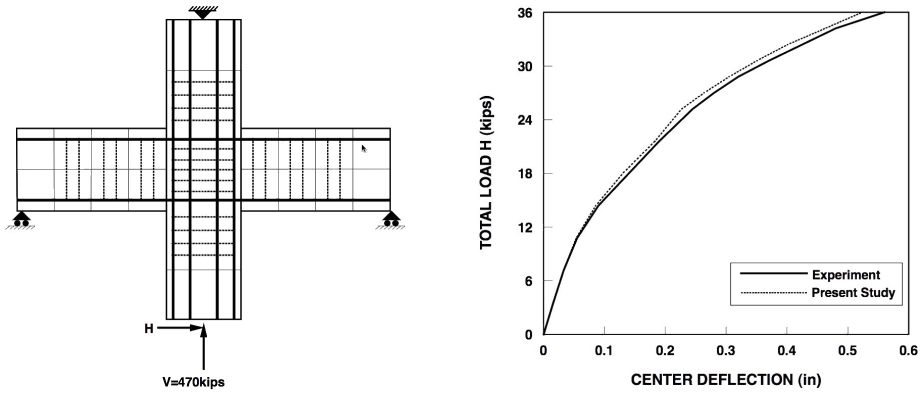

Figure A.5: Representative mesh and load-deflection response—Kwak and Filippou 1990 [113]

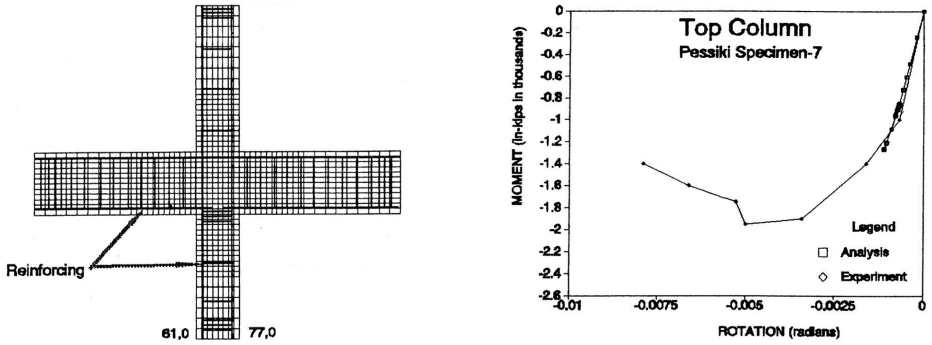

Figure A.6: Representative mesh and upper column moment-rotation response—Conley 1993 [39]

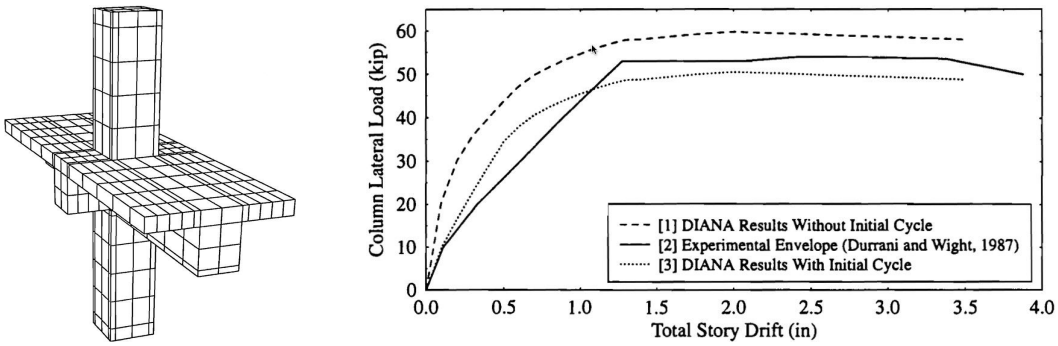

Figure A.7: Representative mesh and load-deflection response—Mosalam, Gergely, and White 1994 [152]

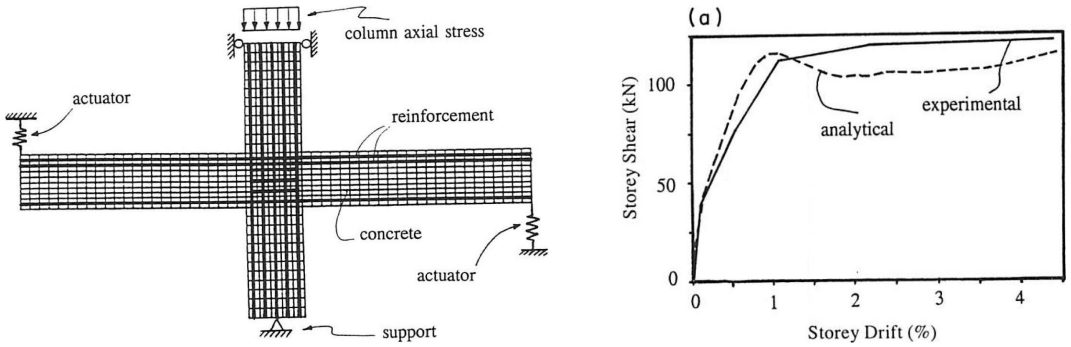

Figure A.8: Representative mesh and force-drift response—Pantazopoulou and Bonacci 1994 [173]

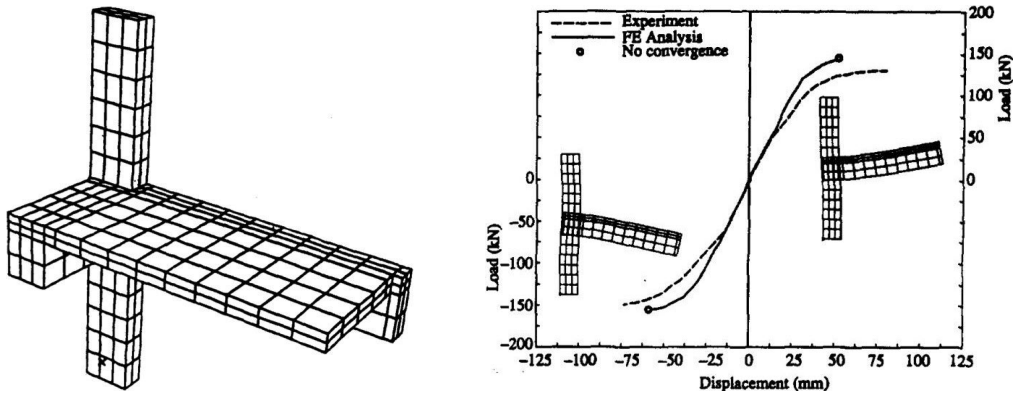

Figure A.9: Representative mesh and load-deflection response—Barzegar and Maddipudi 1997 [23]

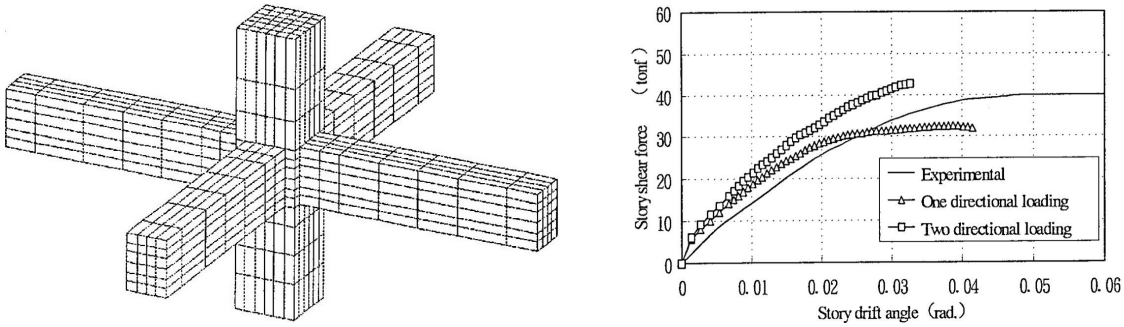

Figure A.10: Representative mesh and force-drift response—Noguchi and Kashiwazaki 1997 [159]

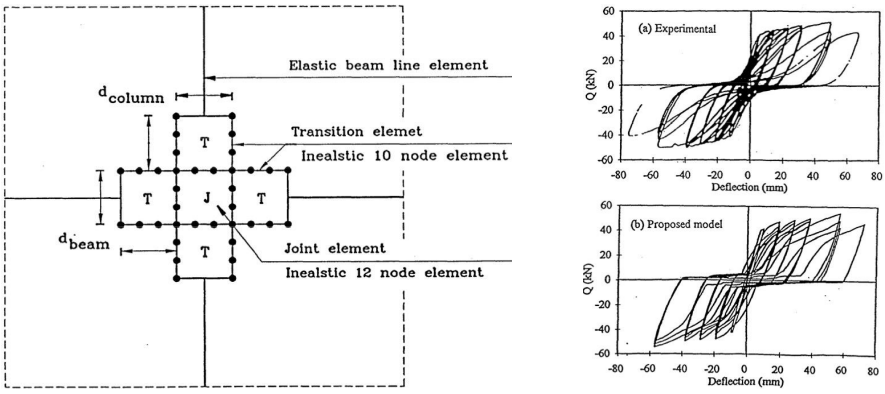

Figure A.11: Representative mesh and load-deflection response—Elmorsi, Kianoush, and Tso 1998 [55]

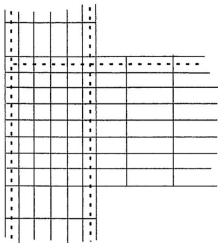

Joint stirrups	Predicted failure load kN	Observed failure load kN
None	62.7	118
T8.200[1]	81.2	-
T8.100[2]	104.8	130
T8.67	94.5	-

Figure A.12: Representative mesh and predicted failure load response—Vollum 1998 [230]

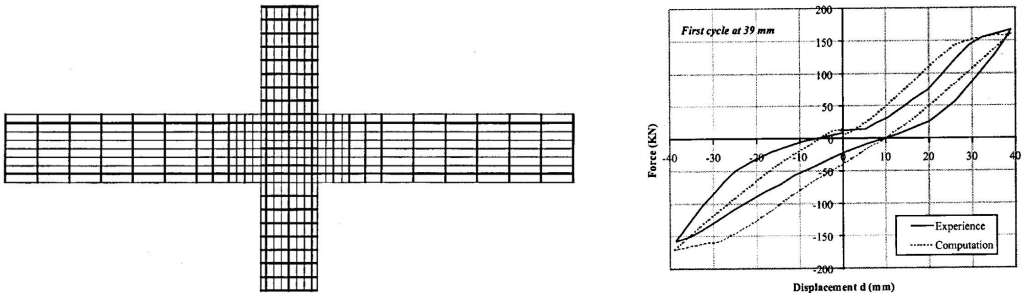

Figure A.13: Representative mesh and force-displacement response—Fleury, Reynouard, and Merabet 1999 [64]

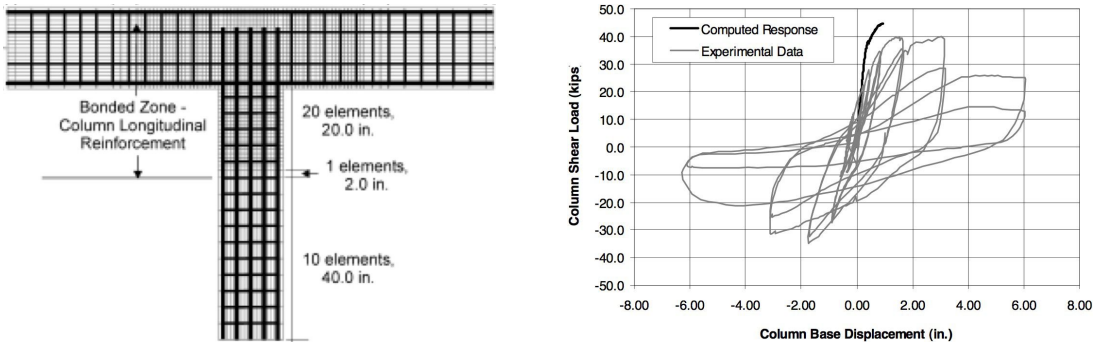

Figure A.14: Representative mesh and load-displacement response—Lowes 1999 [123]

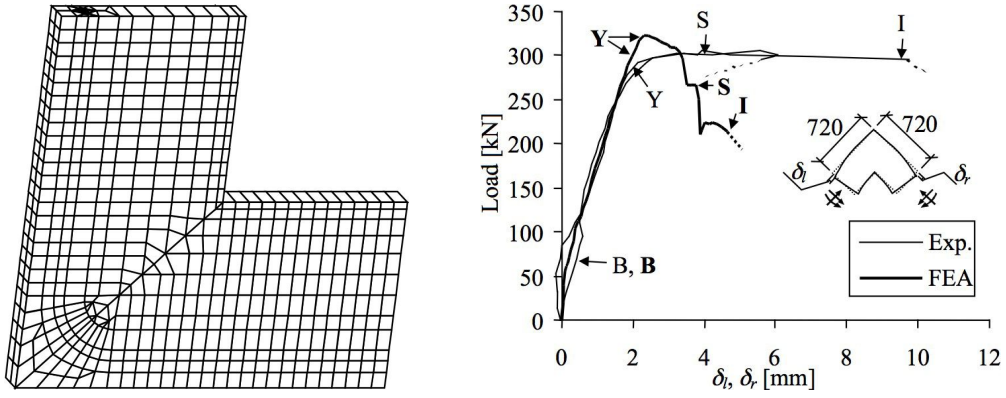

Figure A.15: Representative mesh and load-deflection response—Lundgren 1999 [129]

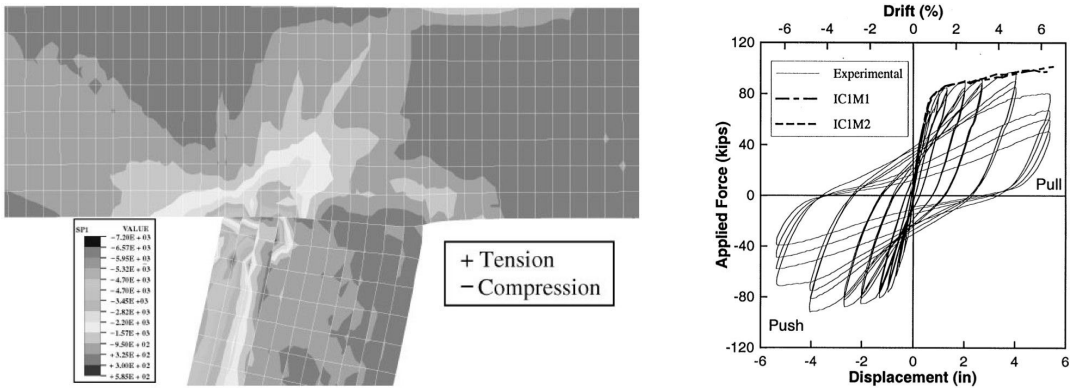

Figure A.16: Representative mesh and load-displacement response—Sritharan, Priestley, and Seibel 2000 [209]

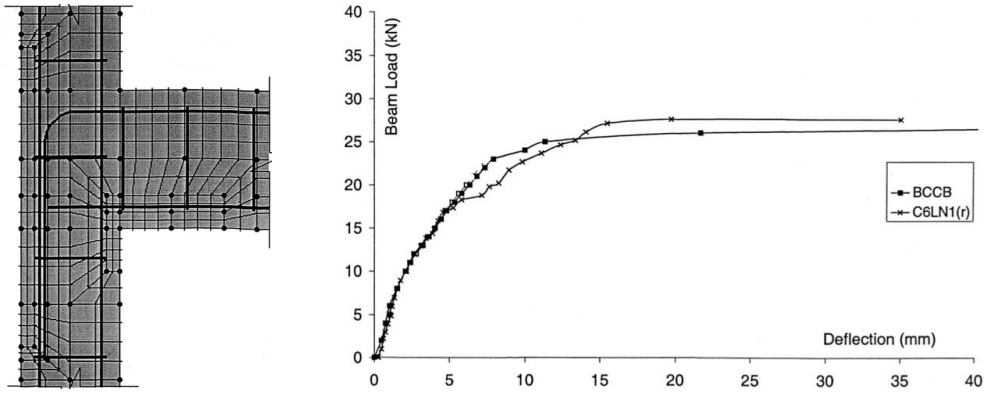

Figure A.17: Representative mesh and load-deflection response—Hamil 2000 [75]

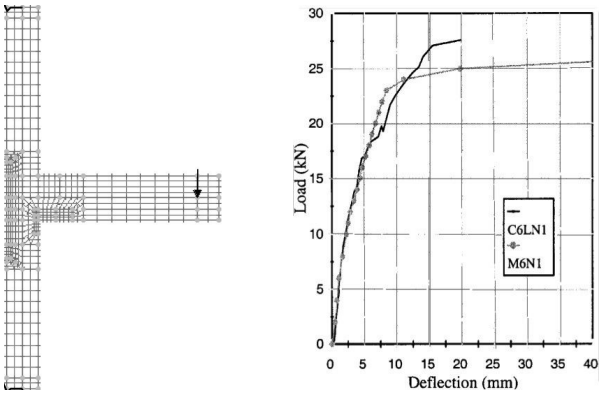

Figure A.18: Representative mesh and load-deflection response—Baglin and Scott 2000 [19]

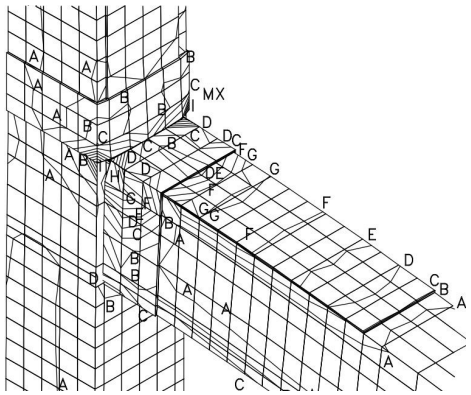

Figure A.19: Representative mesh—Parvin and Granata 2000 [181]

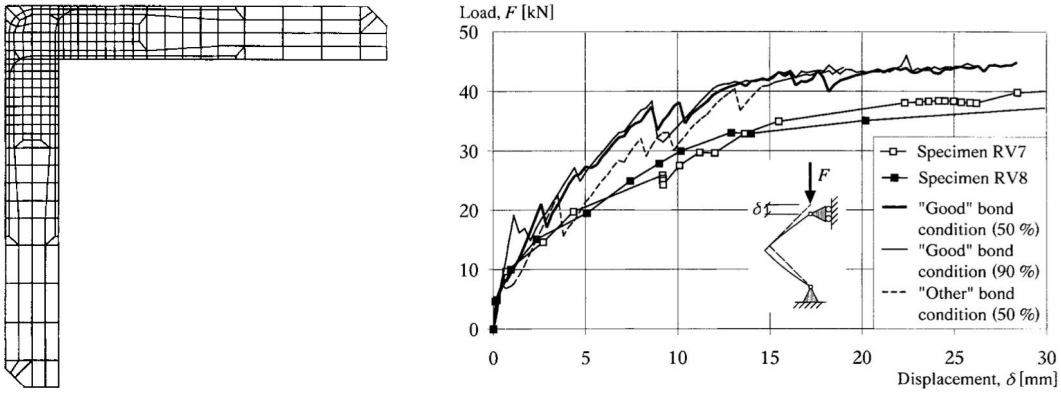

Figure A.20: Representative mesh and load-displacement response—Johansson 2000 [92]

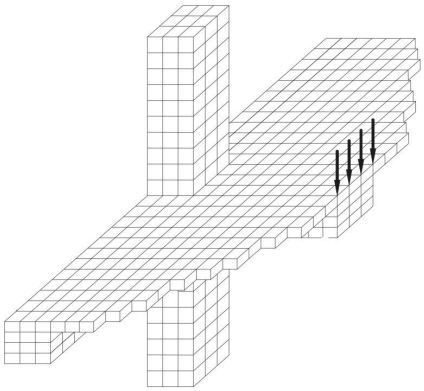

Figure A.21: Representative mesh—Emara and Hosny 2001 [59]

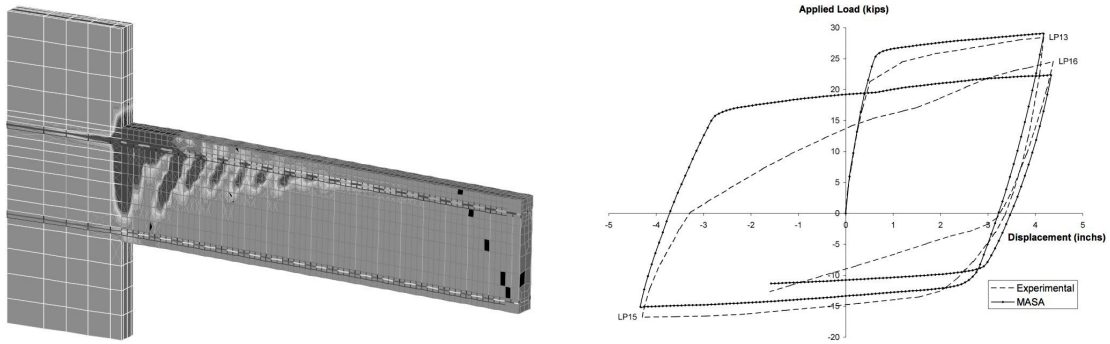

Figure A.22: Representative mesh and load-deflection response—Hoehler and Ožbolt 2001 [81]

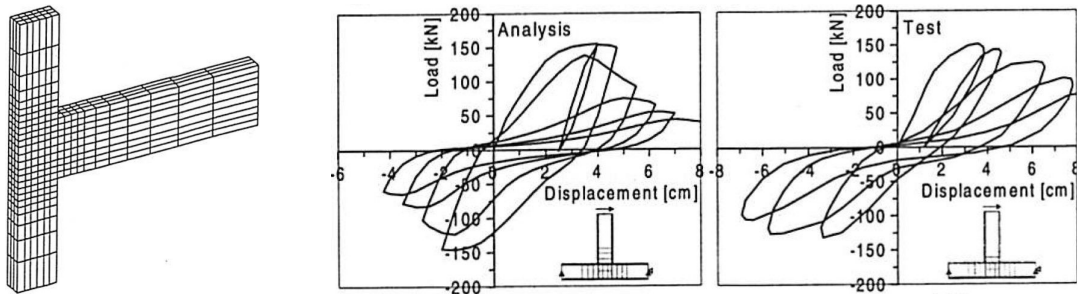

Figure A.23: Representative mesh and load-displacement response—Ožbolt, Mayer, and Vocke 2001 [168]

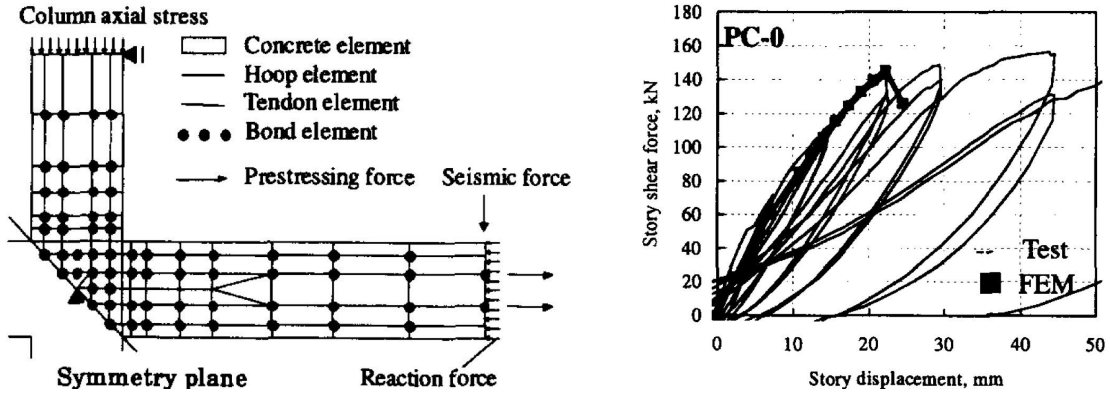

Figure A.24: Representative mesh and force-displacement response—Kashiwazaki and Noguchi 2001 [102]

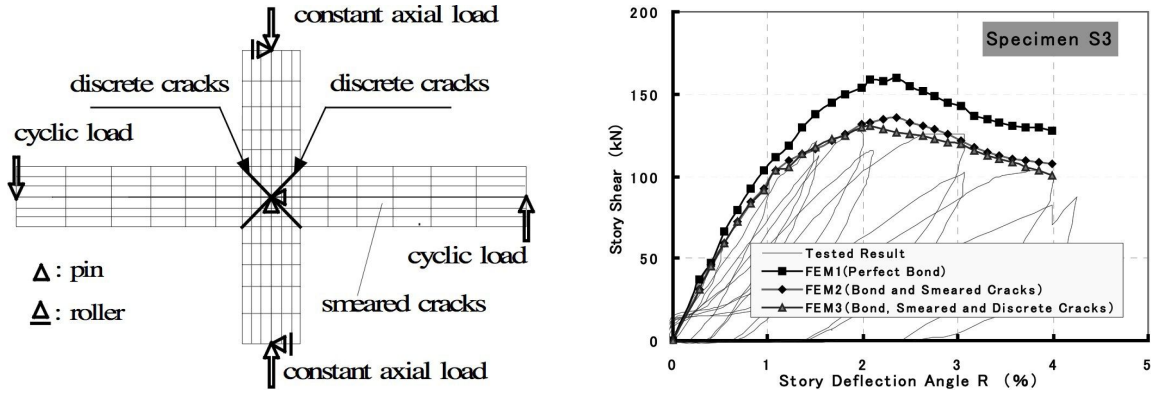

Figure A.25: Representative mesh and story shear response—Zhang, Noguchi, and Kashiwazaki 2002 [235]

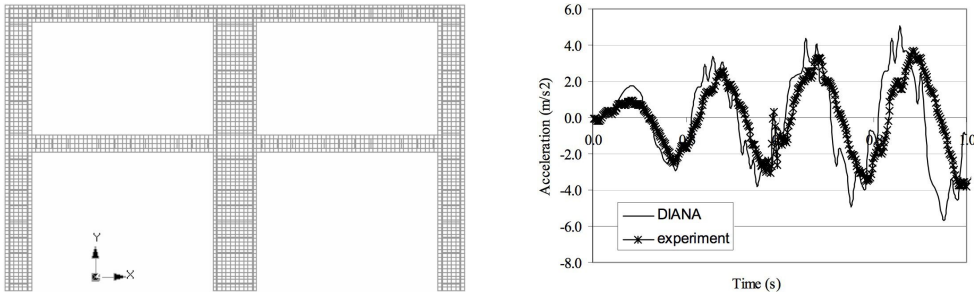

Figure A.26: Representative mesh and roof acceleration response—Quek and Bian 2002 [186]

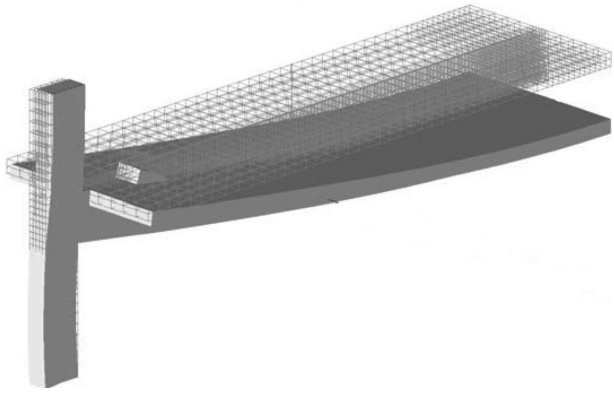

Figure A.27: Representative mesh—Cervenka 2002 [34]

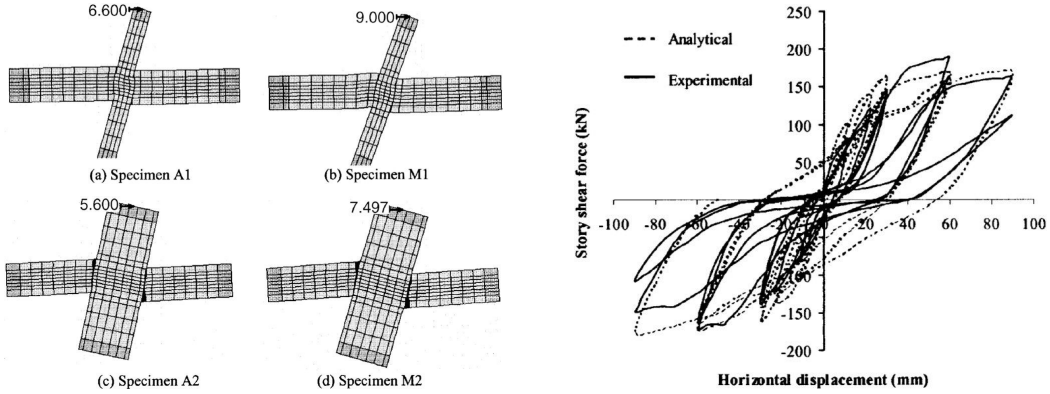

Figure A.28: Representative mesh and story shear force-deflection response—Li, Wu, and Pan 2003 [119]

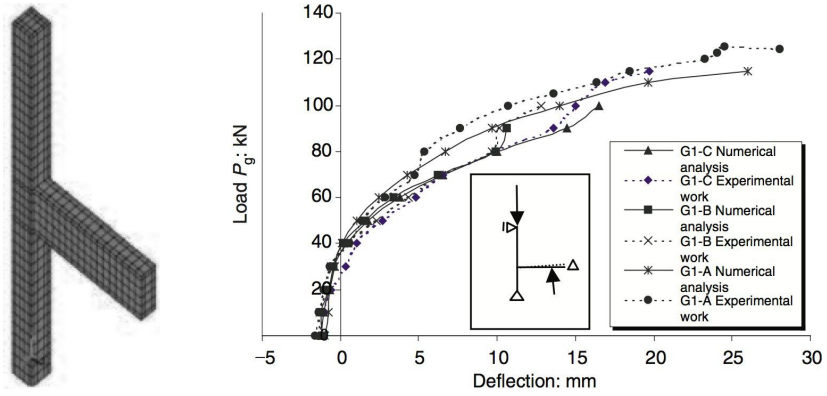

Figure A.29: Representative mesh and load-deflection response—El Nabawy Atta et al. 2004 [50]

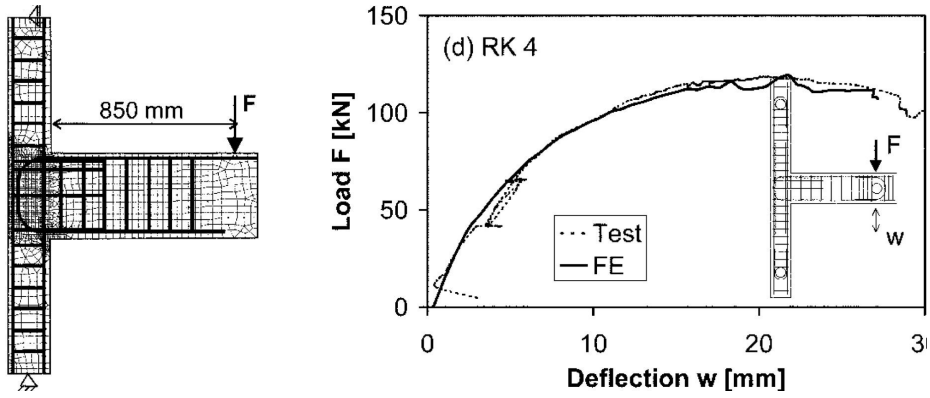

Figure A.30: Representative mesh and load-deflection response—Hegger, Sherif, and Roeser 2004 [79]

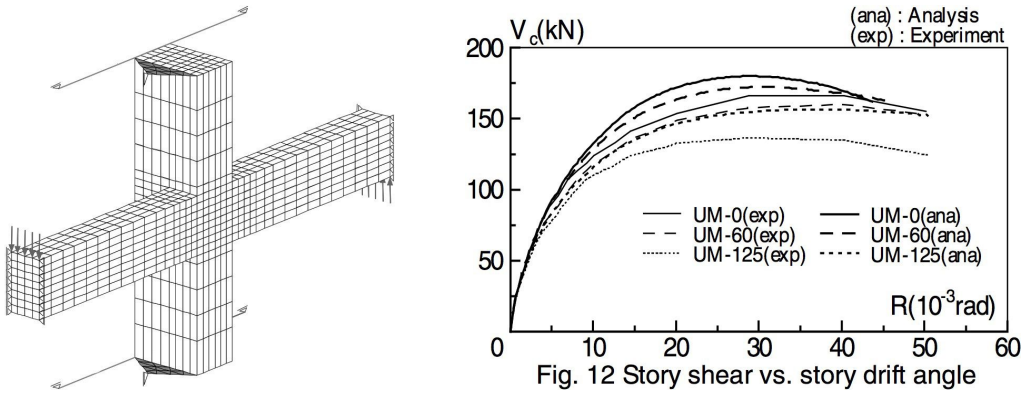

Figure A.31: Representative mesh and story shear response—Goto and Joh 2004 [69]

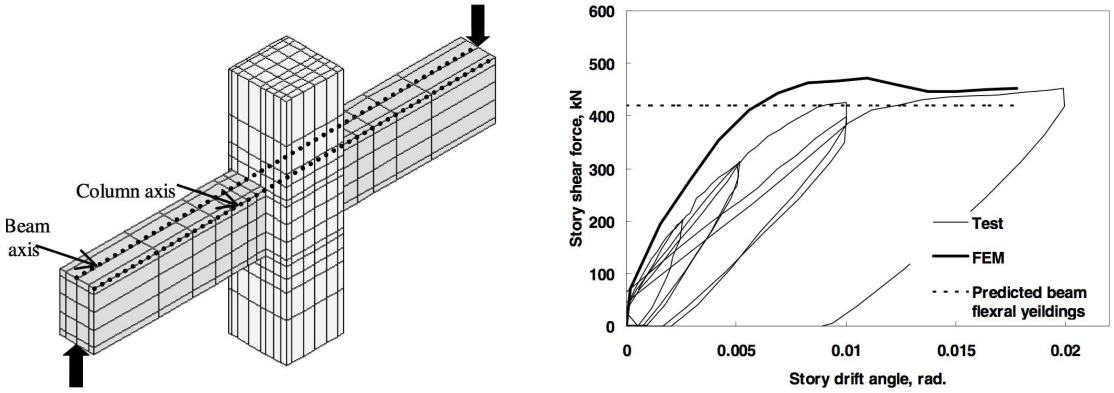

Figure A.32: Representative mesh and story shear-drift response—Kashiwazaki and Noguchi 2004 [103]

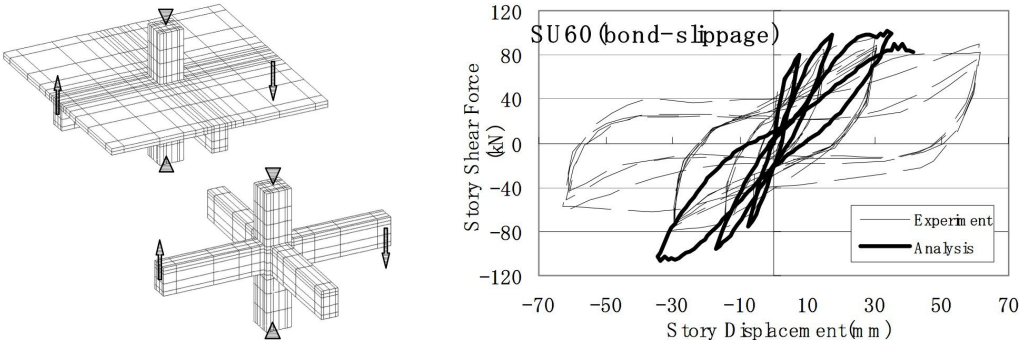

Figure A.33: Representative mesh and force-drift response—Noguchi and Kashiwazaki 2004 [160]

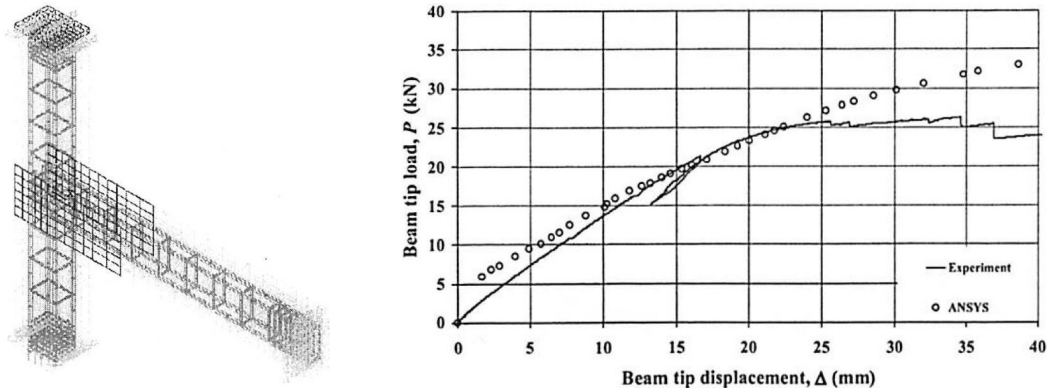

Figure A.34: Representative mesh and load-displacement response—Mahini 2005 [136]

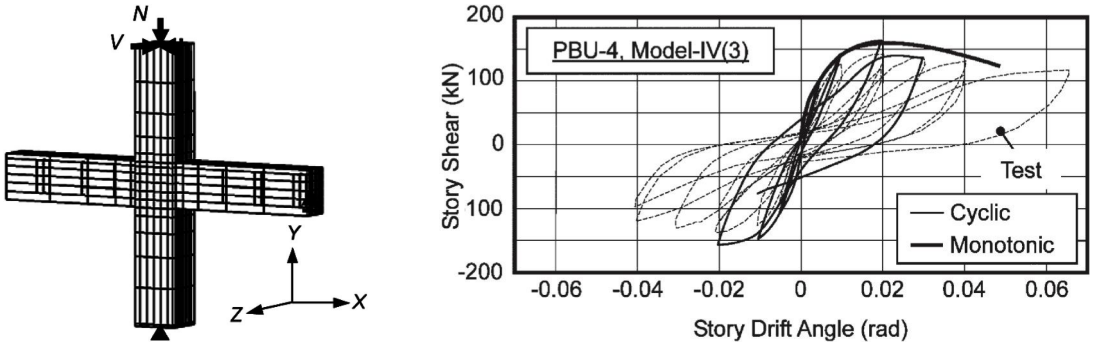

Figure A.35: Representative mesh and story shear force-drift response—Shirai, Tajima and Mishima 2006 [206]

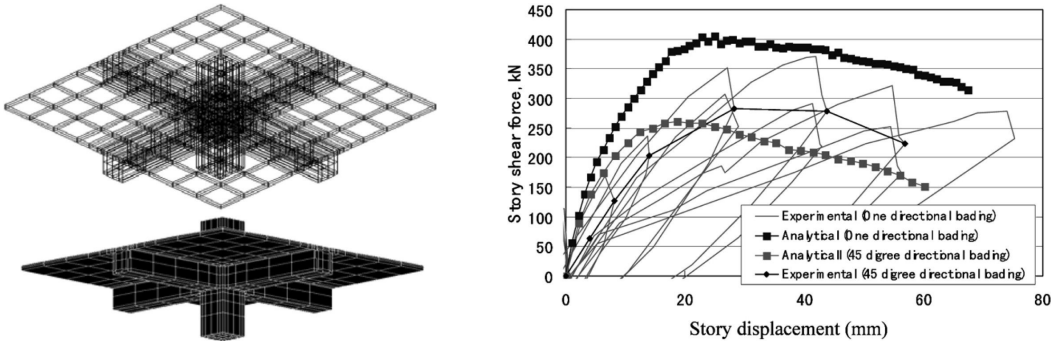

Figure A.36: Representative mesh and force-displacement response—Noguchi 2006 [158]

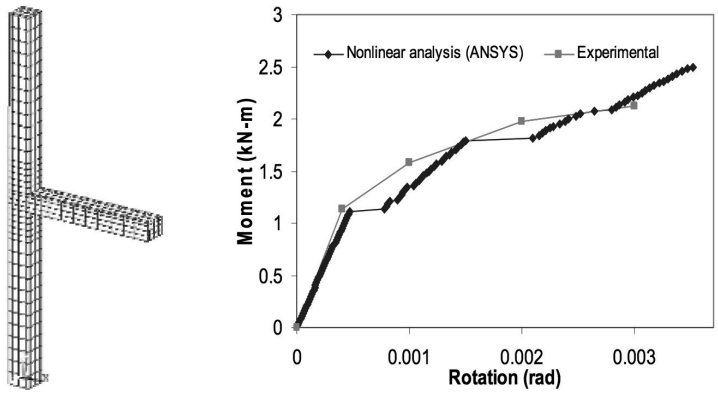

Figure A.37: Representative mesh and moment-rotation response—Mostofinejad and Talaeitaba 2006 [153]

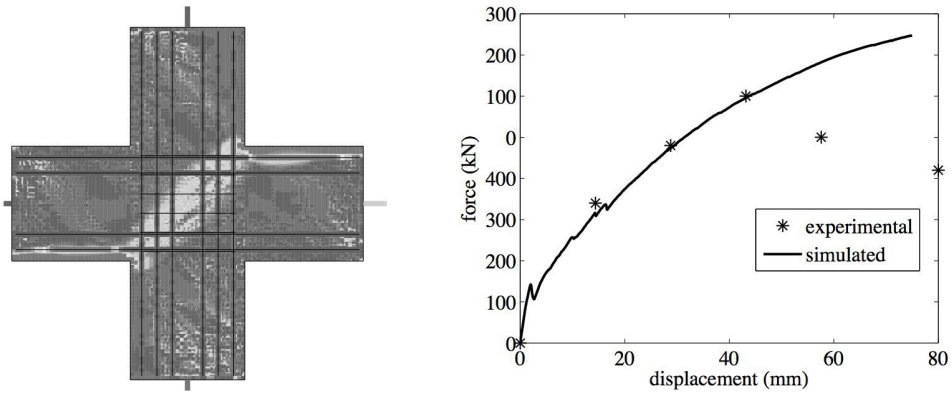

Figure A.38: Representative mesh and force-displacement response—Mitra 2007 [146]

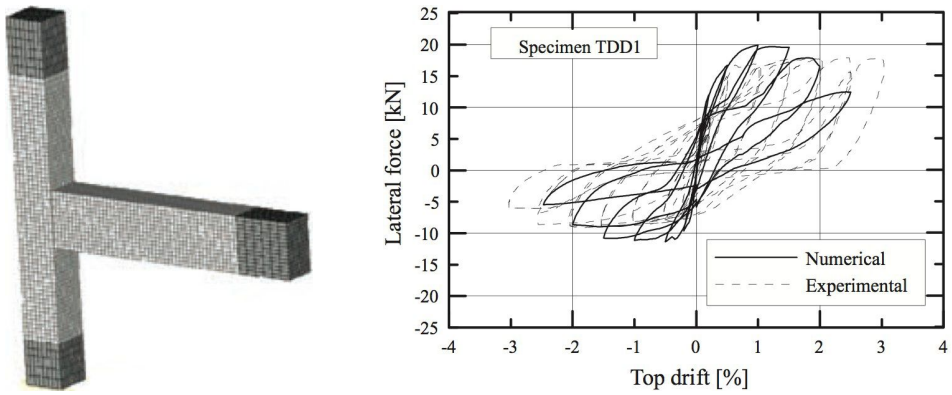

Figure A.39: Representative mesh and force-drift response—Eligehausen et al. 2008 [52]

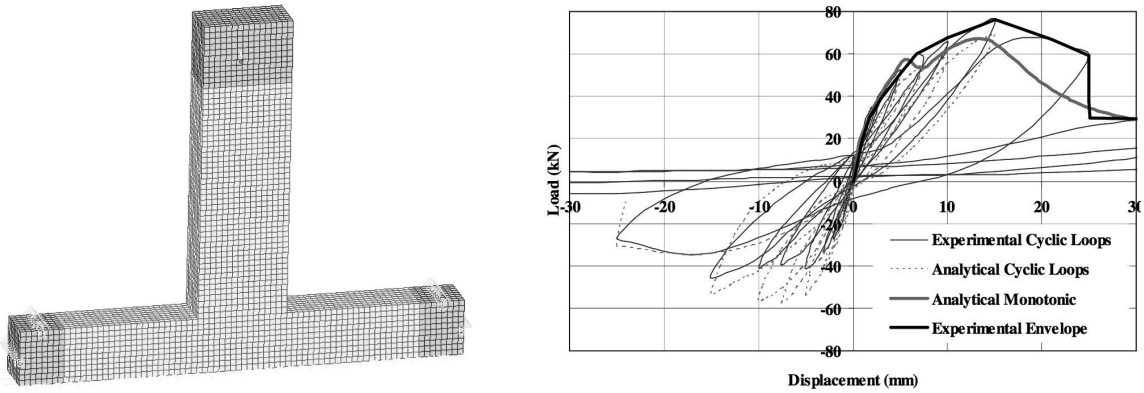

Figure A.40: Representative mesh and load-displacement response—Sharma, Eligehausen, et al. 2008 [203]

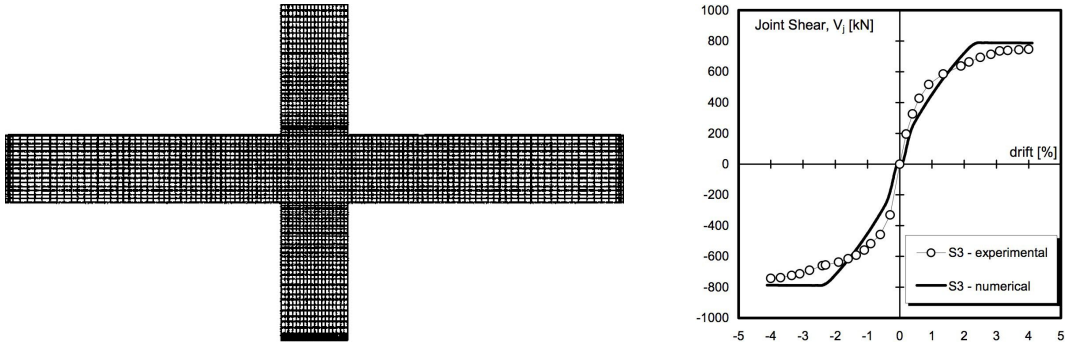

Figure A.41: Representative mesh and joint shear response—Manfredi, Verderame, and Lignola 2008 [140]

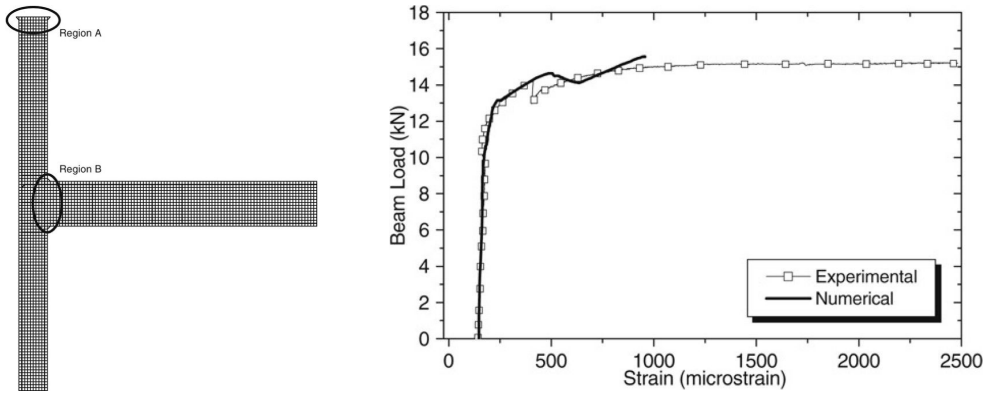

Figure A.42: Representative mesh and beam load vs. stirrup strain response—Haach et al. 2008 [73]

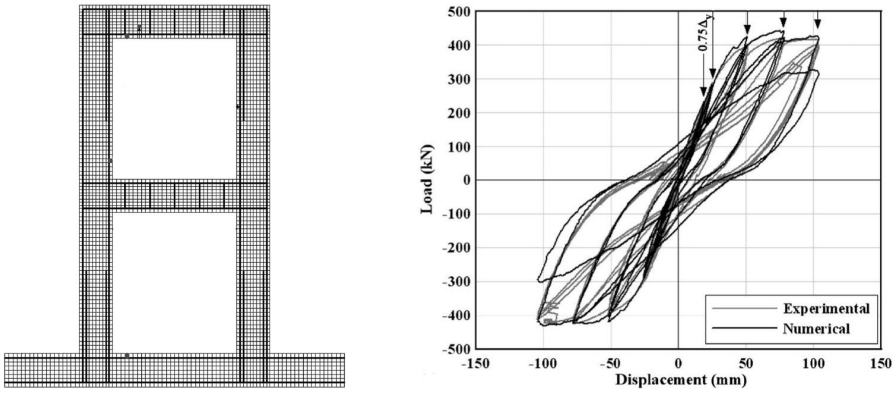

Figure A.43: Representative mesh and load-displacement response—Kim and Vecchio 2008 [106]

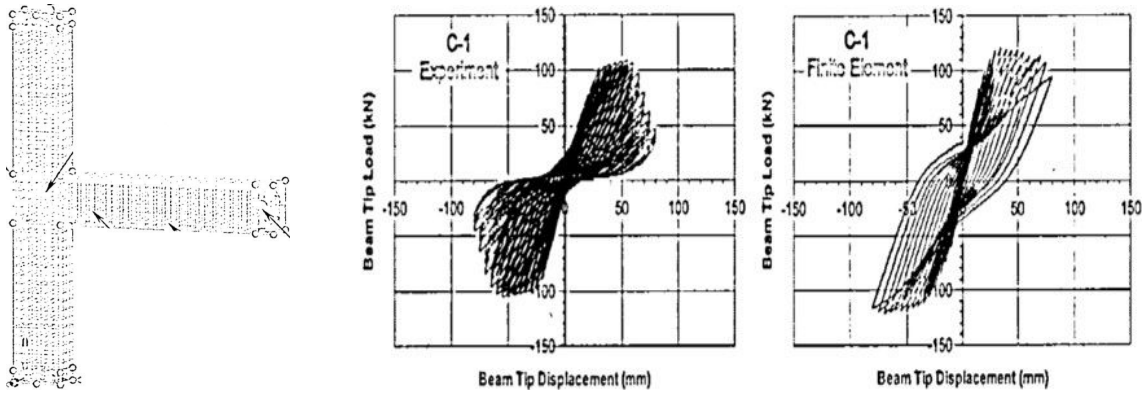

Figure A.44: Representative mesh and load-displacement response—Ibrahim and El-Badry 2008 [88]

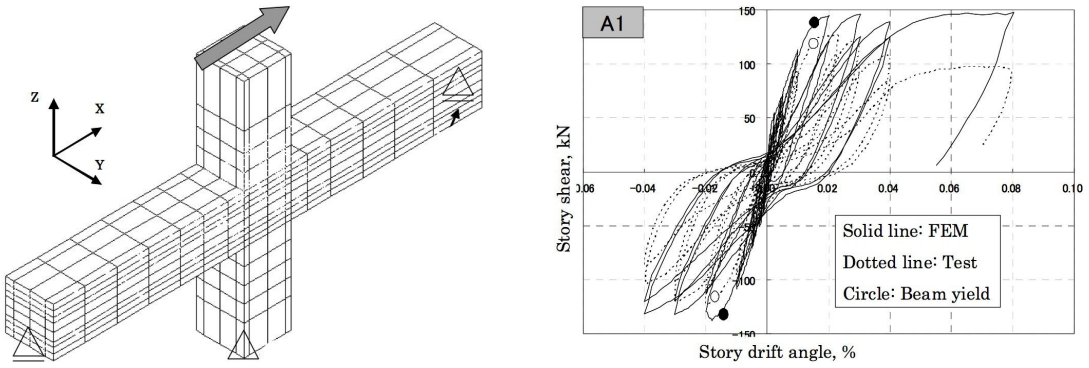

Figure A.45: Representative mesh and story shear response—Kashiwazaki and Noguchi 2008 [104]

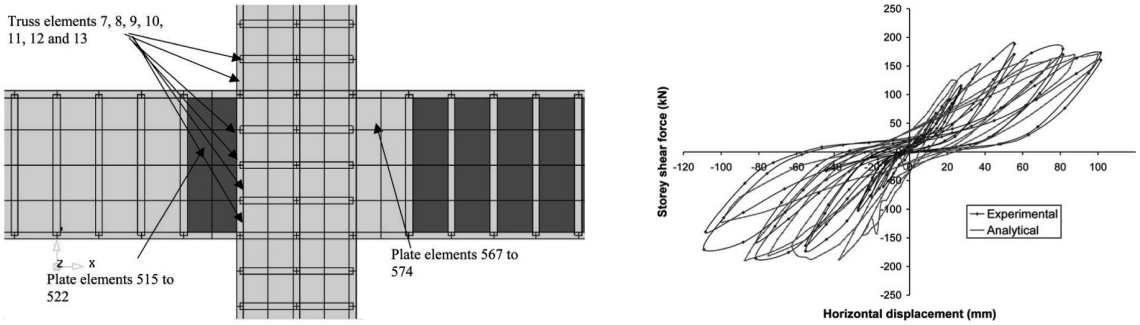

Figure A.46: Representative mesh and story shear response—Kulkarni, Li, and Yip 2008 [109]

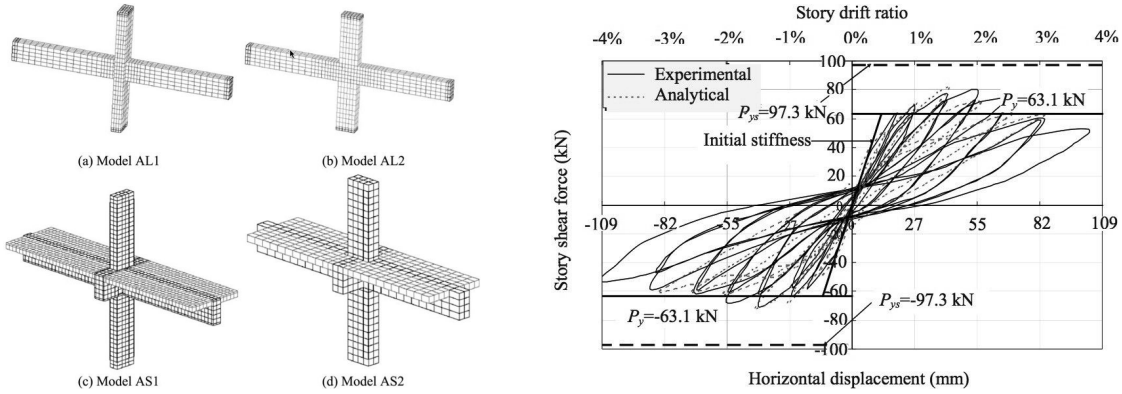

Figure A.47: Representative mesh and force-drift response—Li, Tran, and Pan 2009 [121]

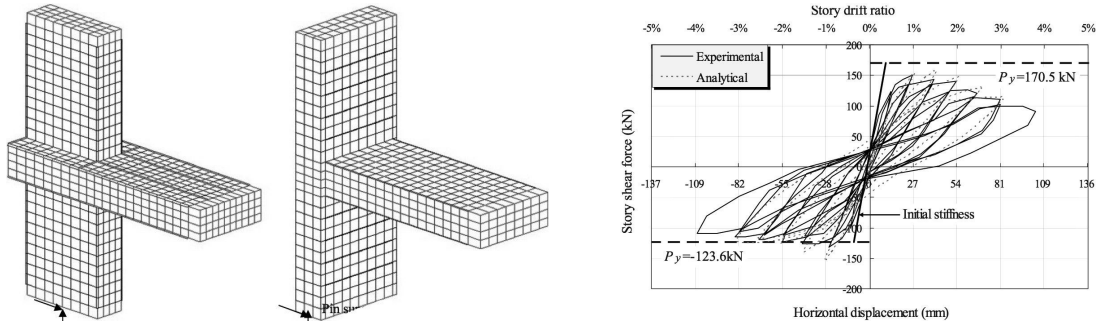

Figure A.48: Representative mesh and story shear response—Kulkarni and Li 2009/2010 [110]

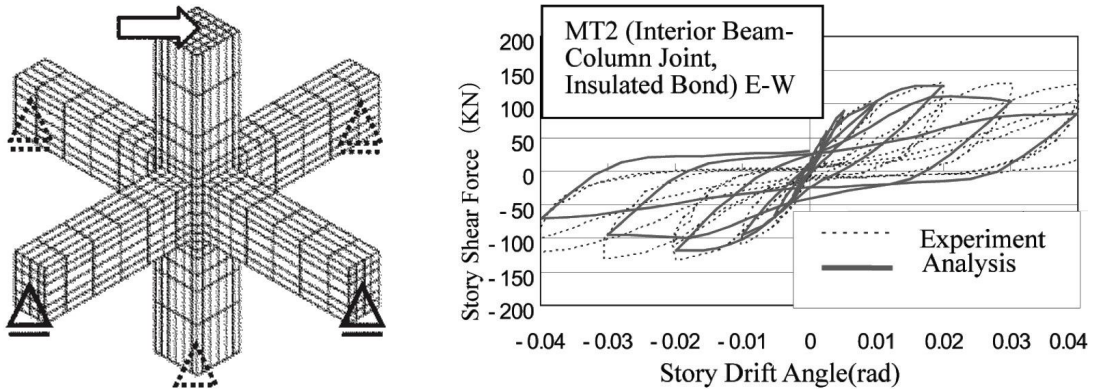

Figure A.49: Representative mesh and story shear response—Noguchi, Kashiwazaki, and Miura 2009 [163]

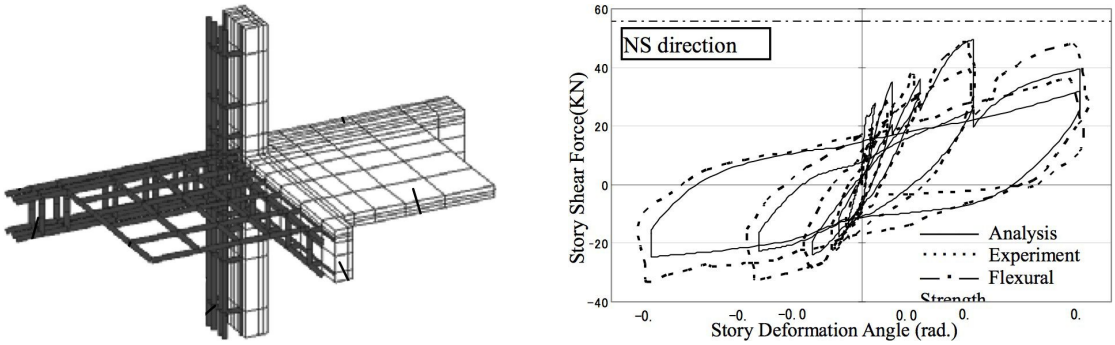

Figure A.50: Representative mesh and story shear response—Noguchi and Kashiwazaki 2009 [161]

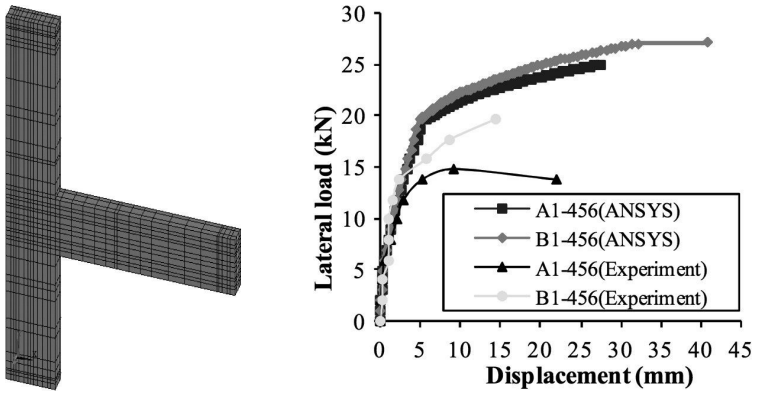

Figure A.51: Representative mesh and load-displacement response—Bhindi and Jaya 2010 [28]

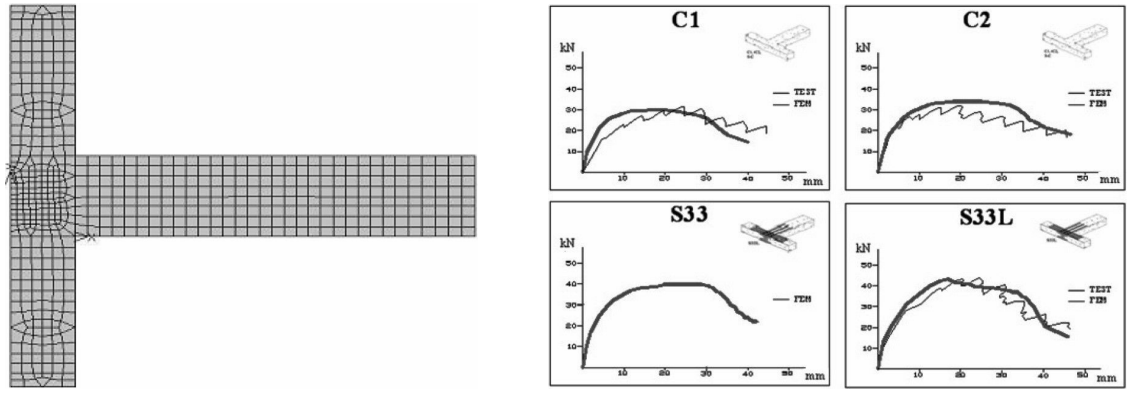

Figure A.52: Representative mesh and load-displacement response—Pennucci, Beccarini, and Ianniruberto 2010 [182]

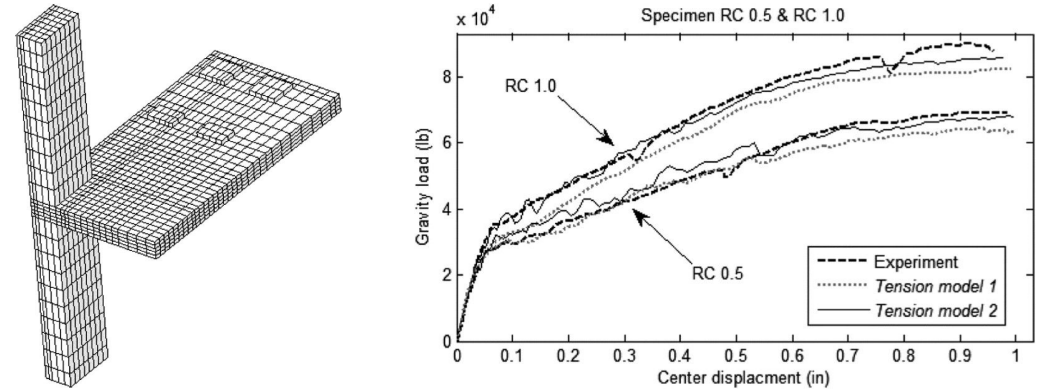

Figure A.53: Representative mesh and force-displacement response—Kang et al. 2011 [97]

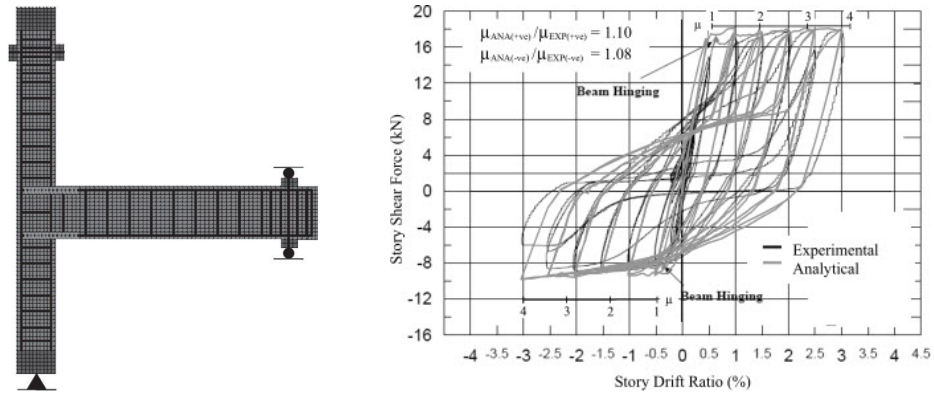

Figure A.54: Representative mesh and column shear-drift response—Sagbas, Vecchio, and Christopoulous 2011 [192]

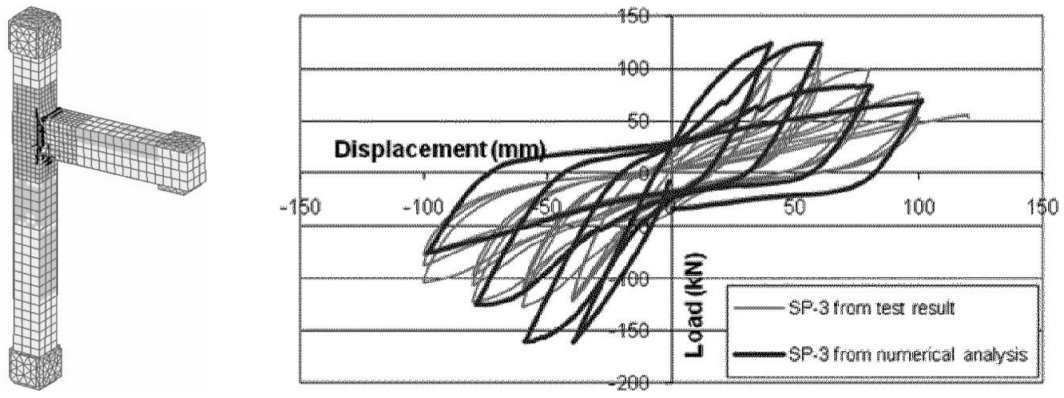

Figure A.55: Representative mesh and load-displacement response—Sasmal et al. 2011 [195]

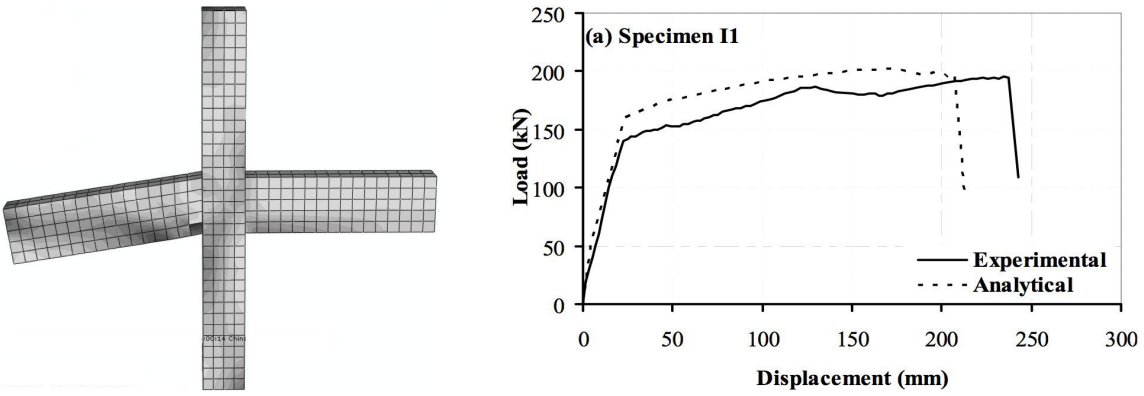

Figure A.56: Representative mesh and load-displacement response—Kai and Li 2011 [94]

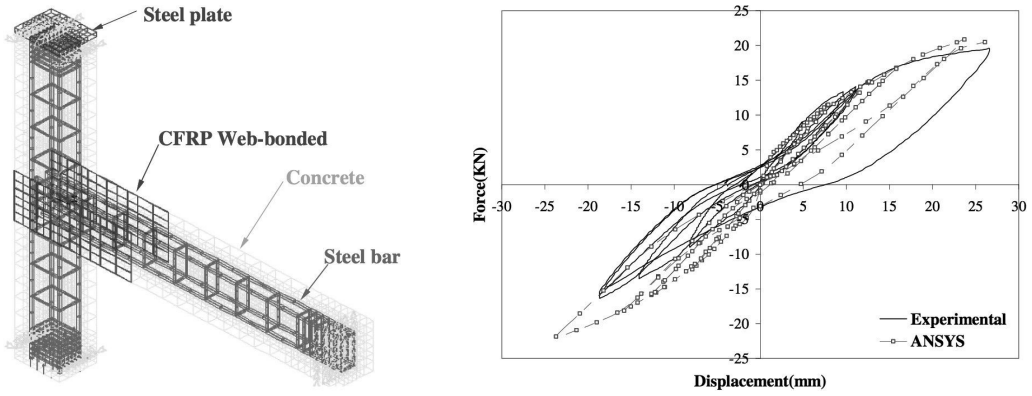

Figure A.57: Representative mesh and force-displacement response—Mahini and Ronagh 2011 [137]

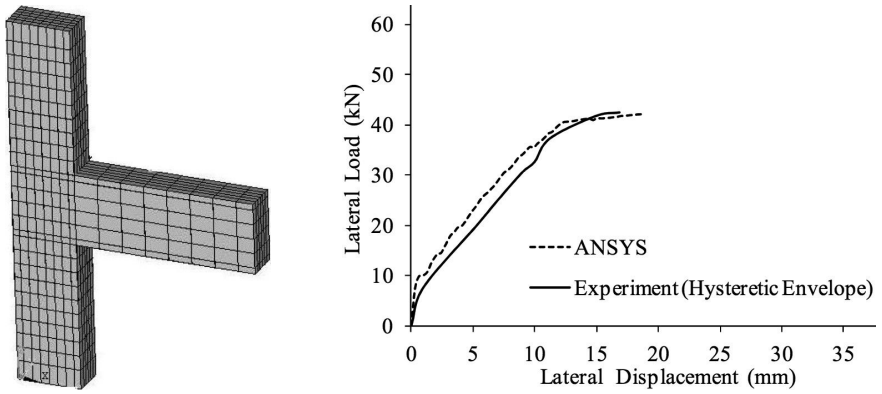

Figure A.58: Representative mesh and load-deflection response—Al-Haddad et al. 2011 [12]

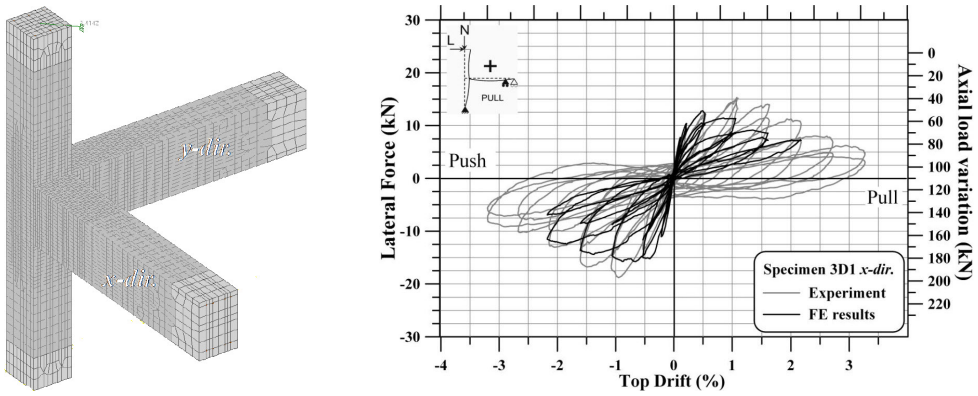

Figure A.59: Representative mesh and force-drift response—Akguzel 2011 [9]

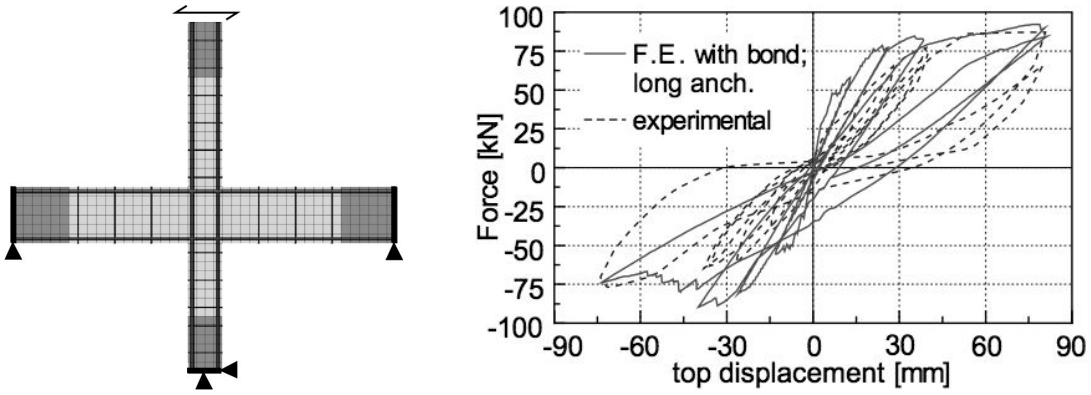

Figure A.60: Representative mesh and force-displacement response—Mazzarolo et al. 2012 [141]

APPENDIX B

SUPPORTING CODE AND INPUT FILES

B.1 Disclaimer

All code provided in this appendix is available on an "as-is" basis with no warranty as to its correctness or completeness. It has not been subjected to quality control or quality assurance processes. Use at your own risk.

B.2 Software Used and Computer Specifications

All analytical results presented in this document were generated using a combination of DIANA and Midas FX+ for model pre- and post-processing. The Python programming language was used throughout this research for all data processing, numerical computation, and production of plots. Python was chosen because it is open source, free, multi-platform, easy to use, and has excellent scientific computing libraries (NumPy, SciPy, and Matplotlib). The specific version numbers for all packages employed in simulations and supporting code are listed in Table B.1.

All computations were completed on a workstation running Windows 7 Enterprise 64-bit with 6 GB of RAM and an Intel Core i7 Processor running at 2.67 GHz.

B.3 Process for Model Creation, Analysis, and Results Visualization

The following section outlines the steps necessary to complete an entire analysis with DIANA as used for all models presented in this document. A flowchart illustrating these steps is provided in Figure B.1.

Table B.1: Software Versions Used

Software Name	Version Number
DIANA	9.4.4
Midas FX+	3.1.0
Enthought Python Distribution	7.2-2
Python	2.7.2
NumPy	1.6.1
SciPy	0.10.0
Matplotlib	1.1.0
DigitizeIt	1.5.8b

The model creation process begins in FX+ for DIANA. The subassemblage geometry is reproduced using a collection of solids, defined by `Geometry › Primitive Feature › Box`, which are placed adjacently to build the subassemblage geometry. Each region is assigned its own box, such as the joint core, beams, and stiffened regions near supports. The geometry of each reinforcing bar segment is placed using `Geometry › Curve › Create 3D › Polyline (Wire)`. Next, geometric section (`Analysis › Property`) and material (`Analysis › Material`) properties must be created for each region of the mesh and reinforcing bar segment. At this stage, only linear elastic properties are specified; these will be later replaced with nonlinear material definitions. These properties must be created prior to mesh generation. The concrete mesh regions are generated using `Mesh › Map Mesh › Solid` while reinforcing bar elements are generated using `Mesh › Auto Mesh › Edge`.

Once the mesh has been generated, boundary conditions are generated using `Analysis › BC › Constraint`. Then, displacement controlled loads are applied via `Analysis › Load › Displacement`. Force and pressure loadings may be similarly specified. Cyclic displacements were not specified at this stage; instead, a "dummy" unit displacement was created and later manually replaced with the full displacement histories in the text input.

The final step of model creation within FX+ is to export the model to text input.

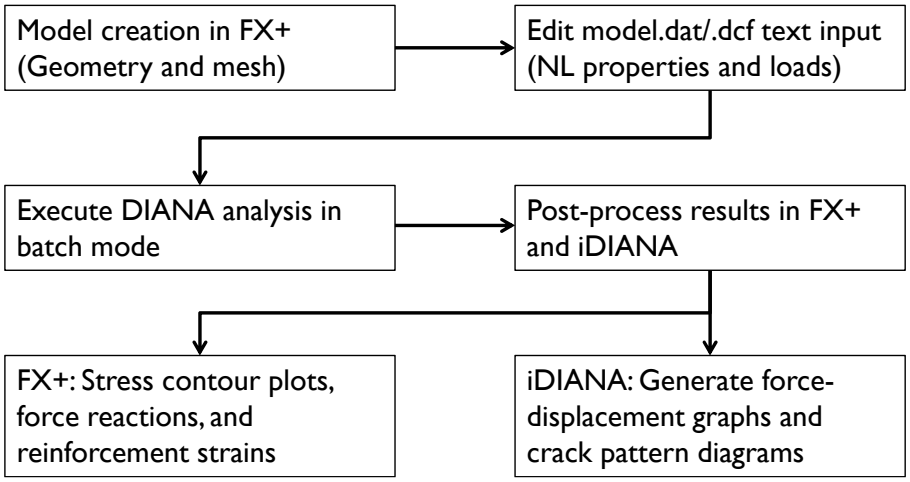

Figure B.1: DIANA Simulation Flowchart

The file may be exported via `Analysis > Edit model with DIANA mesh-editor`. This will open the DIANA Mesh Editor where the `.dat` file may be exported via `File > Save As`. A linear elastic analysis may be easily launched from this graphical user interface for model checking. For convenience, all model files are given the same name: `model.*`.

The remainder of the model is manually created in the file `model.dat` by manipulating the raw text input. The first step in this stage is to replace the elastic material properties for concrete and steel reinforcement elements with nonlinear material properties. These definitions were generated using the function `materials` in the Python file `DIANA.py`. Then, reinforcing bars are converted from embedded reinforcements with perfect bond to bond-slip reinforcements by modifying the `'DATA'` and `'GEOMETRY'` assignments. The final text input for nonlinear material properties as well as bond-slip reinforcement data assignments is provided for the beam-column joint models later in this appendix. Then, cyclic load histories must be generated and incorporated in the input files. These inputs are generated using custom Python scripts for each analysis, which are also provided in the following sections. The commands for step execution and nonlinear solution controls are stored in the file `model.dcf`.

The analysis is then executed in batch mode on the Windows command line. Since both the `*.dat` and `*.dcf` files share the common name (`model.*`), the analysis is invoked

simply by the terminal command `DIANA MODEL`. The DIANA analysis engine performs the commands in the file `model.dcf` using the model definition from the file `model.dat`, and the real-time progress of the simulation may be monitored by reviewing the file `model.out`.

Once the analysis has completed, the results are post-processed using both FX+ and iDIANA. FX+ was typically used for model review and checking general results such as deformed shape, stress and strain contour plots, and support reactions. Then, iDIANA was used to generate force-displacement curves using the `UTILITY TABULATE PRINTFILE` and `PRESENT GRAPH RESULTS` commands. This combination of commands writes the xy-data for each plot to a text file. These results are then plotted using the `DIANA.py` Python scripts; the function `readDianaOutput` was used to read in the output of the `UTILITY TABULATE` command, and the `plotExpFea` function was used to plot numerical vs. experimental results. Crack patterns were visualized in iDIANA by invoking the result `RESULTS GAUSSIAN EL.EKNN1 EKNN`, followed by the `PRESENT DISC` command. The series of commands used to generate these results can be executed within iDIANA using the `*.fgi` batch command file format.

B.4 DIANA.py

The program `DIANA.py` was developed as an archive of helper code to aid in automation of analyses using DIANA. It is used to generate (perhaps among other things):

- Material property computations
- Uniaxial consitutive response curves
- FEA output filters
- DIANA output parsers
- DIANA material definition input

E:/Dropbox/PHD/SIM/diana.py

```
"""
Name:   diana.py
Author: JBD
Units:  Newtons, mm, MPa
"""

#============================================================
#  To use diana.py
#
#  1. Place diana.py in Python path, such as:
#     'C:/Python27/Lib/site-packages/diana.py'
#  2. Invoke in a Python script as below using the command
#     'import diana'
#  3. Call any function within diana.py as:
#     'fcp_mpa = diana.psiToMpa(fcp_psi)'
#

#============================================================
#  Dependencies
#
import numpy as np
from math import *
from pylab import *
import matplotlib
import sys
from scipy import signal

#============================================================
#  Print header
#
print "Using DIANA python module"

#============================================================
# GENERAL HELPER FUNCTIONS
#

def psiToMpa(x): return 0.006895*x

def filterEveryN(data,n=10):
    """
    Accept a NumPy array and return array with every nth point
    """
    ntot = data.shape[0]
    pts = int(ntot/n)
    print "reduced number of points =", pts
    data2 = np.zeros(pts)
    for i in range(0, pts):
        data2[i] = data[i*n]
    return data2

def scaleArray(data,x0=1.0,x1=1.0):
    data[:,0] = data[:,0]*x0
    data[:,1] = data[:,1]*x1
    return data

def logDist(x1,x2,npts,reverse=False):
    """
    Map logarithmic distribution of points between
    (0.0,1.0) to (x1,x2).
    If reverse=True, reverse the order of the log
    distribution so points are concentrated toward
    x2 instead of x1.
    """
    en = np.logspace(0,1,npts)
```

```
65          if reverse == 1:
66              enrev = en[::-1]; en = enrev
67          xdist = x1 + (en-en[0])*(x2-x1)/(en[npts-1]-en[0])
68          return xdist
69
70      def printCurve(name,dat1,dat2):
71          npts = len(dat1)
72          print "    ",name,"", dat1[0], dat2[0]
73          for n in range(1,npts):
74              print "            ", dat1[n], dat2[n]
75
76      def readDianaOutput(name):
77          """
78          This function accepts a string containing the name of a
79          text file of DIANA output generated by the command:
80          "PRESENT GRAPH NODE n". It ignores all lines beginning
81          with ";" and stores the 2nd and 3rd columns of remaining
                data.
82          """
83          print 'Reading input from file: ',name
84          result = np.zeros((25000,2))
85          result = np.loadtxt(name,comments=';',delimiter=',',
                usecols=(1,2),unpack=False)
86          xdat = result[:,0]
87          ydat = result[:,1]
88          return xdat,ydat
89
90      def readDianaOutputSing(name):
91          """
92          This function accepts a string containing the name of a
93          text file of DIANA output generated by the command:
94          "PRESENT GRAPH NODE n". It ignores all lines beginning
95          with ";" and stores the 3nd column of remaining data.
96          """
97          print 'Reading input from file: ',name
98          result = np.zeros((25000,1))
99          result = np.loadtxt(name,comments=';',delimiter=',',
                usecols=(1,2),unpack=False)
100         dat = result[:,1] # extract column 3 only
101         return dat
102
103     def plotAnaFea(xana,yana,xfea,yfea,xlabel,ylabel,
104             xmin=-1.,xmax=-1.,ymin=-1.,ymax=-1.):
105         """
106         Plot analytical vs FEA response.
107         """
108         fig = plt.figure()
109         ax = fig.add_subplot(111)
110         ax.plot(xana,yana,'-',color='k',linewidth=1.0,label="ANA")
111         ax.plot(xfea,yfea,'o',color='r',linewidth=0.5,alpha=0.75,
                ms=5.0,label="FEA")
112         ax.legend()
113         # if xmin>-0.9 :
114         ax.axis([xmin,xmax,ymin,ymax]) # ,xmin,xmax,ymin,ymax
115         ax.set_xlabel(xlabel)
116         ax.set_ylabel(ylabel)
117         savefig('plotAnaFea.pdf')
118         show()
119         return
120
121     def plotExpFea(xexp,yexp,xfea,yfea,xlabel,ylabel,
```

```
122             xmin=-1.,xmax=1.,ymin=-1.,ymax=1.,explabel=-1,fealabel
                    =-1,legendloc=1,last=False,filter=1,filename='
                    plotExpFea.pdf',showStats=True,datum=0.0,xstyle='--
                    ',ystyle='-'):
123         """
124         Plot experimental vs FEA response.
125         """
126         # Compute some stats
127         # Var 'datum' corrects stats when cycling around non-zero
                datum
128         ratioPos  = (amax(yfea)-datum)/(amax(yexp)-datum)
129         ratioNeg  = (amin(yfea)-datum)/(amin(yexp)-datum)
130         print 'Ratio of FEA/EXP (pos) = ',ratioPos
131         print 'Ratio of FEA/EXP (neg) = ',ratioNeg
132         # Create figure
133         fig = plt.figure()
134         ax = fig.add_subplot(111)
135         if explabel<0: explabel="EXP"
136         if fealabel<0: fealabel="FEA"
137         ax.plot(xexp,yexp, xstyle,color='b',linewidth=0.5,label=
                explabel,dashes=(1,1))
138         ax.plot(xfea,yfea, ystyle,color='k',linewidth=1.0,label=
                fealabel)
139         if last==1:
140             np=len(xfea)
141             ax.plot(xfea[np-1],yfea[np-1],'x',color='r',ms=10,
                    markeredgewidth=3)
142         if showStats==1:
143             rc('font', family='sans-serif')
144             ax.text(xmin*0.9,ymax*0.95,r"$\frac{FEA_{max}}{EXP_{
                    max}} = $ %.3f" % (ratioPos),verticalalignment='top'
                    ,fontsize=9)
145             ax.text(xmin*0.9,ymax*0.70,r"$\frac{FEA_{min}}{EXP_{
                    min}} = $ %.3f" % (ratioNeg),verticalalignment='top'
                    ,fontsize=9)
146         ax.legend(loc=legendloc)
147         ax.axis([xmin,xmax,ymin,ymax])
148         ax.set_xlabel(xlabel)
149         ax.set_ylabel(ylabel)
150         savefig(filename, transparent=True)
151         show()
152         return
153
154     def plotSensitivity(xexp,yexp,x1,y1,x2,y2,x3,y3,xlabel,ylabel,
155             xmin=-1.,xmax=1.,ymin=-1.,ymax=1.,label1=-1,label2=-1,
                    label3=-1,label4=-1,legendloc=1,last=False,filter
                    =1,filename='plotExpFea.pdf'):
156         """
157         Plot sensitivity studies.
158         """
159         fig = plt.figure()
160         ax = fig.add_subplot(111)
161         ax.plot(xexp,yexp,'--',color='b',linewidth=0.5,dashes
                =(1,1),label=label1)
162         ax.plot(x1,y1,'-',color='k',linewidth=1.0,label=label2)
163         ax.plot(x2,y2,'--',color='c',linewidth=1.0,label=label3,)
164         ax.plot(x3,y3,'-.',color='r',linewidth=1.0,label=label4)
165         ax.legend(loc=legendloc)
166         ax.axis([xmin,xmax,ymin,ymax])
167         ax.set_xlabel(xlabel)
168         ax.set_ylabel(ylabel)
```

```
169         savefig(filename)
170         show()
171         return
172
173     #=========================================================
174     # FILTER FEA RESULTS
175     #
176     def filter(xorg,yorg,window=50,overlap=20,npass=25):
177         print '␣'
178         print '␣Filtering␣data...'
179         print '␣'
180         # COMPUTE LENGTH FROM EACH POINT TO THE ORIGIN
181         # Normalize xy coordinates so difference in scales doesn't
                damp out
182         #    important effects. Data should be in units you plan
               to plot in.
183         xnorm=xorg/abs(xorg).max()
184         ynorm=yorg/abs(yorg).max()
185         def distances(x,y): return sqrt(x**2+y**2)
186         lengths=distances(xnorm,ynorm)
187         # FIND LOCAL MAXIMA AND MINIMA
188         windowsize=window
189         windowoverlap=overlap
190         npts=len(xorg)  # number of points in original data
191         nwindows=int(npts/(windowsize-windowoverlap))
192         maxindex = zeros(npts)
193         xmaxes   = zeros(npts)
194         ymaxes   = zeros(npts)
195         n=0 # maxes detected.
196         for i in range(0,nwindows):
197             start = windowsize*i-windowoverlap*i
198             end   = start+windowsize
199             # find candidate for maximum length from origin in
                    bounds
200             maxcand = argmax(lengths[start:end],axis=0)+start
201             # check to see if maxcand is the start or end node of
                    the window
202             if maxcand != start and maxcand != end-1 :
203                 # print 'actual local max detected!
                        <======='
204                 maxindex[n]=maxcand
205                 n=n+1
206             # find candidate for maximum x
207             maxcand = argmax(abs(xnorm[start:end]),axis=0)+start
208             # check to see if maxcand is the start or end node of
                    the window
209             if maxcand != start and maxcand != end-1 :
210                 # print 'actual local max detected!
                        <======='
211                 maxindex[n]=maxcand
212                 n=n+1
213             # find candidate for maximum y
214             maxcand = argmax(abs(ynorm[start:end]),axis=0)+start
215             # check to see if maxcand is the start or end node of
                    the window
216             if maxcand != start and maxcand != end-1 :
217                 # print 'actual local max detected!
                        <======='
218                 maxindex[n]=maxcand
219                 n=n+1
220             # find candidate for minimum x
221             maxcand = argmin(abs(xnorm[start:end]),axis=0)+start
222             # check to see if maxcand is the start or end node of
                    the window
```

```
223             if maxcand != start and maxcand != end-1 :
224                 # print 'actual local max detected!
                        <=======>'
225                 maxindex[n]=maxcand
226                 n=n+1
227
228         # Store xy coordinates of maxes for plotting to check
229         for nn in range(0,n):
230             xmaxes[nn]=xorg[maxindex[nn]]
231             ymaxes[nn]=yorg[maxindex[nn]]
232             # print "Max detected at:", xmaxes[nn], ymaxes[nn]
233
234         # LOOP OVER ALL POINTS COMPUTING WEIGHTED AVERAGE
235         xfilt = 1.0*xorg
236         yfilt = 1.0*yorg
237         npasses=npass
238         xstart=xfilt
239         ystart=yfilt
240         for i in range(0,npasses):
241             for ii in range(1,npts-1):
242                 # do not move points in maxindex
243                 if (ii in maxindex[0:n]) == 0 : # i.e. is false
244                     # compute average
245                     xfilt[ii]=0.5*(xstart[ii-1]+xstart[ii+1])
246                     yfilt[ii]=0.5*(ystart[ii-1]+ystart[ii+1])
247                     xstart=xfilt
248                     ystart=yfilt
249
250         xmaxes=xmaxes[0:n]
251         ymaxes=ymaxes[0:n]
252         return xfilt,yfilt,xmaxes,ymaxes
253
254     #=========================================================
255     # GENERAL CONCRETE PROPERTIES FUNCTIONS
256     #
257     def modulusYoungACI(fcp):
258         return 4700.*sqrt(fcp)
259     def modulusYoungMC90(fcp):
260         return (2.15e4)*((fcp+8)/10)**0.33333333
261     def modulusYoungThor(fcp,e0):
262         n = 0.80 + fcp/(17); return (fcp/e0)*n/(n-1)
263     def poisson():
264         return 0.2
265     def modulusShear(Ec):
266         v = poisson()
267         return Ec/(2*(1+v))
268     def steelPoisson():
269         return 0.3
270     def tensileStrengthTenth(fcp):
271         return fcp/10.
272     def tensileStrengthMC90(fcp):
273         return 0.3*(fcp)**0.666667
274     def modulusRuptureACI(fcp): # this is still in English units!
275         return 7.5*sqrt(fcp)
276     def strainCompressionMax(fcp,Ec):
277         return 1.8*fcp/Ec # from Hognestad
278     def strainTensionMax(ft,Ec):
279         return ft/Ec
280     def fractureEnergyMC90(fcp):
281         return 0.030*(fcp/10)**0.7
282     def fractureEnergyRemmel(fcp): # Remmel1994/Sasmal2011
283         return 65*math.log(1+fcp/10)/1000
284     def strainHardeningRatio(): # steel ratio hardening modulus to
            initial
```

```
285         return 0.02
286 
287     def properties(fcp=26,Ec=-1.0,pr=-1.0,ft=-1.0,
288                    fr=-1.0,e0=-1.0,et=-1.0,Gf=-1.0):
289         """
290         Compute default suite of concrete material properties.
291         Usage: Ec,pr,ft,fr,e0,et,Gf = diana.properties(fcp)
292         """
293         Ec = modulusYoungACI(fcp)
294         Ec2 = modulusYoungMC90(fcp)
295         pr = poisson()
296         ft2 = tensileStrengthTenth(fcp)
297         ft = tensileStrengthMC90(fcp)
298         fr = modulusRuptureACI(fcp)
299         e0 = strainCompressionMax(fcp,Ec)
300         et = strainTensionMax(ft,Ec)
301         Gf2 = fractureEnergyMC90(fcp)
302         Gf= fractureEnergyRemmel(fcp)
303         print ' '
304         print 'Material properties (default denoted by *):'
305         print '  Compressive strength       Fcp =', fcp
306         print ' *Elastic modulus ACI        Ec =', Ec
307         print '  Elastic modulus MC90       Ec =', Ec2
308         print '  Poisson ratio              pr =', pr
309         print '  Tensile strength 1/10th    ft =', ft2
310         print ' *Tensile strength MC90      ft =', ft
311         print '  Modulus of rupture ACI     fr =', fr
312         print '  Strain at max compression e0 =', e0
313         print '  Strain at max tension      et =', et
314         print '  Fracture energy MC90       Gf =', Gf2
315         print ' *Fracture energy Remmel     Gf =', Gf
316         print ' '
317         return Ec,pr,ft,fr,e0,et,Gf
318 
319     #=========================================================
320     # MATERIAL MODELS
321     #
322     def VecchioTensionStiff(Ec,ft,plot=0):
323         """
324         Vecchio and Collins 1982 tension stiffening model
325         """
326         n   = 30
327         et  = strainTensionMax(ft,Ec)
328         e1   = logDist(et,0.2,n,reverse=False)
329         f1  = ft / (1 + sqrt(200.0*e1))
330         eoutlier = 100.
331         foutlier = ft / (1 + sqrt(200.0*eoutlier))
332         e1 = np.hstack([0.,et,e1[0:],eoutlier])
333         f1 = np.hstack([0.,ft,f1[0:],foutlier])
334         if plot==1:
335             fig = plt.figure()
336             ax = fig.add_subplot(111)
337             ax.plot(e1, f1, 'o-')
338             ax.axis([0.0, 100., 0., ft*1.1 ])
339             ax.grid()
340             show()
341         printCurve('TENPAR',f1,e1)
342         return e1,f1
343 
344     def Menegotto(sy): # Menegotto-Pinto steel model input
345         br = strainHardeningRatio() # ratio hardening modulus to
                initial
346         r0 = 22.   # initial curvature parameter
```

```
347         a1 = 18.5.
348         a2 = 0.15
349         a3 = 0.15
350         a4 = 0.
351         print '      YIELD   MENEGP'
352         print '      YLDVAL  ',sy,br,r0,a1,a2,a3,a4
353
354     def VonMises(sy,Es):
355         """
356         Generate DIANA input for Von Mises plasticity model
357         w/ elastic perfectly plastic behavior.
358         """
359         # Write Diana Material Input
360         print "      YIELD   VMISES"
361         print "      YLDVAL  ", sy
362         return
363
364     def VonMisesHarden(sy,Es,br=0.001):
365         """
366         Generate cohesion vs. equiv. plastic strain curve and
                write
367         DIANA input for Von Mises plasticity model.
368         """
369         outlier=100.
370         su = sy + br*Es*(outlier-sy/Es)
371         e = array([0.0,sy/Es,outlier])
372         f = array([0.0,sy,su])
373         # Compute equivalent plastic strain:
374         kap = e - f/Es
375         coh = f
376         # Write Diana Material Input
377         print "      YIELD   VMISES"
378         # print "     YLDVAL ", sy
379         # print "     HARDEN  WORK "
380         printCurve('HARDIA',coh,kap)
381         return
382
383     def VonMisesKin(sy,Es=200000.0,b=0.001):
384         """
385         Generate cohesion vs. equiv. plastic strain curve for
                kinematic hardening and write input.
386         Note: b = ratio of E_sh to E_initial
387         """
388         outlier=1.
389         s2 = sy + b*Es*(outlier-sy/Es)
390         e2 = outlier-sy/Es
391         # Write Diana Material Input
392         #==========
393         print ': MAT n: Von Mises with Kinematic Hardening'
394         print '   n YOUNG  ', Es
395         print '      POISON  0.3'
396         print "      YIELD   VONMIS"
397         print "      HARDIA ",sy,0.0,s2,e2
398         print "      ISOHAR  0.0"
399         return
400
401     def cebBond(fcp,alpha=0.4,s1=1.0,s2=3.0,s3=10.5,tmax_fac=2.5,
            tf_fac=0.4,plot=False,method=0):
402         """
403         Bond model from CEB-FIP Model Code 1990, pg 83
404         """
405         # Constants (default for confined/good condition)
406         if method==1: # confined / good
407             alpha    = 0.4
408             s1       = 1.0
```

```
            s2       = 3.0
            s3       = 10.5  # clear rib spacing
            tmax_fac = 2.5
            tf_fac   = 0.40
        if method==2: # unconfined / good
            alpha    = 0.4
            s1       = 0.6
            s2       = 0.601
            s3       = 1.0
            tmax_fac = 2.0
            tf_fac   = 0.15
        if method==3: # confined / other
            alpha    = 0.4
            s1       = 1.0
            s2       = 3.0
            s3       = 10.5  # clear rib spacing
            tmax_fac = 1.25
            tf_fac   = 0.40
        if method==4: # unconfined / other
            alpha    = 0.4
            s1       = 0.6
            s2       = 0.601
            s3       = 2.5
            tmax_fac = 1.0
            tf_fac   = 0.15

        s = np.zeros(100)
        t = np.zeros(100)
        # (Modify for other quality/confinement here)
        # Update tmax and tf
        tmax = tmax_fac*sqrt(fcp)
        # tmax = 1.0
        tf = tf_fac*tmax
        # generate ascending portion of curve
        n   = 20
        s   = logDist(0.0,s1,n,reverse=False)
        tau = tmax * (s/s1)**alpha
        # Combine into entire curve
        outlier = 100.
        s = np.hstack([s[0:],s2,s3,outlier])
        tau = np.hstack([tau[0:],tmax,tf,tf])
        # Plot curve for verification
        if plot==1:
            fig = plt.figure()
            ax = fig.add_subplot(111)
            ax.plot(s, tau, 'o-')
            ax.axis([0.0, s3*1.2, 0., tmax*1.1 ])
            ax.grid()
            show()
        # Compute initial stiffness for DSTIF specification
        d22 = 0.99*(tau[1]-tau[0])/(s[1]-s[0]) # initial bond-slip
            stiffness
        d11 = 10*d22
        # Display DIANA material input
        print "      DSTIF  ",d11,d22
        print "      BONDSL  3 "
        printCurve("SLPVAL",tau,s)
        print ":            Generated using:"
        print ":            alpha    = ",alpha
        print ":            s1       = ",s1
        print ":            s2       = ",s2
        print ":            s3       = ",s3
        print ":            tmax_fac = ",tmax_fac
        print ":            tf_fac   = ",tf_fac
```

```
472         return s,tau
473 
474     def thorenfeldt(fcp,Ec,npts=200):
475         """
476         Thorenfeldt (1987): Uniaxial concrete compression curve.
477         """
478         # Generate base strain curve
479         eratio = np.linspace(0.0,10.0,npts)
480         f = np.zeros(len(eratio))
481         # Compute Thorenfeldt parameters
482         n = 0.80 + fcp/(17)
483         k = 0.67 + fcp/(62)
484         e0 = (fcp/Ec)*n/(n-1)
485         if k < 1.0:  k=1.0
486         print '  Thorenfeldt parameters = n,k,e0 =',n,k,e0
487         # Compute stress-strain curve
488         for i in range(len(eratio)):
489             if eratio[i] <= 1.0:
490                 f[i] = fcp * eratio[i] * n/(n-1+(eratio[i])**(n
                        *1.0))
491             else:
492                 f[i] = fcp * eratio[i] * n/(n-1+(eratio[i])**(n*k)
                        )
493         # Scale eratio by strain at compressive peak
494         e = eratio*e0
495         return e,f
496 
497     def hordijk(ft,Ec,Gf,h=1.,npts=100):
498         """
499         Hordijk uniaxial concrete tension curve.
500         """
501         # Generate base strain curve
502         x = np.linspace(0.0,1.0,npts-1)
503         f = np.zeros(len(x))
504         # Parameters
505         c1 = 3.
506         c2 = 6.93
507         a  = (1.+(c1*x)**3)*exp(-c2*x)-x*(1.+c1**3)*exp(-c2)
508         emax    = 5.136*Gf/(h*ft)
509         # print "emax    = ",emax
510         emaxmin = 6.957*ft/Ec
511         # print "emaxmin = ",emaxmin
512         if emax < emaxmin :
513             emax = emaxmin
514             # ft = ( 0.739*Gf*Ec/h )**0.5
515             print "ft =", ft
516         f = a*ft
517         e = emax*x + f/Ec # add in current elastic portion
518         return e,f
519 
520     #=========================================================
521     # WRITE DIANA MATERIAL DEFINITIONS FILE
522     #
523     def concProto(fcp=26,Ec=-1.,pr=-1.,ft=-1.,Gf=-1.,crackband
            =-1.):
524         """
525         Define a suite of DIANA material definitions for RC
                analysis.
526         """
527         # Define base material properties from
528         # concrete compressive strength
529         if Ec < 0.0: Ec = modulusYoungACI(fcp)
530         if pr < 0.0: pr = poisson()
531         if ft < 0.0: ft = tensileStrengthMC90(fcp)
```

```
532         if Gf < 0.0: Gf= fractureEnergyRemmel(fcp)
533         if crackband < 0.0: crackband = 1.0
534         print ':␣PROPERTIES:'
535         print ':␣␣␣␣Compressive␣strength␣␣␣␣␣␣Fcp␣=', fcp
536         print ':␣␣␣␣Elastic␣modulus␣␣␣␣␣␣␣␣␣␣Ec␣␣=', Ec
537         print ':␣␣␣␣Poisson␣ratio␣␣␣␣␣␣␣␣␣␣␣␣pr␣␣=', pr
538         print ':␣␣␣␣Tensile␣strength␣␣␣␣␣␣␣␣ft␣␣=', ft
539         print ':␣␣␣␣Fracture␣energy␣␣␣␣␣␣␣␣␣␣Gf␣␣=', Gf
540         print ':'
541         #==========
542         print ':␣MAT␣n:␣Vecchio␣concrete␣plain'
543         print '␣␣␣n␣YOUNG␣␣', Ec
544         print '␣␣␣␣␣POISON␣', pr
545         print '␣␣␣␣␣TOTCRK␣␣ROTATE'
546         print '␣␣␣␣␣COMCRV␣␣THOREN'
547         print '␣␣␣␣␣CNFCRV␣␣VECCHI'
548         print '␣␣␣␣␣COMSTR␣', fcp
549         print '␣␣␣␣␣TENCRV␣␣HORDYK'
550         print '␣␣␣␣␣TENSTR␣', ft
551         print '␣␣␣␣␣GF1␣␣␣␣', Gf
552         print ':'
553
554     #=========================================================
555     # WRITE SAMPLE DIANA MATERIAL DEFINITIONS FILE
556     #
557     def materials(fcp=26,Ec=-1.,pr=-1.,ft=-1.,Gf=-1.,
558                   Es=200000.,sy=300,spr=-1.,bond=1,crackband=-1.,
                          method=1,br=0.001):
559         """
560         Define a suite of sample DIANA material definitions for RC
                analysis.
561         """
562         # Set output stream
563         sys.stdout = open('model-materials.dat','w')
564         # Print header:
565         print "'MATERIALS'"
566         print ':'
567         print ':␣UNITS:␣Newton,␣mm,␣MPa'
568         print ':'
569         # Define base material properties from
570         # concrete compressive strength
571         if Ec < 0.0: Ec = modulusYoungACI(fcp)
572         if pr < 0.0: pr = poisson()
573         if ft < 0.0: ft = tensileStrengthMC90(fcp)
574         if Gf < 0.0: Gf= fractureEnergyRemmel(fcp)
575         if spr< 0.0: spr= steelPoisson()
576         if crackband < 0.0: crackband = 1.0
577         print ':␣PROPERTIES:'
578         print ':␣␣␣␣Compressive␣strength␣␣␣␣␣␣Fcp␣=', fcp
579         print ':␣␣␣␣Elastic␣modulus␣␣␣␣␣␣␣␣␣␣Ec␣␣=', Ec
580         print ':␣␣␣␣Poisson␣ratio␣␣␣␣␣␣␣␣␣␣␣␣pr␣␣=', pr
581         print ':␣␣␣␣Tensile␣strength␣␣␣␣␣␣␣␣ft␣␣=', ft
582         print ':␣␣␣␣Fracture␣energy␣␣␣␣␣␣␣␣␣␣Gf␣␣=', Gf
583         print ':␣␣␣␣Steel␣elastic␣modulus␣␣␣␣␣Es␣␣=', Es
584         print ':␣␣␣␣Steel␣yield␣stress␣␣␣␣␣␣␣␣sy␣␣=', sy
585         print ':␣␣␣␣Steel␣poisson␣ratio␣␣␣␣␣␣␣spr␣=', spr
586         print ':'
587         #==========
588         print ':␣MAT␣1:␣Concrete␣linear␣elastic'
589         print '␣␣␣1␣YOUNG␣␣',  Ec
590         print '␣␣␣␣␣POISON␣',  pr
591         print ':'
592         #==========
593         print ':␣MAT␣2:␣Vecchio␣concrete␣plain'
594         print '␣␣␣2␣YOUNG␣␣', Ec
595         print '␣␣␣␣␣POISON␣', pr
```

```
596         print '     TOTCRK  ROTATE'
597         print '     COMCRV  THOREN'
598         print '     CNFCRV  VECCHI'
599         print '     COMSTR ', fcp
600         print '     TENCRV  HORDYK'
601         print '     TENSTR ', ft
602         print '     GF1    ', Gf
603         print ':'
604         #==========
605         print ': MAT 3: Von Mises EPP + Bond'
606         print '   3 YOUNG  ', Es
607         print '     POISON ', spr
608         VonMises(sy,Es)
609         cebBond(fcp,method=method)
610         print ':'
611         #==========
612         print ': MAT 4: Von Mises w/ strain hardening + Bond'
613         print '   4 YOUNG  ', Es
614         print '     POISON ', spr
615         VonMisesHarden(sy,Es,br=0.02)
616         cebBond(fcp,method=method)
617         print ':'
618         #==========
619         print ': MAT 5: Vecchio concrete tension stiffening'
620         print '   5 YOUNG  ', Ec
621         print '     POISON ', pr
622         print '     TOTCRK  ROTATE'
623         print '     COMCRV  THOREN'
624         print '     CNFCRV  VECCHI'
625         print '     COMSTR ', fcp
626         print '     TENCRV  MULTLN'
627         VecchioTensionStiff(Ec,ft)
628         print ':'
629         #==========
630         print ': MAT 6: Steel linear elastic'
631         print '   6 YOUNG  ', Es
632         print '     POISON ', spr
633         print ':'
634         #==========
635         print ': MAT 7: Weak material for rebar calibration'
636         print '   7 YOUNG  20.0'
637         print '     POISON 0.2'
638         print ':'
639         return
640
641     #============================================================
642     # POSTPROCESSING ROUTINES
643     #
644
645     def jointStrain(ax,ay,bx,by,cx,cy,dx,dy,width,height):
646         """
647         Purpose: Compute joint shear strain.
648         Input: Arrays of nodal displacements.
649         Ref: Akguzel (2011), pg 153
650         Location of source points:
651         ^y
652         |
653         D---C
654         |   |
655         A---B -->x
656         """
657         d    = sqrt(height**2 + width**2)
658         lac  = sqrt((cx-ax)**2 + (cy-ay)**2)
659         lbd  = sqrt((dx-bx)**2 + (dy-by)**2)
660         del1 = lac-d
661         del2 = lbd-d
```

```
662         gamma = (del1-del2)*d/(2*width*height)
663         return gamma
664
665     def gammaXZ(ephi,ex,ez,phi,sign=-1):
666         # Engindeniz Thesis, pg 222-223
667         return (ephi-ex*(cos(phi)**2)-ez*(sin(phi)**2))/(sign*sin(
                phi)*cos(phi))
668
669     def jointStrain2(ax,az,bx,bz,cx,cz,dx,dz,width,height):
670         """
671         Purpose: Compute joint shear strain.
672         Input: Arrays of nodal displacements.
673         Ref: Engindeniz (2008) pg 222
674         Location of source points:
675         ^z
676         |
677         D---C
678         |   |
679         A---B --->x
680         """
681         phi = math.atan(height/width)
682         print 'phi = ',phi
683         e1  = (bx-ax)/width
684         e2  = (cz-bz)/height
685         e3  = (cx-dx)/width
686         e4  = (dz-az)/height
687         dia = sqrt(height**2 + width**2)
688         print 'dia = ', dia
689         e5  = ( sqrt( (cx-ax)**2 + (cz-az)**2 ) ) / dia
690         e6  = ( sqrt( (dx-bx)**2 + (dz-bz)**2 ) ) / dia
691         gam1 = gammaXZ(e6,e1,e4,phi,-1)
692         gam2 = gammaXZ(e5,e1,e2,phi,1)
693         gam3 = gammaXZ(e5,e3,e4,phi,1)
694         gam4 = gammaXZ(e6,e3,e2,phi,-1)
695         gamma = (gam1+gam2+gam3+gam4)/4
696         return gamma
697
698     def forceDriftMetricsPerCycle(xfea,yfea,n1,n2):
699         n=n2-n1
700         # n1=n1-1
701         # n2=n2-1
702         x=zeros(n)
703         y=zeros(n)
704         x=xfea[n1:n2]
705         y=yfea[n1:n2]
706         Ecyc = trapz(y,x)
707         ymax = np.max(y)
708         ymin = np.min(y)
709         xmax = x[argmax(y)]
710         xmin = x[argmin(y)]
711         print ymax,ymin,xmax,xmin
712         Kppi = (ymax-ymin)/(xmax-xmin)
713         print 'Cycle energy    =',Ecyc
714         print 'Cycle stiffness =',Kppi
715         return Ecyc,Kppi
716
717     #=============================================================
718     # End of file
719     #=============================================================
```

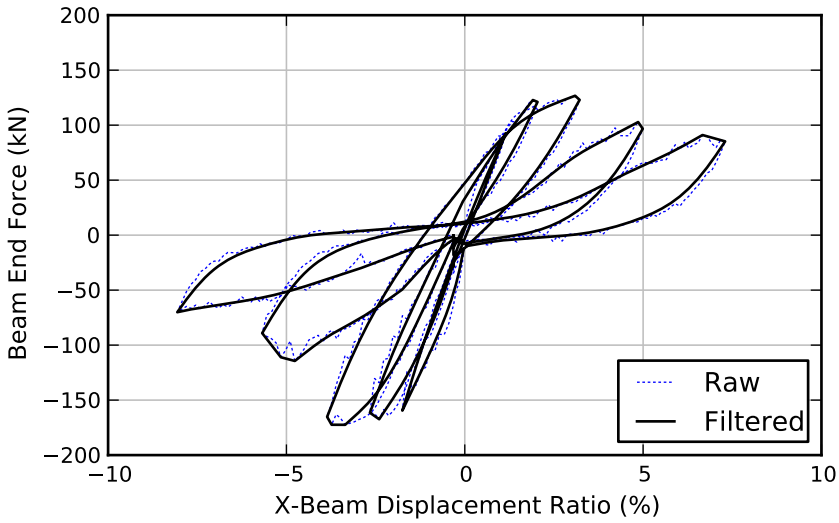

Figure B.2: Raw vs. Post-Processed Force-Displacement Curve

B.5 FEA Result Filter

Finite element results were typically post-processed to improve the aesthetic presentation of plots. The filter used a moving window weighted average, and local maxima and minima were preserved within the window so that the response was anchored against the computed backbone. Thus, force-displacement curves appear smoother, but the location of all critical points was maintained. The filter Python code is included within the file `diana.py`, listed in the previous section.

All force-displacement metrics described in Section 5.1 were computed using the raw FEA output prior to smoothing with the filter.

B.6 Pantelides Simulation Supporting Materials

B.6.1 Material and Geometric Properties Block

inputs/pantelides–definitions.txt

```
: Units: N,mm
'MATERI'
   1 NAME   "ConcElastic"
     DENSIT  2.4028E-06
     YOUNG   31946.17
```

```
        POISON  0.2
        TOTCRK  ROTATE
        COMCRV  THOREN
        CNFCRV  VECCHI
        COMSTR  46.2
        TENCRV  HORDYK
        TENSTR  3.86263015493
        GF1     0.112211558154
      2 NAME   "RigidPlateMat"
        DENSIT  2.4028E-06
        YOUNG   1.00000E+007
        POISON  0.00000E+000
      3 NAME   "SteelElastic"
        DENSIT  1.0000E-09
        YOUNG   2.00000E+005
        POISON  3.00000E-001
      4 NAME   "SteelBeamBars"
        DENSIT  1.0000E-09
        YOUNG   200000.0
        POISON  0.3
        YIELD   VONMIS
        HARDIA  454.4 0.0 4445.312 0.997728
        ISOHAR  0.0
        DSTIF   155.918511514 155.918511514
        BONDSL  3
        SLPVAL  0.0 0.0
                2.25456928149 0.0143153212983
                3.05014595859 0.0304749984115
                3.67971452592 0.0487166542542
                4.23699363904 0.0693085265765
                4.75663820264 0.0925534123147
                5.25605209671 0.118793120124
                5.74556185214 0.148413496566
                6.23201604811 0.181850099859
                6.72034875698 0.219594604626
                7.21435595566 0.262202031809
                7.71711985807 0.310298910081
                8.23125834004 0.364592488747
                8.75908029709 0.425881137619
                9.30268716028 0.495066086797
                9.86404200986 0.573164678962
                10.4450183708 0.661325329086
                11.0474358268 0.760844411502
                11.6730868373 0.873185322678
                12.3237575439 1.0
                12.3237575439 3.0
                4.92950301755 5.0
                4.92950301755 100.0
      5 NAME   "SteelColumnBars"
        DENSIT  1.0000E-09
        YOUNG   200000.0
        POISON  0.3
        YIELD   VONMIS
        HARDIA  469.5 0.0 4460.11 0.9976525
        ISOHAR  0.0
        DSTIF   155.918511514 155.918511514
        BONDSL  3
        SLPVAL  0.0 0.0
                2.25456928149 0.0143153212983
                3.05014595859 0.0304749984115
                3.67971452592 0.0487166542542
                4.23699363904 0.0693085265765
                4.75663820264 0.0925534123147
                5.25605209671 0.118793120124
                5.74556185214 0.148413496566
```

```
                6.23201604811 0.181850099859
                6.72034875698 0.219594604626
                7.21435595566 0.262202031809
                7.71711985807 0.310298910081
                8.23125834004 0.364592488747
                8.75908029709 0.425881137619
                9.30268716028 0.495066086797
                9.86404200986 0.573164678962
                10.4450183708 0.661325329086
                11.0474358268 0.760844411502
                11.6730868373 0.873185322678
                12.3237575439 1.0
                12.3237575439 3.0
                4.92950301755 5.0
                4.92950301755 100.0
      6 NAME    "SteelTies"
        DENSIT  1.0000E-09
        YOUNG   200000.0
        POISON  0.3
        DSTIF   155.918511514 155.918511514
        BONDSL  3
        SLPVAL  0.0 0.0
                2.25456928149 0.0143153212983
                3.05014595859 0.0304749984115
                3.67971452592 0.0487166542542
                4.23699363904 0.0693085265765
                4.75663820264 0.0925534123147
                5.25605209671 0.118793120124
                5.74556185214 0.148413496566
                6.23201604811 0.181850099859
                6.72034875698 0.219594604626
                7.21435595566 0.262202031809
                7.71711985807 0.310298910081
                8.23125834004 0.364592488747
                8.75908029709 0.425881137619
                9.30268716028 0.495066086797
                9.86404200986 0.573164678962
                10.4450183708 0.661325329086
                11.0474358268 0.760844411502
                11.6730868373 0.873185322678
                12.3237575439 1.0
                12.3237575439 3.0
                4.92950301755 10.5
                4.92950301755 100.0
                1.01955872808 100.0
      8 NAME    "ColTipSpring"
        DENSIT  1.0000E-09
        SPRING  306710.2136
  'GEOMET'
      1 NAME    "ColTipSpringID"
        AXIS     0. 0. 1.
      2 NAME    "ConcProp"
      3 NAME    "RigidProp"
      4 NAME    "SevenBar"
        CIRCLE  22.2
        ZAXIS   -1. 0. 0.
        PERIME  69.8
      5 NAME    "NineBar"
        CIRCLE  28.6
        ZAXIS   0. 1. 0.
        PERIME  89.8
      6 NAME    "ThreeBarCol"
        CIRCLE  9.5
        ZAXIS   0. 0. 1.
        PERIME  29.9
```

```
      7 NAME   ”ThreeBarBeam”
        CIRCLE  9.5
        ZAXIS   1. 0. 0.
        PERIME  29.9
'DATA'
      1 NAME   ”ConcPropData”
      9 NAME   ”ColTipSpringDataID”
      3 NAME   ”DataSevenBar”
        INTERF BEAM
      5 NAME   ”NineBarData”
        INTERF BEAM
      7 NAME   ”ThreeBarCol”
        INTERF BEAM
     10 NAME   ”ThreeBarBeam”
        INTERF BEAM
: End of Pantelides input
```

B.7 Akgüzel Simulation Supporting Materials

B.7.1 Load Generation Script

E:/Dropbox/PHD/SIM/Akguzel/LoadGen/loadGen.py

```
1
2   import numpy as np
3   from math import *
4   from pylab import *
5   import matplotlib
6   import sys
7
8   # Build analytical load curves used in experiment
9   thetas    =linspace(0.0,360.0,360)*pi/180.0
10  R         = 1.0/(cos(pi/4))
11  r         = R*sin(2*thetas)
12  xexpunit  = r*cos(thetas)
13  yexpunit  = r*sin(thetas)
14  drifts    = array([0.1, 0.2, 0.5, 1.0, 1.5, 2.0, 2.5, 3.0])
15  # drifts    = array([3.0])
16  disp      = drifts*20.0
17  numlevels = len(drifts)
18  xexp      = disp[0]*xexpunit
19  yexp      = disp[0]*yexpunit
20  for i in range(1,numlevels):
21      xexp =  hstack([xexp,disp[i]*xexpunit])
22      yexp =  hstack([yexp,disp[i]*yexpunit])
23
24  # Build load input for each quadrant
25  q=0 # Quadrant 1
26  angles = array([12.0,24.0,35.6,45.0,54.4,66.0,78.0,90.0])*pi
        /180.
27  # angles = array([0.0,12.0,24.0,35.6,45.0,54.4])*pi/180.
28  r      = R*sin(2*angles)
29  xlbase = r*cos(angles)
30  ylbase = r*sin(angles)
31  # Set directions for each quadrant 1—4
```

```
xq1 =  ylbase
yq1 =  xlbase
xq2 = -xlbase
yq2 = -ylbase
xq3 = -ylbase
yq3 =  xlbase
xq4 =  xlbase
yq4 = -ylbase
xfeaunit=hstack([xq1,xq2,xq3,xq4]) # unit x-displacements
yfeaunit=hstack([yq1,yq2,yq3,yq4]) # unit y-displacements

# Build per each drift
axfact = array([0.20,0.50,0.90,1.0,0.90,0.50,0.20,0.0]) # axial factors
axialperdrifts = zeros((10,10))
axialperdrifts = loadtxt("axialLoads.txt") # read in exp axial forces
print axialperdrifts
driftstouse = array([2,3,4,5,6,7]) # "drifts to use", i.e., 3rd,4th,6th,8th
numlevels = len(driftstouse) # how many displacement levels to simulate
driftsload = zeros(numlevels) # init list of drifts to use
for nn in range(0,numlevels):
    driftsload[nn] = axialperdrifts[driftstouse[nn],0]
disploads = driftsload*20.0 # scale from %-drift to displacement

xfea      = disploads[0]*xfeaunit
yfea      = disploads[0]*yfeaunit
axq1=axialperdrifts[driftstouse[0],1]*axfact
axq2=axialperdrifts[driftstouse[0],2]*axfact
axq3=axialperdrifts[driftstouse[0],3]*axfact
axq4=axialperdrifts[driftstouse[0],4]*axfact
axial = hstack([axq1,axq2,axq3,axq4])
for i in range(1,numlevels):
    xfea =  hstack([xfea,disploads[i]*xfeaunit])
    yfea =  hstack([yfea,disploads[i]*yfeaunit])
    axq1=axialperdrifts[driftstouse[i],1]*axfact
    axq2=axialperdrifts[driftstouse[i],2]*axfact
    axq3=axialperdrifts[driftstouse[i],3]*axfact
    axq4=axialperdrifts[driftstouse[i],4]*axfact
    axial = hstack([axial,axq1,axq2,axq3,axq4])

print 'number of load cases =', len(xfea)
print 'number of load cases =', len(axial)
print axial

# Plot the final result
fig = figure(1, figsize=(8.0, 3.5))
fig = plt.figure(1, figsize=(3.25, 3))
ax = fig.add_subplot(311)
ax = subplot(121)
ax.plot(xexp,yexp,'--',color='b',linewidth=1.0,dashes=(1,1), label="EXP")
ax.plot(xfea,yfea,'-',color='k',linewidth=1.0,label="FEA Input")
ax.legend()
ax.set_xlabel('x-displacement (mm)')
ax.set_ylabel('y-displacement (mm)')
ax.set_aspect('equal')

# Plot load histories
```

```
88    t = range(0,len(xfea))
89    s1 = xfea
90    s2 = yfea
91    s3 = axial
92    ax1 = fig.add_subplot(322)
93    plot(t,s1,'-',color='k',linewidth=1.0)
94    setp( ax1.get_xticklabels(), visible=False)
95    ax1.set_ylabel('x (mm)')
96    ax1.axis([0,len(t),-80.0,80.0])
97    ## share x only
98    ax2 = fig.add_subplot(324, sharex=ax1)
99    plot(t, s2,'-',color='k',linewidth=1.0)
100   # make these tick labels invisible
101   setp( ax2.get_xticklabels(), visible=False)
102   ax2.set_ylabel('y (mm)')
103   ax2.axis([0,len(t),-80.0,80.0])
104   # share x
105   ax3 = fig.add_subplot(326,  sharex=ax1)
106   setp( ax3.get_xticklabels(), visible=False)
107   ax3.set_xlabel('Time')
108   ax3.set_ylabel('Compression (kN)')
109   ax3.axis([0,len(t),0.0,200.0])
110   tbase=array([0,len(xfea)])
111   sbase=array([115.0,115.0])
112   plot(tbase,sbase,'--',color='k',linewidth=1.0,dashes=(1,1))
113   ax3.legend()
114   plot(t, -(s3-115),'-',color='k',linewidth=1.0)
115   savefig('loadHistory.pdf')
116   show()
117
118   # Plot 3D load history
119   from mpl_toolkits.mplot3d import Axes3D
120   fig2 = plt.figure(1, figsize=(5, 3.5))
121   ax6 = fig2.gca(projection='3d')
122   theta = np.linspace(-4 * np.pi, 4 * np.pi, 100)
123   z = np.linspace(-2, 2, 100)
124   r = z**2 + 1
125   x = r * np.sin(theta)
126   y = r * np.cos(theta)
127
128   ax6.plot(xfea, yfea, 0.0, zdir='z',linestyle='-',color='0.50',
          linewidth=0.3)
129   ax6.plot(yfea, -(axial-115), 80.0, zdir='y',linestyle='-',
          color='0.50',linewidth=0.3)
130   ax6.plot(xfea, -(axial-115), -80.0, zdir='x',linestyle='-',
          color='0.50',linewidth=0.3)
131   # contour color the line:
132   # http://stackoverflow.com/questions/8500700/how-to-plot-a-
          gradient-color-line-in-matplotlib
133   npoints=len(xfea)
134   map='autumn' # http://www.scipy.org/Cookbook/Matplotlib/
          Show_colormaps
135   cm = plt.get_cmap(map)
136   ax6.set_color_cycle
137   axialplot = -(axial-115)
138
139   ax6.plot(xfea, yfea, -(axial-115),color='r',linewidth=1.0)
140   ax6.set_xlim(-80.,80.)
141   # ax6.set_xlim(ax6.get_xlim()[::-1])
142   ax6.set_ylim(-80,80)
143   ax6.set_zlim(0.,200.)
144   ax6.set_xlabel('x-displacement (mm)')
```

```
145   ax6.set_ylabel('y-displacement (mm)')
146   ax6.set_zlabel('Compression (kN)')
147   savefig('loadHistory3D.pdf')
148   show()
149
150   # Build arrays of delta's between each point
151   # These are the incremental displacements and axial forces
152   def increments(a): #
153       n=len(a)
154       out=zeros(n)
155       out[0]=a[0]-0.0
156       for i in range(1,n):
157           out[i]=a[i]-a[i-1]
158       return out
159   incrementedoutput=increments(xfea)
160   print 'xfea w/ length',len(xfea)
161   print xfea
162   print 'Incremented xfea w/ length',len(incrementedoutput)
163   print incrementedoutput
164   xload=increments(xfea)
165   yload=increments(yfea)
166   axload=increments(axial)
167
168   # Write DIANA load and analysis input
169   sys.stdout = open('load-input.txt', 'w')
170   node=739
171   nloads=len(xload)
172   # print 'number of loads =',nloads
173   print "'LOADS'"
174   for n in range(2,nloads+2):
175       print 'CASE',n
176       print 'NODAL'
177       print node, 'FORCE   3',axload[n-2]*1000
178       print 'DEFORM'
179       print node, 'TR      1',xload[n-2]
180       print node, 'TR      2',yload[n-2]
181   print ' '
182   print ' <================================> '
183   print ' '
184   for n in range(2,nloads+2):
185       print 'BEGIN EXECUT'
186       print '   BEGIN ITERAT'
187       print '      METHOD SECANT BROYDE'
188       print '      MAXITE 500'
189       print '      BEGIN CONVER'
190       print '      FORCE TOLCON=0.01'
191       print '         DISPLA OFF '
192       print '         ENERGY TOLCON=0.0025 '
193       print '      END CONVER'
194       print '   END ITERAT'
195       print ' BEGIN LOAD'
196       print '  LOADNR=',n
197       print '  STEPS EXPLIC SIZES 0.1(10) '
198       print ' END LOAD'
199       print 'END EXECUT'
200       print ' '
201
202   # End of file
```

Axial loads are specified via the file `axialLoads.txt`. The first column contains the drift levels, while the following columns contain the column axial force excursion for each quadrant I-IV of the cloverleaf bi-directional cyclic load history.

E:/Dropbox/PHD/SIM/Akguzel/LoadGen/axialLoads.txt

```
0.10  32.87   −4.90  16.59  18.04
0.20  43.91  −20.90  14.60  16.59
0.50  56.93  −55.60   3.40  12.10
1.00  60.01  −79.50  −2.00  10.40
1.50  62.72  −65.00  10.30  11.70
2.00  52.95  −50.30   7.40   7.50
2.50  41.37  −41.30   1.60   6.30
3.00  32.15  −30.60   5.70   3.00
```

B.7.2 Material and Geometric Properties Block

inputs/akguzel–definitions.txt

```
: Units:  N, mm, MPa

'MATERI'
   1 NAME   "Conc"
     YOUNG   19605.2543977
     POISON  0.2
     TOTCRK  ROTATE
     COMCRV  THOREN
     CNFCRV  VECCHI
     COMSTR  17.4
     TENCRV  HORDYK
     TENSTR  2.2
     GF1     0.065517264826
   2 NAME   "RigidEnd"
     YOUNG   1.00000E+007
     POISON  0.0
   3 NAME   "SteelMain"
     YOUNG   200000.0
     POISON  0.3
     YIELD   VMISES
     YLDVAL  340.0
     DSTIF   100.0 100.0
     BONDSL  3
     SLPVAL  0.0 0.0
             0.119646651847 0.00143153212983
             0.174570897951 0.00304749984115
             0.220718495496 0.00487166542542
             0.263265126017 0.00693085265765
             0.304225923147 0.00925534123147
             0.344663778375 0.0118793120124
             0.385244722956 0.0148413496566
             0.426438858289 0.0181850099859
```

```
                0.468609223795 0.0219594604626
                0.512056668553 0.0262202031809
                0.557044800785 0.0310298910081
                0.603814945779 0.0364592488747
                0.652595692308 0.0425881137619
                0.703609328247 0.0495066086797
                0.757076402328 0.0573164678962
                0.813219115052 0.0661325329086
                0.87226395747 0.0760844411502
                0.934443857424 0.0873185322678
                1.0 0.1
                1.0 0.11
                0.2 0.3
                0.2 100.0
      4 NAME   ”SteelTies”
        YOUNG   200000.0
        POISON  0.3
        YIELD   VMISES
        YLDVAL  408.0

   ’GEOMET’
      1 NAME   ”ConcID”
      2 NAME   ”RigidID”
      3 NAME   ”R10x”
        CIRCLE 10.0
        ZAXIS  0. 1. 0.
        PERIME 31.4
      4 NAME   ”R10y”
        CIRCLE 10.0
        ZAXIS  —1. 0. 0.
        PERIME 31.4
      5 NAME   R6
        CIRCLE 6.0

   ’DATA’
      1 NAME   ”ConcDat”
      2 NAME   ”RigidDat”
      3 NAME   ”R10xData”
        INTERF BEAM
      5 NAME   ”R6Data”
      7 NAME   ”R10yData”
        INTERF BEAM

   : End of Akguzel input
```

B.8 Park Simulation Supporting Materials

B.8.1 Load Generation Script

E:/Dropbox/PHD/SIM/Park/loadgen/loadGen.py

```
1
2   import numpy as np
3   from math import *
4   from pylab import *
5   import matplotlib
6   import sys
```

```
7
8   # Read in load data
9   axialperdrifts = zeros((10,10))
10  loaddata = loadtxt("load-data.txt") # read in exp axial forces
11  print loaddata
12  # print 'number of load levels =',len(loaddata)
13
14  # "drifts to use", i.e., 3rd,4th,6th,8th
15  groupsToUse = array([4,5,6,7,8])
16  numlevels = len(groupsToUse) # how many disp levels to
        simulate
17  displacementMags = -loaddata[:,1]
18  # print displacementMags
19  stepsizemm = 3.5
20  stepspergroup = displacementMags/stepsizemm+1
21  numstepspergroup = stepspergroup.astype(int)
22  print numstepspergroup
23  stepssizepergroup = 1.0/numstepspergroup
24  print stepssizepergroup
25
26  # Plot
27  num = 100
28  vdatum = loaddata[0,1]
29  axdatum = loaddata[0,5]
30  xdisp = zeros(num)+vdatum
31  ydisp = zeros(num)+vdatum
32  axial = zeros(num)+axdatum
33  xdisp[0] = 0.0
34  ydisp[0] = 0.0
35  axial[0] = 0.0
36  k = 1
37  for n in range(4,9):
38      xdisp[k+1] = vdatum+loaddata[n,1]
39      xdisp[k+3] = vdatum+loaddata[n,2]
40      ydisp[k+5] = vdatum+loaddata[n,3]
41      ydisp[k+7] = vdatum+loaddata[n,4]
42      axial[k+1] = axdatum+loaddata[n,5]
43      axial[k+3] = axdatum+loaddata[n,6]
44      axial[k+5] = axdatum+loaddata[n,5]
45      axial[k+7] = axdatum+loaddata[n,6]
46      k=k+8
47
48  # Plot the final result
49  fig = figure(1, figsize=(6., 3.5))
50  # fig = figure(1)
51  # Plot load histories
52  t = range(0,k)
53  s1 = xdisp[0:k]
54  s2 = ydisp[0:k]
55  s3 = -axial[0:k]
56  ax1 = fig.add_subplot(311)
57  plot(t,s1,'-',color='k',linewidth=1.0)
58  setp( ax1.get_xticklabels(), visible=False)
59  ax1.set_ylabel('x-beam (mm)')
60  ax1.axis([0,len(t),-250.0,250.0])
61  ## share x only
62  ax2 = fig.add_subplot(312, sharex=ax1)
63  plot(t, s2,'-',color='k',linewidth=1.0)
64  # make these tick labels invisible
65  setp( ax2.get_xticklabels(), visible=False)
66  ax2.set_ylabel('y-beam (mm)')
67  ax2.axis([0,len(t),-250.0,250.0])
```

```
68  # share x
69  ax3 = fig.add_subplot(313,  sharex=ax1)
70  setp( ax3.get_xticklabels(), visible=False)
71  ax3.set_xlabel('Time')
72  ax3.set_ylabel('Compression (kN)')
73  ax3.set_xticks(np.arange(-3,100,4))
74  ax3.axis([0,len(t),-500.0,1500.0])
75  ax3.legend()
76  plot(t, s3,'-',color='k',linewidth=1.0)
77  savefig('loadHistory.pdf')
78  show()
79
80  # Write DIANA load and analysis input
81  sys.stdout = open('diana-input.txt', 'w')
82  nodez=5814  # tip of column
83  nodex=4246  # tip of EW beam, x-direction beam
84  nodey=4295  # tip of NS beam, y-direction beam
85
86  # Case 1: Displace to datum
87  print "'LOADS'"
88  nloads=1
89  print 'CASE',nloads
90  print 'NODAL'
91  print nodez, 'FORCE   3',loaddata[0,5]*1000
92  print 'DEFORM'
93  print nodex, 'TR      3',loaddata[0,1]
94  print nodey, 'TR      3',loaddata[0,3]
95
96  # Cycle over following load groups
97  for g in range(0,numlevels):
98      group=groupsToUse[g]
99      # EW DOWN
100     nloads=nloads+1
101     print 'CASE',nloads
102     print ': EW DOWN -- GROUP ',group
103     print 'NODAL'
104     print nodez, 'FORCE   3',loaddata[groupsToUse[g],5]*1000
105     print 'DEFORM'
106     print nodex, 'TR      3',loaddata[groupsToUse[g],1]
107     print nodey, 'TR      3',0.0
108     # EW UP
109     nloads=nloads+1
110     print 'CASE',nloads
111     print ': EW UP -- GROUP ',group
112     print 'NODAL'
113     print nodez, 'FORCE   3',loaddata[groupsToUse[g],6]*1000
114     print 'DEFORM'
115     print nodex, 'TR      3',loaddata[groupsToUse[g],2]
116     print nodey, 'TR      3',0.0
117     # NS DOWN
118     nloads=nloads+1
119     print 'CASE',nloads
120     print ': NS DOWN -- GROUP ',group
121     print 'NODAL'
122     print nodez, 'FORCE   3',loaddata[groupsToUse[g],5]*1000
123     print 'DEFORM'
124     print nodex, 'TR      3',0.0
125     print nodey, 'TR      3',loaddata[groupsToUse[g],3]
126     # NS up
127     nloads=nloads+1
128     print 'CASE',nloads
129     print ': NS UP -- GROUP ',group
130     print 'NODAL'
131     print nodez, 'FORCE   3',loaddata[groupsToUse[g],6]*1000
```

```
132         print 'DEFORM'
133         print nodex, 'TR      3',0.0
134         print nodey, 'TR      3',loaddata[groupsToUse[g],4]
135         print ' '
136
137
138     print ' '
139     print ' <================================> '
140     print ' '
141
142     # Write out DCF file data
143     l=1
144     # Load 1
145     print 'BEGIN EXECUT'
146     print '   BEGIN ITERAT'
147     print '      METHOD SECANT BROYDE'
148     print '      MAXITE 500'
149     print '      BEGIN CONVER'
150     print '      FORCE TOLCON=0.01'
151     print '         DISPLA OFF '
152     print '         ENERGY TOLCON=0.0025 '
153     print '      END CONVER'
154     print '   END ITERAT'
155     print ' BEGIN LOAD'
156     print '  LOADNR=1'
157     print '  STEPS EXPLIC SIZES 0.1(10) '
158     print ' END LOAD'
159     print 'END EXECUT'
160     print ' '
161
162     for g in range(0,numlevels):
163         group=groupsToUse[g]
164         # print group
165         for i in range(1,5):
166             l=l+1
167             print ': LOAD CASE', l
168             print 'BEGIN EXECUT'
169             print '   BEGIN ITERAT'
170             print '      METHOD SECANT BROYDE'
171             print '      MAXITE 800'
172             print '      BEGIN CONVER'
173             print '      FORCE TOLCON=0.01'
174             print '         DISPLA OFF '
175             print '         ENERGY TOLCON=0.0025 '
176             print '      END CONVER'
177             print '   END ITERAT'
178             print ' BEGIN LOAD'
179             print '  LOADNR=',
180             sys.stdout.softspace=0
181             print l
182             print '  STEPS EXPLIC SIZES ',
183             sys.stdout.softspace=0
184             print stepssizepergroup[group],
185             sys.stdout.softspace=0
186             print '(',
187             sys.stdout.softspace=0
188             print numstepspergroup[group],
189             sys.stdout.softspace=0
190             print ') -',
191             sys.stdout.softspace=0
192             print stepssizepergroup[group],
193             sys.stdout.softspace=0
194             print '(',
195             sys.stdout.softspace=0
196             print numstepspergroup[group],
```

```
197             sys.stdout.softspace=0
198             print ')'
199             print ' END LOAD'
200             print 'END EXECUT'
201             print ' '
202
203     # End of file
```

Relative (to the last increment) column axial force and beam displacement loads are specified via the file `load-data.txt`. Column 1 contains load group number, column 2 contains EW downward displacement, column 3 contains EW upward displacement, column 4 contains NS downward displacement, column 5 contains NS upward displacement, column 6 contains the column axial force when beam is displaced downward, and column 7 contains the column axial force when beam is displaced upward.

E:/Dropbox/PHD/SIM/Park/loadgen/load–data.txt

```
1   0     −8.44     0.00     −8.44     0.00   −544.88     0.00
2   1     −6.76     7.91     −6.76     8.18   −322.48    55.60
3   2    −14.76    15.64    −15.03    15.91   −389.20   211.28
4   3    −22.76    23.38    −22.49    23.64   −522.64   322.48
5   4    −38.23    39.11    −38.50    39.91   −611.60   455.92
6   5    −62.50    62.85    −62.50    63.38   −500.40   589.36
7   6    −94.50    94.32    −95.04    94.85   −433.68   589.36
8   7   −143.04   141.53   −143.58   142.06   −278.00   544.88
9   8   −206.52   203.13   −206.25   203.40   −211.28   500.40
```

B.8.2 Material and Geometric Properties Block

inputs/park–definitions.txt

```
1   : UNITS: N,MM,MPA
2   'MATERI'
3      1 NAME    "Conc"
4        YOUNG   23192.3948628
5        POISON  0.2
6        TOTCRK  ROTATE
7        COMCRV  THOREN
8        CNFCRV  VECCHI
9        COMSTR  24.3
10       TENCRV  HORDYK
11       TENSTR  2.34
```

```
        GF1     0.0801164169766
      2 NAME   ”RigidEnd”
        YOUNG   2.00000E+006
        POISON  0.00000E+000
      3 NAME   ”3bar”
        YOUNG   200000
        POISON  0.3
        YIELD   VONMIS
        HARDIA  507.0 0.0 4496.86 0.997465
        ISOHAR  0.0
        DSTIF   1559.18511514 155.918511514
        BONDSL  3
        SLPVAL  0.0 0.0
                2.25456928149 0.0143153212983
                3.05014595859 0.0304749984115
                3.67971452592 0.0487166542542
                4.23699363904 0.0693085265765
                4.75663820264 0.0925534123147
                5.25605209671 0.118793120124
                5.74556185214 0.148413496566
                6.23201604811 0.181850099859
                6.72034875698 0.219594604626
                7.21435595566 0.262202031809
                7.71711985807 0.310298910081
                8.23125834004 0.364592488747
                8.75908029709 0.425881137619
                9.30268716028 0.495066086797
                9.86404200986 0.573164678962
                10.4450183708 0.661325329086
                11.0474358268 0.760844411502
                11.6730868373 0.873185322678
                12.3237575439 1.0
                12.3237575439 3.0
                4.92950301755 10.5
                4.92950301755 100.0
      4 NAME   ”7bar”
        YOUNG   200000
        POISON  0.3
        YIELD   VONMIS
        HARDIA  505.0 0.0 4494.9 0.997475
        ISOHAR  0.0
        DSTIF   1559.18511514 155.918511514
        BONDSL  3
        SLPVAL  0.0 0.0
                2.25456928149 0.0143153212983
                3.05014595859 0.0304749984115
                3.67971452592 0.0487166542542
                4.23699363904 0.0693085265765
                4.75663820264 0.0925534123147
                5.25605209671 0.118793120124
                5.74556185214 0.148413496566
                6.23201604811 0.181850099859
                6.72034875698 0.219594604626
                7.21435595566 0.262202031809
                7.71711985807 0.310298910081
                8.23125834004 0.364592488747
                8.75908029709 0.425881137619
                9.30268716028 0.495066086797
                9.86404200986 0.573164678962
                10.4450183708 0.661325329086
                11.0474358268 0.760844411502
                11.6730868373 0.873185322678
                12.3237575439 1.0
                12.3237575439 3.0
                4.92950301755 10.5
```

```
                4.92950301755 100.0
      5 NAME    ”8bar”
        YOUNG   200000
        POISON  0.3
        YIELD   VONMIS
        HARDIA  498.0 0.0 4488.04 0.99751
        ISOHAR  0.0
        DSTIF   1559.18511514 155.918511514
        BONDSL  3
        SLPVAL  0.0 0.0
                2.25456928149 0.0143153212983
                3.05014595859 0.0304749984115
                3.67971452592 0.0487166542542
                4.23699363904 0.0693085265765
                4.75663820264 0.0925534123147
                5.25605209671 0.118793120124
                5.74556185214 0.148413496566
                6.23201604811 0.181850099859
                6.72034875698 0.219594604626
                7.21435595566 0.262202031809
                7.71711985807 0.310298910081
                8.23125834004 0.364592488747
                8.75908029709 0.425881137619
                9.30268716028 0.495066086797
                9.86404200986 0.573164678962
                10.4450183708 0.661325329086
                11.0474358268 0.760844411502
                11.6730868373 0.873185322678
                12.3237575439 1.0
                12.3237575439 3.0
                4.92950301755 10.5
                4.92950301755 100.0

   ’GEOMET’
      1 NAME    ”Conc”
      2 NAME    ”Rigid”
      3 NAME    ”3bary”
        CIRCLE  9.5
        ZAXIS   1. 0. 0.
        PERIME  29.9
      4 NAME    ”3barx”
        CIRCLE  9.5
        ZAXIS   0. 1. 0.
        PERIME  29.9
      5 NAME    ”3barz”
        CIRCLE  9.5
        ZAXIS   0. 0. 1.
        PERIME  29.9
      6 NAME    ”7barx”
        CIRCLE  22.2
        ZAXIS   0. 1. 0.
        PERIME  69.8
      7 NAME    ”7bary”
        CIRCLE  22.2
        ZAXIS   1. 0. 0.
        PERIME  69.8
      8 NAME    ”8barx”
        CIRCLE  25.4
        ZAXIS   0. 1. 0.
        PERIME  79.8
      9 NAME    ”8bary”
        CIRCLE  25.4
        ZAXIS   1. 0. 0.
        PERIME  79.8
   ’DATA’
```

```
142       1 NAME   ”ConcData”
143       2 NAME   ”RigidData”
144       3 NAME   ”3bary”
145         INTERF TRUSS
146       4 NAME   ”3barx”
147         INTERF TRUSS
148       5 NAME   ”3barz”
149         INTERF TRUSS
150       6 NAME   ”7barx”
151         INTERF TRUSS
152       7 NAME   ”7bary”
153         INTERF TRUSS
154       8 NAME   ”8barx”
155         INTERF TRUSS
156       9 NAME   ”8bary”
157         INTERF TRUSS
158
159    : END OF FILE
```

B.9 Engindeniz Simulation Supporting Materials

B.9.1 Load Generation Script

This represents cycles 0, 1a, 1b (NS/EW), 4a, 4b, 7a, 7b, 10a, 10b. One full cycle is completed at each displacement level, whereas experimentally three cycles were conducted at each level.

E:/Dropbox/PHD/SIM/Engin/loadgen/loadGen.py

```
1
2    import numpy as np
3    from math import *
4    from pylab import *
5    import matplotlib
6    import sys
7
8    # Read in load data
9    loaddata = loadtxt(”beamDispCorrected.txt”)
10   print loaddata
11   numlevels = len(loaddata)
12   dispx = loaddata[:,0]
13   dispy = loaddata[:,1]
14   maxperlevel = np.amax(abs(loaddata[:,:]),axis=1)
15   print 'maxperlevel:'
16   print maxperlevel
17   stepsizemm = 1.0
18   stepspergroup = maxperlevel/stepsizemm+1
19   numstepspergroup = stepspergroup.astype(int)
20   print numstepspergroup
21   stepssizepergroup = 1.0/numstepspergroup
22   print stepssizepergroup
23
24   # Write DIANA load and analysis input
```

```
25  sys.stdout = open('diana-input.txt', 'w')
26  nodex=5422  # tip of x-direction beam
27  nodey=5707  # tip of y-direction beam
28
29  # Case 1: Displace to datum
30  print "'LOADS'"
31  nloads=1
32  print 'CASE',nloads
33  print ': apply self-weight'
34  print 'WEIGHT'
35  print '   4    9.8'
36  print ': initial conditions from Murat thesis pg 243-244'
37  print 'DEFORM'
38  print '70000 TR 3 -2.66552'
39  print '5422  TR 3 -1.60848'
40  print '5707  TR 3 -1.15112'
41  print ''
42
43  # Cycle over following load groups
44  for g in range(0,numlevels):
45      # EW DOWN
46      nloads=nloads+1
47      print 'CASE',nloads
48      print 'DEFORM'
49      print nodex, 'TR     3',loaddata[g,0]
50      print nodey, 'TR     3',loaddata[g,1]
51      print ' '
52
53  print ' '
54  print ' <================================> '
55  print ' <================================> '
56  print ' <================================> '
57  print ' '
58
59  # Write out DCF file data
60  l=1
61  # Load 1
62  print 'BEGIN EXECUT'
63  print '   BEGIN ITERAT'
64  print '      METHOD SECANT BROYDE'
65  print '      MAXITE 1000'
66  print '      BEGIN CONVER'
67  print '      FORCE TOLCON=0.01'
68  print '      DISPLA OFF '
69  print '      ENERGY TOLCON=0.0025 '
70  print '      END CONVER'
71  print '   END ITERAT'
72  print ' BEGIN LOAD'
73  print '  LOADNR=1'
74  print '  STEPS EXPLIC SIZES 0.0 0.1(10) '
75  print ' END LOAD'
76  print 'END EXECUT'
77  print ' '
78
79  for g in range(0,numlevels):
80      l=l+1
81      print ': LOAD CASE', l
82      print 'BEGIN EXECUT'
83      print '   BEGIN ITERAT'
84      print '      METHOD SECANT BROYDE'
85      print '      MAXITE 1000'
86      print '      BEGIN CONVER'
87      print '      FORCE TOLCON=0.01'
88      print '      DISPLA OFF '
89      print '      ENERGY TOLCON=0.0025 '
90      print '      END CONVER'
```

```
91          print '␣␣␣END␣ITERAT'
92          print '␣BEGIN␣LOAD'
93          print '␣␣LOADNR=',
94          sys.stdout.softspace=0
95          print l
96          print '␣␣STEPS␣EXPLIC␣SIZES␣',
97          sys.stdout.softspace=0
98          print stepssizepergroup[g],
99          sys.stdout.softspace=0
100         print '(',
101         sys.stdout.softspace=0
102         print numstepspergroup[g],
103         sys.stdout.softspace=0
104         print ')␣—',
105         sys.stdout.softspace=0
106         print stepssizepergroup[g],
107         sys.stdout.softspace=0
108         print '(',
109         sys.stdout.softspace=0
110         print numstepspergroup[g],
111         sys.stdout.softspace=0
112         print ')'
113         print '␣END␣LOAD'
114         print 'END␣EXECUT'
115         print '␣'
116
117     # End of file
```

The following input file contains the input displacements. Column 1 lists the x-direction beam end displacements, while column 2 lists the y-direction beam end displacements.

E:/Dropbox/PHD/SIM/Engin/loadgen/beamDispCorrected.txt

```
1    —23.468   0.0
2     28.6195  0.0
3      0.0    —26.2128
4      0.0     28.3972
5    —23.939 —26.2382
6     29.9158  28.3972
7    —34.899 —40.4622
8     45.589  42.545
9    —44.6801 —54.483
10    65.0337  56.7944
```

B.9.2 Material and Geometric Properties Block

E:/Dropbox/PHD/SIM/Engin/engindeniz–definitions.txt

```
: Units: N, mm, MPa

'MATERI'
   1 NAME   "Conc1"
     DENSIT  2.4028E-06
     YOUNG   21700.0
     POISON  0.2
     TOTCRK  ROTATE
     COMCRV  THOREN
     CNFCRV  VECCHI
     COMSTR  25.8
     TENCRV  HORDYK
     TENSTR  2.61939822711
     GF1     0.0828985820268
   2 NAME   "Conc2"
     DENSIT  2.4028E-06
     YOUNG   20200.0
     POISON  0.2
     TOTCRK  ROTATE
     COMCRV  THOREN
     CNFCRV  VECCHI
     COMSTR  34.1
     TENCRV  HORDYK
     TENSTR  3.15469965506
     GF1     0.0964518548148
   3 NAME   "Rigid"
     DENSIT  2.4028E-06
     YOUNG   25000.0
     POISON  0.2
   4 NAME   "5bar"
     DENSIT  1.0E-08
     YOUNG   200000
     POISON  0.3
     YIELD   VONMIS
     HARDIA  352.0 0.0 4344.96 0.99824
     ISOHAR  0.0
     DSTIF   107.105836457 107.105836457
     BONDSL  3
     SLPVAL  0.0 0.0
             0.929245128366 0.00858919277898
             1.25715066558 0.0182849990469
             1.51663416381 0.0292299925525
             1.74632278117 0.0415851159459
             1.96049991166 0.0555320473888
             2.16633875277 0.0712758720743
             2.36809549596 0.0890480979393
             2.56859285724 0.109110059915
             2.76986446795 0.131756762775
             2.97347488105 0.157321219086
             3.18069446434 0.186179346049
             3.39260220371 0.218755493248
             3.6101497354 0.255528682571
             3.834203187 0.297039652078
             4.06557166324 0.343898807377
             4.30502735773 0.396795197452
             4.5533202316 0.456506646901
             4.81118906641 0.523911193607
```

```
                5.07937003968 0.6
                5.07937003968 0.6
                0.761905505952 1.0
                0.761905505952 100.0
      5 NAME    ”3bar”
        DENSIT  1.0E−08
        YOUNG   200000
        POISON  0.3
        YIELD   VONMIS
        HARDIA  367.0 0.0 4359.66 0.998165
        ISOHAR  0.0
        DSTIF   107.105836457 107.105836457
        BONDSL  3
        SLPVAL  0.0 0.0
                0.929245128366 0.00858919277898
                1.25715066558 0.0182849990469
                1.51663416381 0.0292299925525
                1.74632278117 0.0415851159459
                1.96049991166 0.0555320473888
                2.16633875277 0.0712758720743
                2.36809549596 0.0890480979393
                2.56859285724 0.109110059915
                2.76986446795 0.131756762775
                2.97347488105 0.157321219086
                3.18069446434 0.186179346049
                3.39260220371 0.218755493248
                3.6101497354 0.255528682571
                3.834203187 0.297039652078
                4.06557166324 0.343898807377
                4.30502735773 0.396795197452
                4.5533202316 0.456506646901
                4.81118906641 0.523911193607
                5.07937003968 0.6
                5.07937003968 0.6
                0.761905505952 1.0
                0.761905505952 100.0
      6 NAME    ”6bot”
        DENSIT  1.0E−08
        YOUNG   200000.0
        POISON  0.3
        YIELD   VONMIS
        HARDIA  315.0 0.0 4308.7 0.998425
        ISOHAR  0.0
        DSTIF   107.105836457 107.105836457
        BONDSL  3
        SLPVAL  0.0 0.0
                0.929245128366 0.00858919277898
                1.25715066558 0.0182849990469
                1.51663416381 0.0292299925525
                1.74632278117 0.0415851159459
                1.96049991166 0.0555320473888
                2.16633875277 0.0712758720743
                2.36809549596 0.0890480979393
                2.56859285724 0.109110059915
                2.76986446795 0.131756762775
                2.97347488105 0.157321219086
                3.18069446434 0.186179346049
                3.39260220371 0.218755493248
                3.6101497354 0.255528682571
                3.834203187 0.297039652078
                4.06557166324 0.343898807377
                4.30502735773 0.396795197452
                4.5533202316 0.456506646901
                4.81118906641 0.523911193607
                5.07937003968 0.6
```

```
                5.07937003968 0.6
                0.761905505952 1.0
                0.761905505952 100.0
      7 NAME    ”6top”
        DENSIT  1.0E—08
        YOUNG   200000.0
        POISON  0.3
        YIELD   VONMIS
        HARDIA  315.0 0.0 4308.7 0.998425
        ISOHAR  0.0
        DSTIF   107.105836457 107.105836457
        BONDSL  3
        SLPVAL  0.0 0.0
                0.929245128366 0.00858919277898
                1.25715066558 0.0182849990469
                1.51663416381 0.0292299925525
                1.74632278117 0.0415851159459
                1.96049991166 0.0555320473888
                2.16633875277 0.0712758720743
                2.36809549596 0.0890480979393
                2.56859285724 0.109110059915
                2.76986446795 0.131756762775
                2.97347488105 0.157321219086
                3.18069446434 0.186179346049
                3.39260220371 0.218755493248
                3.6101497354 0.255528682571
                3.834203187 0.297039652078
                4.06557166324 0.343898807377
                4.30502735773 0.396795197452
                4.5533202316 0.456506646901
                4.81118906641 0.523911193607
                5.07937003968 0.6
                5.07937003968 0.6
                0.761905505952 1.0
                0.761905505952 100.0
      8 NAME    ”3slab”
        DENSIT  1.0E—08
        YOUNG   200000.0
        POISON  0.3
        YIELD   VONMIS
        HARDIA  367.0 0.0 4359.66 0.998165
        ISOHAR  0.0
        DSTIF   107.105836457 107.105836457
        BONDSL  3
        SLPVAL  0.0 0.0
                0.929245128366 0.00858919277898
                1.25715066558 0.0182849990469
                1.51663416381 0.0292299925525
                1.74632278117 0.0415851159459
                1.96049991166 0.0555320473888
                2.16633875277 0.0712758720743
                2.36809549596 0.0890480979393
                2.56859285724 0.109110059915
                2.76986446795 0.131756762775
                2.97347488105 0.157321219086
                3.18069446434 0.186179346049
                3.39260220371 0.218755493248
                3.6101497354 0.255528682571
                3.834203187 0.297039652078
                4.06557166324 0.343898807377
                4.30502735773 0.396795197452
                4.5533202316 0.456506646901
                4.81118906641 0.523911193607
                5.07937003968 0.6
                5.07937003968 0.6
```

```
                0.761905505952 1.0
                0.761905505952 100.0
      9 NAME    ”ColSpring”
        DENSIT  1.0E−08
     10 NAME    ”SteelElastic”
        YOUNG   200000.0
        POISON  3.00000E−001
        DENSIT  7.9E−06
     11 NAME    ”BaseSupport”
        DENSIT  2.4028E−06
        YOUNG   25000.0
        POISON  2.00000E−001
     12 NAME    ”ColSpring”
        DENSIT  1.0E−08
        SPRING  206086.0
'GEOMET'
      1 NAME    ”ColTip”
        AXIS    0.00000E+000  0.00000E+000  1.00000E+000
      2 NAME    ”BallTube”
        PIPE    1.52400E+002  10.0
        ECCENT  0.00000E+000  0.00000E+000  0.00000E+000  0.00000
           E+000
                0.00000E+000  0.00000E+000
        ZAXIS   1.00000E+000  0.00000E+000  0.00000E+000
      3 NAME    HSS
        CROSSE  7.37902E+003
      4 NAME    ”Wvert”
        BOX     4.06400E+002  4.06400E+002  2.54000E+001  2.54000
           E+001
                2.54000E+001  2.54000E+001
        ECCENT  0.00000E+000  0.00000E+000  0.00000E+000  0.00000
           E+000
                0.00000E+000  0.00000E+000
        ZAXIS   1.00000E+000  0.00000E+000  0.00000E+000
      5 NAME    ”BeamTopPlate”
        RECTAN  355.6  25.4
        ECCENT  0.00000E+000  0.00000E+000  0.00000E+000  0.00000
           E+000
                1.27000E+001  1.27000E+001
        ZAXIS   0.00000E+000  0.00000E+000  1.00000E+000
      6 NAME    ”Conc1”
      7 NAME    ”BaseSupport”
      8 NAME    ”Conc2”
      9 NAME    ”Rigid”
     10 NAME    ”Colbar1”
        CIRCLE  15.9
        ZAXIS   1. −1. 0.
        PERIME  49.9
     11 NAME    ”Colbar2”
        CIRCLE  15.9
        ZAXIS   1. 1. 0.
        PERIME  49.9
     12 NAME    ”Coltie”
        CIRCLE  9.5
        ZAXIS   0. 0. 1.
        PERIME  29.9
     13 NAME    ”xbtie”
        CIRCLE  9.5
        ZAXIS   1. 0. 0.
        PERIME  29.9
     14 NAME    ”ybtie”
        CIRCLE  9.5
        ZAXIS   0. 1. 0.
        PERIME  29.9
     15 NAME    ”xbot”
```

```
        CIRCLE  19.1
        ZAXIS   0. 1. 0.
        PERIME  59.8
     16 NAME   ”ybot”
        CIRCLE  19.1
        ZAXIS   1. 0. 0.
        PERIME  59.8
     17 NAME   ”xtop”
        CIRCLE  19.1
        ZAXIS   0. 1. 0.
        PERIME  59.8
     18 NAME   ”ytop”
        CIRCLE  19.1
        ZAXIS   1. 0. 0.
        PERIME  59.8
     19 NAME   ”yslab”
        CIRCLE  9.5
        ZAXIS   1. 0. 0.
        PERIME  29.9
     20 NAME   ”xslab”
        CIRCLE  9.5
        ZAXIS   0. 1. 0.
        PERIME  29.9
   ’DATA’
      1 NAME   ”Conc1”
     30 NAME   ”BaseSupport”
     29 NAME   ”BallTube”
     31 NAME   ”Wvert”
     32 NAME   ”BeamTopPlate”
     27 NAME   ”Wsection”
     28 NAME   ”HSS”
     26 NAME   ”ColTip”
      4 NAME   ”Colbar1dat”
        INTERF TRUSS
      6 NAME   ”Colbar2dat”
        INTERF TRUSS
      8 NAME   ”Coltie”
        INTERF TRUSS
     10 NAME   ”xbtie”
        INTERF TRUSS
     12 NAME   ”ybtie”
        INTERF TRUSS
     14 NAME   ”xbot”
        INTERF TRUSS
     16 NAME   ”ybot”
        INTERF TRUSS
     18 NAME   ”xtop”
        INTERF TRUSS
     20 NAME   ”ytop”
        INTERF TRUSS
     22 NAME   ”xslab”
        INTERF TRUSS
     24 NAME   ”yslab”
        INTERF TRUSS

   : End of Engindeniz specimen input
```

REFERENCES

[1] *NZS95:1955. New Zealand Standard – Model Building By-Laws: Part IV and V*. New Zealand Standard Inst., Wellington, NZ, 1953. Cited on page(s) 160

[2] "Bond of reinforcement in concrete," State of the art Bulletin 10, International Federation for Structural Concrete (*fib*), 2000. Cited on page(s) 109, 110, 111

[3] "Practitioners' guide to finite element modeling of reinforced concrete structures," State of the art Bulletin 45, *federation internationale du beton (fib)*, 2008. Cited on page(s) 33, 97

[4] "DIANA," Release 9.4.4, TNO DIANA BV, Delft, The Netherlands, 2012. Cited on page(s) 73, 74, 85, 100, 101, 111, 112, 135, 144, 219, 226

[5] ACI, *ACI 318-63: Building code requirements for structural concrete and commentary*. ACI Committee 318, American Concrete Institute, Detroit, Michigan, 1963. Cited on page(s) 145, 197

[6] ACI, *ACI352R-02: Recommendations for Design of Beam-Column Connections in Monolithic Reinforced Concrete Structures*. ACI-ASCE Committee 352, American Concrete Institute, Farmington Hills, Michigan, 2002. Cited on page(s) 6, 11

[7] ACI, *ACI 318-11: Building code requirements for structural concrete and commentary*. ACI Committee 318, American Concrete Institute, Farmington Hills, Michigan, 2011. Cited on page(s) 78, 135

[8] ACI, *ACI 408.2R-12: Report on Bond of Steel Reinforcing Bars Under Cyclic Loads*. ACI-ASCE Committee 408, American Concrete Institute, Farmington Hills, Michigan, 2012. Cited on page(s) 109, 110, 123

[9] AKGÜZEL, U., *Seismic performance of FRP retrofitted exterior RC beam-column joints under varying axial and bidirectional loading*. PhD thesis, University of Canterbury, Christchurch, New Zealand, January 2011. Cited on page(s) viii, xii, xviii, 4, 5, 6, 55, 59, 60, 63, 68, 139, 158, 161, 172, 176, 178, 225, 229, 253

[10] AKGÜZEL, U. and PAMPANIN, S., "Effects of variation of axial load and bidirectional loading on seismic performance of GFRP retrofitted reinforced concrete exterior beam-column joints," *ASCE Journal of Composites for Construction*, vol. 14, pp. 94–104, Jan-Feb 2010. Cited on page(s) 4, 55, 59, 158

[11] AKGÜZEL, U. and PAMPANIN, S., "Assessment and design procedure for the seismic retrofit of reinforced concrete beam-column joints using FRP composite materials," *ASCE Journal of Composites for Construction*, vol. 16, pp. 21–34, Jan-Feb 2012. Cited on page(s) 4, 55, 59, 158

[12] Al-Haddad, M., Siddiqui, N. A., Abadel, A., Alsayed, S. H., and Al-Salloum, Y. A., "Numerical investigations on the seismic behavior of FRP and TRM upgraded RC exterior beam-column joints," *ASCE Journal of Composites for Construction*, vol. 16, no. 3, pp. 308–321, 2012. Cited on page(s) xviii, 56, 60, 253

[13] Al-Salloum, Y. A., Almusallam, T. H., Alsayed, S. H., and Siddiqui, N. A., "Seismic behavior of as-built, ACI-complying, and CFRP-repaired exterior RC beam-column joints," *ASCE Journal of Composites for Construction*, vol. 15, pp. 522–534, July-August 2011. Cited on page(s) 57

[14] Alath, S. and Kunnath, S., "Modeling inelastic shear deformations in RC beam-column joints," in *Engineering Mechanics Proceedings of 10th Conference*, vol. 2, pp. 822–825, Univ. of Colorado at Boulder, ASCE, 1995. Cited on page(s) 12

[15] Alkhrdaji, T. and Silva, P. F., eds., *Seismic Strengthening of Concrete Buildings using FRP Composites*, no. SP-258, (Farmington Hills, Michigan), American Concrete Institute, 2008. Cited on page(s) 298

[16] Altoontash, A., *Simulation and damage models for performance assessment of reinforced concrete beam-column joints*. PhD thesis, Stanford University, Stanford, California, 2004. Cited on page(s) 12

[17] Antonopoulos, C. and Triantafillou, T., "Experimental investigation of FRP-strengthened RC beam-column joints," *ASCE Journal of Composites for Construction*, vol. 7, pp. 39–49, February 2003. Cited on page(s) 51

[18] Atrach, O., "Behaviour of interior and exterior beam-column joints under earthquake conditions," Master's thesis, University of Toronto, Toronto, Ontario, 1992. Cited on page(s) 20

[19] Baglin, P. and Scott, R., "Finite element modeling of reinforced concrete beam-column connections," *ACI Structural Journal*, vol. 97, pp. 886–894, Nov-Dec 2000. Cited on page(s) xvii, 26, 59, 60, 239

[20] Balàzs, G., "Fatigue of bond," *ACI Materials Journal*, vol. 88, pp. 620–629, Nov-Dec 1991. Cited on page(s) 111

[21] Balsamo, A., Manfredi, G., Mola, E., Negro, P., and Prota, A., "Seismic rehabilitation of a full-scale RC structure using GFRP laminates," in *7th International Symposium on Fiber-Reinforced Polymer (FRP) Reinforcement for Concrete Structures*, no. SP-230, (Farmington Hills, Michigan), pp. 1325–1344, American Concrete Institute, 2005. Cited on page(s) 5

[22] Barzegar, F. and Maddipudi, S., "Three-dimensional modeling of concrete structures. I: Plain concrete," *ASCE Journal of Structural Engineering*, vol. 123, no. 10, pp. 1339–1346, 1997. Cited on page(s) 20

[23] Barzegar, F. and Maddipudi, S., "Three-dimensional modeling of concrete structures. II: Reinforced concrete," *ASCE Journal of Structural Engineering*, vol. 123, no. 10, pp. 1347–1356, 1997. Cited on page(s) xvi, 20, 58, 60, 236

[24] Bažant, Z. and Oh, B., "Crack band theory for fracture of concrete," *Materials and Structures*, vol. 16, no. 93, pp. 155–177, 1983. Cited on page(s) 20

[25] Belarbi, A. and Hsu, T., "Constitutive laws of concrete in tension and reinforcing bars stiffened by concrete," *ACI Structural Journal*, vol. 91, pp. 465–474, July-August 1994. Cited on page(s) 84, 97

[26] Beres, A., Pessiki, S., White, R., and Gergely, P., "Implications of experiments on the seismic behavior of gravity load designed RC beam-to-column connections," *Earthquake Spectra*, vol. 12, pp. 185–198, May 1996. Cited on page(s) 3, 4, 19

[27] Biddah, A. and Ghobarah, A., "Modelling of shear deformation and bond slip in reinforced concrete joints," *Structural Engineering and Mechanics*, vol. 7, no. 4, pp. 413–432, 1999. Cited on page(s) 12

[28] Bindhu, K. and Jaya, K., "Strength and behaviour of exterior beam column joints with diagonal cross bracing bars," *Asian Journal of Civil Engineering (Building and Housing)*, vol. 11, no. 3, pp. 397–410, 2010. Cited on page(s) xviii, 50, 60, 250

[29] Carreira, D. and Chu, K., "Stress-strain relationship for plain concrete in compression," *ACI Journal, Proceedings*, vol. 82, pp. 797–804, Nov-Dec 1985. Cited on page(s) 52

[30] CEB-FIP, *Model Code 1990,* Design code. Lausanne, Switzerland: Thomas Telford, 1993. Cited on page(s) xiii, 24, 28, 36, 43, 45, 47, 51, 54, 58, 65, 85, 93, 97, 111, 114, 115, 118, 121, 122, 135, 148, 164, 184, 201, 222, 226, 228

[31] Celik, O., *Probabilistic Assessment of Non-Ductile Reinforced Concrete Frames Susceptible to Mid-America Ground Motions*. PhD thesis, Georgia Institute of Technology, Atlanta, GA, August 2007. Cited on page(s) 3, 12, 13

[32] Celik, O. and Ellingwood, B., "Modeling beam-column joints in fragility assessment of gravity load designed reinforced concrete frames," *Journal of Earthquake Engineering*, vol. 12, pp. 357–381, 2008. Cited on page(s) 12

[33] Cervenka, J. and Cervenka, V., "Three-dimensional combined fracture-plastic material model for concrete," in *Proceedings of the 5th U.S. National Congress on Computational Mechanics*, (Boulder, Colorado), August 1999. Cited on page(s) 33

[34] Cervenka, V., "Computer simulation of failure of concrete structures for practice," in *The First* fib *Congress - Concrete structures in the 21st century*, (Osaka, Japan), 2002. Cited on page(s) xvii, 33, 60, 242

[35] Chen, T., "Retrofit strategy of non-seismically designed frame systems based on a metallic haunch system," Master's thesis, University of Canterbury, Christchurch, New Zealand, 2006. Cited on page(s) 4

[36] Chen, W.-F., *Plasticity in Reinforced Concrete*. J. Ross Publishing, 2007. Cited on page(s) 17, 45, 53, 64

[37] Ciampi, V., Eligehausen, R., Bertero, V., and Popov, E., "Analytical model for concrete anchorages of reinforcing bars under generalized excitations," Report No. EERC82-83, Earthquake Engineering Research Center (EERC), Berkeley, CA, Dec 1982. Cited on page(s) 111

[38] Clyde, C., Pantelides, C., and Reaveley, L., "Performance-based evaluation of exterior reinforced concrete building joints for seismic excitation," PEER Report 2000/05, Pacific Earthquake Engineering Research Center, University of California, Berkeley, July 2000. Cited on page(s) 145, 158

[39] Conley, C., "Chapter 9 – specific applications," in *Finite Element Analysis of Reinforced Concrete Structures II – Proceedings of the Int'l Workshop* (Isenberg, J., ed.), (New York, NY), ASCE, 1993. Cited on page(s) xvi, 8, 18, 60, 235

[40] Darwin, D. and Pecknold, D., "Nonlinear biaxial stress-strain law for concrete," *ASCE Journal of Engineering Mechanics*, vol. 103, pp. 229–241, April 1977. Cited on page(s) 16, 17, 31, 32, 36, 37, 39, 46, 49, 50

[41] de Borst, R. and Nauta, P., "Non-orthogonal cracks in a smeared finite element model," *Engineering Computations*, vol. 2, pp. 34–46, 1985. Cited on page(s) 19, 20, 28, 64, 73

[42] Del Toro Rivera, R., *Behaviour of reinforced concrete beam-column joints under alternated loading*. PhD thesis, Ecole Nationale des Ponts et Chaussées, Paris, France, 1988. Cited on page(s) 23

[43] Desayi, P. and Krishnan, S., "Equation for the stress-strain curve of concrete," *ACI Structural Journal*, vol. 61, pp. 345–350, 1964. Cited on page(s) 50

[44] Di Ludovico, M., Manfredi, G., Mola, E., Negro, P., and Prota, A., "Seismic behavior of a full-scale RC structure retrofitted using GFRP laminates," *ASCE Journal of Structural Engineering*, vol. 134, pp. 810–821, May 2008. Cited on page(s) 5

[45] Drucker, D. and Prager, W., "Soil mechanics and plastic analysis or limit design," *Quarterly Journal of Applied Mathematics*, vol. 10, no. 2, pp. 157–165, 1952. Cited on page(s) 28, 33, 36, 39, 40, 45, 46, 47, 64, 73

[46] Duong, K., Sheikh, S., and Vecchio, F., "Seismic behavior of shear-critical reinforced concrete frame: experimental investigation," *ACI Structural Journal*, vol. 104, no. 3, p. 304, 2007. Cited on page(s) 44

[47] Durrani, A. and Wight, J., "Earthquake resistance of reinforced concrete interior connections including a floor slab," *ACI Structural Journal*, vol. 84, pp. 400–406, Sep-Oct 1987. Cited on page(s) 19

[48] Durrani, A. and Zerbe, H., "Seismic resistance of R/C exterior connections with a floor slab," *ASCE Journal of Structural Engineering*, vol. 113, no. 8, pp. 1850–1864, 1987. Cited on page(s) 20

[49] Ehsani, M. and Wight, J., "Exterior reinforced concrete beam-to-column connections subjected to earthquake-type loading," *ACI Journal Proceedings*, vol. 82, July-August 1985. Cited on page(s) 30

[50] El-Nabawy Atta, A., Famy Taher, S., Khalil, A.-H. A., and El-Metwally, S., "Behaviour of reinforced high-strength concrete beam-column joint. part II: numerical simulation," *Structural Concrete (fib)*, vol. 5, no. 3, pp. 101 –112, 2004. Cited on page(s) xvii, 34, 60, 243

[51] Eligehausen, R., Bertero, V., and Popov, E., "Hysteretic behavior of reinforcing deformed hooked bars in R/C joints," in *Proceedings of the Seventh European Conference on Earthquake Engineering*, vol. 4, (Athens), pp. 171–178, September 1982. Cited on page(s) 123

[52] Eligehausen, R., Genesio, G., Ožbolt, J., and Pampanin, S., "3D analysis of seismic response of RC beam-column exterior joints before and after retrofit," in *Proc. of the 2nd International Conference on Concrete Repair, Rehabilitation and Retrofitting, ICCRRR* (et al. A., ed.), (Cape Town, South Africa), 2008. Cited on page(s) xvii, 41, 42, 59, 60, 72, 246

[53] Eligehausen, R., Ožbolt, J., Genesio, G., Hoehler, M., and Pampanin, S., "Three-dimensional modelling of poorly detailed RC frame joints," in *Proceedings of the New Zealand Society for Earthquake Engineering (NZSEE) Conference*, 2006. Cited on page(s) 41, 66, 124

[54] Eligehausen, R., Popov, E., and Bertero, V., "Local bond stress slip relationship of deformed bars under generalized excitations," EERC Report 83-23, Earthquake Engineering Research Center (EERC), University of California, Berkeley, 1983. Cited on page(s) xiii, 22, 23, 41, 53, 56, 65, 110, 111, 113, 231

[55] Elmorsi, M., *Analytical Modeling of Reinforced Concrete Beam Column Connections for Seismic Loading*. PhD thesis, McMaster University, Canada, June 1998. Cited on page(s) xvi, 21, 60, 237

[56] Elmorsi, M., Kianoush, M., and Tso, W., "Nonlinear analysis of cyclically loaded reinforced concrete structures," *ACI Structural Journal*, vol. 95, pp. 725–739, Nov-Dec 1998. Cited on page(s) 22

[57] Elmorsi, M., Kianoush, M., and Tso, W., "Modeling bond-slip deformations in reinforced concrete beam-column joints," *Canadian Journal of Civil Engineering*, vol. 27, pp. 490–505, 2000. Cited on page(s) 21

[58] Elwi, E. and Hrudey, M., "Finite element model for curved embedded reinforcement," *ASCE Journal of Engineering Mechanics*, vol. 115, no. 4, pp. 740–754, 1989. Cited on page(s) 20

[59] Emara, M. and Hosny, H., "Nonlinear finite element analysis of slab effects in reinforced concrete structures subjected to earthquake loads," in *Proceedings of the Eighth International Conference on Civil and Structural Engineering Computing* (Topping, B., ed.), (Stirling, Scotland), Civil-Comp Press, 2001. Cited on page(s) xvii, 28, 60, 240

[60] Engindeniz, M., *Repair and Strengthening of Pre-1970 Reinforced Concrete Corner Beam-Column Joints Using CFRP Composites*. PhD thesis, Georgia Institute of Technology, Atlanta, GA, August 2008. Cited on page(s) ix, xii, xv, 1, 4, 5, 6, 68, 139, 194, 197, 199, 200, 201, 212, 225, 228, 229

[61] Engindeniz, M., Kahn, L. F., and Zureick, A.-H., "Repair and strengthening of reinforced concrete beam-column joints: State of the art," *ACI Structural Journal*, vol. 102, pp. 1–14, March-April 2005. Cited on page(s) 3

[62] Engindeniz, M., Kahn, L. F., and Zureick, A.-H., "Performance of an RC corner beam-column joint severaly damaged under bidirectional loading and rehabilitated with FRP composites," in Alkhrdaji and Silva [15]. Cited on page(s) 4, 194

[63] Fafitis, A. and Shah, S., "Lateral reinforcement for high-strength concrete columns," in *ACI Special Publication SP-87*, pp. 213–232, 1985. Cited on page(s) 21, 39

[64] Fleury, F., Reynouard, J., and Merabet, O., "Finite element implementation of a steel-concrete bond law for nonlinear analysis of beam-column joints subjected to earthquake type loading," *Structural Engineering and Mechanics*, vol. 7, no. 1, pp. 35–52, 1999. Cited on page(s) xvi, 22, 60, 65, 99, 238

[65] Fleury, F., Reynouard, J., and Merabet, O., "Multicomponent model of reinforced concrete joints for cyclic loading," *ASCE Journal of Engineering Mechanics*, vol. 126, pp. 804–811, August 2000. Cited on page(s) 23

[66] Foutch, D., Gamble, W., and Sunidja, H., "Test of post-tensioned concrete slab-edge column connections," *ACI Structural Journal*, vol. 87, pp. 167–179, March-April 1990. Cited on page(s) 52

[67] French, C. and Moehle, J., "Effect of floor slab on behavior of slab-beam-column connections," No. SP-237, (Farmington Hills, Michigan), pp. 225–258, American Concrete Institute, 1991. Cited on page(s) 67

[68] Gopalaratnam, V. and Shah, S., "Softening response of plain concrete in direct tension," *ACI Journal*, vol. 82, pp. 310–323, May-June 1985. Cited on page(s) vii, xii, 54, 85, 86, 87, 88, 89, 90, 91, 92, 95

[69] Goto, Y. and Joh, O., "Shear resistance of RC interior eccentric beam-column joints," in *Proceedings of the 13th World Conference on Earthquake Engineering (13WCEE)*, (Vancouver, B.C., Canada), 2004. Cited on page(s) xvii, 36, 59, 60, 244

[70] Govindjee, S. and Hall, G., "A local integration method for coupled damage and plasticity," Tech. Rep. UCB/SEMM-98/01, SEMM University of California, Berkeley, 1997. Cited on page(s) 23

[71] Govindjee, S., Kay, G., and Simo, J., "Anisotropic modelling and numerical simulation of brittle damage in concrete," *International Journal for Numerical Methods in Engineering*, vol. 38, no. 21, pp. 3611–3633, 1995. Cited on page(s) 23

[72] Gylltoft, K., *Fracture mechanics models for fatigue in concrete structures*. PhD thesis, Div. of Concrete Struct. LuleåUniversity of Technology, Luleå, Sweden, 1983. Cited on page(s) 28

[73] Haach, V., El Debs, A., and El Debs, M., "Evaluation of the influence of the column axial load on the behavior of monotonically loaded R/C exterior beam-column joints through numerical simulations," *Engineering Structures*, vol. 30, pp. 965–975, 2008. Cited on page(s) xvii, 43, 60, 247

[74] Hajime, O. and Kohichi, M., "Nonlinear analysis and constitutive models for reinforced concrete," Gihodo, Tokyo, 1991. Cited on page(s) 48

[75] Hamil, S. J., *Reinforced Concrete Beam-Column Connection Behavior*. PhD thesis, University of Durham, England, 2000. Cited on page(s) xvii, 26, 60, 239

[76] Hawkins, N., Lin, I., and Jeang, F., "Local bond strength of concrete for cyclic reversed actions," in *Proceedings, Bond in Concrete*, pp. 151–161, Applied Science Publishers London, 1982. Cited on page(s) 111

[77] Hawkins, N., Lin, I., and Ueda, T., "Anchorage of reinforcing bars for seismic forces," *ACI Structural Journal*, vol. 84, pp. 407–418, Sept-Oct 1987. Cited on page(s) viii, 123, 125, 126, 129

[78] Hayashi, K., Kanoh, Y., Teraoka, M., and Mollick, A., "Experimental study on reinforced concrete interior beam-column joints when axis of beam and axis of column are not concurrent," *Proc. of the Japan Concrete Institute*, vol. 13, no. 2, pp. 507–512, 1991. Cited on page(s) 36

[79] Hegger, J., Sherif, A., and Roeser, W., "Nonlinear finite element analysis of reinforced concrete beam-column connections," *ACI Structural Journal*, vol. 101, pp. 604–614, Sep-Oct 2004. Cited on page(s) xvii, 35, 59, 60, 243

[80] Hertanto, E., "Seismic assessment of pre-1970s reinforced concrete structure," Master's thesis, University of Canterbury, Christchurch, New Zealand, 2005. Cited on page(s) 4

[81] Hoehler, M. and Ožbolt, J., "Three-dimensional reversed-cyclic analysis of reinforced concrete members using the microplane model," *Otto-Graf Journal*, vol. 12, pp. 93–114, 2001. Cited on page(s) xvii, 29, 59, 60, 65, 72, 99, 241

[82] Hognestad, E., "A study of combined bending and axial load in reinforced concrete members," Bulletin Series no. 399, Bulletin no. 1, University of Illinois Engineering Experiment Station, 1951. Cited on page(s) 17, 57

[83] Hognestad, E., "Inelastic behavior in tests of eccentrically loaded short reinforced concrete columns," *Journal of the American Concrete Institute*, vol. 124, pp. 177–139, Oct 1952. Cited on page(s) 77

[84] Hordijk, D., *Local approach to fatigue of concrete*. PhD thesis, Delft University of Technology, Delft, The Netherlands, 1991. Cited on page(s) xii, 24, 36, 41, 57, 85, 86, 93, 135, 148, 226

[85] Hoshikuma, J., Kawashima, K., Nagaya, K., and Taylor, A., "Stress-strain model for confined reinforced concrete in bridge piers," *ASCE Journal of Structural Engineering*, vol. 123, no. 5, pp. 624–633, 1997. Cited on page(s) 78

[86] Hseih, S., Ting, E., and Chen, W.-F., "An elastic-fracture model for concrete," in *Proceedings of the 3rd Engineering Mechanics Division Special Conference*, (Austin, TX), pp. 437–440, ASCE, 1979. Cited on page(s) 76

[87] Huang, Y., Kang, T. H.-K., Ramseyer, C., and Rha, C., "Background to multiscle modelling of unbonded post-tensioned concrete structures," *Int. J. Theoretical and Applied Multiscale Mechanics*, vol. 1, no. 3, pp. 219–230, 2009. Cited on page(s) 51

[88] Ibrahim, H. and El-Badry, M., "Nonlinear 3D finite element analysis of exterior beam-column joints reinforced with double studs for shear resistance under cyclic loading," in *Proceedings of the Annual Conference*, vol. 4, (Montreal, QC, Canada), pp. 2527–2537, Canadian Society for Civil Engineering, 2008. Cited on page(s) xvii, 45, 59, 60, 248

[89] Ihzuka, T. and Noguchi, H., "Nonlinear finite element analysis of reinforced concrete members with normal to high strength materials," *Proceedings of the Japan Concrete Institute*, vol. 14, no. 2, pp. 9–14, 1992. Cited on page(s) 31

[90] Ismail, M. and Jirsa, J., "Bond deterioration in reinforced concrete subjected to low-cycle loads," *ACI Journal Proceedings*, vol. 69, pp. 334–343, June 1972. Cited on page(s) 123

[91] Jain, S. and Murty, C., "Experimental investigation of cyclic behavior of RC flexural members," Consolidated Technical Report for Atomic Energy Regulatory Board, Indian Institute of Technology, Kanpur, India, 1999. Cited on page(s) 42

[92] Johansson, M., "Nonlinear finite-element analyses of concrete frame corners," *ASCE Journal of Structural Engineering*, vol. 126, pp. 190–199, February 2000. Cited on page(s) xvii, 28, 60, 69, 240

[93] Johnson, L. and Jirsa, J., "The influence of short embedment and close spacing on the strength of hooked bar anchorages," PMFSEL Report No. 81-2, The University of Texas at Austin, Austin, TX, April 1981. Cited on page(s) 123

[94] Kai, Q. and Li, B., "Experimental and analytical assessment on RC interior beam-column subassemblages for progressive collapse," *ASCE Journal of Performance of Constructed Facilities*, 2011. Accepted. Cited on page(s) xviii, 54, 60, 252

[95] Kaku, T. and Asakusa, H., "Ductility estimation of exterior beam-column subassemblages in RC frames," in *Design of Beam-Column Joints for Seismic Resistance*, no. SP-123, American Concrete Institute, 1991. Cited on page(s) 22

[96] Kamimura, T. and Hamada, D., "Experimental study on reinforced concrete beam-column joints: Part 1-3," in *Proc. Annual Conv., AIJ*, pp. 1673–74, September 1978. Cited on page(s) 15

[97] Kang, T. H.-K. and Huang, Y., "Nonlinear finite element analyses of unbonded post-tensioned slab-column connections," *PTI Journal*, vol. In press, 2011. Cited on page(s) xviii, 51, 60, 251

[98] Karsan, I. and Jirsa, J., "Behavior of concrete under compressive loadings," *ASCE J. of the Structural Division*, vol. 95, pp. 2543–2563, December 1969. Cited on page(s) vii, xii, 77, 78, 79, 80, 81, 82, 83

[99] Kashiwazaki, T. and Noguchi, H., "Experimental study on the shear performance of of R/C interior beam-column joints with ultra high-strength materials," *Proc. of the Japan Concrete Institute*, vol. 13, no. 2, pp. 475–478 (in Japanese), 1991. Cited on page(s) 21

[100] Kashiwazaki, T. and Noguchi, H., "Three-dimensional nonlinear finite element analysis on the shear strength of RC interior beam-column joints with ultra high-strength materials, paper no. 476," in *Proceedings of the 11th World Conference on Earthquake Engineering*, (Acapulco, Mexico), June 1996. Cited on page(s) 21

[101] Kashiwazaki, T. and Noguchi, H., "FEM analysis on the effects of joint lateral reinforcement on the shear strength of RC interior beam-column joints," *Trans. of the Japan Concrete Institute*, vol. 19, pp. 287–294, 1997. Cited on page(s) 31

[102] Kashiwazaki, T. and Noguchi, H., "Shear performance of prestressed RC interior beam-column joints," in *Modeling of Inelastic Behavior of RC Structures Under Seismic Loads* (Shing, P. and Tanabe, T.-A., eds.), pp. 580–589, ASCE/SEI, 2001. Cited on page(s) xvii, 31, 60, 241

[103] Kashiwazaki, T. and Noguchi, H., "Seismic performance evaluation of RC eccentric beam-column joints using three-dimensional FEM analysis," in *Proceedings of the 13th World Conference on Earthquake Engineering (13WCEE)*, (Vancouver, B.C., Canada), August 2004. Cited on page(s) xvii, 36, 60, 244

[104] Kashiwazaki, T. and Noguchi, H., "Blind analysis of RC beam-column joints subjected to multi-axial combined loadings using 3D nonlinear FEM," in *Proceedings of the 14th World Conference on Earthquake Engineering (14WCEE)*, (Beijing, China), October 2008. Cited on page(s) xvii, 46, 58, 60, 248

[105] Kent, D. and Park, R., "Flexural members with confined concrete," *ASCE J. of the Structural Division*, vol. 7, pp. 1969–1990, 1971. Cited on page(s) 21, 31, 78

[106] Kim, S.-W. and Vecchio, F., "Modeling of shear-critical reinforced concrete structures repaired with fiber-reinforced polymer composites," *ASCE Journal of Structural Engineering*, vol. 134, pp. 1288–1299, August 2008. Cited on page(s) xvii, 44, 60, 65, 69, 72, 248

[107] Kishida, S., Moriyama, K., Kitayama, K., and Nishikawa, T., "Study on shear characteristics of RC 3-dimensional beam column joints with variable bond characteristics of beam reinforcement," *Proc. of the JCI Annual Conference*, vol. 27, no. 5, pp. 385–390, 2005. Cited on page(s) 49

[108] Kitayama, K., Otani, S., and Aoyama, H., "Develop of design criteria for RC interior beam-column joints," in *Design of Beam-Column Joints for Seismic Resistance, ACI Special Publication SP-123*, (Detroit, Michigan), pp. 97–123, American Concrete Institute, 1991. Cited on page(s) 19

[109] Kulkarni, S., Li, B., and Yip, W., "Finite element analysis of precast hybrid-steel concrete connections under cyclic loading," *J. Constr. Steel Res.*, vol. 64, pp. 190–201, 2008. Cited on page(s) xviii, 46, 48, 60, 66, 249

[110] Kulkarni, S. and Li, B., "Seismic behavior of reinforced concrete interior wide-beam column joints," *Journal of Earthquake Engineering*, vol. 13, pp. 80–99, 2009. Cited on page(s) xviii, 48, 58, 60, 249

[111] Kupfer, H., Hilsdorf, H., and Rusch, H., "Behavior of concrete under biaxial stresses," *ACI Journal, Proceedings*, vol. 66, pp. 656–666, August 1969. Cited on page(s) 17, 27, 33, 35

[112] Kurose, Y., Guimaraes, G., Zuhua, L., Kreger, M., and Jirsa, J., "Evaluation fo slab-beam-column connections subjected to bidirectional loading," in *Design of Beam-Column Joints for Seismic Resistance, ACI Special Publication SP-123* (Jirsa, J., ed.), (Farmington Hills, Michigan), pp. 39–67, American Concrete Institute, 1991. Cited on page(s) 29

[113] Kwak, H.-G. and Filippou, F. C., "Finite element analysis of reinforced concrete structures under monotonic loads," Tech. Rep. UCB/SEMM-90/14, University of California, Berkeley, November 1990. Cited on page(s) xvi, 17, 38, 55, 60, 64, 235

[114] Lee, J. and Fenves, G., "Plastic-damage model for cyclic loading of concrete structures," *ASCE Journal of Engineering Mechanics*, vol. 124, no. 8, pp. 892–900, 1998. Cited on page(s) 51, 54, 73

[115] Lee, S., Kitayama, K., Otani, S., and Aoyama, H., "Shear strength of reinforced concrete interior beam-column joints using high-strength materials," *Proc. of the Japan Concrete Institute*, vol. 14, no. 2, pp. 379–384 (in Japanese), 1992. Cited on page(s) 21

[116] Leon, R. and Jirsa, J. O., "Bidirectional loading of R.C. beam-column joints," *Earthquake Spectra*, vol. 2, no. 3, pp. 537–564, 1986. Cited on page(s) 6, 67

[117] Lettow, S., *Ein Verbundelement fur nichtlineare Finite Elementa Analysen—Anwendung auf Ubergreifungsstrose*. PhD thesis, IWB UNiversistat Stuttgart, Germany (in German), 2007. Cited on page(s) 42

[118] Li, B., Wu, Y., and Pan, T., "Seismic behavior of nonseismically detailed interior beam-wide column joints - part I: Experimental results and observed behavior," *ACI Structural Journal*, vol. 99, pp. 791–802, Nov-Dec 2002. Cited on page(s) 34

[119] Li, B., Wu, Y., and Pan, T., "Seismic behavior of nonseismically detailed interior beam-wide column joints - part II: Theoretical comparisons and analytical studies," *ACI Structural Journal*, vol. 100, pp. 56–65, Jan-Feb 2003. Cited on page(s) xvii, 34, 58, 60, 243

[120] Li, B. and Kulkarni, S., "Seismic behavior of reinforced concrete exterior wide beam-column joints," *ASCE Journal of Structural Engineering*, vol. 136, pp. 26–36, January 2010. Cited on page(s) 48, 58, 60, 72

[121] Li, B., Tran, C. T. N., and Pan, T.-C., "Experimental and numerical investigations on the seismic behavior of lightly reinforced concrete beam-column joints," *ASCE Journal of Structural Engineering*, vol. 135, pp. 1007–1018, September 2009. Cited on page(s) xviii, 47, 48, 58, 60, 64, 72, 249

[122] Lin, I. and Hawkins, N., "Anchorage characteristics for reinforcing bars for reversed cyclic loading," Report No. SM82-1, Department of Civil Engineering, Univeristy of Washington, Seattle, Washington, June 1982. Cited on page(s) 123, 125

[123] Lowes, L., *Finite Element Modeling of Reinforced Concrete Beam-Column Bridge Connections*. PhD thesis, University of California, Berkeley, 1999. Cited on page(s) xvi, 23, 60, 238

[124] Lowes, L. and Fillipou, F., eds., *Finite Element Analysis of Reinforced Concrete Structures*, no. SP-237, (Farmington Hills, Michigan), American Concrete Institute, 2006. Cited on page(s) 306, 311

[125] Lowes, L. N., "Finite element analysis of RC beam-column bridge connections," (Reston, Virginia), pp. 276–296, ASCE/SEI, 2001. Cited on page(s) 23

[126] Lowes, L. N., Moehle, J., and Govindjee, S., "Concrete-steel bond model for use in finite element modeling of reinforced concrete structures," *ACI Structural Journal*, vol. 101, pp. 501–511, July 2004. Cited on page(s) 24

[127] Lowes, L. and Altoontash, A., "Modeling reinforced-concrete beam-column joints subjected to cyclic loading," *ASCE Journal of Structural Engineering*, vol. 129, no. 12, pp. 1686–1697, 2003. Cited on page(s) 12

[128] Lubliner, J., Oliver, J., Oller, J., and Oñate, E., "A plastic-damage model for concrete," *Int. J. Solids and Structures*, vol. 25, no. 3, pp. 299–326, 1989. Cited on page(s) 51, 54, 73

[129] Lundgren, K., *Three-dimensional modelling of bond in reinforced concrete*. PhD thesis, Chalmers University of Technology, Göteborg, Sweden, 1999. Cited on page(s) xvi, 24, 60, 64, 65, 72, 238

[130] Lundgren, K. and Magnusson, J., "Three-dimensional modeling of anchorage zones in reinforced concrete," *ASCE Journal of Engineering Mechanics*, vol. 127, pp. 693–699, July 2001. Cited on page(s) 24

[131] Ma, S.-Y., Bertero, V., and Popov, E., "Experimental and analytical studies on the hysteretic behaviour of reinforced concrete rectangular and T-beams," Tech. Rep. UBC/EERC 76-2, Earthquake Engineering Research Center (EERC), University of California, Berkeley, 1976. Cited on page(s) 29, 100, 101, 106, 127

[132] MacGregor, J. G., *Reinforced Concrete*. Prentice Hall, third ed., 1997. Cited on page(s) 142

[133] Maekawa, K., Takemura, J., Irawan, P., and Irie, M., "Continuum fracture in concrete nonlinearity under triaxial confinement," *Proc. of JSCE*, vol. 18, pp. 113–122, February 1993. Cited on page(s) 73

[134] Maekawa, K., Takemura, J., Irawan, P., and Irie, M., "Plasticity in concrete nonlinearity under triaxial confinement," *Proc. of JSCE*, vol. 18, pp. 123–130, February 1993. Cited on page(s) 73

[135] Maekawa, K., Takemura, J., Irawan, P., and Irie, M., "Triaxial elastoplastic and fracture model for concrete," *Proc. of JSCE*, vol. 18, pp. 131–138, February 1993. Cited on page(s) 73

[136] Mahini, S., *Rehabilitation of Exterior RC Beam-Column Joints using CFRP Sheets*. PhD thesis, University of Queensland, Australia, 2005. Cited on page(s) xvii, 37, 55, 60, 245

[137] Mahini, S. and Ronagh, H., "Web-bonded FRP's for relocation of plastic hinges away from the column face in exterior RC joints," *Composite Structures*, 2011. Cited on page(s) xviii, 55, 59, 60, 252

[138] Mander, J., Priestley, J., and Park, R., "Observed stress-strain behavior of confined concrete," *ASCE Journal of Structural Engineering*, vol. 114, pp. 1827–1849, August 1988. Cited on page(s) 78

[139] Mander, J., Priestley, J., and Park, R., "Theoretical stress-strain model for confined concrete," *ASCE Journal of Structural Engineering*, vol. 114, pp. 1804–1826, August 1988. Cited on page(s) 25, 43, 78

[140] Manfredi, G., Verderame, G., and Lignola, G., "A F.E.M. model for the evaluation of the seismic behavior of internal joints in reinforced concrete frames," in *Proceedings of the 14th World Conference on Earthquake Engineering (14WCEE)*, (Beijing, China), 2008. Cited on page(s) xvii, 42, 60, 247

[141] Mazzarolo, E., Scotta, R., Berto, L., and Saetta, A., "Long anchorage bond-slip formulation for modeling of R.C. elements and joints," *Engineering Structures*, vol. 34, pp. 330–341, 2012. Cited on page(s) xviii, 57, 59, 60, 253

[142] Menegotto, M. and Pinto, E., "Method of analysis for cyclically loaded reinforced concrete plane frames including changes in geometry and non-elastic behaviour of elements under combined normal force and bending," in *IABSE Symposium on the Resistance and Ultimate Deformability of Structures Acted on by Well-Defined Repeated Loads*, (Lisbon), 1973. Cited on page(s) 22, 24, 31, 45, 51, 53, 65, 99, 100, 101

[143] Menètrey, P. and Willam, K., "Triaxial failure criterion for concrete and its generalization," *ACI Structural Journal*, vol. 92, no. 3, pp. 311–318, 1995. Cited on page(s) 33, 45, 53

[144] Minor, J. and Jirsa, J., "Behavior of bent bar anchorages," *ACI Journal Proceedings*, vol. 72, pp. 141–149, April 1975. Cited on page(s) 123

[145] Mitra, N. and Lowes, L., "Evaluation, calibration, and verification of a reinforced concrete beam-column joint model," *ASCE Journal of Structural Engineering*, vol. 133, no. 1, pp. 105–120, 2007. Cited on page(s) 12

[146] Mitra, N., *An Analytical Study of Reinforced Concrete Beam-Column Joint Behavior Under Seismic Loading*. PhD thesis, University of Washington, 2007. Cited on page(s) xvii, 40, 60, 246

[147] Mitra, N., "Continuum model for RC interior beam-column connection regions," in *Proceedings of the 14th World Conference on Earthquake Engineering (14WCEE)*, (Beijing, China), October 2008. Cited on page(s) 41

[148] Monti, G. and Nuti, C., "Nonlinear cyclic behavior of reinforcing bars including buckling," *ASCE Journal of Structural Engineering*, vol. 118, no. 12, p. 32683284, 1992. Cited on page(s) 99, 101

[149] Monti, G., Renzelli, M., and Luciani, P., "FRP adhesion in uncracked and cracked concrete zones," in *Proc. of the 6th international symposium on FRP reinforcement of concrete structures*, pp. 183–192, 2003. Cited on page(s) 51

[150] Montoya, E., *Behavior and analysis of confined concrete*. PhD thesis, University of Toronto, Toronto, Canada, 2003. Cited on page(s) 44

[151] Morita, S. and Kaku, T., "Bond-slip relationship under repeated loading," *Transactions of the Architectural Institute of Japan*, no. 299, pp. 15–24, 1975. Cited on page(s) 16, 31, 32, 36, 37, 39, 46, 49, 50, 65, 111, 231

[152] Mosalam, K., Gergely, P., and White, R., "Three dimensional analysis of RC frame-slab building systems," in *Proceedings of the 5th U.S. National Conference on Earthquake Engineering*, vol. I, (Chicago, IL), pp. 75–84, Earthquake Engineering Research Institute (EERI), July 1994. Cited on page(s) xvi, 18, 58, 60, 236

[153] Mostofinejad, D. and Talaeitaba, S., "Finite element modeling of RC connections strengthened with FRP laminates," *Iranian Journal of Science and Technology, Transaction B, Engineering*, vol. 30, no. B1, 2006. Cited on page(s) xvii, 40, 60, 246

[154] Naganuma, K. and Ohkubo, M., "An analytical model for RC panels under cyclic stresses," *Journal of Structural and Construction Engineering, Architectural Institute of Japan*, no. 536, pp. 135–142, 2000. Cited on page(s) 31

[155] Ngo, D. and Scordelis, A., "Finite element analysis of reinforced concrete beams," *Journal of American Concrete Institute*, vol. 64, no. 14, pp. 152–163, 1967. Cited on page(s) 16, 65, 111

[156] Nito, Y., Yoshimura, T., Hukazawa, K., Tachibana, M., and Nakano, K., "Effect of bi-directional loading on crack behaviour of inner R/C structure under bi-directional earthquake motions," in *Summaries of Technical Papers of Annual Meeting of Architectural Institute of Japan (in Japanese)*, no. C-2, pp. 507–512, 1994. Cited on page(s) 39

[157] Noguchi, H., "Nonlinear finite element analysis of reinforced concrete beam-column joints," in *IABSE Colloquium*, (Delft, The Netherlands), pp. 639–653, IABSE, 1981. Cited on page(s) xvi, 15, 16, 60, 71, 234

[158] Noguchi, H., "Three-dimensional FEM analysis of RC beam-column joints subjected to two-directional loads," in Lowes and Fillipou [124]. Cited on page(s) xvii, 39, 58, 60, 72, 245

[159] Noguchi, H. and Kashiwazaki, T., "Finite element analysis of RC beam-column joints with high-strength materials," *Structural Engineering and Mechanics*, vol. 5, no. 5, pp. 625–634, 1997. Cited on page(s) xvi, 21, 60, 237

[160] Noguchi, H. and Kashiwazaki, T., "FEM analysis of structural performance deterioration of RC elements subjected to seismic reversed cyclic shear," in *Proceedings of the 13th World Conference on Earthquake Engineering (13WCEE)*, (Vancouver, B.C., Canada), August 2004. Cited on page(s) xvii, 37, 58, 60, 244

[161] Noguchi, H. and Kashiwazaki, T., "FEM analysis of interaction effects of 3-D RC members subjected to multi-directional cyclic loading," in *Proceedings of the 2009 Structures Congress*, pp. 1209–1218, ASCE, 2009. Cited on page(s) xviii, 49, 58, 60, 250

[162] Noguchi, H., Kashiwazaki, T., and Hong, J., "FEM analysis of three-dimensional interaction of RC frames subjected to multi-directional cyclic loading," in *Proceedings of the 14th World Conference on Earthquake Engineering (14WCEE)*, (Beijing, China), 2008. Cited on page(s) 49, 63, 68, 69

[163] Noguchi, H., Kashiwazaki, T., and Miura, K., "Finite element analysis of reinforced concrete joints subjected to multi-axial loading," in *SP-265: Thomas T.C. Hsu Symposium: Shear and Torsion in Concrete Structures* (Belarbi, A., Mo, Y., and Ayoub, A., eds.), American Concrete Institute, 2009. Cited on page(s) xviii, 49, 60, 72, 250

[164] Noguchi, H., Kashiwazaki, T., Uchida, K., and Nozaki, Y., "FEM analysis for structural performance design of concrete structures," in *Modeling of Inelastic Behavior of RC Structures Under Seismic Loads* (Shing, P. and Tanabe, T.-A., eds.), pp. 257–275, ASCE/SEI, 2001. Cited on page(s) 30

[165] Noguchi, H. and Naganuma, K., "Nonlinear finite element analysis of restoring force characteristics of reinforced concrete beam-column joints," in *Proceedings of the 8th World Conference on Earthquake Engineering*, (San Francisco, CA), pp. 543–550, 1984. Cited on page(s) xvi, 16, 58, 60, 71, 234

[166] Oka, K. and Shiohara, H., "Tests on high-strength concrete interior beam-column joint subassemblages," in *Proceedings of the 10th World Conference on Earthquake Engineering*, (Madrid, Spain), pp. 3211–3217, 1992. Cited on page(s) 41

[167] Ožbolt, J., Li, Y.-J., and Kožar, L., "Microplane model for concrete with relaxed kinematic constraint," *Int. J. Solids and Structures*, vol. 38, pp. 2683–2711, 2001. Cited on page(s) 29, 30, 41, 42, 56, 64, 168

[168] Ožbolt, J., Mayer, U., and Vocke, H., "Smeared fracture FE-analysis of reinforced concrete structures – theory and examples," in *Modeling of Inelastic Behavior of RC Structures Under Seismic Loads* (Shing, P. and Tanabe, T.-A., eds.), pp. 234–256, ASCE, 2001. Cited on page(s) xvii, 30, 60, 241

[169] Palermo, D., *Behaviour and Analysis of Reinforced Concrete Walls Subjected to Reversed Cyclic Loading*. PhD thesis, University of Toronto, Canada, May 2002. Cited on page(s) 232

[170] Palermo, D. and Vecchio, F., "Behaviour and analysis of reinforced concrete walls subjected to reversed cyclic loading," Publication No. 2002-1, Dept. of Civil Engineering, University of Toronto, Toronto, Canada, May 2002. Cited on page(s) 44, 53

[171] Pampanin, S., Calvi, G., and Moratti, M., "Seismic behaviour of R.C. beam-column joints designed for gravity only," in *Proceedings of the 12th European Conference on Earthquake Engineering*, (London), 2002. Cited on page(s) 41

[172] Pampanin, S., Christopoulos, C., and Chen, T.-H., "Development and validation of a metallic haunch retrofit solution for existing under-designed RC frame buildings," *Earthquake Engineering and Structural Dynamics*, vol. 35, pp. 1739–1766, 2006. Cited on page(s) 41

[173] Pantazopoulou, S. and Bonacci, J., "On earthquake resistant reinforced concrete frame connections," *Canadian Journal of Civil Engineering*, vol. 21, pp. 307–328, 1994. Cited on page(s) xvi, 19, 60, 65, 72, 236

[174] Pantelides, C., Clyde, C., and Reaveley, L., "Performance-based evaluation of reinforced concrete building exterior joints for seismic excitation," *Earthquake Spectra*, vol. 18, pp. 449–480, Aug 2002. Cited on page(s) viii, 139, 145, 147, 157, 158, 225, 229

[175] Park, R., "A summary of results of simulated seismic load tests on reinforced concrete beam-column joints, beams and columns with substandard reinforcing details," *Journal of Earthquake Engineering*, vol. 6, no. 2, pp. 147–174, 2002. Cited on page(s) 57

[176] Park, R. and Gamble, W., *Reinforced Concrete Slabs*. Wiley, 2nd ed., 2000. Cited on page(s) 216

[177] Park, R., Priestley, M., and Gill, W., "Ductility of square-confined concrete columns," *ASCE J. of the Structural Division*, vol. 108, no. 4, pp. 929–950, 1982. Cited on page(s) 31, 32, 36, 37, 39, 46, 49, 50, 53, 64

[178] Park, S. and Mosalam, K., "Shear strength models of exterior beam-column joints without transverse reinforcement," PEER Report 2009/106, Pacific Earthquake Engineering Research Center, University of California, Berkeley, November 2009. Cited on page(s) 3, 11

[179] Park, S., *Experimental and Analytical Studies on Old Reinforced Concrete Buildings with Seismically Vulnerable Beam-Column Joints*. PhD thesis, University of California, Berkeley, Berkeley, CA, 2010. Cited on page(s) viii, xii, 4, 5, 139, 179, 180, 182, 225, 229

[180] Park, S. and Mosalam, K., "Experimental investigation of non-ductile reinforced concrete corner beam-column joints with floor slabs," *ASCE Journal of Structural Engineering (posted ahead of print)*, February 2012. Cited on page(s) 4, 179

[181] Parvin, A. and Granata, P., "Investigation on the effects of fiber composites at concrete joints," *Composites: Part B*, vol. 31, pp. 499–509, 2000. Cited on page(s) xvii, 27, 60, 240

[182] Pennucci, D., Beccarini, S., and Ianniruberto, U., "Numerical analysis of beam-column concrete joints retrofitted with FRP," in *14th European Conference on Earthquake Engineering (14ECEE)*, (Ohrid, Macedonia), 2010. Cited on page(s) xviii, 51, 60, 66, 251

[183] Pessiki, S., Conley, C., Gergely, P., and White, R., "Seismic behavior of lightly reinforced concrete column and beam-column joint details," Report NCEER-90-0014, National Center for Earthquake Engineering Research, SUNY at Buffalo, Buffalo, NY, August 1990. Cited on page(s) 18

[184] Pochanart, S. and Harmon, T., "Bond-slip model for generalized excitation including fatigue," *ACI Materials Journal*, vol. 86, pp. 465–476, Sept-Oct 1989. Cited on page(s) 111

[185] Popovics, S., "A numerical approach to the complete stress-strain curve of concrete," *Cement and Concrete Research*, vol. 3, no. 5, pp. 583–599, 1973. Cited on page(s) 40, 44, 77

[186] Quek, S. and Bian, C., "Nonlinear behavior of low ductility RC frame under base excitations," in *Finite Elements in Civil Engineering Applications: Third DIANA World Conference* (Hendriks, M. and Rots, J., eds.), (Tokyo, Japan), pp. 503–508, Taylor and Francis, October 2002. Cited on page(s) xvii, 32, 60, 63, 69, 242

[187] Rashid, Y., "Ultimate strength analysis of prestressed concrete pressure vessels," *Nuclear Engineering and Design*, vol. 7, no. 4, pp. 334–344, 1968. Cited on page(s) 25

[188] Reinhardt, H., Cornelissen, H., and Hordijk, D., "Tensile tests and failure analysis of concrete," *ASCE Journal of Structural Engineering*, vol. 112, pp. 2642–2477, November 1986. Cited on page(s) vii, xii, 85, 87, 88, 89, 90, 91, 92, 94, 95, 96

[189] Remmel, G., "Zum zug und schubtragverhalten von bauteilen aus hochfestem beton," tech. rep., Deutscher Ausschuss für Stahlbeton, Beuth Verlag, Berlin, Germany, 1994. Cited on page(s) 85, 93, 135

[190] Reys de Ortiz, I., *Strut and tie modeling of reinforced concrete short beams and beam-column joints*. PhD thesis, University of Westminster, 1993. Cited on page(s) 22

[191] Saenz, L., "Discussion of 'Equation for the stress-strain curve of concrete' by Desayi and Krishnan," *Proc. of ACI*, vol. 61, no. 9, pp. 1229–1235, 1964. Cited on page(s) 31, 32, 36, 37, 39, 46, 49, 50, 54, 77, 78

[192] Sagbas, G., Vecchio, F., and Christopoulos, C., "Computational modeling of the seismic performance of beam-column subassemblies," *Journal of Earthquake Engineering*, vol. 15, no. 4, pp. 640–663, 2011. Cited on page(s) xviii, 52, 59, 60, 64, 65, 66, 68, 72, 123, 251

[193] Sagbas, G., "Nonlinear finite element analysis of beam-column subassemblies," Master's thesis, University of Toronto, 2007. Cited on page(s) 52, 59

[194] Sasmal, S., Novák, B., and Ramanjaneyulu, K., "Numerical analysis of underdesigned reinforced concrete beam–column sub-assemblages under cyclic loading," *Computers and Concrete, An International Journal*, vol. 7, no. 3, pp. 203–220, 2010. Cited on page(s) 53, 59, 65, 66, 99

[195] Sasmal, S., Novák, B., and Ramanjaneyulu, K., "Numerical analysis of fiber composite-steel plate upgraded beam-column sub-assemblages under cyclic loading," *Composite Structures*, vol. 93, pp. 599–610, 2011. Cited on page(s) xviii, 53, 59, 60, 252

[196] Sato, T. and Shirai, N., "Elasto-plastic behavior of RC shear walls," in *Summaries of Technical Papers of Annual Meeting, C-2*, pp. 1615–1618, 1978. Cited on page(s) 31, 32, 36, 37, 39, 46, 49, 50

[197] Scott, R., "Intrinsic mechanisms in reinforced concrete beam-column connection behavior," *ACI Structural Journal*, vol. 93, no. 3, pp. 336–346, 1996. Cited on page(s) 34

[198] Seckin, M., *Hysteretic Behaviour of Cast-in-place Exterior Beam-Column-Slab Subassemblies*. PhD thesis, University of Toronto, Canada, 1981. Cited on page(s) 53, 65, 99

[199] Selby, R. and Vecchio, F., "Three-dimensional constitutive relations for reinforced concrete," Tech. Rep. 93-02, Univ. of Toronto, Dept. of Civil Engineering, Toronto, Canada, 1993. Cited on page(s) 24

[200] Selby, R. and Vecchio, F., "A constitutive model for analysis of reinforced concrete solids," *Canadian Journal of Civil Engineering*, vol. 24, pp. 460–470, 1997. Cited on page(s) 74, 76, 77, 135, 226

[201] Selby, R., Vecchio, F., and Collins, M., "Analysis of reinforced concrete members subject to shear and axial compression," *ACI Structural Journal*, vol. 93, May-June 1996. Cited on page(s) 74, 135, 226

[202] Sezen, H., Elwood, K., Whittaker, A., Mosalam, K., Wallace, J., and Stanton, J., "Structural engineering reconnaissance of the August 17, 1999, Kocaeli (Izmit), Turkey, earthquake," PEER Report 2000/09, Pacific Earthquake Engineering Research Center, University of California, Berkeley, December 2000. Cited on page(s) 1, 2

[203] Sharma, A., Eligehausen, R., Reddy, G., Vaze, K., Ghosh, A., and Kushwaha, H., "Investigations on inelastic behavior of non-seismically detailed reinforced concrete beam-column joints under cyclic excitations," BARC External Report No. BARC/2008/E/017, Bhabha Atomic Research Centre, Mumbai, India, 2008. Cited on page(s) xvii, 42, 60, 72, 247

[204] Shin, M. and LaFave, J., "Modeling of cyclic joint shear deformation contributions in RC beam-column connections to overall frame behavior," *Structural Engineering and Mechanics*, vol. 18, no. 5, pp. 645–670, 2004. Cited on page(s) 12

[205] Shiohara, H., Okada, K., and Kusuhara, F., "Benchmark test on R/C beam-column joints subjected to multi-axial combined loading conditions," *Proc. of the Japan Concrete Institute (in Japanese)*, vol. 13, no. 2, pp. 421–426, 2005. Cited on page(s) 46

[206] Shirai, N., "Evaluation of cyclic deterioration and post-peak behavior of RC beam-column joint assemblages by 3D FE analysis," in Lowes and Fillipou [124]. Cited on page(s) xvii, 38, 59, 60, 72, 245

[207] Sinha, B., Gerstle, K., and Tulin, L., "Stress-strain relations for concrete under cyclic loading," *ACI Journal Proceedings*, vol. 61, no. 2, pp. 195–212, 1964. Cited on page(s) vii, xii, 78, 80, 81, 82, 83, 84

[208] Soroushian, P., Obaseki, K., Nagi, M., and Rojas, M., "Pullout behavior of hooked bars in exterior beam-column connections," *ACI Structural Journal*, vol. 85, no. 6, pp. 269–279, 1988. Cited on page(s) 40

[209] Sritharan, S., Priestley, M. J. N., and Seible, F., "Nonlinear finite element analyses of concrete bridge joint systems subjected to seismic actions," *Finite Elements in Analysis and Design*, vol. 36, no. 3-4, pp. 215 – 233, 2000. Cited on page(s) xvi, 25, 60, 64, 239

[210] Stankowski, T. and Gerstle, K., "Simple formulation of concrete behavior under multiaxial load histories," *ACI Journal*, vol. 82, no. 2, pp. 213–221, 1985. Cited on page(s) 20

[211] Strobrand, J. and Kolpa, J., "The behaviour of reinforced concrete column-to-beam joints – Part 1: Corner joints subjeted to negative moments," Research Report 5-83-9, Delft University of Technology, Dept. of Civil Engineering, The Netherlands, 1983. Cited on page(s) 17

[212] Suzuki, N., Joshie, K., Otani, S., and Aoyama, H., "Behaviour of reinforced concrete beam-column subassemblages with and without slab," tech. rep., Department of Architecture, Faculty of of Engineering, University of Tokyo, 1984. Cited on page(s) 37

[213] Tajima, K., Kitayama, K., Okuda, M., and Kishida, S., "Influences of beam and column bar bond on failure mechanism in reinforced concrete interior beam-column joints," *Proc. of the Japan Concrete Institute (in Japanese)*, no. 3, pp. 697–702, 2000. Cited on page(s) 38

[214] Tajima, K., Mishima, T., and Shirai, N., "3-D finite element cyclic analysis of RC beam-column joint using special bond model," in *Proceedings of the 13th World Conference on Earthquake Engineering (13WCEE)*, (Vancouver, B.C., Canada), August 2004. Cited on page(s) 38

[215] Tassios, T., "Properties of bond between concrete and steel under load cycles idealising seismic actions," in *AICAP-CEB Symposium: Structural Concrete Under Seismic Action, CEB Bulletin d' Information*, vol. 1, (Rome), 1979. Cited on page(s) 111

[216] Thiess, A., "Modeling the earthquake response of older reinforced concrete beam-column building joints," Master's thesis, University of Washington, 2005. Cited on page(s) 12

[217] Thorenfeldt, E., Tomaszewicz, A., and Jensen, J., "Mechanical properties of high-strength concrete and applications in design," in *Proc. Symp. Utilization of High-Strength Concrete*, (Stavanger, Norway), 1987. Cited on page(s) xii, 24, 57, 77, 78, 79, 135, 226

[218] Tian, Y., Jirsa, J., Bayrak, O., Widianto, and Arqudo, J., "Behavior of slab-column connections of existing flat-plate structures," *ACI Structural Journal*, vol. 105, pp. 561–569, Sept-Oct 2008. Cited on page(s) 52

[219] Tubosaki, H., Oka, K., Hurukawa, J., and Shiohara, H., "Evaluation of slab-beam-column joints subjected to bidirectional loading," in *Summaries of Technical Papers of Annual Meeting of Architectural Institute of Japan (in Japanese)*, pp. 877–882, 1993. Cited on page(s) 39

[220] Ueda, T., Lin, I., and Hawkins, N., "Beam bar anchorage in exterior column-beam connections," *ACI Journal*, vol. 83, pp. 412–422, May-June 1986. Cited on page(s) 123, 125

[221] Uzumeri, S., Bond, J., and Goyal, A., "Ductility of reinforced concrete beam-column connections under seismic loading," Research Report 72-03, University of Toronto, Dept. of Civil Engineering, 1972. Cited on page(s) 15

[222] van Mier, J., "Examples of non-linear analysis of reinforced concrete structures with DIANA," *Heron (Delft Univ. of Technology)*, vol. 32, no. 3, pp. 1–147, 1987. Cited on page(s) xvi, 16, 60, 235

[223] Vecchio, F., "Towards cyclic load modeling of reinforced concrete," *ACI Structural Journal*, vol. 96, no. 2, pp. 193–202, 1999. Cited on page(s) 130, 131, 135

[224] Vecchio, F., "Disturbed stress field model for reinforced concrete: Formulation," *ASCE Journal of Structural Engineering*, vol. 126, pp. 1070–1077, September 2000. Cited on page(s) 44, 52

[225] Vecchio, F. and Collins, M., "Response of reinforced concrete to in-plane shear and normal stresses," Publ. No. 82-03, Dept. of Civil Engineering, Univ. of Toronto, Canada, 1982. Cited on page(s) 97

[226] Vecchio, F. and Collins, M., "The modified compression-field theory for reinforced concrete elements subjected to shear," *ACI Journal*, vol. 83, pp. 219–231, March 1986. Cited on page(s) 19, 24, 44, 74, 130

[227] Vecchio, F. and Collins, M., "Compression response of cracked reinforced concrete," *ASCE Journal of Structural Engineering*, vol. 119, no. 12, pp. 3590–3610, 1993. Cited on page(s) 77, 135

[228] Viwathanatepa, S., Popov, E., and Bertero, V., "Effects of generalized loadings on bond of reinforcing bars embedded in confined concrete blocks," Tech. Rep. UCB/EERC-79/22, Earthquake Engineering Research Center (EERC), University of California, Berkeley, 1979. Cited on page(s) vii, xiii, 22, 41, 110, 111, 115, 117, 121, 122

[229] Viwathanatepa, S., Popov, E., and Bertero, V., "Seismic behavior of reinforced concrete interior beam-column subassemblages," Report EERC 79-22, Earthquake Engineering Research Center (EERC), University of California, Berkeley, 1979. Cited on page(s) 17

[230] Vollum, R., *Design and Analysis of Reinforced Concrete Beam-Column Joints*. PhD thesis, Imperial College, London, 1998. Cited on page(s) xvi, 22, 60, 237

[231] Will, G., Uzumeri, S., and Sinha, S., "Application of finite element method to the analysis of reinforced concrete beam-column joints," in *Proc. of Specialty Conf. on Finite Element Method in Civil Engineering*, (Canada), pp. 745–766, CSCE, June 1972. Cited on page(s) xvi, 15, 60, 71, 234

[232] Willam, K. J. and Warnke, E. P., "Constitutive models for the triaxial behavior of concrete," in *Proceedings of the International Assoc. for Bridge and Structural Engineering*, vol. 19, pp. 1– 30, 1975. Cited on page(s) 20, 21, 22, 31, 32, 34, 36, 37, 39, 40, 46, 49, 50, 57, 64

[233] Youssef, M. and Ghobarah, A., "Modelling of RC beam-column joints and structural walls," *Journal of Earthquake Engineering*, vol. 5, no. 1, pp. 93–111, 2001. Cited on page(s) 12

[234] Zaid, S., Shiohara, H., and Otani, S., "Test of a joint reinforcing detail improving joint capacity of R/C interior beam-column joint," in *The 1st Japan-Korea Joint Seminar on Earthquake Engineering for Building Structures*, (Seoul, Korea), Seoul National Univ., 1999. Cited on page(s) 32, 42

[235] Zhang, D., Noguchi, H., and Kashiwazaki, T., "Two-dimensional finite element analysis on shear performance of RC interior beam-column joints reinforced by a new reinforcing method," in *Finite Elements in Civil Engineering Applications: Third DIANA World Conference* (Hendriks, M. and Rots, J., eds.), (Tokyo, Japan), pp. 455–465, Taylor and Francis, October 2002. Cited on page(s) xvii, 31, 58, 60, 242

COLOPHON

This thesis was typeset by the author using the XeTeX flavor of LaTeX. The body is set in Monotype Bembo Book, titles and headings in Gill Sans, and mathematics in AMS Euler. Where the Institute Thesis Manual allowed, adherence was sought to Robert Bringhurst's *The Elements of Typographic Style* and Edward Tufte's *The Visual Display of Quantitative Information*.

VITA

James Benjamin Deaton was born in Atlanta, GA in 1980. He completed a B.S., M.S., and Ph.D. in Civil and Environmental Engineering at the Georgia Institute of Technology in 2003, 2005, and 2012, respectively. His doctoral research explored the vulnerability of seismically deficient exterior beam-column joints during reversed cyclic loading using nonlinear finite element analysis. His master's research focused on the evaluation of various numerical algorithms for the design of reinforced concrete slab systems and their implementation in the commercial finite element software GT STRUDL. Other research topics investigated during graduate school include automated mesh generation algorithms, incorporation of torsion effects in numerical slab design procedures, analysis of continuously reinforced concrete pavements, and various other forensic engineering projects. During graduate school, he also taught undergraduate mechanics courses for eight semesters in the Georgia Tech College of Engineering. He previously worked as a structural engineering analyst for The Southern Company. He is a voting member of ACI Committee 447 (Finite Element Analysis of Reinforced Concrete). He may be permanently contacted through the website: `http://jamesbdeaton.com`